

ADVANCED CHARACTERIZATION OF AQUEOUS INORGANIC NANOSCALE
CLUSTERS

by

MILTON NEILL JACKSON, JR.

A DISSERTATION

Presented to the Department of Chemistry and Biochemistry
and the Graduate School of the University of Oregon
in partial fulfillment of the requirements
for the degree of
Doctor of Philosophy

June 2015

DISSERTATION APPROVAL PAGE

Student: Milton Neill Jackson, Jr.

Title: Advanced Characterization of Aqueous Inorganic Nanoscale Clusters

This dissertation has been accepted and approved in partial fulfillment of the requirements for the Doctor of Philosophy degree in the Department of Chemistry and Biochemistry by:

Catherine Page	Chairperson
Darren W. Johnson	Advisor
Shannon W. Boettcher	Core Member
Richard P. Taylor	Institutional Representative

and

Scott L. Pratt	Dean of the Graduate School
----------------	-----------------------------

Original approval signatures are on file with the University of Oregon Graduate School.

Degree awarded June 2015

© 2015 Milton Neill Jackson, Jr.

DISSERTATION ABSTRACT

Milton Neill Jackson, Jr.

Doctor of Philosophy

Department of Chemistry and Biochemistry

June 2015

Title: Advanced Characterization of Aqueous Inorganic Nanoscale Clusters

Inorganic nanoscale clusters have garnered significant interest for many practical applications within the fields of materials chemistry, inorganic chemistry, geochemistry, and environmental chemistry. However, the fundamental inner workings of how these materials interact in the solid state and solution continues to be a very elusive problem for scientists. My dissertation focuses on taking non-traditional approaches and characterization techniques to further understand the dynamic interactions of some of the aforementioned clusters. Chapter I is a comprehensive survey and perspective on selected characterization techniques used to study Group 13 aqueous nanoscale clusters and other polyoxometalates in solution. Chapter II focuses on utilizing Raman spectroscopy, infrared spectroscopy, and quantum mechanical computations to unambiguously identify Group 13 tridecameric species in the solid state and aqueous solution. Chapter IV discusses the first instance of transmetalation of aqueous aluminum clusters via salt addition of $\text{In}(\text{NO}_3)_3$ in aqueous or methanol. Chapters IV and V explore the effects that aprotic and protic solvents can have on the solution speciation of the flat aluminum tridecamer. Chapter VI discusses the utility of using electrochemically synthesized gallium tridecamer and its functional use as a thin film semiconductor. Chapter VII describes a unique graduate level chemistry course designed to allow students to conduct

and generate publication-worthy research within the timeframe of the course. Chapter VIII ventures out beyond the group 13 cluster and introduces techniques used to study the formation and stability of aqueous hafnium clusters. Chapter IX details the synthesis and characterization of rhombic structured copper clusters in the solid state. Finally, chapter X highlights my unfinished projects that can propel future research within the lab.

This dissertation includes previously published and unpublished co-authored material.

CURRICULUM VITAE

NAME OF AUTHOR: Milton Neill Jackson, Jr.

GRADUATE AND UNDERGRADUATE SCHOOLS ATTENDED:

University of Oregon, Eugene, Oregon
Prairie View A&M University, Prairie View, Texas
Grambling State University, Grambling, Louisiana

DEGREES AWARDED:

Doctor of Philosophy, Chemistry, 2015, University of Oregon
Master of Science, Chemistry, 2011, University of Oregon
Bachelor of Science, Chemistry, 2009, Prairie View A&M University

AREAS OF SPECIAL INTEREST:

Sustainable materials chemistry
Polyoxometalate cluster chemistry
Polymer chemistry
Inorganic chemistry
Chemistry education and outreach

PROFESSIONAL EXPERIENCE:

Graduate student research assistant, University of Oregon, 2012-2015
Co-director for pipeline to higher learning, University of Oregon, 2013-2015
Research Chemist Intern, Bend Research, 2011
Undergraduate Research Assistant, Prairie View A&M University, 2007-2009

GRANTS, AWARDS, AND HONORS:

CSMC informal science education fellowship, University of Oregon, 2014-2015
OMSI science communication fellow, Oregon Museum of Science and Industry, 2014
CSMC Hermiston Fellowship, University of Oregon, 2013-2014
CMSC Chemistry Fellowship, University of Oregon, 2010-2013
Ebony Man of the Year, Black Women of Achievement, 2013

Black Student Union's "Most Accomplished" Award, Black Student Union, 2012

Welch's Foundation Scholarship, Prairie View A&M University, 2007-2009
Distinguished Student Scholarship, Prairie View A&M University, 2006-2009
Science Technology Engineering Mathematics (STEM) scholarship, Prairie View A&M University, 2007-2009
Science and Engineering Alliance (SEA) Fellowship, Prairie View A&M University, 2007

PUBLICATIONS:

Jackson Jr., M.N.; Devonish, M.K.; Wills, L.A.; Ma, Z.; Cheong, P.H.; Nyman, M.; Hayes, S.; Johnson, D.W., Critical overview and perspective of characterization techniques used in polyoxometalate cluster chemistry. *Dalton Trans.* ***In press.***

Carnes, M.E.; Knutson, C.C.; Nadarajah, A.; Jackson, M.N., Jr.; Oliveri, A.F.; Norelli, K.M.; Crockett, B.M.; Bauers, S.R.; Moreno-Luna, H.A.; Taber, B.N.; Pacheco, D.J.; Olson, J.Z.; Brevick, K.R.; Sheehan, C.E.; Johnson, D.W.; Boettcher, S.W., *J. Mater. Chem. C* **2014**, 2, 8492-8496.

Kamunde-Devonish, M.K.; Jackson Jr., M.N.; Mensinger, Z.L.; Zakharov, L.N.; Johnson, D. W., *Inorg. Chem.* **2014**, 53, 7101-7105.

Knutson, C.C.; Jackson, M.N.; Beekman, M.; Carnes, M.E.; Johnson, D.W.; Johnson, D.C.; Keszler, D.A., **2014**, 91, 200-205.

Jackson, M.N., Jr.; Wills, L.A.; Chang, I.Y.; Carnes, M.E.; Scatena, L.F.; Cheong, P.H.; Johnson, D.W., **2013**, 52, 6187-6192.

Alemayehu, M.; Davis, J.E.; Jackson, M.; Lessig, B.; Smith, L.; Sumega, J.D.; Knutson, C.; Beekman, M.; Johnson, D.C.; Keszler, D.A., **2011**, 13, 2037-2040.

ACKNOWLEDGMENTS

I could probably write an entire separate thesis alone while trying to thank everyone whose help motivate, inspire, and support me along the way through this journey. However, I will do my best to limit this one page. First, I would have to give my greatest appreciation to Dave C. Johnson for even paving to the way and giving me chance at a time when no one else would. To this day, May 20, 2010 is without a doubt in my top two greatest moments of my life thus far. My advisor Darren W. Johnson has been nothing short of spectacular to me. I really cannot put into any kind of prospective the amount of respect and admiration I have for him and what his support has meant to me over the years. It would be a crime against humanity if I did not mention my partner in crimes Maisha K. Devonish and Matti Alemayehu. For Matti, we can in together and left together and it was so awe-inspiring and motivating watching you succeed. As such, it made me want to push even harder so that I would not fall behind. And of course Maisha: like Darren, I really cannot express enough gratitude and appreciation in being able to look up to you and model after. Not to mention that whole thing of re-learning how to properly use the English language. I certainly would not have had the success within this program without her. To my two children Alexia G. Smith and Dolly W. Zhen, I have no idea of how I stumbled into you both, but I will be eternally grateful for all the great work you all have done since your first day on October 10, 2014. Watching you both grow into blossoming young chemist and leading by example has been such a joy for me. I have no doubts that the two of you will go on to do wonderful things in the future and I will enjoy reading about you in the headlines. Lastly, I thank many of the students at North Eugene High school (Lizzy, Jasmine, Preston, Issac, AJ, JJ, and Kayleah) for giving my

experience far more more meaning and allowing me to be a source of positive influence
in your lives.

I dedicate this to “fifty-five” as my biggest source of motivation throughout this journey.

TABLE OF CONTENTS

Chapter	Page
I. CURRENT APPROACHES TO THE CHARACTERIZATION OF AQUEOUS INORGANIC CLUSTERS	1
1.1. Introduction.....	1
1.2. Techniques in NMR Spectroscopy	7
1.2.1. ¹ H-NMR.....	10
1.2.2. Diffusion NMR.....	11
1.2.3. Isotope-Exchange Dynamics	15
1.2.4. Solid-state NMR (ssNMR)	21
1.3. Scattering Techniques in Aqueous Cluster Chemistry	28
1.3.1. Studying Clusters via SAXS.....	28
1.3.1.1. Lithium Niobate Thin Films from Cluster Precursors	32
1.3.1.2. Understanding the Mechanism of Linking Clusters	34
1.3.1.3. Investigating the Polymerization of Hf-tetrameric Clusters	34
1.3.2. Dynamic Light Scattering Applied to Cluster Characterization	36
1.3.2.1. Screening for Clusters in Solution.....	38
1.3.2.2. Monitoring the Solution Stability of Hafnium Sulfate Clusters ...	39
1.3.3. Phase Analysis Light Scattering (PALS).....	42
1.3.4. Raman Spectroscopy.....	46
1.4. Computational Studies.....	51
1.4.1. Vibrational Spectroscopy.....	51

Chapter	Page
1.4.2. Thermodynamic Stability.....	53
1.4.3. Dynamics	55
1.4.4. Electronic Properties.....	56
1.5. Conclusions.....	57
1.6. Chapter II Bridge	58
 II. IDENTIFYING NANOSCALE M ₁₃ CLUSTERS IN THE SOLID STATE AND AQUEOUS SOLUTION: VIBRATIONAL SPECTROSCOPY AND THEORETICAL STUDIES.....	
2.1. Introduction.....	59
2.2. Experimental	61
2.2.1. Materials and Sample Preparation	61
2.2.2. Zn Reduction Method for the Synthesis of Ga ₁₃ (μ ₃ -OH) ₆ (μ ₂ - OH) ₁₈ (H ₂ O) ₂₄ (NO ₃) ₁₅	61
2.2.3. Raman and Infrared Instrumentation	62
2.2.4. Computational Methods.....	62
2.3. Al ₁₃ (μ ₃ -OH) ₆ (μ ₂ -OH) ₁₈ (H ₂ O) ₂₄ (NO ₃) ₁₅ : Results and Discussion	63
2.3.1. Raman Spectroscopy: Solid Phase.....	63
2.3.2. Infrared Spectroscopy: Solid Phase	65
2.3.3. Raman Studies: Solution Phase	66
2.4. Ga ₁₃ (μ ₃ -OH) ₆ (μ ₂ -OH) ₁₈ (H ₂ O) ₂₄ (NO ₃) ₁₅ : Results and Discussion	68
2.4.1. Raman Spectra Analysis: Solid Phase.	68
2.4.2. Infrared Results: Solid Phase.....	70

Chapter	Page
2.4.3. Raman Spectra Analysis: Solution Phase	71
2.5. Al ₁₃ vs Ga ₁₃ : Discussion	72
2.6. Conclusions.....	73
2.7. Chapter III Bridge.....	74
III. TRANSMETALLATION OF AQUEOUS INORGANIC CLUSTERS: A USEFUL ROUTE TO THE SYNTHESIS OF HETEROMETALLIC ALUMINUM AND INDIUM HYDROXO-AQUO CLUSTERS.....	
	75
3.1. Introduction.....	75
3.2 Experimental.....	79
3.2.1. General Methods.....	79
3.2.2 General Procedure for the Synthesis of Al ₇ In ₆ and Ga ₇ In ₆	80
3.3. Results and Discussion	80
3.4. Conclusions.....	87
3.5. Chapter IV Bridge.....	87
IV. INVESTIGATION OF THE PROTON EXCHANGE RATE KINETICS OF AQUEOUS [Al ₁₃ (μ ₃ -OH) ₆ (μ ₂ -OH) ₁₈ (H ₂ O) ₂₄] ¹⁵⁺	
	88
4.1. Introduction.....	88
4.2. Experimental.....	90
4.2.1. Materials and Methods.....	90
4.2.2. General Procedure for the Synthesis of f-Al ₁₃	90
4.2.3. ¹ H-NMR Spectroscopy	90

Chapter	Page
4.2.4. Dynamic Light Scattering	91
4.2.5. Infrared Spectroscopy	91
4.2.6 Rate Equations	91
4.3. Results and Discussion	93
4.3.1. H ₂ O/Acetone-d ₆	93
4.3.2. D ₂ O	100
4.4. Conclusions.....	104
4.5. Chapter V Bridge.....	104
 V. FORMATION OF ALUMINIUM NANO-AGGLOMERATES FROM AQUEOUS FLAT-Al ₁₃ (μ ₃ -OH) ₆ (μ ₂ -OH) ₁₈ (H ₂ O) ₂₄ (NO ₃) ₁₅ : INVESTIGATIONS OF SOLVENT EFFECTS ON SOLUTION DYNAMICS	
5.1. Introduction.....	105
5.2. Experimental	108
5.2.1. Materials and Sample Preparation	108
5.2.2. Dynamic and Phase Analysis Light Scattering.....	108
5.2.3. NMR Spectroscopy.....	108
5.2.4. Raman Spectroscopy.....	109
5.3. Results and Discussion	109
5.4. Conclusions.....	117
5.5. Chapter VI Bridge.....	117

Chapter	Page
VI. ELECTROCHEMICAL SYNTHESIS OF FLAT-[Ga _{13-x} In _x (μ ₃ -OH) ₆ (μ-OH) ₁₈ (H ₂ O) ₂₄ (NO ₃) ₁₅] CLUSTERS AS AQUEOUS PRECURSORS FOR SOLUTION-PROCESSED SEMICONDUCTORS.....	118
6.1. Introduction.....	118
6.2. Results and Discussion	121
6.3. Conclusions.....	128
6.4. Chapter VII Bridge	129
VII. MENTORING GRADUATE STUDENTS IN RESEARCH AND TEACHING BY UTILIZING RESEARCH AS A TEMPLATE.....	130
7.1. Introduction.....	130
7.2. Role of Instructors.....	134
7.3. Course Objectives for Students.....	134
7.4. Graduate Instructor Reflections	140
7.5. Former Student Reflections	141
7.6. Evaluation and Evolution.....	142
7.7. Conclusions.....	145
7.8. Chapter VIII Bridge	146
VIII. MECHANISMS DIRECTING THE NANOSCALE PATTERNING OF THIN FILMS OF HAFNIUM CLUSTERS	147
8.1. Introduction.....	147
8.2. Experimental	150
8.2.1. Solution Precursor Preparation	150

Chapter	Page
8.2.2. Film Deposition	150
8.2.3. Dynamic Light Scattering (DLS).....	151
8.2.4. Microscopy	151
8.2.5. Raman Spectroscopy.....	151
8.2.6. Quartz Crystal Microbalance (QCM)	152
8.2.7. X-ray Photoelectron Spectroscopy (XPS)	152
8.2.8. Peroxide Analysis	152
8.3. Results and Discussion	153
8.4. Conclusions.....	163
8.5. Chapter IX Bridge.....	163
 IX. SYNTHESIS AND STRUCTURAL DETERMINATION OF A 1-D CHAIN COORDINATION POLYMER COMPOSED OF $\{M(\mu\text{-OH})_2M\}$ RHOMB- CENTERED TETRANUCLEAR COPPER SUBUNITS	
	164
9.1. Introduction.....	164
9.2. Experimental	166
9.2.1. Materials and Methods.....	166
9.2.2. Synthesis of $\{(C_5H_6N)_2[Cu_4(OH)_2(SO_4)_4(H_2O)_4]\}_n$	166
9.2.3. Crystal Structure Determination	166
9.2.4. Raman Spectroscopic Analysis.....	167
9.3. Results and Discussion	167
9.4. Conclusions.....	171
9.5. Chapter X Bridge.....	173

Chapter	Page
X. CONCLUDING REMARKS.....	174
APPENDIX: SUPPLEMENTAL INFORMATION.....	175
REFERENCES CITED.....	214

LIST OF FIGURES

Figure	Page
<p>1.1. Examples of discrete metal-oxo/hydroxo clusters (A and B) and polynuclear ‘prenucleation’ clusters (C). From left to right: A) The Lindqvist ion $[M_6O_{19}]^{x-}$ ($M = Mo, W, Nb, Ta; x = 2-8$), the Keggin ion $[TM_{12}O_{40}]^{y-}$ ($M = Mo, W, Nb; T = Al, Si, P, etc. x = 3-16$), $[M_8(OH)_8(H_2O)_{12}]^{8+}$ ($M=Zr,Hf$). B) Side and planar projections of the flat tridecamer $[M_{13}(OH)_{24}(H_2O)_{24}]^{15+}$ ($M=Al,Ga,In$) with and without the counterions present. The hydrogen atoms are removed in the side projection to make to view easier to look at. C) Prenucleation clusters illustrating the nondiscrete linking and assembly of metal-oxo/hydroxyl/aqua octahedra through corner-sharing, edge-sharing and face-sharing. This is illustrative of the process that takes place with hydrolysis and condensation of metals that do not form discrete, isolatable clusters without the use of protective ligands. (i.e. open shell transition metals including Fe, Ni, Mn). Color legend: Figure 1A and 1C - Metal atoms = green, oxygen = red, hydrogen = white. For Figure 1B - Metal atoms = purple, oxygen = red, nitrogen = blue, hydrogen = white.</p>	4
<p>1.2. 1H-NMR of 2 mM f-Ga₁₃ and each heterometallic f-Ga_xIn_{13-x} cluster in d₆-DMSO</p>	11
<p>1.3. Representative DOSY spectrum of a hydrated f-Ga₁₃ cluster in d₆-DMSO ($D_{avg} = 0.955 \times 10^{-10} \pm 0.064 \times 10^{-10} m^2/s$). (■) H₂O peak and (●) DMSO peak</p>	14
<p>1.4. (a) A large uranyl-pyrophosphate cluster has two forms in aqueous solution. The two forms differ in the dimpling or symmetry and the nominal stoichiometry of the cluster is $[(UO_2)_{24}(O_2)_{24}(P_2O_7)_{12}]^{48-}$, excluding associated counterions. In the image, yellow are uranyl-oxide polyhedra, the gray tetrahedra are pyrophosphates and the spheres are sodium counterions. (b) ^{31}P-NMR spectra show the progressive coalescence of the two ^{31}P sites in the structure as the rates of isomerization increase with temperature; (c) the reaction rates are affected by the counterion chosen for the system. Tetramethyl ammonium ion selects for the asymmetric form. The system is an excellent example of two-site exchange in an NMR system, although in this case the two sites are within the same molecule and become magnetically equivalent as the structure isomerizes rapidly</p>	16

Figure	Page
1.5. Space-filling polyhedral representation of the f-Ga ₁₃ molecular cluster from a geometry-optimized calculation (a) top down view, (b) side view, (c) individual polyhedral representation of the three gallium sites: core (blue), middle ring (orange), and outer ring (green).....	24
1.6. ⁷¹ Ga MAS NMR spectral data for the f-Ga ₁₃ molecular cluster at two magnetic fields, (a) 13.9T and (b) 21.1T. Experimental spectra data are shown in black, the individual line shapes are shown in blue (core), orange (middle ring), and green (outer ring), and the red spectrum is the compiled model. Asterisks denote spinning side bands of the central transition, and the double dagger indicates the position of the gallium nitrate impurity resonance	25
1.7. A geometry-optimized structure of the f-Ga ₁₃ molecular structure computed from CASTEP (a) top view and (b) side view. Atoms are color coded as in Figure 1 and the electric field gradient depicted as distorted grey shapes (ellipsoids) around the gallium atoms. The core gallium, which is highly symmetric, has a small EFG, which is difficult to see in this rendering. The individual sites have been extracted to depict the electric field gradients surrounding each atom: (c) the core site, (d) middle ring, and (e) outer ring. The core EFG in figure 3c was multiplied by a factor of 2	27
1.8. One dimensional data extracted from a two dimensional scattering pattern. (left) Pair distance distribution functions indicative of particle shape (right)	31
1.9. SAXS scattering curves for Li₆ (left) and Li₈ (right) along with a total curve fit (dotted line) for the highest concentration. For Li₆ , the curves feature a broad peak around $\ln(q)=1 \text{ nm}^{-1}$, which indicates interactions between clusters. The Li₈ curves were fit with two-phase models, where the phase of larger scattering species (curve fit between $\ln(q) = -4$ to -3 nm^{-1}) indicates incipient crystallization of the clusters	32
1.10. PDDF analysis of Cs (left) and Rb salts (right) of dodecaniobate $[(\text{Nb}=\text{O})\text{GeNb}_{12}\text{O}_{40}]^{13-}$. Black peak is the monomeric unit, green peaks are long axis of dimers, red dots are experimental data, and blue is the multipeak Gaussian fit.....	33
1.11. PDDF for 500 mM hafnium-sulfate solution aged for 0h (green), 24h (blue), and 72h (red).....	35

Figure	Page
1.12. Time stability study of 500 mM hafnium sulfate (HafSO _x) with added H ₂ O ₂ (grey) and without H ₂ O ₂ (black). The large error that is prominent at the later times is due to a high degree of polydispersity that is inherent with HafSO _x over time	40
1.13. Simple model of a charge particle and its surrounding charges. The intermediate distance away from the surface at which the surrounding ions release from the core particle's attractive pull and "slip" into equilibrium is defines where the zeta potential is found	45
1.14. Plot of electrophoretic mobility (black diamonds) and zeta potential (grey squares) vs pH of f-Al ₁₃ . Mobility data is shown to demonstrate the direct relationship it has with zeta potential. The isoelectric point for f-Al ₁₃ is shown to be at pH = 9	47
1.15. Stacked Raman spectra of Bismuth nitrate (black) and a bismuth hexamer (red). Notable peaks that distinguishes this cluster from bismuth nitrate include the two stretching Bi—O bands at 179 cm ⁻¹ and 409 cm ⁻¹ . The small peak at 816 cm ⁻¹ corresponds to a μ—OH bridge of the cluster. Additionally, spectral shifts of the symmetric and anti-symmetric bands of NO ₃ ⁻ ion are present. The symmetric stretching band at 1033 cm ⁻¹ for Bi(NO ₃) ₃ is blue shifted to 1054 cm ⁻¹ while the anti-symmetric band at 1483 cm ⁻¹ for Bi(NO ₃) ₃ is red shifted to 1381 cm ⁻¹ for the bismuth cluster	49
1.16. Stacked Raman spectra of f-Al ₁₃ titrated with various equivalents of HNO ₃ . The bottom spectrum represents a solution of 1 M f-Al ₁₃ with no added HNO ₃ as indicated by the ratios shown on the right of the graph	51
1.17. Top. Simulated and experimental IR overlay spectra from 500 cm ⁻¹ – 2000 cm ⁻¹ of solid state f-Ga ₁₃ . Bottom. Simulated and experimental Raman spectra from 200 - 2000 cm ⁻¹ of crystalline f-Ga ₁₃ at 25 °C. The feature shown at 464 cm ⁻¹ arises from the primary breathing mode of the cluster.....	54
2.1. Al ₁₃ Raman spectrum from 200-2000 cm ⁻¹ . The symmetric stretch of the cluster is highlighted at 478 cm ⁻¹ . The RMSD for this LSFC Raman spectrum is 0.52 %.....	64

Figure	Page
2.2. Experimental IR spectra of solid Al ₁₃ cluster from 400-1800 cm ⁻¹ displaying computational peak analysis. The RMSD for this LSFC IR spectrum is 2.0 %. A μ ₃ -OH ligand is a hydroxide group that bridges the center Al ³⁺ with two adjacent core Al ³⁺ ; μ ₂ -OH _{core} is a hydroxide group that connects two neighboring core Al ³⁺ ; μ ₂ -OH _{shell} is a hydroxide group that links one core Al ³⁺ and its closest shell Al ³⁺ ; and η-H ₂ O is a terminal water group on the shell Al ³⁺	67
2.3. Overlay of simulated (black) and experimental (gray) Raman spectra of Al ₁₃ in 1 M solution at 25 °C. All of the weak modes seen in the solid phase have merged into one broad feature ranging from 450-675 cm ⁻¹ . The RMSD for this LSFC Raman spectrum is 0.59 %.....	67
2.4. Simulated and experimental Raman spectra from 200-2000 cm ⁻¹ of crystalline Ga ₁₃ at 25 °C. The feature shown at 464 cm ⁻¹ arises from the primary breathing mode of the cluster. The RMSD for this LSFC Raman spectrum is 0.40 %.....	69
2.5. Experimental and simulated IR spectra of Ga ₁₃ in the solid phase from 400-2000 cm ⁻¹ with computational peak analysis shown. The RMSD for this LSFC IR spectrum is 1.7%	71
2.6. Simulated (A) and experimental (B) Raman spectra of the Ga ₁₃ cluster in solution phase from 350-650 cm ⁻¹ . The RMSD for this LSFC Raman spectrum is 0.57 %. The Ga-O modes coalesce into a broad feature at 502 cm ⁻¹ . Upon dilution, only the peak intensity changes with dilution suggesting that the species remains persistent in solution (bottom insert). A plot of the intensity of the peak at 502 cm ⁻¹ versus concentration shows a linear decrease with dilution. In spite of the limitations observed with IR, it is clear that with the use of vibrational spectroscopy, particularly Raman in conjunction with quantum mechanical calculations, we can characterize and identify the Ga ₁₃ cluster and distinguish it from similar species in solution and the solid state.....	73
3.1. Simple representation of the transformation from Al ₁₃ to Al ₇ In ₆ upon addition of In(NO ₃) ₃ . In ³⁺ ions (green) displace Al ³⁺ ions (purple) on the labile outer shell of the cluster. Images are wireframe and ball structures generated from the crystal structures of Al ₁₃ and Al ₇ In ₆	76
3.2. ¹ H-NMR of Al ₁₃ (A), Al ₇ In ₆ (B), and Al(NO ₃) ₃ (C).....	81

Figure	Page
3.3. <i>Top</i> : (A) Autocorrelation function of 2 mM Al ₁₃ (black) and 2 mM Al ₇ In ₆ (grey) in <i>d</i> ₆ -DMSO (traces stack on top of each other). Hydrodynamic radii of Al ₁₃ (B) and Al ₇ In ₆ (C) in <i>d</i> ₆ -DMSO are displayed in the insets. <i>Bottom</i> : (A) Autocorrelation function of 0.2 M Al ₁₃ (black) and 0.2 M Al ₇ In ₆ (grey) in H ₂ O. Hydrodynamic radii of Al ₁₃ (B) and Al ₇ In ₆ (C) in H ₂ O are displayed in the insets.....	83
3.4. Solid state Raman spectra of Al ₁₃ (black) and Al ₇ In ₆ (grey) between 100 cm ⁻¹ and 800 cm ⁻¹	84
3.5. <i>Top</i> : EDX analysis of the solution processed Al ₇ In ₆ precursor and cross-sectional TEM (top insert) of the Al _{13-x} In _x O _y thin film. The white circle represents the spot on which the EDX scan was performed. <i>Bottom</i> : AFM 3D side view of Al _{13-x} In _x O _y thin film (16 μm ²).....	86
4.1. ¹ H-NMR spectra (-5 °C to -20 °C) of f-Al ₁₃ in a 2.5:1 (v/v) mix of H ₂ O/acetone- <i>d</i> ₆ . The peak centered at 5.2 ppm is associated with bulk water in the solution. The peak at 9.8 ppm represents the hexaaqua [Al(H ₂ O) ₆] ³⁺ complex seen in the spectra for Al(NO ₃) ₃ . Peaks A, B, and C integrate to 1:1:2, respectively.....	94
4.2. Diagram of f-Al ₁₃ showing the different types of protons coordinated to the core (μ ₃ -OH, purple), middle (μ ₂ -OH, green), and outer (μ ₂ -OH', yellow) shells of aluminium metal ions. Water molecules are color-coded to reflect differences based upon symmetry, not coordination	95
4.3. Hydrodynamic radius of f-Al ₁₃ as a function of mol % acetone.....	98
4.4. Conductivity and zeta potential measurements for f-Al₁₃	98
4.5. Stacked ATR-IR spectra of 1M f-Al₁₃ at 14 mol% acetone, 14% acetone in water mixture, and pure acetone.....	99
4.6. ¹ H-NMR spectra of variable-temperature experiment for f-Al ₁₃ in D ₂ O. H ₂ O/ DMSO- <i>d</i> ₆ , respectively.....	101
4.7. ¹ H-NMR spectra of variable-temperature experiment for f-Al₁₃ in 1:2 (v/v) solution of H ₂ O/DMSO- <i>d</i> ₆	101
4.8. Plot of the kinetics data for the μ ₂ -OH proton of f-Al₁₃ in 1:2 (v/v) solution of H ₂ O/ DMSO- <i>d</i> ₆	102

Figure	Page
5.1. Hydrodynamic radius and ζ -potential of f-Al ₁₃ as a function of the mole fraction of methanol and Al ³⁺ concentration. The molarity for f-Al ₁₃ was held constant throughout each solvent mixture. Each point in the figure were collected upon immediate dissolution of f-Al ₁₃	110
5.2. Hydrodynamic radius as a function of mole fraction of alcohol for three different alcohols. Each solution mix was prepared at 100 mM Al ³⁺ concentration.....	112
5.3. Size (red) and conductivity (black) plot of 0.1 M f-Al ₁₃ in methanol as a function of time compared to 0.1 M f-Al ₁₃ in water (grey).....	113
5.4. DOSY-NMR spectra of 100 mM f-Al ₁₃	114
5.5. Stacked Raman from 700 cm ⁻¹ to 1200 cm ⁻¹ spectra various MeOH:H ₂ O mixtures of 1 M f-Al ₁₃	116
6.1. Comparison of M ₁₃ cluster synthesis routes	120
6.2. ¹ H-NMR (<i>d</i> ₆ -dmsO) spectra of washed and unwashed precipitated cluster products from DBNA and electrochemical syntheses. Based on comparison to the DBNA-derived control samples, the unwashed electrochemical product is assigned the composition Ga ₉ In ₄ , while the washed electrochemical product is assigned the composition Ga ₈ In ₅	128
6.3. Solid-state Raman spectra of nitrate salts and electrochemically generated cluster samples. Spectra for cluster compounds were collected on a single crystal using a Raman microscope and are largely free of metal nitrate impurities. Note the red-shift in the ν_1 breathing mode center for the In-substituted cluster (449 ± 1 cm ⁻¹) when compared to that for the Ga cluster (464 ± 1 cm ⁻¹). The uncertainties given are associated with the error in fitting the peak center.....	126

- 6.4. (a) Transmission electron microscopy image demonstrating the uniform morphology of thin films processed from the electrochemically-synthesized precursor. (b) Average transfer curve compiled from five bottom-gate TFTs processed using the electrochemically synthesized $\text{Ga}_{13-x}\text{In}_x$ heterometallic clusters to generate channel layers. (c) Representative transfer plots for 550 °C air-annealed In-Ga-O films created using the electrochemically synthesized $\text{Ga}_{13-x}\text{In}_x$ heterometallic cluster and starting salt solution precursors. (d) Average channel mobility determined at $V_{\text{GS}} = 40 \text{ V}$ for films made at various electrolyzed time intervals (and thus different average numbers of electrons passed into the solution per metal ion). Device performance is increased with longer electrolysis, consistent with removal of nitrate and formation of clusters. The devices consist of the following structures: Al/Si (p+)/ SiO_2 (100 nm)/In-Ga-O(15 nm)/Al, length = 150 μm , width = 1000 μm , and $V_{\text{DS}} = 0.1 \text{ V}$ (V_{DS} = drain source voltage; V_{GS} = gate source voltage; I_{D} = drain current)129
- 8.1. (a) Structure of hafnium tetramer. White: hafnium; Green: hydroxyl oxygen; Purple: oxygen in bound water. (b) DLS size analysis for a 150 mM HafSO_x solution as a function of solution age. (c) TEM image of hafnium sulfate clusters. (d) Cross-sectional TEM image of a spin-coated HafSO_x film on a Si/ SiO_x substrate with amorphous carbon protecting layer156
- 8.2. Raman spectra of (a) hydrogen peroxide, sulfuric acid, the HafSO_x precursor solution, and HafSO_x films made with and without peroxide. (b) HfOCl_2 solutions with increasing concentrations of hydrogen peroxide. (c) HafSO_x films annealed at increasingly high temperatures. (d) a HafSO_x film before and after exposure to electron beam radiation.....157
- 8.3. (a) XPS O1s spectra of a HafSO_x film collected after a long X-ray exposure time (> 30 mins). (b) XPS O1s peak evolution with increasing number of scans. (c) Quantitative comparison of O 1s peak evolution for HafSO_x films with increasing amounts of peroxide. (d) Quantitative comparison of O 1s peak evolution for HafSO_x films with increasing amounts of sulfate.....158

Figure	Page
8.4. QCM measurements of the dissolution of (a) HafSO _x films with and without peroxide developed in 5% TMAH. (b) HafSO _x films with sulfate: Hf ratio of 0.5 and 0.8 annealed at increasing temperatures and developed in 25% TMAH. (c) HafSO _x films with increasing sulfate: Hf ratio developed in 5% TMAH. (d) HafSO _x films with increasing sulfate: Hf ratio developed in 25% TMAH	160
8.5. (a-b) SEM images of contrast arrays generated by patterning films at increasing electron beam exposure doses. The HafSO _x films have sulfate: Hf ratios of (a) 0.7 (b) 0.85. (c) Contrast curve generated from AFM images of contrast arrays similar to those shown in (a-b).....	162
9.1. Ball and stick representation of the $\{(C_5H_6N)_2[Cu_4(OH)_2(SO_4)_4(H_2O)_4]\}_n$ tetramer. The pyridinium cation hydrogen bonds to the μ_3 -sulfato ligand and water ligand of two adjacent Cu ₄ subunits. The oxygen and sulfur atoms neighboring Cu1 and Cu2 are labeled (hydrogen labels omitted for clarity).....	168
9.2. Polyhedral representation of $\{(C_5H_6N)_2[Cu_4(OH)_2(SO_4)_4(H_2O)_4]\}_n$ along the a axis. The Cu subunits hydrogen-bond to pyridinium cations that π - π stack to form a 1-D chain. Copper metal ions are blue, sulfur atoms are yellow, and oxygen atoms are red.....	169
9.3. Selected bond lengths and angles for the rhomboid $\{M-(\mu-OH)_2-M\}$ core of $\{(C_5H_6N)_2[Cu_4(OH)_2(SO_4)_4(H_2O)_4]\}_n$. For clarity, atoms are not shown to scale.....	170
9.4. Bond lengths and angles for $\{(C_5H_6N)_2[Cu_4(OH)_2(SO_4)_4(H_2O)_4]\}_n$ (left) and ranges observed for the rhomboid core in related $M(\mu-O)_2$ sites (right). Image on the right from Que, et. al. ²⁵ Atoms are not shown to scale.....	170
9.5. Stacked Raman spectra of pyridine (green), cupric sulfate (red), and $\{(C_5H_6N)_2[Cu_4(OH)_2(SO_4)_4(H_2O)_4]\}_n$ (black). A) 100 cm ⁻¹ – 1700 cm ⁻¹ B) 2800 cm ⁻¹ – 3700 cm ⁻¹ . C) inset of the copper cluster from 2800 cm ⁻¹ to 3700 cm ⁻¹	172

LIST OF TABLES

Table	Page
1.1. Properties of atomic nuclei for NMR spectroscopy. Relative frequency calculated at 600 MHz (14T).....	9
1.2. Ratio of the viscosities of DMSO- <i>d</i> ₆ and DMF- <i>d</i> ₇ relative to D ₂ O and H ₂ O at 25 °C	13
4.1. Diagram of <i>f</i> -Al ₁₃ showing the different types of protons coordinated to the core (μ ₃ -OH, purple), middle (μ ₂ -OH, green), and outer (μ ₂ -OH', yellow) shells of aluminium metal ions. Water molecules are color-coded to reflect differences based upon symmetry, not coordination	96
4.2. Full-width half-max (FWHM) values for the peaks of <i>f</i> -Al ₁₃ at 3.61 ppm in 1:2 (v/v) solution of H ₂ O/ DMSO- <i>d</i> ₆	102
4.3. Residency times and activation parameters for proton sites on <i>f</i> -Al ₁₃ . Standard errors are in parentheses.	103
8.1. Normalized atomic percent of Hf, O, S for HafSO _x films with increasing SO ₄ ²⁻ :Hf molar ratios from XPS analysis. An approximate film stoichiometry derived from the XPS composition is also shown.....	163

CHAPTER I

CURRENT APPROACHES TO THE CHARACTERIZATION OF AQUEOUS INORGANIC CLUSTERS

1.1. INTRODUCTION

For this review article and subsequent first chapter of my thesis, a large team of chemist worked together to construct this ambitious review article. This team included the services of Lindsay Wills and Paul Cheong (QMC), William Casey (ESI-MS), Blake Hammann and Sophia Hayes (ssNMR), Maisha Devonish ($^1\text{H-NMR}$), Lauren Fullmore and May Nayman (SAXS). My contribution to this piece was the original conception of the idea and organization of the writing process. I also wrote three of sections on DLS, PALS, and Raman spectroscopy. I would like to thank Wyatt Technology for providing helpful discussions in explaining the schematic concepts for dynamic and phase analysis light scattering in this review, and specifically in Figure 16 in the phase analysis light scattering section. I acknowledge Dolly W. Zhen for conducting isoelectric point studies on **f-Al₁₃** using phase analysis light scattering as well. Lastly, I thank Alexia G. Smith for performing experiments on **f-Al₁₃** to $\text{Al}(\text{OH}_2)_6^{3+}$ dissociation studies using Raman spectroscopy and dynamic light scattering analysis on $\text{Al}(\text{NO}_3)_3$ in aqueous solution.

This prospective article highlights some of the traditional and non-traditional analytical tools that are presently used to characterize aqueous inorganic nanoscale clusters and polyoxometalate ions. The techniques discussed in this article include

nuclear magnetic resonance spectroscopy (NMR), small angle x-ray scattering (SAXS), dynamic and phase analysis light scattering (DLS and PALS), Raman spectroscopy, and quantum mechanical computations (QMC). For each method we briefly describe how it functions and illustrate how these techniques are used to study cluster species in the solid state and in solution through several representative case studies. In addition to highlighting the utility of these techniques, we also discuss limitations of each approach and measures that can be applied to circumvent such limits as it pertains to aqueous inorganic cluster characterization.

There are many types of widely-studied nanomaterials that are termed ‘clusters’, and a variety of characterization techniques have been applied to determine their structure in solution and the solid state. This prospective highlights some of the current and emerging approaches to cluster characterization in the context of several case studies on hydrated nanoscale clusters. We begin with a short discussion establishing what constitutes a “cluster” for the purposes of this review. A cluster is broadly defined as a species that contains several metal cations (usually 4 or more, but may contain up to several hundred) linked by ligands, and surface passivated or functionalized by additional ligands that 1) are similar to the linking ligands, or 2) organic ligands of a different nature. The ligands are most often Group 16 dianions O^{2-} , S^{2-} , or Se^{2-} , or their protonated derivatives¹ and we are limiting our focus to hydrated inorganic clusters composed only of ligands derived from water (aqua ligands), including H_2O , OH^- , or O^{2-} . For completeness, we also include tetrahedral oxoanions such as $PO_4H_x^{(3-x)-}$, $P_2O_7H_x^{(4-x)-}$, and SO_4^{2-} that may serve as counterions and/or assist in cluster coordination. There are many clusters that contain aqua ligands in their interior; but are surface-passivated by organic ligands including

alkoxides, carboxylates, amines, etc.^{2,3} Many of the characterization techniques described herein would be suitable for these clusters, but they are not a focus of the case studies in this review. We also differentiate between molecular clusters and non-molecular clusters and provide studies of both categories (Figure 1.1).

Molecular clusters have a discrete and absolute formula. Molecular clusters generally self-assemble in aqueous solution through pH control, concentration effects, counterion influence, etc, and are subsequently purified via selective crystallization. Clusters that fall into this category are predominantly the Group V/VI polyoxometalates (POMs)⁴ that are stabilized by the ubiquitous multiply bonded oxo ligand on the surface of the cluster (Figure 1.1A). Due to the strong and relatively inert M=O bond (M = V, Nb, Ta, Mo, or W) of most POMs, the propensity for agglomeration and/or precipitation via hydrolysis and condensation reactions is not of prominent concern. While POMs carry a negative charge (polyoxoanions); others such as Group 13 metals (such as Al and Ga) form polyoxocations (Figure 1.1B).⁵ These clusters tend to have similar nanoscale sizes as POMs (1-2 nm), but the Group 13 polyoxocations do not possess terminal M=O bonds and the ligands are typically protic species such as OH⁻ and H₂O instead of the oxo ligand of the POMs, thus leading to their overall positive charge. What differentiates these clusters from the non-molecular clusters discussed below is that they are sufficiently stable to condensation reactions that would lead to aggregation, allowing these species to be isolated and studied in solution over certain pH and concentration ranges. Moreover, they can be crystallized as discrete and monodisperse entities. These are the properties that the POMs and Group 13 polyoxocations share uniquely, and few other classes of metal oxo clusters have been identified that provide this level of stability in solution.

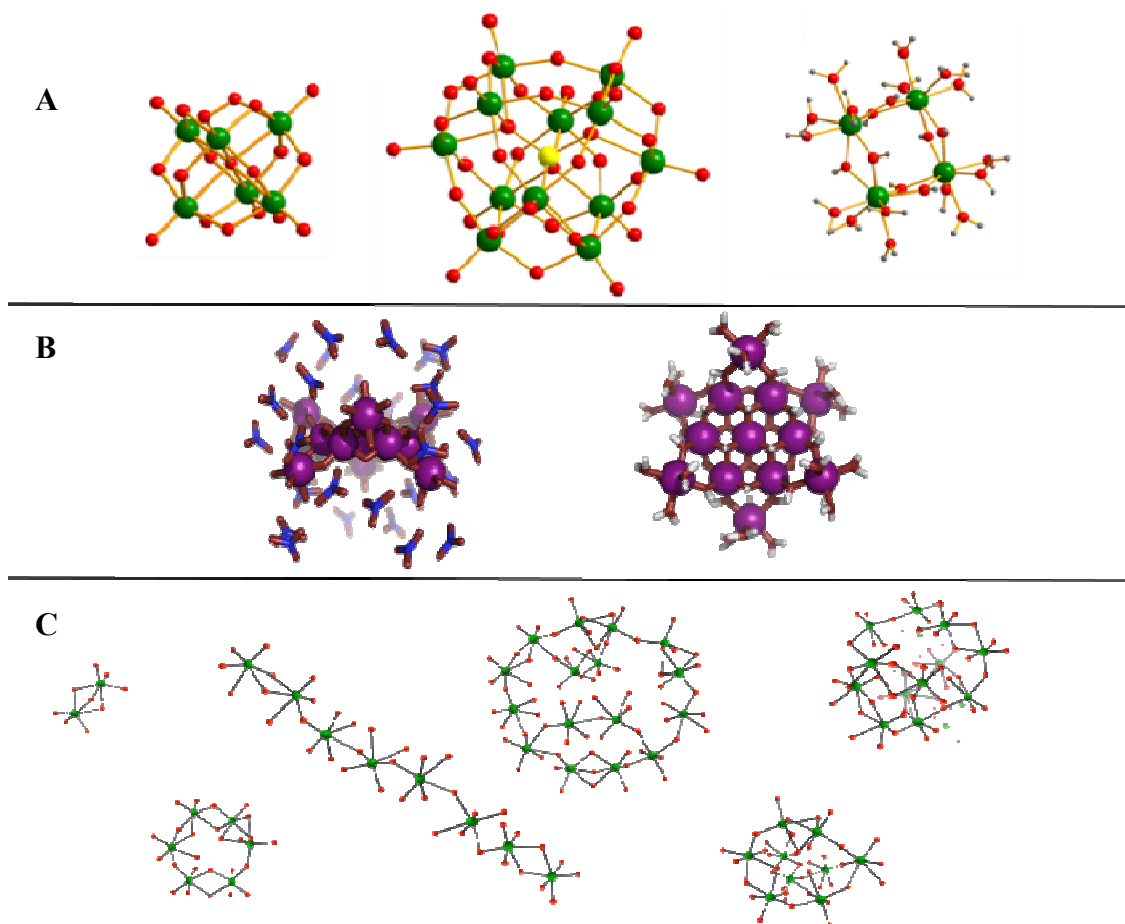


Figure 1.1. Examples of discrete metal-oxo/hydroxo clusters (A and B) and polynuclear ‘prenucleation’ clusters (C). From left to right: A) The Lindqvist ion $[M_6O_{19}]^{x-}$ ($M = Mo, W, Nb, Ta; x = 2-8$), the Keggin ion $[TM_{12}O_{40}]^{y-}$ ($M = Mo, W, Nb; T = Al, Si, P, etc. x = 3-16$), $[M_8(OH)_8(H_2O)_{12}]^{8+}$ ($M=Zr,Hf$). B) Side and planar projections of the flat tridecamer $[M_{13}(OH)_{24}(H_2O)_{24}]^{15+}$ ($M=Al,Ga,In$) with and without the counterions present. The hydrogen atoms are removed in the side projection to make to view easier to look at. C) Prenuclelation clusters illustrating the nondiscrete linking and assembly of metal-oxo/hydroxyl/aqua octahedra through corner-sharing, edge-sharing and face-sharing. This is illustrative of the process that takes place with hydrolysis and condensation of metals that do not form discrete, isolatable clusters without the use of protective ligands. (i.e. open shell transition metals including Fe, Ni, Mn). Color legend: Figure 1A and 1C - Metal atoms = green, oxygen = red, hydrogen = white. For Figure 1B - Metal atoms = purple, oxygen = red, nitrogen = blue, hydrogen = white.

In contrast to molecular clusters, non-molecular clusters (also referred to as pre-nucleation clusters or inorganic polymers) are far less understood. These are generally a mixture of soluble species, anionic or cationic, that are small aggregates or nuclei that

form prior to precipitation of a metal oxide or related solid. They form by essentially the same aqueous chemistry of pH controlled hydrolysis and condensation reactions that provide both the POMs and polyoxocations. These pre-nucleation clusters can be considered the intermediate state between a monomeric metal cation and a precipitated solid. They are not well understood because they difficult to isolate for study, are highly reactive and therefore dynamic, transient, and polydispersed. These characteristics present considerable challenges towards characterization. However, understanding how both natural and synthetic materials form is critical in order to controllably formulate new nanomaterials. In theory, any metal on the periodic table can possess this intermediate state between monomer and metal oxide solid, but few such systems have been studied in detail. Most of the pre-nucleation clusters that have been investigated to date are those in the natural world including aluminosilicates, iron oxyhydroxide (FeOOH) and calcium carbonate [Ca(CO₃)].⁶ Also of considerable interest are pre-nucleation clusters of oxide materials comprising metal cations coordinated by oxoanions, such as aluminum phosphate⁷ and zirconium/hafnium sulfate.⁸

In addition to studying pre-nucleation clusters to inform metal ion speciation in water, there is much motivation to investigate any persistent, discrete aqueous clusters that may exist under certain hydrolysis or dissolution conditions. These materials have found use in catalysis, in biochemical and biomedical applications, as precursors for materials, in water purification, in chemical surface polishing, as anticorrosion materials and in analytical chemistry.⁹⁻¹² Furthermore, the simple discovery of new cluster geometries and chemistries inspires us in their elegance and advances the field of inorganic synthesis. Pushing the boundaries of cluster size and shape as exemplified by two decades of

fruitful exploration of giant molybdate clusters¹³ inspires synthetic pursuits and blends the borders between “molecular” and “nano”. Discovery of new clusters typically begins with a solid-state single-crystal X-ray structure. Knowing the arrangement of the atoms is the single--most powerful tool to explain structure-function relationships and drive the science forward to more discovery. However, a structure is not nearly enough to understand self-assembly processes and mechanisms of reactions that take place in water, and in the case of non-molecular clusters, determination of single-crystal X-ray structures is not possible. For these reasons solution characterization techniques, while more challenging to interpret unambiguously, are extremely important and provide considerable depth to our understanding of aqueous cluster chemistry.

The solid-state structures of clusters are very helpful in interpreting solution characterization. As a very straightforward example, ²⁹Si NMR spectroscopy might be used to determine if a Si-containing POM is stable in solution. To interpret the solution ²⁹Si NMR spectrum, we need to know how many Si-sites are present in the POM, and in what ratio, which is information readily obtained from the crystal structure. Since the clusters of focus here are derived from water (and soluble in water) they are necessarily charged, they have counterions, and they can protonate or deprotonate in water. These characteristics drive their association and structures in water and can be studied by methods covered in this prospective. Furthermore, the single crystal structures provide information of the interaction between the charged clusters and their counterions, which cannot be ignored in understanding their solution speciation. Finally the single-crystal X-ray structure can provide opportunity to simulate spectroscopic data, in order to determine if the form and structuring of clusters in solution mimics what is observed in

the solid-state. In addition, modern quantum mechanical computations have enabled additional insight on nanoscale clusters and their interactions in solution, which can greatly inform the interpretation of the analytical data.

In this prospective we provide an overview of a variety of characterization techniques that inform the solution and solid-state characterization of clusters, and describe how the techniques complement and/or corroborate each other. Through case studies provided within each highlighted technique, several clusters will be discussed, including: Keggin ($\text{Al}_{13}\text{O}_4(\text{OH})_{24}(\text{H}_2\text{O})_{12}$)⁷⁺ (**k-Al₁₃**), flat- $[\text{M}_{13}(\text{OH})_{24}(\text{H}_2\text{O})_{24}]^{15+}$ (**f-M₁₃** where M = Al or Ga), uranyl peroxy-pyrophosphate $[(\text{UO}_2)_{24}(\text{O}_2)_{24}(\text{P}_2\text{O}_7)_{12}]^{48-}$, Lindqvist ions $(\text{H}_2[\text{Nb}_6\text{O}_{19}])^{6-}$, hafnium tetramer $[\text{Hf}_4(\text{OH})_8(\text{OH}_2)_{16}]^{8+}$, Niobium phosphate $\{\text{H}_{10}[\text{Nb}_6\text{P}_4\text{O}_{24}(\text{O}_2)_6]\}^{14}$ and bismuth nitrate $[\text{Bi}_6\text{O}_4(\text{OH})_4(\text{NO}_3)_6 \cdot \text{H}_2\text{O}]$. The following techniques are highlighted, in order of: 2-dimensional NMR spectroscopic techniques, electrospray ionization-mass spectrometry (ESI-MS), solid-state NMR spectroscopy, small-angle X-ray scattering (SAXS), dynamic and phase-analysis light scattering (DLS and PALS), Raman spectroscopy, simulations and computational studies. Emphasis will be placed on highlighting the functional uses and limitations of each method.

1.2. TECHNIQUES IN NMR SPECTROSCOPY

Nuclear magnetic resonance spectroscopy (NMR) uses the quantum-mechanical properties of atomic nuclei in a magnetic field resonating at characteristic frequencies to ascertain how atoms within a molecule bond to one another, thus making it a powerful tool for structural analysis that is on par with X-ray diffraction (XRD). Single-crystal XRD provides information about the measurable dimensions such as bond lengths and angles of molecules, but some structural information is more difficult to determine. NMR

chemical shifts of nuclei due to properties including molecular geometry or effects related to the electronegativity of nearby atoms can be used to determine more detailed structural features of a molecule. Interactions such as J coupling and the nuclear Overhauser effect (NOE) can also provide information about the interactions between atoms near one another and through space, respectively, to piece together entire structures.¹⁵ NMR was first described 75 years ago and has been used extensively in organic chemistry for almost as long. However, it has gained substantial ground for analysis in inorganic chemistry as well once methods were developed for probing quadrupolar nuclei (nuclear spin quantum number, $I > 1/2$), including high magnetic fields and ultra-fast magic-angle spinning (MAS) NMR to overcome the inherently large linewidths of typical quadrupolar species.^{16,17} For instance, we have developed techniques to synthesize a variety of aqueous hydroxy-aquo M_{13} cations (e.g., Figure 1.1B) that have benefited from these NMR methods. Solution and solid-state NMR spectroscopy have been vital in providing information about the different local environments for each atom in the structure and demonstrating that the solution structure of these clusters is largely the same as their single crystal counterparts.^{18,19} NMR methods have also proven key for establishing the dynamics for reaction of these clusters, including ligand-exchange and isomerization rates.

Several related studies have employed ^{27}Al , $^{69/71}\text{Ga}$, and ^{17}O NMR spectroscopy to investigate the structural features of Keggin-structured Al_{13} and Ga_{13} oxy-hydroxy cations as well as other ionic cluster species both in the solid and solution states.²⁰⁻²⁸ While the quadrupolar nature of Al and Ga nuclei often hampers their observation due to a combination of rapid relaxation and very large linewidths (see section 2.IV below,

Table 1.1), solid-state NMR (ssNMR) nevertheless has provided information on the local coordination environment of gallium sites and the coordination number of aluminum sites (e.g., tetrahedral vs. octahedral).^{29,30}

Table 1.1. Properties of atomic nuclei for NMR spectroscopy. Relative frequency calculated at 600 MHz (14T).

Nuclei	¹ H	¹⁷ O	²⁷ Al	⁶⁹ Ga	⁷¹ Ga	¹¹⁵ In	¹¹³ In
Abundance (%)	99.99	0.037	100	60.4	39.6	95.7	4.3
Spin	1/2	5/2	5/2	3/2	3/2	9/2	9/2
Relative Frequency (MHz)	600.0	75.3	156.6	144.0	183.6	132.0	132.0
Relative Sensitivity (vs. ¹ H)	1.00	1.1 x 10 ⁻⁵	0.21	0.004	0.057	0.33	0.0015
Magnetogyric ratio, γ (10 ⁷ rad T ⁻¹ s ⁻¹)	26.75	-3.63	6.97	6.70	8.18	5.90	5.89

NMR methods have long been used to follow reactions affecting the symmetric Keggin-structure ions, but recently, more advanced ssNMR methods have been used to study aluminum and gallium-based hydroxy-aquo cations (referred to earlier as “**f-Al₁₃**” and “**f-Ga₁₃**” and shown in detail in Figure 1.1B). From this we have gained information about the unique M(III) environments within these cations, and now apply solution (¹H) NMR and complementary computations to provide a window into the complex proton spectra of the these clusters in solution.³² Thus solution ¹H NMR is a valuable technique that can complement ssNMR to inform aqueous cluster speciation even in wet, polar solvents where proton exchange with solvent does not always prevent NMR analysis.

The enormous range of NMR timescales, microseconds to seconds, makes this method particularly suited to detect the structural transitions affecting these clusters in both solid state and in solution. One expects an assortment of labilities even in a single multi-metal cluster. Using the Group 13 monomer ions as an example of the range, the rate of aquo ligand exchange at 298K of $[\text{Al}(\text{H}_2\text{O})_6]^{3+}$ is 1.3 s^{-1} ; that of $[\text{Ga}(\text{H}_2\text{O})_6]^{3+}$ is 420 s^{-1} and $[\text{In}(\text{H}_2\text{O})_6]^{3+}$ is $40,000 \text{ s}^{-1}$.³³ This wide range of timescales is also expected to be manifested at these metals when they are exposed at the surfaces of the Group 13 clusters. These differences have made peak analysis considerably challenging for **f-Al₁₃** in comparison to its **f-Ga₁₃** and heterometallic **f-Ga_{13-x}In_x** counterparts because the chemical shifts for peaks that would normally be time-averaged singlets are all observed, leading to spectra with complex splitting motifs.⁹ However, this complicating factor also enables NMR to investigate the kinetics of ligand-exchange reactions and other dynamic species in these clusters. The following sections provide more specific case studies of NMR spectroscopy applied to cluster characterization, beginning with a discussion of ¹H-NMR.

1.2.1. ¹H-NMR. While ¹H solution-phase NMR is among the most ubiquitous techniques used for structure characterization in chemistry, metal-hydroxo clusters have a unique set of challenges due to enormous, unexpected complexity of peaks present in the spectra. More specifically, the two tridecamers **f-Ga₁₃** and **f-Ga₇In₆** have identical symmetry and should present with the same number of proton signals. However, the spectra of **f-Ga₁₃** is significantly more complex and contains more proton signals due to the slower rate of exchange of the capping water molecules with the solvent DMSO on the gallium compared to indium ions. Recent first-principles calculations and

computational studies have addressed the complexity of these spectra and assigned the peaks for each cluster (Figure 1.2). This work has led to a better understanding of the ranges and relative chemical shifts for different types of protons in the $f\text{-Ga}_{13-x}\text{In}_x$ series of clusters.³²

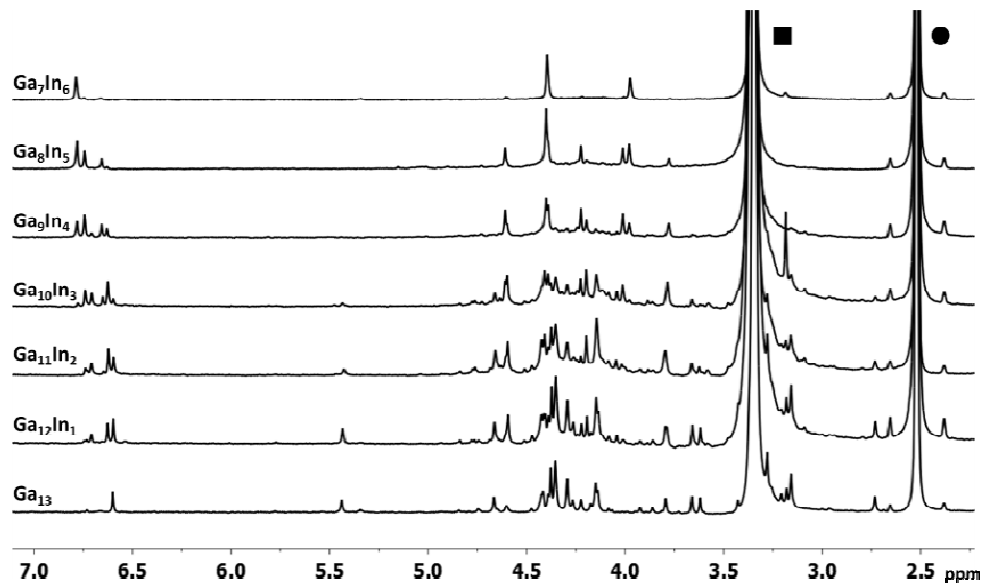


Figure 1.2. $^1\text{H-NMR}$ of 2 mM $f\text{-Ga}_{13}$ and each heterometallic $f\text{-Ga}_x\text{In}_{13-x}$ cluster in $d_6\text{-DMSO}$.

1.2.2. Diffusion NMR. In trying to decipher the NMR spectrum of a solution containing putative clusters, one is often left struggling to decide if the solution is truly monospecific, or if the various peaks are from different molecules, such as dissociation products or intermediates left over from formation of the cluster ion. Another technique used to characterize Group 13 polynuclear cations is diffusion NMR. Ideally the method can be used to assign experimental diffusion coefficients to different peaks in a spectrum and the Stokes-Einstein relation used to estimate the hydrated radius of the corresponding ion. This provides information regarding the size of these structures in solution, which is important in establishing the solution speciation of these clusters at different

concentrations (a topic germane to the use of clusters as inks, as precursors for thin films or in polishing slurries).

In the simplest sense, the diffusion of a molecule in solution is a result of translational motion relative to the solvent caused by Brownian motion.⁹ This physical diffusion effects the dephasing of magnetism in the transverse plane and is detectable in certain NMR experiments. From knowledge of the viscosity of solvent and the Stokes-Einstein equation: $D = (kT/6\pi\eta R_h)$, where k is the Boltzmann constant, T is temperature, η is solvent viscosity, and R_h is the hydrodynamic radius of the molecule,³⁴ one can estimate the molecule's diffusion coefficient (D) and size of the solvation sphere of a spherical species.

In this model D is inversely proportional to the hydrodynamic radius R_h , and thus molecules with larger radii have smaller diffusion coefficients. Therefore, 2D NMR diffusion experiments such as diffusion ordered spectroscopy (DOSY) can be used “to spectroscopically resolve” compounds based upon their transport properties in solution. DOSY maps chemical shift on the vertical axis against diffusion coefficient on the horizontal axis. Peaks with diffusion coefficients that pass through the same horizontal line are related to molecular species with the same hydrodynamic radius. As one example, in the case of a two-solvent (DMSO/DMF) experiment aimed at understanding **f-Al₁₃** speciation, the R_h for **f-Al₁₃** in DMSO- d_6 ($0.97 \text{ nm} \pm 0.08 \text{ nm}$) and DMF- d_7 ($0.68 \text{ nm} \pm 0.02 \text{ nm}$) are different owing to the change in solvent viscosity, η . Molecules in solvents with higher viscosity will move slower and thus have apparently larger R_h values (explained in greater detail later). Relative viscosity informs us that we expect R_h in

DMSO- d_6 to be larger compared to that in DMF- d_7 (Table 1.2) even for the same cluster species.^{35,36}

Table 1.2. Ratio of the viscosities of DMSO- d_6 and DMF- d_7 relative to D₂O and H₂O at 25 °C.

	DMSO-d_6^b	DMF-d_7^c
D₂O^a	1.818	0.732
H₂O^a	2.227	0.897

^a Viscosity of D₂O and H₂O are 1.095 mPa·s and 0.894 mPa·s, respectively.

^b Viscosity of DMSO- d_6 is 1.991 mPa·s.

^c Viscosity of DMF- d_7 is 0.802 mPa·s.

An early example of identifying clusters in solution via ¹H-NMR spectroscopy was with 2 mM **f-Ga₁₃** in DMSO- d_6 (Figure 1.3).⁹ Additionally, it was revealed the slight differences between diffusion coefficients produced by the signals of the cluster can be ascribed to a number of factors including water exchange, overlapping of peaks, and/or data processing. The similarity in hydrated radius is evidence that the signals originate from a single cluster molecule, or at least from cluster molecules of similar sizes.

DOSY NMR is conceptually simple---the rates of transverse relaxation ($1/T_2$) are measured in a standard spin-echo experiment and then re-measured in the presence of a magnetic gradient. The difference in rates relates to the reorientation rate of the nucleus, and thus to diffusion coefficients. The most important parameters in our experience are the diffusion period (Δ), gradient pulse length (δ), and the gradient pulse strength (G_{\max}/\min). Smaller species like the **f-M₁₃** clusters (ca. 1-2 nm diameter with ca. 70-80 non H atoms) require less time to move through the solvent compared to larger molecules such a proteins (ca. 10+ nm diameter), so the following values have worked well in our case: $50 \text{ ms} \leq \Delta \leq 100 \text{ ms}$, $2 \text{ }\mu\text{s} \leq \delta \leq 3 \text{ }\mu\text{s}$ and $G = 500\text{-}20000$.

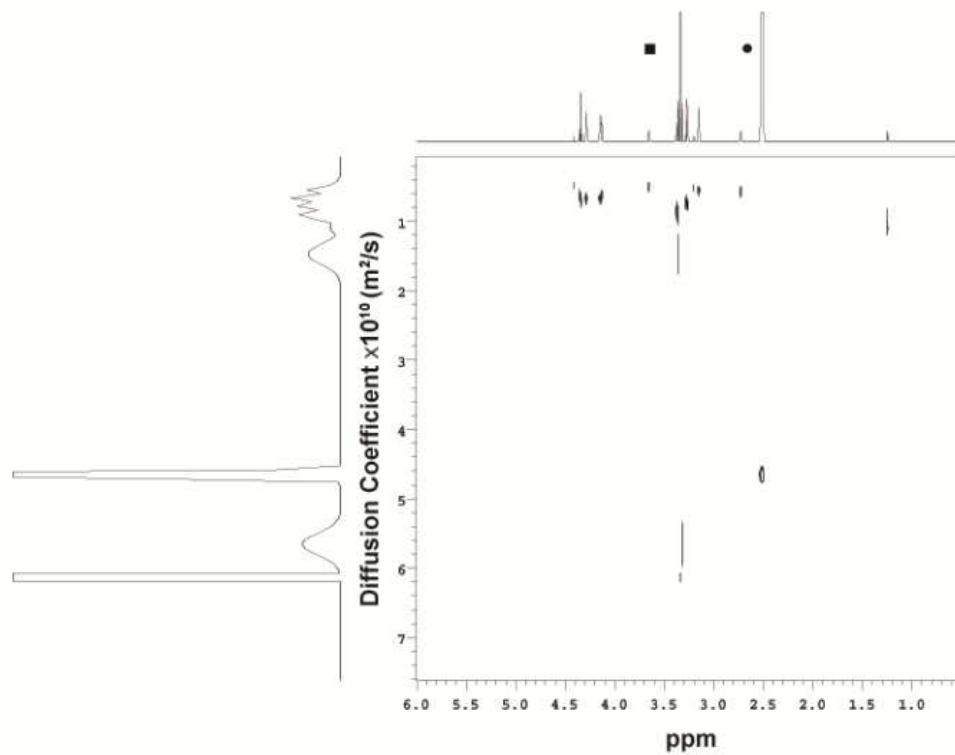


Figure 1.3. Representative DOSY spectrum of a hydrated $f\text{-Ga}_{13}$ cluster in $d_6\text{-DMSO}$ ($D_{\text{avg}} = 0.955 \times 10^{-10} \pm 0.064 \times 10^{-10} \text{ m}^2/\text{s}$). (■) H_2O peak and (●) DMSO peak.

G_{max} and G_{min} can change based upon the amount of attenuation necessary for reliable results and often depends on the particular sample, requiring optimization for specific clusters. Another issue that can arise in collecting DOSY data is when measurements are taken at non-ambient temperatures. Practically, not all spectrometer probes maintain a constant temperature well. Therefore, a temperature gradient can exist within the sample. Since η will change with temperature it is important to minimize temperature variations within the sample. Using pulse programs with convection current

compensations can help. In addition, loading the minimal amount of solution into the NMR tube required for a signal can also improve data quality.

1.2.3. Isotope-Exchange Dynamic. Isotope-exchange has been used to study a variety of dynamic processes in cluster chemistry, such as ligand exchange and cluster-species interconversion using multinuclear NMR spectroscopy. These studies have established a set of not-inviolate rules for understanding some of the isotope exchanges, which we discuss below. As an example of reaction dynamics, ^{31}P -NMR spectroscopy on the very large uranium [U(VI)] molecule shown in Figure 1.4A revealed that this cluster exists in two equilibrating forms in solution: one an asymmetric dimpled structure that is stable at ambient conditions and the other a spherical form stable at slightly elevated temperatures. The molecule contains 24 uranyl (U) moieties, 12 pyrophosphate units³⁹ that are detectable via ^{31}P NMR, and a nominal stoichiometry of $[(\text{UO}_2)_{24}(\text{O}_2)_{24}(\text{P}_2\text{O}_7)_{12}]^{48-}$.

A surprising feature of this molecule is that the two isomeric forms can be caused to interconvert in second to millisecond time scales, and the rate depends on the temperature, pressure and the counterions present.⁴⁰ Interestingly, the asymmetric form is also made stable by increased pressure and by choice of tetramethylammonium as a counterion. This example illustrates the importance of solvation forces in affecting these large oxide ions in solution. High pressure selects for the more highly solvated species that provides a more efficient packing of water molecules. Because these clusters are often stabilized by solvation forces, the use of high pressure NMR may become an important tool in unravelling the chemistry that makes particular forms prevalent.

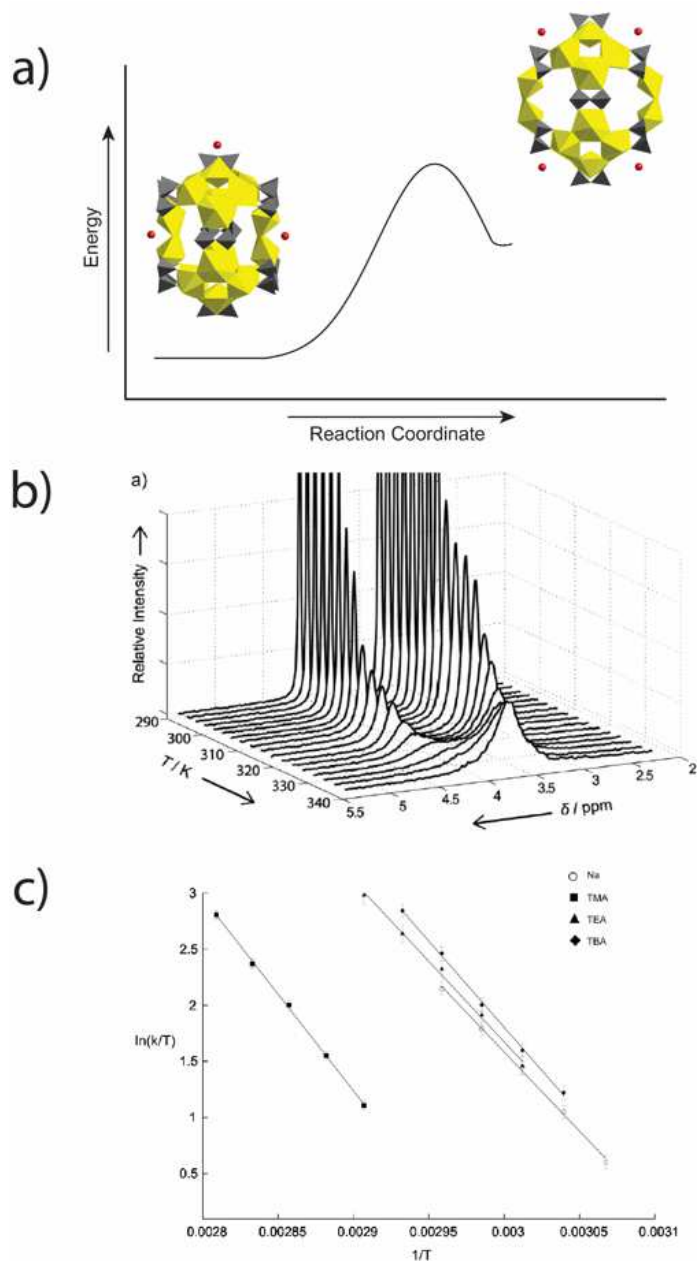


Figure 1.4. (a) A large uranyl-pyrophosphate cluster has two forms in aqueous solution. The two forms differ in the dimpling or symmetry and the nominal stoichiometry of the cluster is $[(\text{UO}_2)_{24}(\text{O}_2)_{24}(\text{P}_2\text{O}_7)_{12}]^{48-}$, excluding associated counterions. In the image, yellow are uranyl-oxide polyhedra, the gray tetrahedra are pyrophosphates and the spheres are sodium counterions. (b) ^{31}P -NMR spectra show the progressive coalescence of the two ^{31}P sites in the structure as the rates of isomerization increase with temperature; (c) the reaction rates are affected by the counterion chosen for the system. Tetramethyl ammonium ion selects for the asymmetric form. The system is an excellent example of two-site exchange in an NMR system, although in this case the two sites are within the same molecule and become magnetically equivalent as the structure isomerizes rapidly.

This example of the large uranium ion also illustrates the wider point that these large clusters are commonly equilibrating with metastable forms. For many dense clusters, these metastable forms control the rates of isotope exchanges into the structure from solution, the kinetics of dissociation of the clusters and, probably, the access to lacunary structures. Access to the intermediate forms involves concerted motions of much of the dense ion structure, which is why a single-metal substitution into a structure often has a mitigating effect on the kinetics of oxygen-isotope exchanges^{41,42} the substitution suppresses or enhances the stability of the metastable form. The NMR studies of oxygen-isotope-exchange pathways suggest a series of steps are common to these reactions: (i) a metastable structure forms from the partial detachment of a surface metal from an underlying over-bonded oxygen; (ii) this loose metastable structure allows water or oxygen solutes to add to the newly under-coordinated metal; (iii) protons transfer to basic oxygens in the metastable structure; and (iv) isotope shuffling occurs between relatively low-coordinated oxygens and, finally, (v) the metastable structure collapses into the stable form. The series of steps accounts for much of the observed data on rates of isotope exchanges in oxo clusters like the niobate anions or aluminate cations. The rates of isotope substitution are regiospecific, are affected by choice of counterion, and yet the pH variation is similar for most oxygens in the structure, even though they may differ by orders of magnitude in reactivity. Counterions and solvation forces are important because charge separation is essential to forming the metastable structure.

The methods of following such reactions fall into two broad categories: (i) isotope-injection methods, and (ii) line-broadening methods. The most common methods of detecting oxygen-isotope exchanges in an injection experiment are NMR spectroscopy,

vibrational spectroscopy and electrospray-ionization mass spectroscopy (ESI-MS). The last method has been reviewed recently for applications related to polyoxometalates by Ohlin⁴³ and there exist many good examples of the application.⁴⁴

The difficulties of ESI-MS lie in the ionization step where the cluster ion may fragment, may associate, or may pair with counterions so extensively as to yield uninterpretable spectra. Electrospray ionization depends upon controlled desolvation of a droplet after charge has been imparted at the injector into a stream of drying gas (commonly nitrogen at 300 °C or so). The ionization step requires a potential be placed between solution at the tip of the injector and the instrument. This potential is essential to forming a cone of dispersing solvent but the ionization potential can be a source of artifacts if it induces fragmentation or association of the cluster as well as the droplet. Maps of the m/z signals as a function of ionization potential can help detect misleading signals as the disappearance or appearance of signals as a function of potential. Choice of the solvent type also limits application of ESI-MS to cluster studies as, in general, volatile solvents (e.g., acetonitrile) and counterions (NH_4^+) are better than water and non-volatile counterions (e.g., Na^+).

In the best of cases, the injection method can follow changes in the m/z value for key signals in the ESI-MS spectra. The magnitude of the shift not only shows the efficacy of isotopic substitution but if the stoichiometry of substitution is understood, it also allows one to assign charge to the fragment and to compared fitted and measured spectra. An excellent example is provided by Ohlin et al (2009)⁴⁵ who followed the ^{18}O substitution into a manganese-cubane oxide cluster and could resolve rate data into all four oxygens.

In other cases, and stemming from the earliest days of polyoxometalate chemistry^{22,46-48}, the ^{17}O -NMR signal in the structure is followed as a function of time. Most useful are cases where there remains an oxygen site that is inert to substitution so that the full dissociation of the molecule can be detected as exchange of isotopes with the solvent. For molecules like the MAl_{12} Keggin structures ($\text{M} = \text{Al(III)}, \text{Ga(III)}$ or Ge(IV) ; $[\text{MO}_4\text{Al}_{12}(\text{OH})_{24}(\text{OH}_2)_{12}]^{7/8+}$), the μ_4 -oxo ligands in the center of the molecules are inert to substitution.^{49,50} In a typical injection experiment, ^{17}O is added to the solution and the evolution in signals followed by ^{17}O -NMR. An alternative approach is to synthesize the molecule from ^{17}O -enriched solvent, crystallize the product and dissolve it metathetically in isotopically normal water. This latter approach has been taken by many scientists studying inert-metal clusters, like niobates.⁵¹⁻⁵² The injection methods are simple and differ only in how the isotopic substitution is detected. In a similar manner, vibrational spectroscopy techniques can be used to complement these other two techniques.

The timescale for reaction dynamics in many large clusters fall into the 10^{-9} - 10^{-2} s range, which makes the detection amenable to NMR if there exists a suitable nucleus. The NMR methods used to follow the exchange of isotopes or movement of mass into, and out of, the cluster are dominated by line-broadening approaches,⁵³⁻⁵⁶ although there is no reason that selective-excitation methods cannot also be used. Application simply awaits a polyoxometalate system with appropriately spaced resonances and suitable kinetics of exchange.

The essence of the line-broadening methods is progressive coalescence of NMR signals with rates of substitution enhanced by temperature or pressure. Even for cases where only a single resonance is followed, such as ^1H -NMR studies of exchange in

polyoxometalate ions, implicit in the approach is that the spectra change shape as rates of exchange increase between two sites—one site is the solvent which is largely unaffected, the other site is the proton on a structural oxygen on the polyoxometalate ion. The assumption of two-site exchange is almost invariably invoked because oxygens or protons in the solvent are in such high excess that the change of three-site or multi-site exchange, such as collisions between cluster ions that lead to an exchange event, are highly improbable.

^{17}O -line broadening studies fall into two categories: (i) cases where changes in the peak assignable to the solvent are followed, and (ii) cases where peaks assignable to the solute are followed. The former case is particularly important for solutes of paramagnetic metals in rapid-exchange with bulk waters because the NMR signal for ^{17}O bound to the paramagnetic metal is invisible. The reaction kinetics are inferred from the peak shape for the solvent. This subject, and its assumptions, was recently reviewed.⁵⁷

The second case, where distinct and well-separated NMR signals assignable to nuclei in the cluster are followed, has two subcases. The first, typified by studies of ^1H -NMR and line broadening, is where one exchanging site is in large excess over the site in the solute, here a cluster ion. In this case the contribution to transverse relaxation and linewidth (via $1/T_2$) from chemical exchange must be larger than from all other sources. If this condition is met, then the rate of exchange is directly proportional to the full-width-at-half-maximum of the solute peak. Ideally, one can simply estimate the rates from the full-width-at-half-maximum of the NMR peak. This approach was used by Houston, et al. for the $\mathbf{k}\text{-Al}_{13}$ ion.⁵⁸ Simulations of the Bloch-McConnell equations for NMR line shape, followed by fitting of the approximate equations, shows that this

assumption is generally good to a factor of ~ 2 in values of k_{ex} at their conditions. The validity of the assumption depends upon the ratio of exchangeable nuclei in the two sites, the separation of the NMR peaks in Hz, and the rates of exchange. This assumption should be tested for each case.

The second case is exemplified by Figure 1.4B, where the ^{31}P -NMR signals for this nanometer-sized cluster coalesce with increased temperature. This case also represents a two-site exchange problem, but the two sites are within a single molecule undergoing a reversible isomerization reaction. The two sites broaden with temperature, move together and establish a characteristic exchanging line shape before coalescing into a single peak and becoming increasingly narrow as temperature increases. The two sites are becoming magnetically equivalent because of the rapid interconversion of the large oxo ion and establishment of higher symmetry. The asymmetric and symmetric forms interconvert at rates faster than the separation of the ^{31}P -NMR signals from the two sites (Figure 3C). Deriving rate coefficients from such a case requires a numerical fit to the Bloch-McConnell equations, which was impossible decades ago when approximate solutions were derived and used. Now computers are so fast that the full equations can be solved directly and repeatedly using a nonlinear-least squares algorithm and the rate coefficients derived without approximation.

1.2.4. Solid-state NMR (ssNMR). Quadrupolar solid-state nuclear magnetic resonance (ssNMR) spectroscopy has received increased interest with recent advancements of ultra-high magnetic fields and very fast magic-angle spinning (MAS) NMR probes. With these advancements, ssNMR offers a unique modality for the characterization of molecular clusters for multiple reasons. First, amorphous domains, disorder, and impurities present

in samples are often still observable by NMR, unlike X-ray diffraction (XRD) which is generally unable to discern these due to the lack of long-range order. ssNMR is both element-selective and a quantitative spectroscopic technique where the NMR resonances can be recorded such that the signal is proportional to the number and type of sites present for the isotope being probed in the material.⁵⁸ ssNMR is also a nondestructive technique, where the integrity of the sample remains intact after analysis, allowing other characterization techniques to be employed on the identical sample.

The most familiar experiments performed with NMR involve nuclei with nuclear spin quantum numbers $I = 1/2$, such as ^1H and ^{13}C . However, the vast majority of the periodic table contains quadrupolar nuclei, i.e. spin $I > 1/2$. One such quadrupolar species is gallium which was widely used to explore semiconductor materials since the late 1950's,⁶⁰ and has recently been applied to other materials.^{5,61,62} Gallium has two NMR active isotopes, ^{69}Ga and ^{71}Ga , which are quadrupolar, and both have spin $I = 3/2$. While ^{69}Ga is more naturally abundant at 60.4% compared to ^{71}Ga at 39.6%, its quadrupole moment is approximately twice as large as ^{71}Ga which results in much broader NMR resonances. ^{69}Ga is useful to confirm spectroscopic assignments, ^{71}Ga is typically the isotope of choice to acquire and model NMR spectra.

We have reported the synthesis of a family of **f-M₁₃** clusters, including the gallium hydroxo-aquo cluster, $[\text{Ga}_{13}(\mu_3\text{-OH})_6(\mu_2\text{-OH})_{18}(\text{H}_2\text{O})_{24}](\text{NO}_3)_{15}$ (**f-Ga₁₃**, Figure 1.1B),^{5,62} and we recently reported its solid-state NMR characterization. These spectra revealed three gallium sites (Figure 1.5): a core, a middle ring, and an outer ring site were each present.⁶³ These molecular clusters present a unique challenge for solid-state NMR due to the local environments that lead to significant broadening of the resonances. However,

the three types of sites could be resolved by utilizing multiple magnetic fields and modelling of the $\mathbf{f}\text{-Ga}_{13}$ structure. Herein, we present a brief overview of how solid-state NMR can be used to investigate the gallium coordination environment in solid materials.

The three types of coordination environments observed in the $\mathbf{f}\text{-Ga}_{13}$ cluster all consist of six-coordinate gallium atoms: an outer ring of six gallium sites, a middle ring of six gallium sites, and one site in the center. Each site is in a distorted octahedral environment¹⁸ and a detailed table of bond angles and lengths is provided in the Supplemental Information in the Appendix. The ability of ssNMR to resolve the three coordination environments required the use of two magnetic fields (13.9T and 21.1T) for full characterization due to second-order quadrupolar broadening effects for some sites (which are reduced at higher magnetic fields).^{59,18} At low field, 13.9T, the core and outer ring sites were the most prominent, while the middle ring remains broadened into the baseline and was not well resolved (Figure 1.6a). However, by obtaining the data at higher field (21.1T, Figure 1.6b), all three sites were fully resolved. A small resonance assigned to an impurity left over from the synthesis, which has been identified as gallium nitrate, is denoted by the double dagger.

The quadrupolar parameters give insight into the local structure surrounding each gallium. Since ^{69}Ga and ^{71}Ga isotopes both possess a non-zero quadrupole moment, this quadrupole moment may interact with the electric field gradient (EFG) surrounding each nucleus (Figure 1.3). The EFG is composed of three principal tensor components, V_{xx} , V_{yy} , and V_{zz} , where $|V_{zz}| \geq |V_{xx}| \geq |V_{yy}|$, when diagonalized in the principle axis system.⁶⁵ The orientation and size of the ellipsoids in Figure 1.7 is defined by these principal tensor components. The size and shape of the EFG lead to parameters that aid in

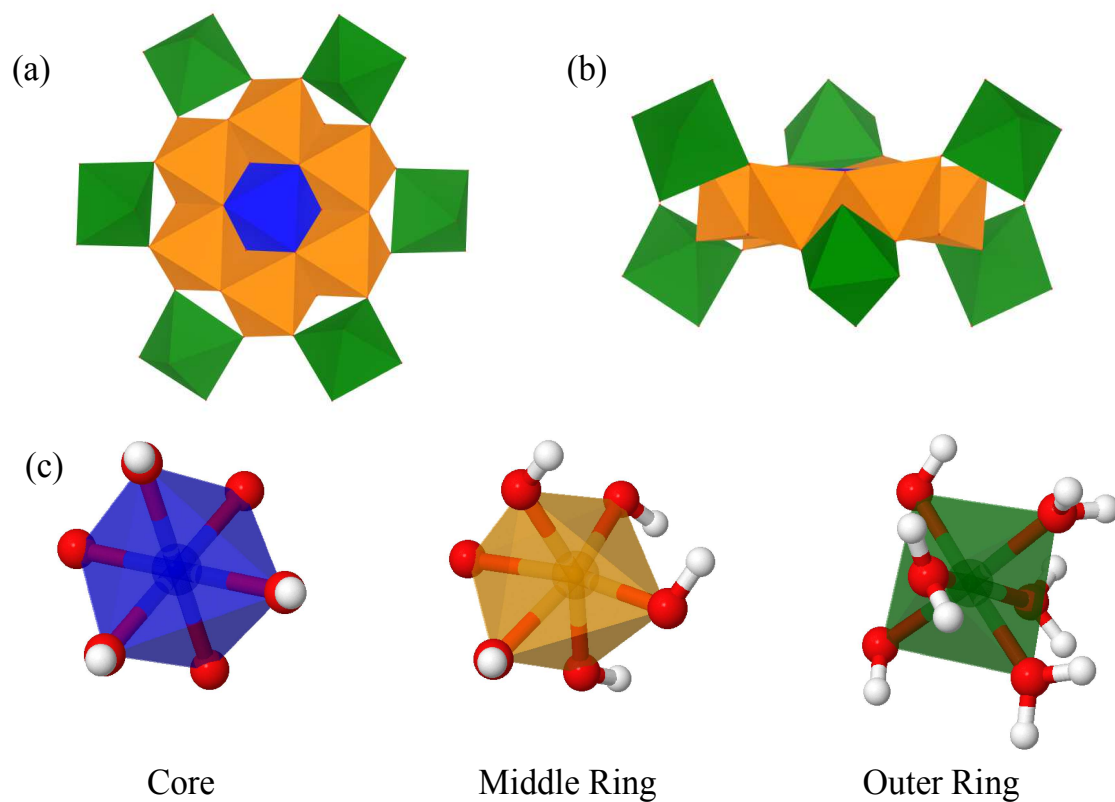


Figure 1.5. Space-filling polyhedral representation of the **f-Ga₁₃** molecular cluster from a geometry-optimized calculation (a) top down view, (b) side view, (c) individual polyhedral representation of the three gallium sites: core (blue), middle ring (orange), and outer ring (green).

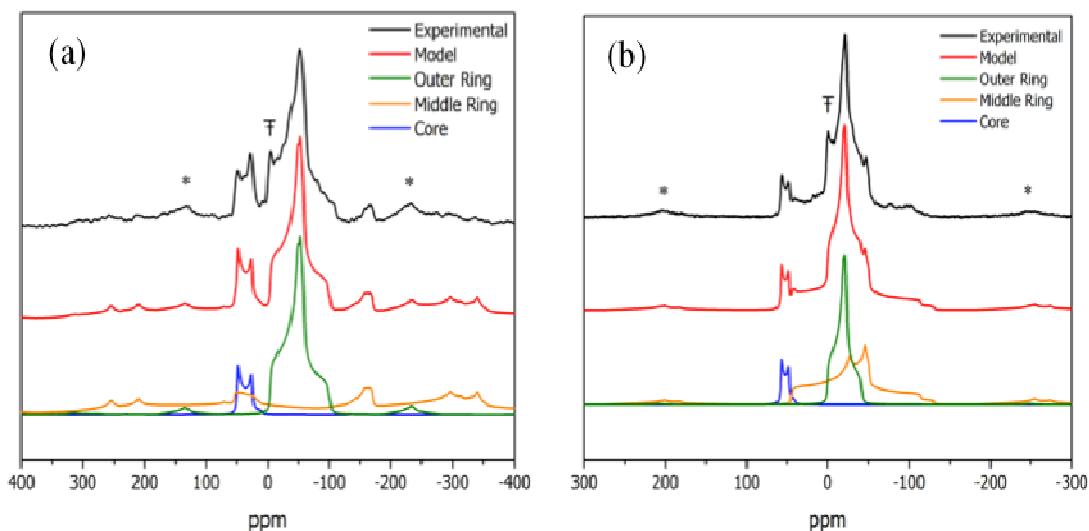


Figure 1.6. ^{71}Ga MAS NMR spectral data for the **f**- Ga_{13} molecular cluster at two magnetic fields, (a) 13.9T and (b) 21.1T. Experimental spectra data are shown in black, the individual line shapes are shown in blue (core), orange (middle ring), and green (outer ring), and the red spectrum is the compiled model. Asterisks denote spinning side bands of the central transition, and the double dagger indicates the position of the gallium nitrate impurity resonance.

the interpretation of the data. The first parameter is the axial asymmetry parameter, η_Q , which is strongly reflected in the shape of the resonance, and the second parameter is the quadrupolar coupling constant, C_Q , which represents the breadth of the resonance. By using the principal tensor components, the axial asymmetry parameter may be calculated from the following equation:

$$\eta_Q = \frac{V_{YY} - V_{XX}}{V_{ZZ}}$$

where $0 \leq \eta_Q \leq 1$. The quadrupolar coupling constant C_Q (in Hz) is defined by the following equation:

$$C_Q = \frac{e^2 q Q}{h}$$

where eq is V_{zz} , eQ is the nuclear quadrupole moment, and h is Planck's constant. Combining these two parameters, the NMR line shapes defined by these two will give insight into the local bonding of the cluster. Using first-principles calculations (CASTEP code),⁶⁶ it was possible to calculate the electric field gradients in a complex system such as this molecular cluster and estimate the quadrupolar parameters η_Q and C_Q . The parameters were then used in conjunction with simulation software (DMFIT⁶⁴), which allows for lineshapes to be simulated based on specific quadrupolar parameters and compared to the experimental data. These values were adjusted to obtain a good match between model and experiment. The size of the electric field gradients provide insight into bond lengths and bond angles, as well as other atoms in the vicinity of each quadrupolar nucleus. In addition to the directly bonded structure, the electric field gradients can be strongly affected by the counterions (nitrates) present around the cluster and can cause significant distortions to the EFGs. In the **f**-Ga₁₃ clusters, the largest quadrupolar coupling constant was observed in the middle ring sites (the largest grey spheres), and the smallest C_Q was the core site (barely visible on this scale). While the outer ring contains a fairly large C_Q , it remained significantly smaller than that of the middle ring.

The core site of the **f**-Ga₁₃ structure had the most axially symmetric environment, meaning that there was little distortion in the EFG $\eta_Q \approx 0$ (Figure 1.7). An axially asymmetric site will contain large distortions to the electric field gradient, i.e. the grey ellipsoids are large in two dimensions, but compressed in one dimension, which yields an $\eta_Q \approx 1$. This type of axially asymmetric site was observed in the middle and outer ring of the **f**-Ga₁₃ molecular structure.

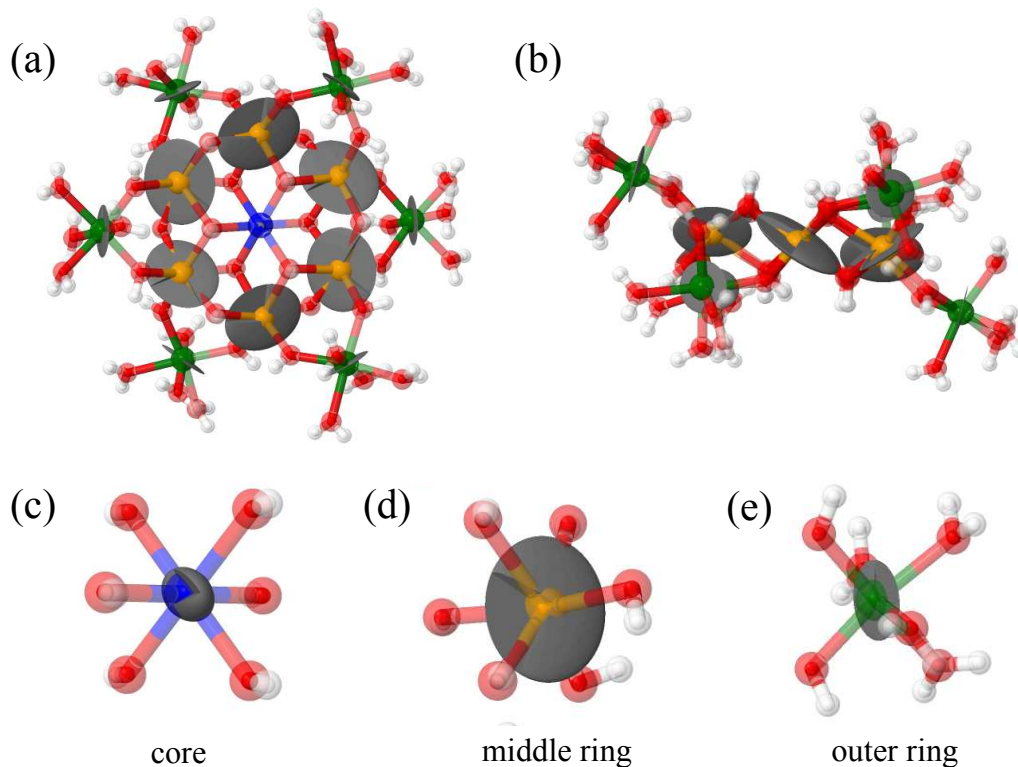


Figure 1.7. A geometry-optimized structure of the f-Ga₁₃ molecular structure computed from CASTEP (a) top view and (b) side view. Atoms are color coded as in Figure 1 and the electric field gradient depicted as distorted grey shapes (ellipsoids) around the gallium atoms. The core gallium, which is highly symmetric, has a small EFG, which is difficult to see in this rendering. The individual sites have been extracted to depict the electric field gradients surrounding each atom: (c) the core site, (d) middle ring, and (e) outer ring. The core EFG in figure 3c was multiplied by a factor of 2.

Solid-state NMR has provided structure characterization of each of the Ga^{III} sites in the molecular cluster. Utilizing multiple fields allows for the sites to be assigned and validated by NMR simulations. The quadrupolar parameters, η_Q and C_Q , give insight into the local environment of the gallium sites. First principle calculations offer a starting point for interpretation of the experimentally-measured data, and here these calculations were utilized to compute the electric field gradients around each nucleus. While very high magnetic fields and high-speed magic-angle spinning are required for analysis of such broad NMR resonances (of such quadrupolar species), the ability to observe (and

potentially quantify) impurities is an invaluable aspect of the technique. Another advantage of ssNMR is that disordered materials and amorphous domains can still be probed by this form of spectroscopy. We can add a cautionary note that disorder in these **f**-M₁₃ systems is sufficient to cause distortions to the EFG's (like those shown in Figure 1.7) in the **f**-Al₁₃ system, such that similar analyses on **f**-Al₁₃ have failed to yield just 3 sites (data not shown).

1.3. SCATTERING TECHNIQUES IN AQUEOUS CLUSTER CHEMISTRY

1.3.1. Studying Clusters via SAXS. During a SAXS experiment, a sample is irradiated by a collimated, monochromatic beam of X-rays. The particles in solution scatter the X-rays while the intensity of this scattering is collected by a detector. SAXS exhibits coherent, elastic scattering where the electrons in the irradiated particles oscillate at the same frequency as the incoming X-rays, and emits X-rays with the same wavelength as the incident beam. The coherent X-rays will then interfere with one another either constructively or destructively creating interference patterns that provide structural information about the clusters.⁶⁷

A scattering measurement is composed of an isotropic average of scattering signals from all particles in all orientations relative to one another. The overall scattering of a solution is the contrast in electron densities between particles of interest and the solvent. X-rays are also scattered by solvent molecules, so data processing is necessary to subtract out bulk solvent as a background and scale relative intensities. More intense scattering is the result of larger differences in electron densities between solute and solvent. For this reason, clusters provide the optimal scenario for SAXS studies since they are composed of high *Z* metals with solvents of low *Z* elements (*Z* = atomic number). The discrete,

monodisperse nature of polyoxometalates and Group 13 polycationic clusters (under most conditions) makes them ideal species to study in solutions with SAXS.⁶⁸ We can also utilize SAXS to observe polydisperse species such as pre-nucleation clusters mentioned previously. Even though a polydisperse system can be identified from scattering measurements, it is not an ideal method for extensive characterization. Monodisperse species are more ideal for SAXS as they can be used as model systems to understand related polydisperse mixtures.

When interpreting SAXS data, one dimensional data is used to extract information about a three dimensional particle. There are a number of mathematical formulae that are derived from scattering contrast, size and shape of particles, and interaction between particles. Some formulae are used for specific regions of the scattering curve such as the Guinier (low q) and Porod (high q) methods; and others are for whole curve fitting, such as the Fourier transform method of Moore.⁶⁷ Thus arriving at the same description of scattering species from multiple methods is optimal, since there is not always one unique solution for every data set. Therefore, reaching the same conclusion by two or more curve-fitting routines lends robustness to the interpretation.

Scattering data on solutions of clusters is often described by a radius of gyration (R_g). R_g is a shape independent root mean square measure of all mass weighted vectors in the particle from the center of mass.^{67,69} The size distribution of particles can also be determined, along with particle shape including spherical, disc-shaped, and cylindrical. Scattering data is dependent on form factors (size, shape, and scattering contrast) and structure factors (interactions between particles).⁷⁰ Another often-used data treatment is the pair distance distribution function (PDDF) from Moore's Fourier transform method.⁷¹

This method transforms the reciprocal space data to real space and yields a geometrical representation of the scattering particle as a probability histogram ($p(r)$ vs. radius). In this representation, the radius is distance from the edge of the particle to any other point within the particle. Therefore the number of equivalent length vectors within the particle is represented as a probability. The shape of the PDDF can give some initial information as to the shape and size of the scattering particle. Where $p(r)$ goes to zero is the maximum linear extent, or roughly the diameter of the scattering species. Figure 1.8 illustrates a variety of PDDFs for different geometric shapes of scattering particles.

We are particularly interested in using SAXS to investigate the process of conversion of 1) discrete metal-oxo clusters in solution to 2) macromolecules or inorganic polymers to 3) extended solid-state materials. These reactions usually are initiated or occur by electrostatic association (i.e., cation-anion association) or formation of covalent bonds, such as by hydrolysis and condensation reactions. The first two states listed above can be monitored by SAXS when species still remain soluble, but the eventual conversion to a solid can be investigated by other X-ray methods such as PDF (pair distribution function). Three case studies are reviewed below: 1) Forming LiNbO_3 thin films with optimal morphology, density and phase purity by taking advantage of H-bonding between clusters in solution.⁷² 2) Understanding the mechanism of linking clusters in solution (formation of macromolecular chains) by varying aqueous conditions.⁷³ 3) Investigating the polymerization of Hf-tetrameric clusters with sulfate anions in solution *en route* to gelation of hafnium sulfate coatings for nanolithography.⁷⁴ All three studies utilize the solid-state structure of discrete clusters, with or without their counterions, to derive reasonable models for complex solution behavior of interacting and reacting clusters.

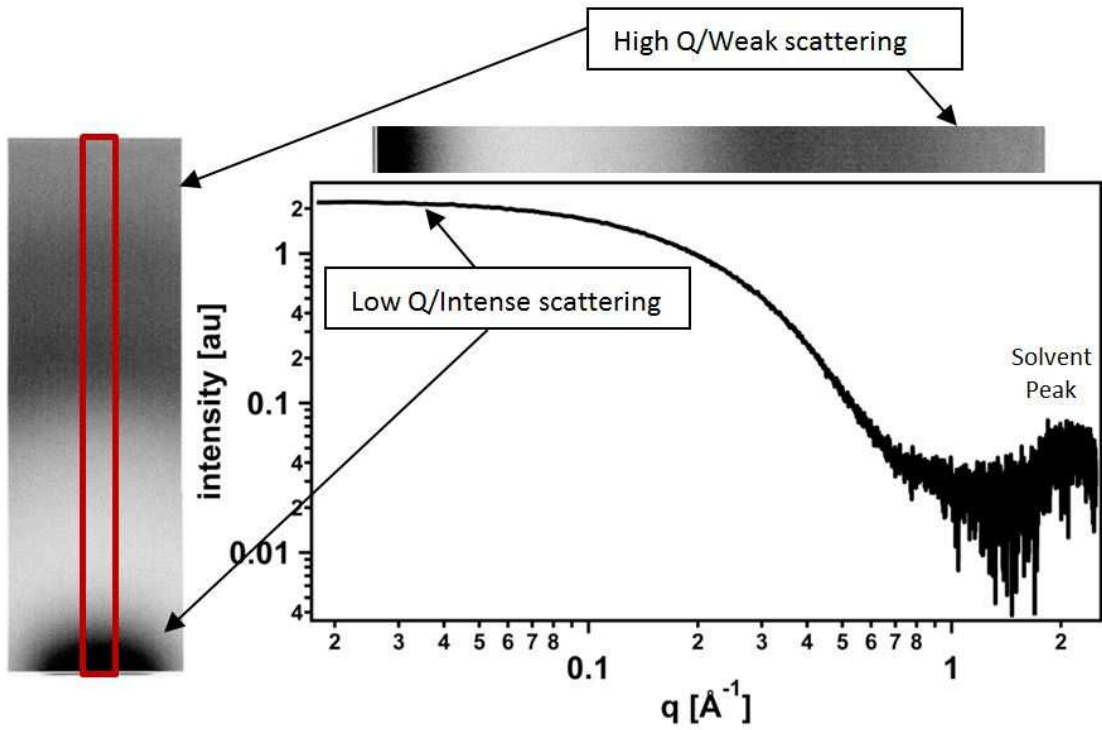
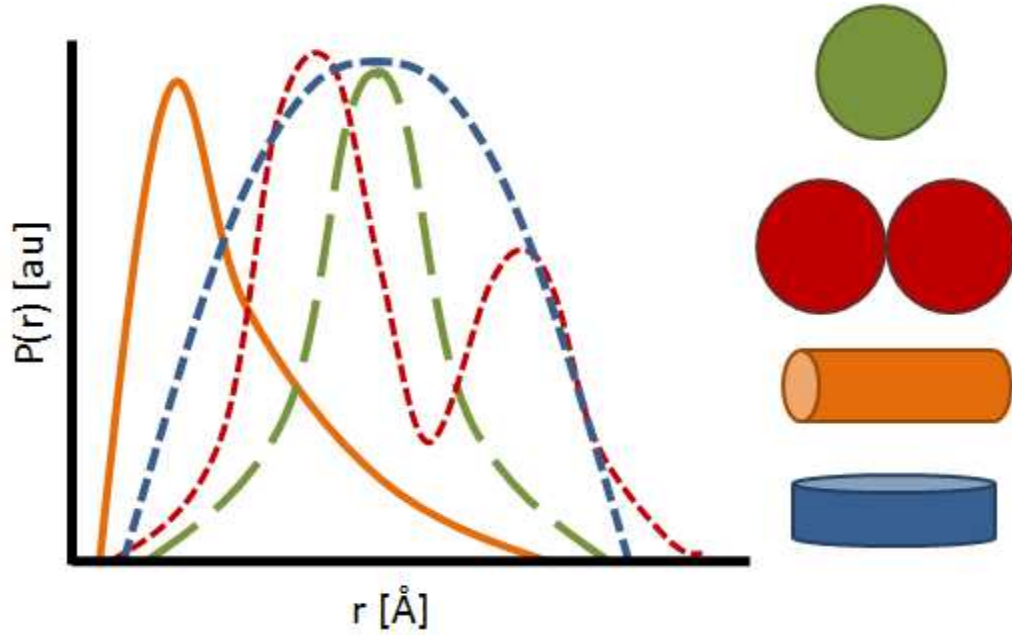


Figure 1.8. One dimensional data extracted from a two dimensional scattering pattern. (left) Pair distance distribution functions indicative of particle shape (right).

1.3.1.1. *Lithium Niobate Thin Films from Cluster Precursors.* Previous studies on decavanadate have surmised that crystallization of the clusters in a lattice occurs through mutual hydrogen bonding of the protonated faces, and that this protonation is solvent dependent.^{75,76} Many diprotonated Lindqvist ions ($\text{H}_2[\text{Nb}_6\text{O}_{19}]^{6-}$) (Figure 1.9) have been structurally characterized in the solid state and have been observed to associate as mutually H-bonded dimers in the crystalline lattice.⁷⁶

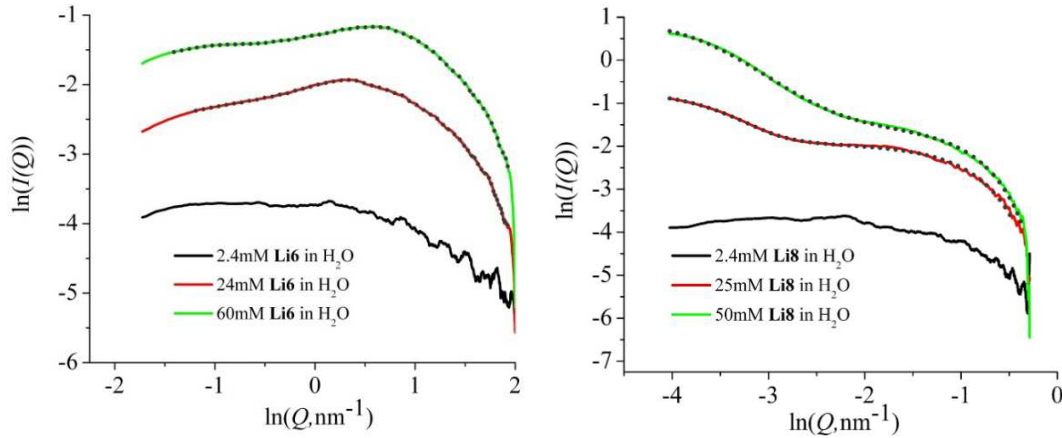


Figure 1.9. SAXS scattering curves for **Li₆** (left) and **Li₈** (right) along with a total curve fit (dotted line) for the highest concentration. For **Li₆**, the curves feature a broad peak around $\ln(q)=1 \text{ nm}^{-1}$, which indicates interactions between clusters. The **Li₈** curves were fit with two-phase models, where the phase of larger scattering species (curve fit between $\ln(q) = -4$ to -3 nm^{-1}) indicates incipient crystallization of the clusters.

This has inspired the investigation of their dimerization behavior in solution using SAXS. By exploiting the protonation behavior of hexaniobate, we can convert $\text{Li}_8[\text{Nb}_6\text{O}_{19}]$ (**Li₈**) to $\text{Li}_6\text{H}_2[\text{Nb}_6\text{O}_{19}]$ (**Li₆**) for use as a precursor for LiNbO_3 thin films.⁷² This simple acidification of the cluster led to improved solubility behavior and better thin film quality in addition to providing the correct Li:Nb ratio for the targeted perovskite material. SAXS studies were used to gain insight into the differences between the **Li₈** and **Li₆** in solution. At low concentrations, both clusters in solution have R_g 's that agree with an unassociated Lindqvist ion; however, high quality films are deposited at higher

precursor concentrations and, therefore, these conditions provide more relevant insight to the processes leading to film formation.

In the **Li₈** solutions pre-nucleation aggregates form and begin to crystallize. This was observed in changes to the slope in the low-*q* region of the scattering curve (Figure 1.9). The aggregation varies with cluster concentration: at lower concentrations there are larger, less abundant aggregates, while the opposite is true for higher concentrations, consistent with incipient crystallization of a solution. For **Li₆** solutions, the PDDF suggests dimerization as we would expect for a protonated cluster. Moreover, association between the dimers in solution was observed in solution, as indicated by a broad coulombic peak in the scattering curve (Figure 1.10). The morphology observed in the thin films from **Li₆** and **Li₈** indicate gelation of the dissolved species with increased concentration, and crystallization of the dissolved species of the substrate, respectively. This is consistent with crystallization behavior of these clusters.

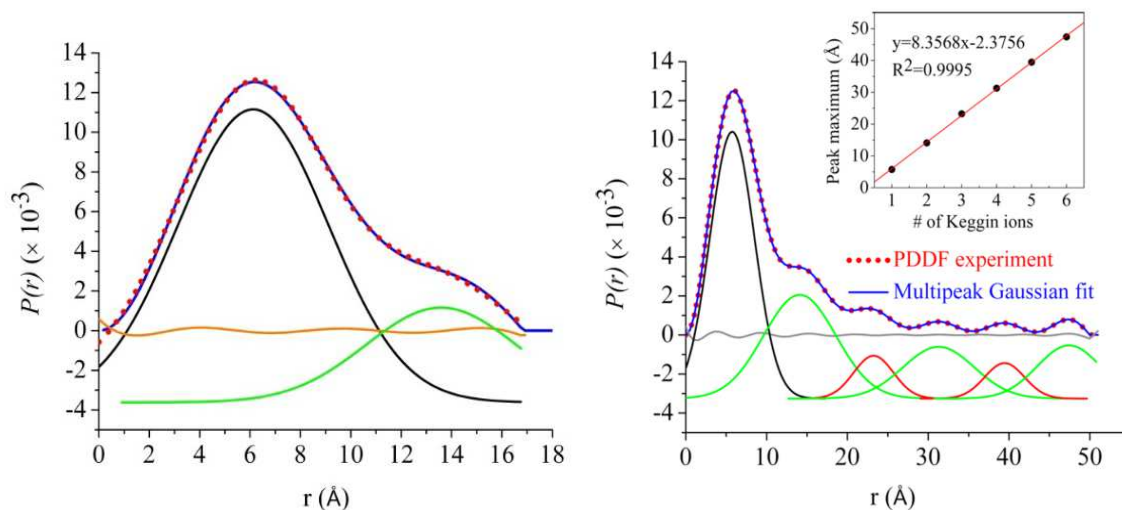


Figure 1.10. PDDF analysis of Cs (left) and Rb salts (right) of dodecaniobate $[(\text{Nb}=\text{O})\text{GeNb}_{12}\text{O}_{40}]^{13-}$. Black peak is the monomeric unit, green peaks are long axis of dimers, red dots are experimental data, and blue is the multipeak Gaussian fit.⁷⁵

1.3.1.2. Understanding the Mechanism of Linking Clusters. Since the first reported dodecaniobate Keggin structure⁷⁷ of $[\text{XNb}_{12}\text{O}_{40}]^{16-}$ (X = Si, Ge; see Figure 1.1 for illustration of Keggin ion), these clusters have been observed to link into infinite anionic chains,⁷⁸⁻⁸⁰ where the linker is a dimer of edge sharing octahedra (MO_6). A monomeric building block of these chains, (as well as a dimer) have been isolated as $[(\text{Nb}=\text{O})\text{GeNb}_{12}\text{O}_{40}]^{13-}$ and $[(\text{Nb}-\text{OH})\text{GeNb}_{12}\text{O}_{40}]_2^{24-}$. Through the structure of the dimer, evidence suggested that the protonation of the Nb=O cap to form Nb—OH is key to promoting polymerization. SAXS was used to study the effect of the counterion and protonation on this polymerization.

Two different aqueous conditions were used to create one environment where protonation prevailed and one where it was inhibited (Figure 1.10). In TMAOH solutions, Cs and Rb salts of the clusters did not protonate and no polymerization was observed. SAXS data suggested solutions of discrete, monodisperse species whose size (as determined by PDDF and Guinier analysis) was representative of the capped Keggin ion. In neat water, the clusters protonate and provide a self-buffering pH of ~10-11. The Cs salt in water revealed mostly monomers and dimers. In the Rb salt solutions, extensive polymerization occurred with a mixture of chain lengths featuring up to six Keggin.

PDDF is a valuable tool in identifying polymerization as multiple, distinct peaks are observed for each additional linkage. This difference in polymerization between Cs and Rb salts can be explained through ion association. Cs provides stronger ion association than Rb. Therefore, less protonation occurs on the cluster and thus less polymerization.⁷⁵

1.3.1.3. Investigating the Polymerization of Hf-tetrameric Clusters. Stemming from another thin film study aimed at developing inorganic photoresists, hafnium sulfate

clusters were studied in solution to gain insight into pre-nucleation and solution speciation.^{12,73,81} By understanding solution speciation and the solution behavior that yields dense smooth films, we can develop design rules for guiding the synthesis of new materials. Early X-ray scattering studies concluded that tetrameric species dominate in solutions of hafnium oxyhalides, which is consistent with the solid state structure.^{82,83} In a more recent study, hafnium sulfate solutions were observed using SAXS. As the solutions age, the average particle size increases significantly. It was found that the data could not be modelled by assuming simple spherical particles, and instead a cylindrical model was more adequate. The length of the cylinder was in good agreement with the maximum linear extent of the PDDF (providing an example of multiple mathematical routes to comparable interpretation), while the radius of the cylinder agreed with the size of the Hf-tetramer (Figure 1.11). A cylinder or rod is the appropriate model for this system because the tetramers are linking into chains. This is evident in the PDDF with periodic changes in the electron density. The extent of oligomerization depends on age and concentration of solution (Figure 1.11).⁷⁶

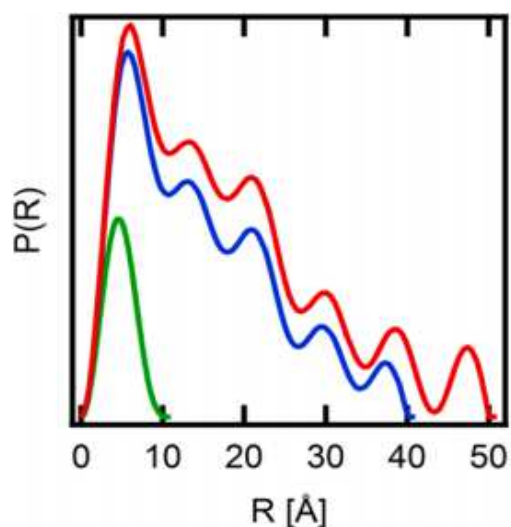


Figure 1.11. PDDF for 500 mM hafnium-sulfate solution aged for 0h (green), 24h (blue), and 72h (red).⁷⁶

The major conclusion drawn from this study was that the robust Hf cationic tetramers remain the major building block of the hafnium-sulfate thin films, despite the fact that they are joined in multiple directions by sulfate anions. The presence of a uniform repeat unit in the form of a discrete cluster is likely the primary reason for the very smooth films and high resolution nanopatterning provided by these precursor solutions.⁸¹ The primary difference between the hafnium-sulfate speciation and the previously described polyoxoniobates is the niobate clusters are limited by the linking chemistry under the mild conditions of the experiments. On the other hand, there are many sites at which the hafnium tetramers can link (i.e., corner-to-corner, edge-to-edge and face-to-face) in addition to forming sulfato bridges. Therefore, it is more challenging to obtain a unique model for scattering data. In this event, it is valuable to model SAXS data from solid-state structures as well.

Finally, SAXS data can be simulated using the program SolX^{84,85} where a solid-state model is developed from single-crystal data files to create a scattering curve, which also fits models to the simulated data. Both the shape of the scattering curve and the PDDF profile should match the experimental data if the data interpretation is correct. R_g data can also be readily obtained, however, the absolute value needs to be considered carefully, as it is very sensitive to the definition of the radius of the atoms that make up the scattering species (i.e. ionic vs. atomic radius). These radii, however, can be optimized iteratively as many scattering data are obtained a variety of clusters featuring different metal cations.

1.3.2. Dynamic Light Scattering Applied to Cluster Characterization. DLS is widely recognized as one of the most popular techniques for size measurements of nanoparticles,

proteins, colloidal species, polymers, and more recently clusters in solution.^{63,86,87} More so, advancements in DLS have allowed for relatively facile and routine detection of species as small as ~1 nm and lower in radius [R_h of 0.1 M $\text{Al}(\text{NO}_3)_3 = 0.35 \text{ nm} \pm 0.11 \text{ nm}$]. Some of the biggest strengths of this technique are that it requires a small sample volume (vol. > 50 μM), data collection can be performed within a matter of seconds, and it is non-destructive (except for light-sensitive materials). Additionally, depending on how well a given sample can scatter light, accurate measurements can be made in very dilute concentrations (sub- μM).⁸⁸ Experimentally, DLS has a wide array of applications including rapid screening of potential target materials, determining relative particle distributions of species in solution, prediction of optimal crystallization conditions, monitoring solution stability and rates of agglomeration/condensation, and determining temperature dependence of solution speciation. DLS is best used as a qualitative complementary or corroboratory piece to other techniques such as transmission electron microscopy (TEM), static light scattering (SLS), SAXS, Raman, and NMR.

While DLS is a fast and simple technique to utilize, it does carry some significant limitations in analyzing clusters in solution. Due to its inherent sensitivity and bias towards detecting larger particles or agglomerates, consistent detection of sub-5 nm species can become quite problematic if that species is unstable in solution (i.e. non-molecular clusters), or if there are larger aggregates in equilibrium at dilute concentrations with the smaller species of interest. DLS is also not particularly accurate in discerning multiple size distributions and the data may not be as reliable if there is no precedent available to calibrate a particular sample. Additionally, since DLS is sensitive

towards detecting larger particles, if the solvent is contaminated or has bubbles present, any data collected could be adversely compromised.

DLS takes advantage of the fact that in solution, any cluster present is generally perturbed to some extent by the solvent in which it is dissolved, suspended, or solvated. This disturbance between the cluster being studied and solvent results in the random motion of molecules in solution, or Brownian motion.^{9,89} As light scatters from the moving cluster, it imparts a random change to the phase of the scattered light, such that when the scattered light from two or more particles are added together, there will be a continuum of destructive or constructive interference as a function of time. These fluctuations in light intensity over time are converted into an autocorrelation function, in which a direct measurement of the rate at which a particle diffuses through the medium (the diffusion coefficient, D_t) is made. Typically, particles and agglomerates with larger radii will diffuse slowly while small particles diffuse more quickly. However, there are many other factors that can affect the measured value of a diffusion coefficient. Intrinsic factors that can alter diffusion rates include asphericity and inter-particle drag due to solvent-solute interactions, while extrinsic factors like solvent viscosity, cluster concentration, and temperature can play significant roles as well. It should be noted that the mass of a given particle has virtually no influence on the rate of particle diffusion, and may safely be ignored. And as stated in the earlier DOSY NMR section, an effective hydrodynamic radius (R_h) can be similarly calculated via the Einstein-Stokes equation.

1.3.2.1. Screening for Clusters in Solution. As a first case study, routine measurements of the following clusters in 500 mM aqueous solution were performed (viscosity effects were negligible): $H_{10}[Nb_6P_4O_{24}(O_2)_6]$ (**Nb₆**),¹⁴ $Hf_4(OH)_8(OH_2)_{16}^{8+}$,

(**Haf(SO_x)**),⁷⁴ and [Al₁₃(OH)₂₄(H₂O)₂₄]¹⁵⁺ (**f-Al₁₃**).⁶³ As expected, analysis revealed that upon immediate dissolution each cluster is approximately ~1 nm in radius and shows strong evidence towards being a discrete, monodisperse species in solution, as suggested by the narrow size distribution of each particle (polydispersity index% or PDI% < 15%). Furthermore, it is clear that each cluster exhibits strikingly different size distributions than the starting material from which each was synthesized.

It should be emphasized that one cannot reasonably differentiate one discrete species from another using DLS since i) each cluster is fit as a spherical molecule, and ii) the error of propagation from the aforementioned factors such as cluster asphericity and cluster-solvent interactions are directly linked to the size measurement. As such, one should not rely on DLS alone as a definitive method for identifying new or unknown clusters in solution as many particles will ultimately have similar diffusion rates. However, it does serve well as a rapid screening technique to identify possible positive leads for identifying clusters in solution.

1.3.2.2. Monitoring the Solution Stability of Hafnium Sulfate Clusters. One of the most practical applications of DLS in cluster analysis is the ability to consistently monitor rates of cluster aggregation or dissociation as a function of time. Figure 1.12 shows a three day study of 500 mM **HafSO_x** with and without the addition of H₂O₂ as discussed in the previous SAXS section.^{73,81}

After a period of ~24 hours, the **HafSO_x** solution without peroxide grows to nearly 4x its original size of 1 nm and agrees well with the **HafSO_x** PDDF experiment described earlier (Figure 1.10 in SAXS section). Over several days the rate of decomposition eventually slows down to reach a high point of approximately 6.3 nm ± 2.7 nm as the

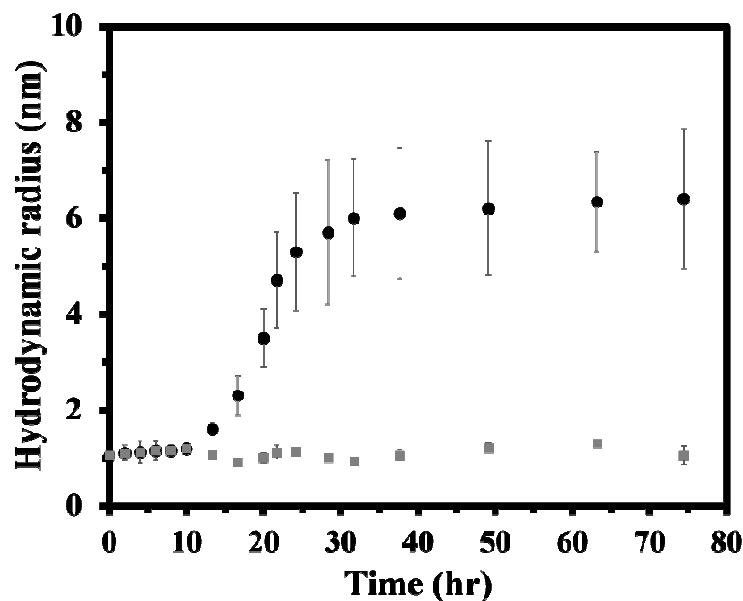


Figure 1.12. Time stability study of 500 mM hafnium sulphate (HafSO_x) with added H₂O₂ (grey) and without H₂O₂ (black). The large error that is prominent at the later times is due to a high degree of polydispersity that is inherent with HafSO_x over time.

solution began to crystallize. However, it should be again noted that unlike SAXS, DLS gives no information about the molecular shape of the nano-agglomerate that forms and thus the large error associated with the increase in particle distribution increases (i.e. increase in polydispersity) is due to the asphericity of the **HafSO_x** agglomerate. Ultimately, DLS is very valuable for determining kinetics qualitatively but can become ambiguous to analyze and quantify such rates if the system is non-ideal or supporting evidence is lacking.

Lastly, we will discuss the importance that concentration, particular high concentrations, can play on data collection and interpretation. Many factors must be taken into account when working with high cluster concentrations (Molarity > 1 M), including: electrostatic interactions, viscosity changes due to the solute, and multiple scattering

species. However, some of these concentration effects can be accounted and compensated for by using the following equation:^{89,90}

$$D_t = D_0(1 + c(2A_2M - f'))$$

where D_t = the translational diffusion coefficient at concentration c , D_0 = the diffusion coefficient extrapolated to zero concentration, A_2 = the second virial coefficient (a temperature-dependent correction term used to quantify and describe non-specific interaction potentials between particles in solution), M = molecular weight and f' = a first order frictional coefficient. In the case where $D_t > D_0$, it is usually indicative that a cluster diffuses faster in a given solvent medium, and thus gives rise to an apparently smaller radius. In this case, the correctional term $c(2A_2M - f')$ will have a large positive value. This apparent decrease in R_h at higher concentrations can be explained by the high value for A_2 . The positive increase of A_2 points to an overall increase in the repulsive forces between clusters. Essentially this exerts an additional force on the particles, causing them to move faster compared to the case of non-interacting particles. Conversely, in the situation where $D_t < D_0$, a cluster is diffusing slower than expected, and a larger R_h would be measured. In this case the opposite is true and would exhibit a large negative value for $c(2A_2M - f')$. In the situation, the cause for the apparent increase in R_h can usually be attributed to either an increase in the physical size of the species observed or an increase in the sample viscosity. To solve this problem, one can simply measure and incorporate the bulk sample viscosity in the Stokes-Einstein equation. After correcting for this viscosity, if R_h is larger than expected, then this likely leads to the scenario in which A_2 is negative and aggregation is occurring.

To elaborate further on the significance of electrostatic interactions, recall that DLS measures the translational diffusion directly, not R_h . The Stokes-Einstein relationship assumes a hard sphere undergoing Brownian motion in a dilute, non-interacting environment. This condition no longer applies when electrostatic interactions are prominent. When equally charged molecules (particularly highly charged molecules) approach one another, repulsion occurs and promotes particle acceleration. Since the Stokes-Einstein relationship assumes faster diffusion, this results in a smaller observed (or apparent) hydrodynamic radius. Experimentally, this can be tested and even mitigated by either sample dilution or by increasing the ionic strength of the solution, though the latter may potentially alter aggregation states or stability of a cluster (as the previously discussed ion-pair interactions in niobate clusters would suggest).

Effects from a significant increase in viscosity will also change the results in that a viscous solution will slow down the rate of diffusion and lead to a calculated R_h that is larger than may be expected. On the other hand, if viscosity is very fluid, this can result in a smaller observed R_h . In this scenario, it cannot be assumed that solution viscosity of a cluster is equal to that of the solvent's viscosity. Thus, it is very critical at higher concentrations to have accurate viscosity data in order to ensure accurate size results. In summary, DLS is powerful complementary techniques when utilized properly to qualitatively study clusters in solution.

1.3.3. Phase Analysis Light Scattering (PALS). Massively-parallel phase analysis light scattering, commonly referred to as PALS, is another light scattering technique that is predominantly used to accurately determine the electrophoretic mobility (μ_e), zeta potential (ζ), and ionic conductivity of a species in solution. In a given PALS experiment,

electrophoretic mobility measurements are acquired by illuminating a sample in a chamber with two electrodes under an alternating electrical field while collecting the scattered light. A reference beam and a redirected second laser beam (or local oscillator) are mixed (heterodyned) directly on the detectors with scattered light from the sample and act both as an optical amplifier and as a phase reference. In such a configuration, PALS is an interferometry method in which one end of the instrument is the modulated local oscillator and the other is the scattered light.

The main disadvantage of the technique is that PALS generally suffers from many of the same drawbacks that are present with DLS, particularly if one is measuring R_h simultaneously. The biggest potential pitfall however comes with samples at high concentrations (generally above 100 mM) which can be quite conductive (conductivity ≥ 10 mS/cm). At such a high conductivity, a sample becomes increasingly susceptible to electrolysis, which would make any analysis completely unreliable. μ_e is a first-principle physical measurement that makes no assumptions regarding the shape, size, etc. for a given species. It is defined as the velocity (v) at which a charged particle moves under the influence of a spatially uniform electric field (E):

$$\mu = \frac{v}{E}$$

In the special case of spherical particles, the opposing frictional force ($F_f \propto 6\pi\eta R_h v$) to the electrical force applied ($F_e \propto QE$, where Q is the charge of the particle) is proportional to the hydrodynamic radius (R_h) of the particle, its velocity (v) and the solution viscosity (η). Under this condition, μ_e can be expanded into the follow equation:

$$\mu = \frac{v}{E} = \frac{Q}{6\pi\eta R_h}$$

μ_e is a particularly useful value in that the zeta potential can be derived using Henry's law:

$$\mu = \frac{2\varepsilon\zeta}{3\eta} f(\kappa R_h)$$

where ε = dielectric constant, ζ = zeta potential, η = viscosity, κ = Debye-Hückel parameter, and $f(\kappa R_h)$ = Henry's function.

Aqueous molecular and non-molecular clusters without a source of external stabilization (e.g., surfactants, supporting ligands) are typically stabilized as charged ions in solution. A given charged cluster will have high density of oppositely charged layers of ions surrounding it, otherwise simply referred as the electrical double layer (surface potential). The surrounding "Stern layer" is less densely charged, but contains tightly bound ions. When the molecules diffuse, both the electrical double layer and the Stern layer will move along with the molecules. This boundary that exists at the Stern layer is called the slipping or shearing plane. The electrokinetic potential of a molecule at this slipping plane is defined as the zeta potential (Figure 1.13).

The primary significance of the value of zeta potential is that it is a predictor of cluster stability in solution. While aggregation of clusters can readily be monitored by DLS and SAXS over time, such long term stability or accelerated aging studies are simply time consuming. Regardless, the magnitude of the zeta potential indicates the degree of electrostatic repulsion between similarly charged clusters in solution. In other words, the higher the zeta potential, the more stable a cluster will be. Generally, a cluster can be predicted to have prolonged stability if the magnitude of the zeta potential is

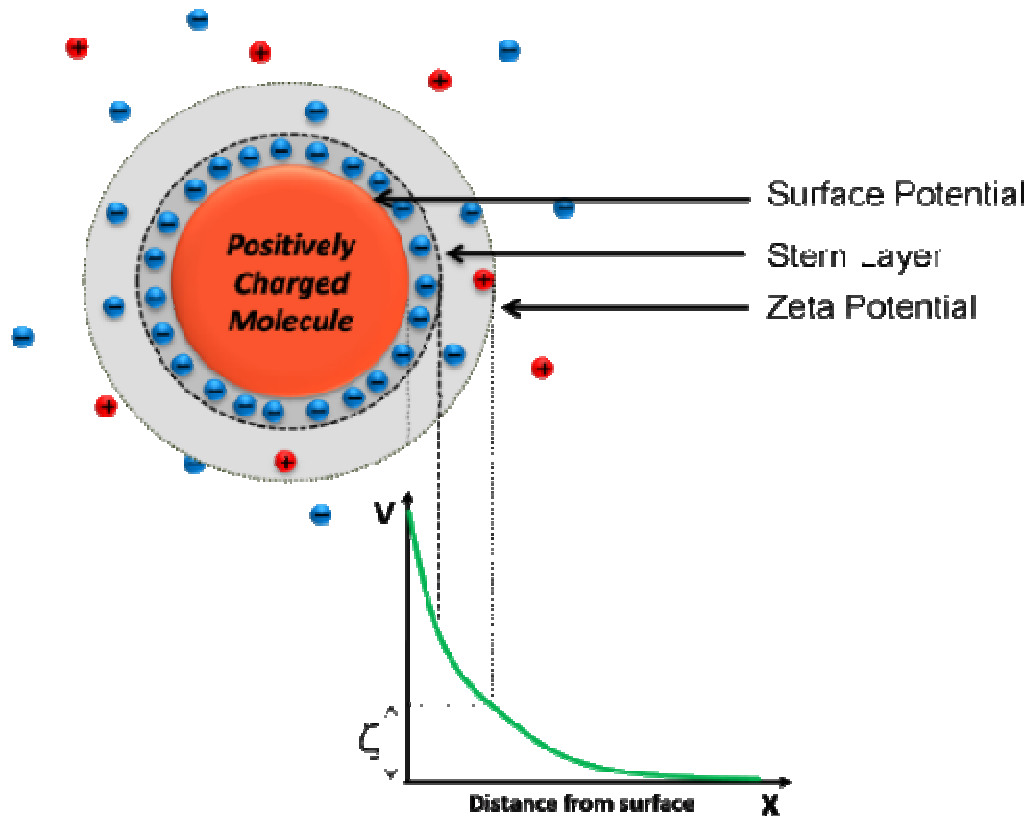


Figure 1.13. Simple model of a charge particle and its surrounding charges.⁹⁰ The intermediate distance away from the surface at which the surrounding ions release from the core particle's attractive pull and "slip" into equilibrium is defines where the zeta potential is found.

greater/less than ± 30 mV. At such high potential values, the repulsive forces will exceed the attractive forces and ultimately allow a cluster to exist as its own discrete species. However, as the magnitude of zeta potential approaches zero, the force of attraction becomes greater than the overall repulsive forces and leads toward rapid instability and flocculation. Zeta potential is particularly useful for cluster analysis in that it provides a direct measure of the isoelectric point (pH at which the charge is 0 mV) and can be corroborated with conductivity and size measurement to further understand phenomena such ion association.

To complement the **HafSO_x** cluster study mentioned in the previous SAXS and DLS sections, initial zeta potential measurement taken of both **HafSO_x** with and without added H₂O₂ revealed that the **HafSO_x** mixture without H₂O₂ had a zeta potential of 10.3 mV ± 1.56 mV while the addition of H₂O₂ to **HafSO_x** increased this value to 28.6 mV ± 2.3 mV. This indicates that H₂O₂ plays a major role in charge stabilization for this particular cluster species. Predictably, the **HafSO_x** solutions that contain no H₂O₂ began to polymerize within a day and crystallized out of solution soon after.

Studies have also been done to determine the isoelectric point of **f-Al₁₃** using PALS. In this study, 50 mM **f-Al₁₃** was titrated with 100 mM NH₄OH from a pH range of 3.5 up to 9, where the zeta potential for **f-Al₁₃** was found to be 0 mV and is by definition the isoelectric point (Figure 1.14).

Interestingly, although agglomeration of the cluster is quite prevalent with the addition of NH₄OH (simultaneous DLS measurement revealed a size increase from 1 nm to ~5 nm), the solutions were shown to still have a fairly high charge of around 35 mV between the pH ranges of 4 to 6. Subsequent flocculation does not occur until around a pH of 8 as the cluster reaches its isoelectric point at a pH of ~9. To conclude, PALS is an excellent tool for predicting cluster stability in solution and can be utilized with virtually any other solution technique to explore and understand the complex nature of charge speciation and dependency in solution.

1.3.4. Raman Spectroscopy. Since its discovery by Dr. C. V. Raman in 1928, Raman spectroscopy has been recognized as a very important analytical tool across numerous disciplines. Due to its sensitivity, high information content, and non-destructive nature, applications span many fields of chemistry and materials science.^{91,92} Often paired with

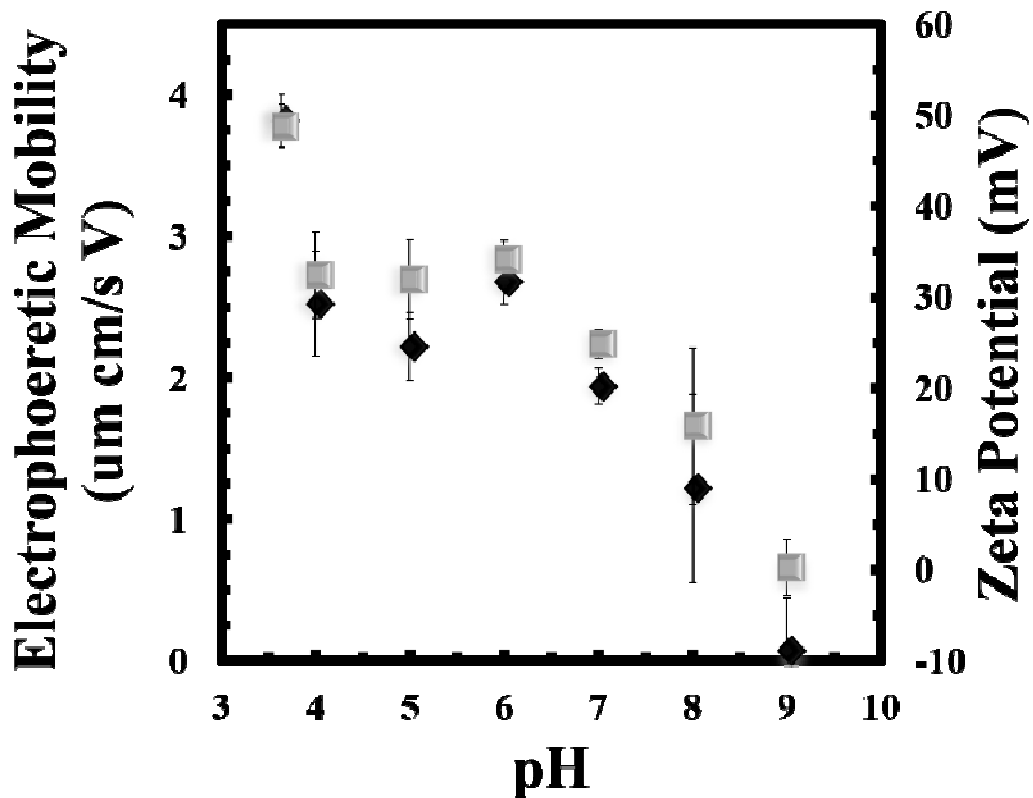


Figure 1.14. Plot of electrophoretic mobility (black diamonds) and zeta potential (grey squares) vs pH of **f-Al₁₃**. Mobility data is shown to demonstrate the direct relationship it has with zeta potential. The isoelectric point for **f-Al₁₃** is shown to be at pH = 9.

IR, both techniques are used complementarily to probe different aspects of a given sample. For instance, while IR is typically sensitive to functional groups and to highly polar bonds, Raman is more sensitive to backbone structures and symmetric bonds. Using both techniques provides twice the information about the vibrational structure than can be obtained by using either technique alone. In addition to providing unique information about a sample, Raman offers several additional benefits, including: minimal to no sample preparation, sampling directly through glass, non-destructive analysis (with exception of light-sensitive materials), non-intrusive analysis, permitting study of more

labile sample features (such as crystal structure), and minimal interference from IR-active species such as H₂O or CO₂.

In Raman spectroscopy, the sample is irradiated with monochromatic light and the photons emitted are either elastically (Rayleigh) or inelastically (Raman) scattered. The inelastically scattered light has lost (Stokes) or gained (anti-Stokes) energy during this interaction and the emitted photon contains information about the molecular structure of the sample, particularly the vibrational modes of a molecule. Since Raman scattering is extremely weak in relation to Rayleigh scattering (1:~10⁷ photons will be Raman scattered), filters are used to limit the observed intensity of the Rayleigh scattering. The other requirement for a vibration to be Raman active is that a given molecular vibration must give rise to a distortion of the electron cloud that surrounds the molecules under the influence of an electric field (polarizability).

While Raman spectroscopy has been widely used in characterization of organic, organometallic and biological molecules among many others, it has been used less frequently in the search to identify inorganic cluster species. For our particular interest, we seek to use this technique as a means for rapid identification of clusters, establishing a database of known clusters in the solid state, screening for potential new targets, and qualitatively and quantitatively investigating the speciation and dynamics of clusters in solution. One can immediately observe qualitative differences between the various vibrational modes in the Raman spectra of crystalline bismuth nitrate and the Bi₆O₄(OH)₄(NO₃)₆•H₂O cluster (Figure 1.15).⁹³

Since crystal structures of both species have been determined, solid state Raman data can be generated for each cluster, which then provides a means of identifying the species

in solution and gaining insight on the cluster speciation through solution Raman spectroscopy. However, this can become increasingly complicated when an exact structure is unknown or when there is little precedent available for an unknown sample. To circumvent such problems, complementary methods such as quantum mechanical computations (discussed below) serve as a powerful tool towards understanding spectral data.

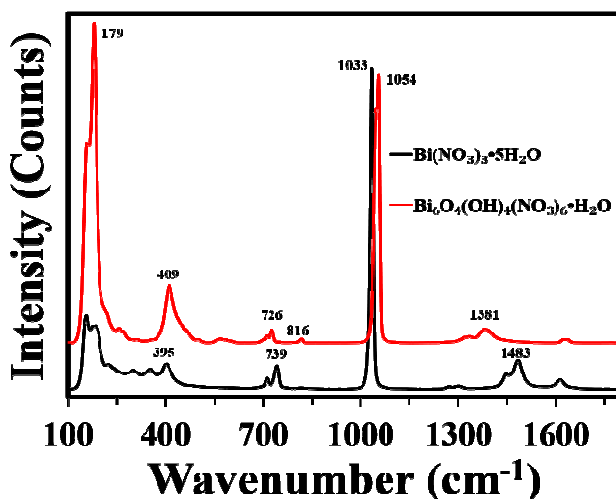


Figure 1.15. Stacked Raman spectra of Bismuth nitrate (black) and a bismuth hexamer (red).⁹³ Notable peaks that distinguishes this cluster from bismuth nitrate include the two stretching Bi—O bands at 179 cm^{-1} and 409 cm^{-1} . The small peak at 816 cm^{-1} corresponds to a μ —OH bridge of the cluster. Additionally, spectral shifts of the symmetric and anti-symmetric bands of NO_3^- ion are present. The symmetric stretching band at 1033 cm^{-1} for $\text{Bi}(\text{NO}_3)_3$ is blue shifted to 1054 cm^{-1} while the anti-symmetric band at 1483 cm^{-1} for $\text{Bi}(\text{NO}_3)_3$ is red shifted to 1381 cm^{-1} for the bismuth cluster.

Raman spectroscopy also allows for qualitative and quantitative investigations of many facets of the dynamic nature of clusters in both the solid state and solution. More specifically, it is useful for studying changing speciation as a result of metal exchange, chemical equilibria, temperature changes, pH changes, solvent effects, as well as observing the formation of clusters from their precursor monomers.⁹⁴ For instance, the dissociation mechanism of the **f-Al**₁₃ cluster in aqueous solution can be studied by Raman

spectroscopy. In this particular study (Figure 1.16) the dissociation/decomposition of **f-Al₁₃** to Al(NO₃)₃ is observed by Raman during the titration of **f-Al₁₃** with HNO₃, as indicated by the appearance of the Al–O symmetric stretch at 525 cm⁻¹ known for Al(OH₂)₆³⁺.^{95,96}

A second peak at 345 cm⁻¹ can also be described as an antisymmetric Al–O vibration. Importantly, while it is possible to quantify data like that shown in Figure 1.16, one must be aware of some of the challenges that are prevalent with solution quantification using Raman. An immediate problem that arises is the fact the many of the molecular vibrations, particularly in solution, associated directly with a cluster of interest (i.e., M–O, M–OH, M–H₂O, etc.) are often several orders of magnitude weaker than overlapping peaks of the counterions or solvent. To combat this issue, techniques such as accumulation of longer scan times and advanced background subtractions such as removing the influence of the solvent peaks are often employed to reveal some of the weaker Raman scatters (as shown in Figure 1.16).⁹⁶ A recent study also utilized differential background subtractions to monitor *in situ* the growth of **f-Al₁₃** from Al(NO₃)₃ via electrochemical titration.⁹⁴ With such a technique, it was revealed that an initial “Al₇” core is established prior to the formation of **f-Al₁₃** and that the Al₇ core exists in solution with the **f-Al₁₃** cluster. In summary, Raman spectroscopy is a relatively facile, but powerful technique to use in conjunction with other methods to explore complex fundamental questions associated with many aqueous inorganic clusters.

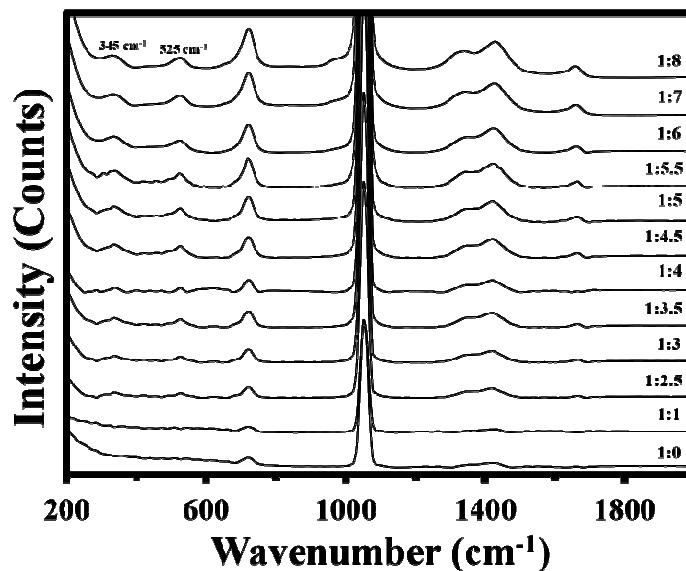


Figure 1.16. Stacked Raman spectra of $f\text{-Al}_{13}$ titrated with various equivalents of HNO_3 . The bottom spectrum represents a solution of 1 M $f\text{-Al}_{13}$ with no added HNO_3 as indicated by the ratios shown on the right of the graph.

1.4. COMPUTATIONAL STUDIES

With the increase in computing power and improvements in theoretical methods over the last several decades, quantum mechanical computations have demonstrated their potential to inform and predict properties of nanoscale materials. However, for a researcher with no experience or background in theory, these computations can prove daunting. There are numerous theoretical methods available in commercial programs available today, with an even larger number of possible basis sets and solvent models. Nonetheless, when used properly, computations can prove to be powerful, assisting in the understanding of the vibrational spectra, thermodynamic stability, dynamics, and electronic properties of nanoscale clusters and particles.

1.4.1. Vibrational Spectroscopy. As mentioned earlier, vibrational spectroscopy is a very common technique for characterizing nanoscale clusters and appealing for analyzing

nanoscale materials due to the relative ease with which these spectra can be collected.⁹⁵ However, for many species, the assignment of signals in these spectra from unknown samples is extremely difficult without computations. With proper assignment, these techniques can be used to identify signature peaks for specific species, allowing for unique identification of these species in subsequent experiments.

Conceptually, IR and Raman are simple, straightforward techniques computationally.⁹⁷ Computing these modes is a relatively simple process when a few factors are kept under consideration. First, the structure of a species needs to be properly computed before determining its vibrational modes. It is tempting to use crystal structures to compute the normal mode vibrations of a species. However, crystal structures cannot be used directly because the frequency calculation is highly sensitive to the geometry. Furthermore, the use of a frequency computation requires that the species be in a true ground state geometry, in the same level of theory used to compute the vibrational modes. If this requirement is not met, the frequency calculation will return both positive and negative frequencies, indicating an unstable geometry. These results are unreliable for use in modeling a vibrational spectrum.

When the vibrational modes have been correctly computed, there are still several steps required to produce a complete spectrum from the computed data. Most crucially, the approximate width of the vibrations must be found, as the width of each vibrational mode is not included in the computed data obtained from modern computational software. Therefore, to model each vibration, the computed frequency and intensity of each vibration is fit to a Gaussian function. The width is then modelled in one of two ways. First, for simplicity, one may consider all the widths approximately the same.^{96,98}

However, this is not always a reasonable approximation, so often the widths of the vibrations are allowed to independently vary. In either case, the widths are typically found by comparing the experimental spectrum with the computed data. This method has been used on a wide array of systems, from organic molecules to metal oxide and hydroxide clusters. This technique was used on the gallium and aluminum tridecameric hydroxide clusters, $[M_{13}(OH)_{24}(H_2O)_{24}](NO_3)_{15}$ or **f-M₁₃**, to find the signature peaks associated with each cluster's vibration (Figure 1.17). Unsurprisingly, this analysis worked better for solid samples than for aqueous solutions. However, for both states, this analysis led to full assignment of each spectrum and led to identification of each cluster's unique signals. This method has also been demonstrated for the α - and β - isomers of the Keggin phosphomolybdate anions. The computed spectra for both of these anionic clusters were in good agreement with the experimental IR spectrum. However, the computed spectra of the α - and β - isomers were too similar to allow for unique identification of isomers via IR.⁹⁷

1.4.2. Thermodynamic Stability. The thermodynamic stability of clusters is conceptually one of the easiest calculations to understand. Any scientist with a strong understanding of Gibbs free energy would be equipped to understand the results of thermodynamic calculations. However, the challenge of thermodynamic stability is in knowing which method will yield accurate results with respect to experiments and the proper determination of the most stable geometry for the species of interest.

There have been many studies examining the stability of nanoscale polyoxometalate clusters. The Keggin cluster family is a popular topic of study because this family of clusters has five different isomers based on the rotation of a trimeric group at the exterior

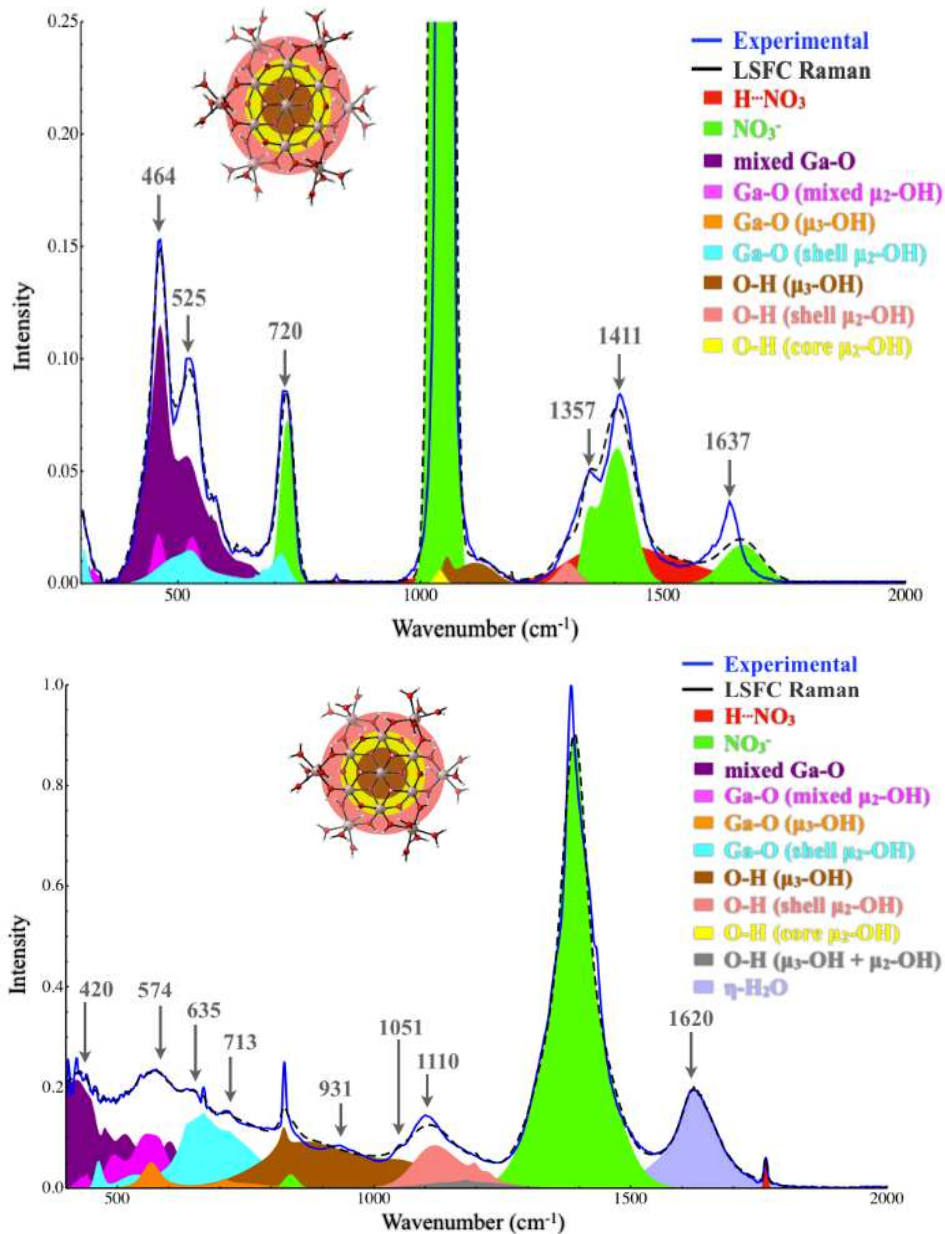


Figure 1.17. Top. Simulated and experimental IR overlay spectra from 500 cm⁻¹ – 2000 cm⁻¹ of solid state **f-Ga₁₃**. Bottom. Simulated and experimental Raman spectra from 200 - 2000 cm⁻¹ of crystalline **f-Ga₁₃** at 25 °C. The feature shown at 464 cm⁻¹ arises from the primary breathing mode of the cluster.

of the cluster. Understanding the stability of these clusters is important for understanding the likelihood of synthesizing one isomer over another, especially if only one isomer is well-suited for a particular application. For the Keggin phosphotungstates, computations were able to reveal the stability of each of the five isomers.⁹⁹ When examining this

stability trend, the authors found that the stability of each isomer was largely determined by how many unfavorable W-W contacts each isomer had, as each contact contributed approximately 8-9 kcal/mol in destabilization. A similar trend was computed for phosphomolybdate Keggin ions, though with a slightly lower destabilization energy per metal-metal contact.¹⁰⁰

Using static calculations to determine the stability of different nanoscale species is severely limited by the ability of the computations to accurately optimize the geometry. In ionic nanoscale species, the solvent effects are often extremely significant to the cluster geometry. This effect is particularly pronounced in aqueous solutions and in systems where the species of interest has a high likelihood of hydrogen bonding with either itself or the solvent. In the case of metal hydroxo clusters, these clusters tend to optimize to distorted geometries due to the hydroxo and water ligands affinity to hydrogen bond with each other, even with the use of implicit solvent models such as PCM and COSMO.

1.4.3. Dynamics. Dynamic calculations have the potential to solve a wide variety of problems. These types of calculations can be divided into primary categories: dynamics performed using molecular mechanics (MM or MD) or those using higher levels of theory, often MD used in conjunction with quantum mechanics. MD calculations are much less computationally expensive because their treatment of atoms and electrons is closer to a classical approach compared to quantum. This means that MD is best suited for extremely large systems where higher levels of theory or static quantum calculations would be unable to yield results in a reasonable time frame. Historically, molecular dynamics simulations have been useful in examining the diffusion of different species in

solution and the interaction of these species with solvent molecules.⁹⁷ MD has also been used to look at exceptionally large species, such as the giant polyoxometalate Mo₁₃₂.¹⁰¹ In addition, these calculations have been used to assist in the understanding of average coordination environments of metal ions, which can provide information about the mechanism of cluster formation.¹⁰²

More rigorous theories for dynamics have yet to be used widely on nanoscale systems, but these methods have potential to inform scientists about a variety of solution behaviour. One of the more appealing options is the use of quantum mechanical and molecular mechanical calculations (QM/MM).¹⁰³ These types of calculations are particularly appealing because they allow for the treatment of certain molecules and/or atoms to be treated with QM and others to be treated with MM. This is appealing for looking at systems where the solute-solvent interactions are of primary interest.¹⁰⁴ Particularly, this type of analysis could be useful in examining reactions where solvent molecules are either consumed in the reaction or serve as a catalyst.

1.4.4. Electronic Properties. Computations of nanoscale species can be used to inform chemists about the electronic properties of their materials. This is typically approached using density functional theory (DFT), often using time-dependent calculations, so as to probe the optical gap of different materials. DFT can also be used to compute the fundamental HOMO-LUMO gap of clusters.¹⁰⁴ These calculations yield not only information about the orbital energies, but can also show the shapes and positions of the orbitals. Studies such as this are often done to understand the fundamental reactivity of many materials.

Perhaps one of the most practical applications of computing the electronic properties of nanomaterials is to determine their redox chemistry. This has been used extensively on nanomaterials from polyoxometalate clusters to nanoparticles.¹⁰⁶⁻¹⁰⁹ Polyoxometalates and nanoparticles often make good oxidizing agents, being reduced by placing an electron in one of its non-bonding metal orbitals.^{97,110} The HOMO-LUMO gaps of different species can be used to determine the relative ability of multiple species to act as oxidizing agents, but the exact values for the HOMO-LUMO gaps cannot be used to determine the redox potential without further information. Much like in experiments, the redox potential must always be described as relative to another reaction, in most cases, the standard hydrogen electrode. To reproduce these values computationally, the reaction of interest needs to be compared to the computed analog of the standard hydrogen electrode.¹¹¹ When properly computed, these calculations can be used to determine the relative oxidizing ability of many different agents and determine the one most suited for a particular application without ever having to enter a laboratory.

1.5. CONCLUSIONS

The grand challenges that exist aimed at understanding the basic fundamental chemistries of the many clusters that preside in nature or through controlled synthesis offer a unique opportunity for researchers to explore and to develop new methods for analysis. In this Prospective we have surveyed some of the emerging combinations of venerable and new techniques that are finding utility currently. Rapid development of new and improved analytical technology and improved basic science understanding are still required for us to delve even deeper as we continue to characterize and explore the dynamics of aqueous inorganic clusters in the solid state and solution, and to provide improved resolution on the speciation of metal ions and their clusters in polar solvents.

As one example, **f-Al₁₃** does not appear on speciation diagrams of aqueous Al hydrolysis; however, the abundance of emerging evidence studying this cluster over wide concentration and pH ranges suggests that this cluster (and perhaps many others) remain to be discovered during controlled metal ion hydrolysis.

1.6. CHAPTER II BRIDGE

Chapter II will discuss how infrared and Raman spectroscopy were used in tandem with quantum mechanical computations to identify and characterize Group 13 aluminum and gallium tridecameric clusters in the solid state and aqueous solution.

CHAPTER II

IDENTIFYING NANOSCALE M_{13} CLUSTERS IN THE SOLID STATE AND AQUEOUS SOLUTION: VIBRATIONAL SPECTROSCOPY AND THEORETICAL STUDIES

2.1. INTRODUCTION

For this chapter, I was the main project lead as well as first author and carried out all of the experimental work for this manuscript. Great thanks should go to Lindsay Wills, Iya Chang, and Paul Cheong for their diligent work in assigning the Raman and infrared spectra in the solid state and solution. This work was published in the ACS journal *Inorganic Chemistry* where it received a featured web page highlight for the month of June 2013.

Raman spectroscopy, infrared spectroscopy, and quantum mechanical computations were used to characterize and assign observed spectral features, highlight structural characteristics, and investigate the bonding environments of $[M_{13}(\mu_3\text{-OH})_6(\mu_2\text{-OH})_{18}(\text{H}_2\text{O})_{24}](\text{NO}_3)_{15}$ ($M = \text{Al}$ or Ga) nanoscale clusters in the solid phase and aqueous solution. Solid phase Raman spectroscopy was used to reveal that the metal-oxygen (M-O) symmetric stretch (breathing mode) for the Al_{13} cluster is observed at 478 cm^{-1} , while this same mode is seen at 464 cm^{-1} in the Ga_{13} cluster. The hydroxide bridges in each cluster are weakly Raman active, but show slightly stronger infrared activity. The

breathing modes associated with the clusters in the solid state are not clearly visible in aqueous solution. This change in behavior in the solution phase may indicate a symmetry breaking of the cluster or exchange events between protons on the ligands and the protic solvent. Overall, each cluster has several unique vibrational modes in the low wavenumber region ($< 1500 \text{ cm}^{-1}$) that are distinct from the parent nitrate salt and other polymeric species with similar structure, which allows for unambiguous identification of the cluster in solution and solid phases.

In recent years, the semiconductor industry has increased research efforts toward developing greener and more cost effective methods of producing thin film devices.^{1,2} Group 13 metal aquo-hydroxo clusters with the formula $[\text{M}_{13}(\mu_3\text{-OH})_6(\mu_2\text{-OH})_{18}(\text{H}_2\text{O})_{24}](\text{NO}_3)_{15}$ ($\text{M} = \text{Al}$ or Ga) offer great promise as precursor materials for a variety of applications associated with the fabrication of thin film devices from aqueous solutions.^{3,4} However, there is limited knowledge about the growth mechanism, kinetics, solution dynamics, and film formation of these clusters in aqueous solution. To date, there are only a few reported studies on the solution speciation of such clusters.^{5,6,7} A recent study revealed that the Ga_{13} cluster was visible via $^1\text{H-NMR}$ in 2 mmol d_6 -DMSO.⁷ However, since solution processed thin films are often fabricated in water and at higher concentrations, d_6 -DMSO is not an ideal solvent to study for thin film development.⁸ As a first step to studying the speciation and solution dynamics in water, this study focuses on characterizing the vibrational modes of the metal clusters in the solid and aqueous solution phase using Raman and infrared spectroscopy, staple techniques which have found limited utility in the characterization of aqueous nanoscale clusters.⁹

The solution speciation and dynamics of these clusters during the spinning, curing, and annealing processes to produce films is of great interest to the material science community as they seek to fine tune the properties of metal oxide thin films. By identifying and characterizing these clusters in solution, we will be better equipped to monitor the evolution of monomeric Al and Ga species to solution intermediates, then to clusters, and eventually, to the production of thin films. By using computations to assign peaks, we have been able to differentiate between monomeric Al and Ga species and the more complex nanoscale Al₁₃ and Ga₁₃ clusters in the solid and solution states. This initial study adds to the arsenal of characterization techniques available for studying such aqueous clusters and shows that Raman spectroscopy in particular is an effective reporter of cluster species in solid and solution phases. These studies will provide a baseline for future investigations into understanding cluster formation mechanisms and dynamics/speciation in solution.

2.2. EXPERIMENTAL

2.2.1. Materials and Sample Preparation. FT-IR grade KBr (Aldrich 99.9%) was used in pellet preparation for infrared analysis. Ga(NO₃)₃•xH₂O (Aldrich 99.9%) and Al(NO₃)₃•9H₂O (STREM 98+%) were used without further purification as references in both the solid state and aqueous solution.⁷ The Al₁₃ cluster was synthesized as previously reported via a zinc reduction method and crystallographically confirmed prior to spectral analysis using single crystal XRD.¹⁰ Herein we show that the Zn reduction method can also be extended to forming the Ga₁₃ cluster as well.

2.2.2. Zn Reduction Method for the Synthesis of Ga₁₃(μ₃-OH)₆(μ₂-OH)₁₈(H₂O)₂₄(NO₃)₁₅. 2.55 g of Ga(NO₃)₃•xH₂O was dissolved in 10 mL of 18.2 MΩ

H₂O. Zinc powder was then added into the solution in a 2:1 molar ratio of Ga:Zn and the solution was stirred until the zinc was fully dissolved. The solution was then filtered and the filtrate was evaporated until crystals formed. The crystals were then washed with isopropyl alcohol to selectively remove excess Zn(NO₃)₂, Ga(NO₃)₃ and yielded ~57% of the final product. DOSY NMR spectra and single crystal XRD matched previous reports. In addition, Raman and IR spectra from a previous synthetic preparation were also identical. Stock solutions of the purified samples were prepared using ultrapure 18.2 MΩ H₂O and exhibited no appreciable changes over the duration of the experiment.

2.2.3. Raman and Infrared Instrumentation. Raman spectra were collected using an Alpha 300S SNOM confocal Raman microscope in a 180° backscattering configuration. A continuous wave pump laser delivered 45 mW of power with an excitation wavelength of 532 nm. A 0.3 m spectrometer equipped with 1800 grooves/mm grating was used to detect stokes Raman scattering and provided a resolution of 1 cm⁻¹. The spectra from each sample were averaged over 2000 accumulations at 0.5 s integration time per scan. The 520.5 cm⁻¹ peak of Si was used as an internal standard.

Infrared spectra for both clusters were acquired with a Nicolet 6700 FTIR spectrometer using a KBr pellet. Spectra spanning the range of 400-4000 cm⁻¹ were obtained with 64 scans at a resolution of 2 cm⁻¹. Multiple spectra of different sample batches were collected with each technique to ensure reproducibility of the results.

2.2.4. Computational Methods. All geometry optimizations and absolute energies were computed at the HF/6-31G(d,p) level of theory with the PCM-UFF continuum solvation model for water in Gaussian09.¹¹ The fundamental frequencies of the nitrate ion vibrations were obtained from literature.¹² To identify the individual vibrational modes, a

Least Squares Fitted Computed (LSFC) spectrum was created from the computed frequencies, as reported earlier.¹³ The juxtaposition of the LSFC spectrum to the experimental spectrum enables the association of all the peaks with specific vibrational normal modes.

2.3. $\text{Al}_{13}(\mu\text{-OH})_6(\mu\text{-OH})_{18}(\text{H}_2\text{O})_{24}]^{15+}$: RESULTS AND DISCUSSION

2.3.1. *Raman Spectroscopy: Solid Phase.* Several weak modes in the Raman spectrum Figure 2.1 of Al_{13} from 200-2000 cm^{-1} were observed that correspond to the Al-O vibrational modes in the core and shells of the clusters and are summarized in greater detail in the Supplemental Information in the Appendix (see Table S6). The peak at 478 cm^{-1} is attributed to the M-O symmetric stretch of the cluster. Quantum mechanical computations reveal several weak modes between 700 - 1200 cm^{-1} for the $\mu\text{-OH}$ hydroxyl bridges of the cluster, including a weak shoulder at $\sim 1100 \text{ cm}^{-1}$. Though this region is expected for Al-(OH)-Al bridging vibrations, the peaks for the hydroxyl bridges are difficult to distinguish experimentally due to overlap with the NO_3^- vibrations.^{14,15,16} The expected vibrational modes at 721 cm^{-1} , 1048 cm^{-1} , 1352 cm^{-1} and 1411 cm^{-1} are in good agreement with previous related reports.¹⁴⁻¹⁶ The cluster also exhibited modes at 1641 cm^{-1} , 3277 cm^{-1} , and 3470 cm^{-1} which are attributed to the out-of-plane O-H water bending ($\text{OH}_2\cdots\text{NO}_3^-$), coordinated O-H stretching ($\text{Al}-\eta\text{H}_2\text{O}$), and O-H stretch of disordered (non-coordinated) waters respectively (Figure S1 in the Appendix).¹⁷

In comparing the spectra of the Al_{13} cluster to that of $\text{Al}(\text{NO}_3)_3\cdot 6\text{H}_2\text{O}$, we discovered that the spectra exhibit some contrasting features. $\text{Al}(\text{NO}_3)_3\cdot 6\text{H}_2\text{O}$ in the solid state contains a single Al-O stretching vibration at 525 cm^{-1} that corresponds to the O_h $\text{Al}(\text{H}_2\text{O})_6^{3+}$ ion and three weaker modes below 300 cm^{-1} that are indicative of an aluminum nitrate species.¹⁸ The weak shoulder at $\sim 1100 \text{ cm}^{-1}$ in the Al_{13} spectrum is

associated with the hydroxide bridges of the cluster and are not present in $\text{Al}(\text{NO}_3)_3 \cdot 9\text{H}_2\text{O}$.¹⁸ There are no significant frequency differences in the NO_3^- ion in the Al_{13} and $\text{Al}(\text{NO}_3)_3 \cdot 9\text{H}_2\text{O}$ spectra, with the exception of a split peak at 1058 cm^{-1} .¹⁷ This suggests that the nitrates in the cluster are not integral to the overall structure and only coordinate to the cluster via hydrogen bonding, consistent with the crystal structure.

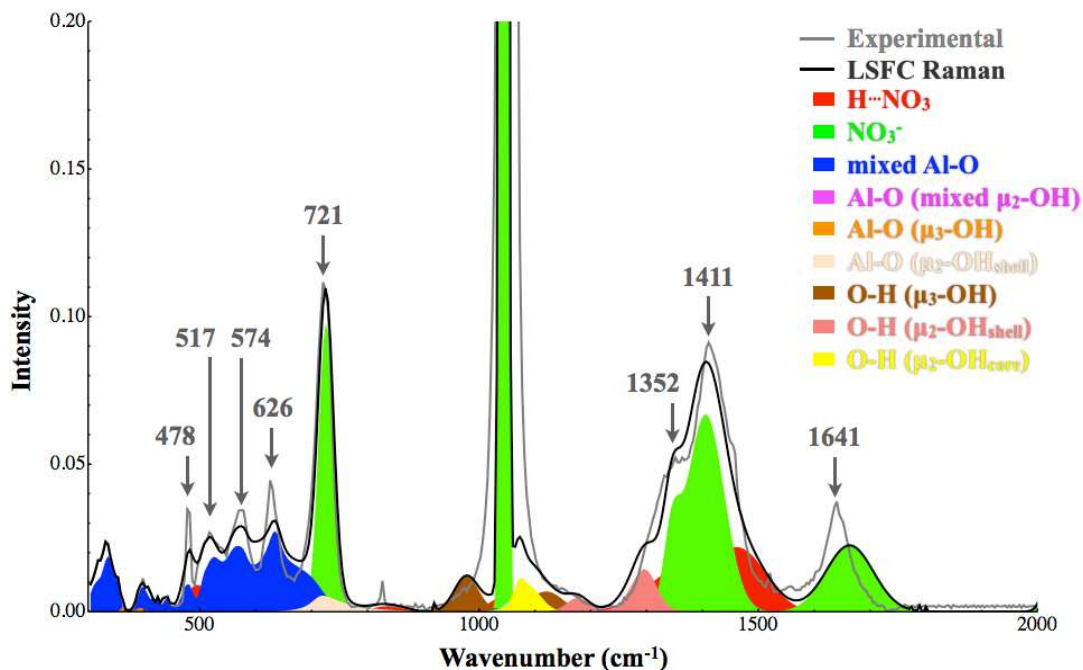


Figure 2.1. Al_{13} Raman spectrum from $200\text{-}2000 \text{ cm}^{-1}$. The symmetric stretch of the cluster is highlighted at 478 cm^{-1} . The RMSD for this LSFC Raman spectrum is 0.52 %.

The Al_{13} cluster, Boehmite ($\eta\text{-AlO}(\text{OH})$) and Gibbsite ($\text{Al}(\text{OH})_3$), share analogous octahedral metal coordination geometries and bridging hydroxides in their crystal structures. In spite of their structural similarities, the Raman spectrum of Al_{13} remains qualitatively different.^{19,20} The Raman spectrum of Boehmite is highlighted by a strong Al-O stretching vibration at 360 cm^{-1} , an Al-(OH)-Al deformation at 1071 cm^{-1} , and two weaker O-H modes spanning from $2900\text{-}3100 \text{ cm}^{-1}$.^{21,22} Gibbsite exhibits 12 Al-O modes from $200\text{-}500 \text{ cm}^{-1}$, 15 Al-(OH)-Al modes from $500\text{-}1100 \text{ cm}^{-1}$, and four intense and

distinct O-H modes from 3300-3600 cm^{-1} .^{18,19} While some of the reported modes are similar to those found in the cluster, in the region from 400-600 cm^{-1} the Al_{13} cluster exhibits vibrational modes that are distinct from both minerals.

2.3.2. Infrared Spectroscopy: Solid Phase. IR spectroscopic studies were performed on solid state samples of the Al_{13} cluster to elucidate information regarding the relationship between vibrational and structural properties (Figure 2.2). The O-H bending mode observed at 1660 cm^{-1} is also associated with the exterior waters ($\eta\text{-H}_2\text{O}$) of the Al_{13} cluster that hydrogen bond with the nitrate ions and are consistent with the water deformation mode at 1637 cm^{-1} observed in the Raman spectrum (see Section 2.1). The modes observed at ~ 1400 cm^{-1} and 825 cm^{-1} are indicative of the asymmetric and symmetric stretching vibrations of the nitrate ions.¹⁷ Three medium intense Al-O vibrations of the exterior shell vibrations are detected at 500 cm^{-1} , 620 cm^{-1} , and 750 cm^{-1} . Smaller weak modes of the bridging hydroxides are observed at 850 cm^{-1} , 1000 cm^{-1} , and 1200 cm^{-1} , as reported for aluminum-containing minerals.¹⁴⁻¹⁶ A strong, broad O-H absorption band also occurs at 3300 cm^{-1} that represents the water features of the cluster (not pictured in Figure 2.1, see supplemental Figures S3 and S6).

The infrared spectrum of the cluster is also different from the respective nitrate salt and mineral. The monomeric species only exhibits a broad Al-O stretch at 600 cm^{-1} , which corresponds to the O_h Al-O stretching vibration of $\text{Al}(\text{H}_2\text{O})_6^{3+}$.¹⁷ Previous studies on $\gamma\text{-AlO}(\text{OH})$ demonstrated several Al-O modes that have similar vibrational characteristics to the Al_{13} cluster.¹⁴⁻¹⁶ However, in contrast to the cluster spectrum, reported values for $\gamma\text{-AlO}(\text{OH})$ highlight various Al-O deformation modes below 400 cm^{-1} as well as Al-O stretching modes at 464 cm^{-1} , 563 cm^{-1} , and 626 cm^{-1} . Despite the

similarities it is apparent from the infrared results that the γ -AlO(OH) species forms a different bonding network than Al₁₃. In summary, solid phase Raman and IR spectroscopy have shown that the Al₁₃ cluster exhibits unique vibrational features from its monomeric parent and related polymeric species and both could be used as a viable option for identifying this cluster in the solid state.

2.3.3. Raman Studies: Solution Phase. Upon dissolution in water, the spectrum of the Al₁₃ cluster (Figure 2.3) reveals that the unique weak vibrational modes featured in the solid state are no longer distinguishable due to broadening of the vibrational modes into one large feature. The disappearance of these features may indicate a break in symmetry of the cluster, an extended, dynamic hydrogen bonding network with the solvent, or cluster dissociation. The observed Al-O modes are weak and broad, spanning from ~450 - 675 cm⁻¹. The weak shoulder associated with the hydroxyl bridge at 1100 cm⁻¹ is also not observed in the solution spectrum. The water features from 2800 - 3600 cm⁻¹ seen in the solid state now resemble bulk water.²³ Upon further inspection, the solution phase Raman spectrum of the cluster is similar to that of aqueous Al(NO₃)₃. The only notable difference in the solution phase spectra arises from an increased broadness of the low frequency Al-O stretch associated with the cluster in relation to the narrower octahedral Al-O stretch at 525 cm⁻¹ observed in Al(NO₃)₃.¹⁷

The broadness of this peak may result from equilibrium exchange dynamics between the cluster and the solvent that give rise to partial dissociation in solution over time. However, aging the sample shows that this feature remains consistently broad for at least a month. Since the peak does not become narrower with aging to resemble Al(H₂O)₆³⁺,

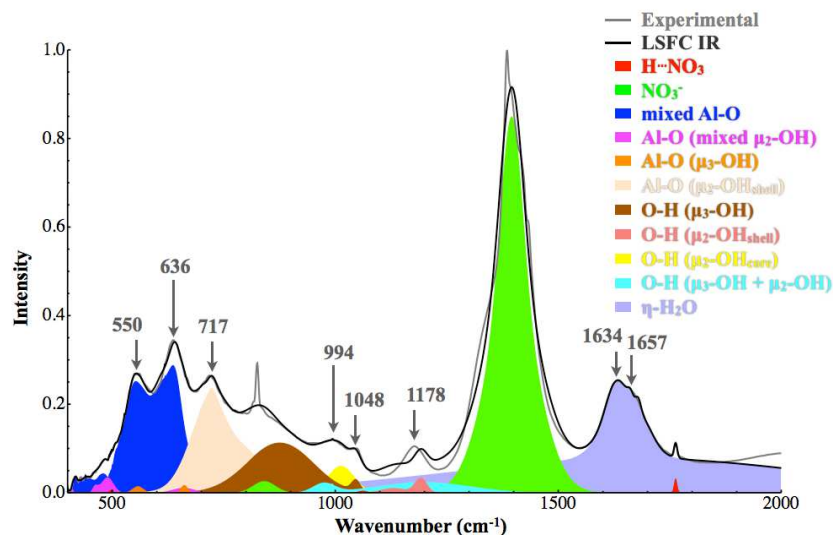


Figure 2.2. Experimental IR spectra of solid Al_{13} cluster from 400-1800 cm^{-1} displaying computational peak analysis. The RMSD for this LSFC IR spectrum is 2.0 %. A μ_3 -OH ligand is a hydroxide group that bridges the center Al^{3+} with two adjacent core Al^{3+} ; μ_2 -OH_{core} is a hydroxide group that connects two neighboring core Al^{3+} ; μ_2 -OH_{shell} is a hydroxide group that links one core Al^{3+} and its closest shell Al^{3+} ; and η -H₂O is a terminal water group on the shell Al^{3+} .

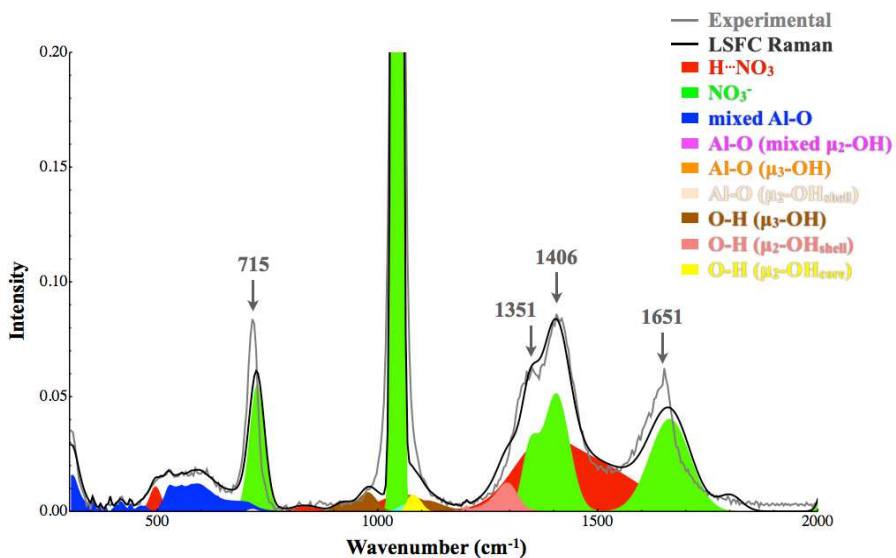


Figure 2.3. Overlay of simulated (black) and experimental (gray) Raman spectra of Al_{13} in 1 M solution at 25 °C. All of the weak modes seen in the solid phase have merged into one broad feature ranging from 450-675 cm^{-1} . The RMSD for this LSFC Raman spectrum is 0.59 %.

we suspect that the cluster is still present in solution over extended periods of time, consistent with solution DOSY, DLS, SAXS and related studies on other similar clusters.^{7,24} LSFC Raman spectra suggest that Al_{13} and $\text{Al}(\text{H}_2\text{O})_6^{3+}$ coexist in aqueous solution because the experimental spectrum is best described by a combination of the Al_{13} and $\text{Al}(\text{H}_2\text{O})_6^{3+}$ species, rather than either species individually (see Figure S2 in the Appendix). These studies reveal that solution phase Raman spectroscopy provides a complementary technique to determine the full, complex solution speciation of these and related clusters.²⁵

2.4. $[\text{Ga}_{13}(\mu_3\text{-OH})_6(\mu_2\text{-OH})_{18}(\text{H}_2\text{O})_{24}]^{15+}$: RESULTS AND DISCUSSION

2.4.1. Raman Analysis: Solid Phase. Raman spectroscopy was also able to provide insight on the vibrational features of the Ga_{13} cluster. A band that appears at 464 cm^{-1} can be attributed to the Ga-O symmetric stretch, or breathing mode, associated with the cluster (Figure 2.4). Two weaker, but distinct bands of moderate intensity at 525 cm^{-1} and 556 cm^{-1} arise from the bending vibrations of the exterior shell of the cluster (See Table S7). Calculations suggest that the bands at 1000 cm^{-1} and 1100 cm^{-1} can be assigned to the $\mu_2\text{-OH}$ and $\mu_3\text{-OH}$ hydroxyl bridges. However, these bands overlap with the symmetric NO_3^- at 1048 cm^{-1} in the same manner as observed in the Al_{13} cluster. The modes at 720 cm^{-1} and the doublet feature at 1357 cm^{-1} and 1411 cm^{-1} are attributed to the asymmetric nitrate frequencies which are also present in the Al_{13} cluster (see above). Two broad water peaks appear in the traditional O-H stretching region at 3250 cm^{-1} and 3425 cm^{-1} . The 3250 cm^{-1} feature can be attributed to tetrahedrally coordinated water molecules with relatively strong hydrogen bonding interactions much like that of H_2O in ice, while the 3425 cm^{-1} feature can be assigned to water molecules with hydrogen

bonding interactions similar to that of bulk water (see Figure S1 in the Appendix).²⁶ A narrow shoulder at 3533 cm^{-1} in the O-H stretching region is also observed and likely due to strongly hydrogen bonded hydroxyl groups incorporated in the crystal lattice of the cluster.^{17,26}

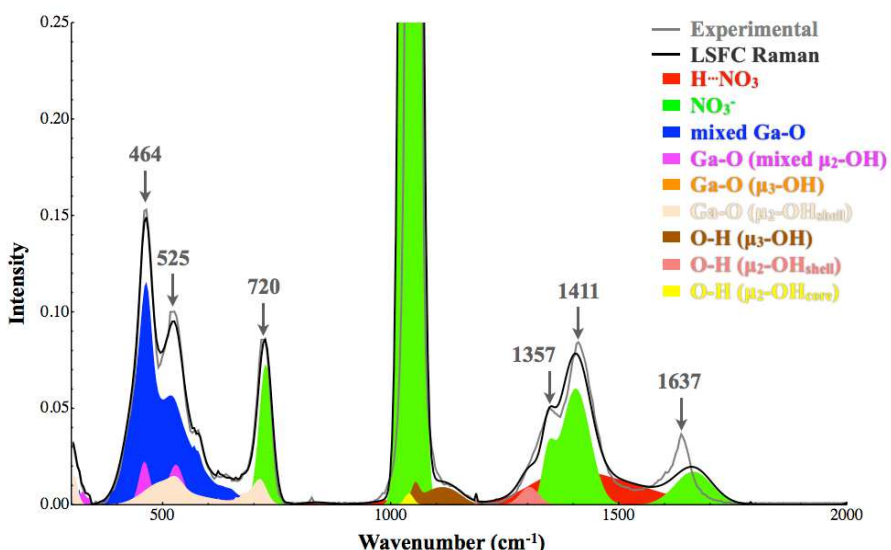


Figure 2.4. Simulated and experimental Raman spectra from 200-2000 cm^{-1} of crystalline Ga_{13} at 25 °C. The feature shown at 464 cm^{-1} arises from the primary breathing mode of the cluster. The RMSD for this LSFC Raman spectrum is 0.40 %.

Ga_{13} , like Al_{13} , shares similar and contrasting features with $\text{Ga}(\text{NO}_3)_3 \cdot x\text{H}_2\text{O}$. The observed breathing mode of the Ga_{13} cluster at 464 cm^{-1} is significantly lower in energy than the breathing mode of the $\text{Ga}(\text{H}_2\text{O})_6^{3+}$ species at 525 cm^{-1} .^{27,28} This observed energy difference can be attributed to elongation of the bonds in the cluster due to the influence of the extra gallium atoms that make up the cluster. Interestingly, the mode observed at 525 cm^{-1} in the cluster is in the same position as $\text{Ga}(\text{H}_2\text{O})_6^{3+}$. The similarity most likely arises from the shell of the cluster oscillating in a nearly identical way to the monomer species. The Raman spectrum for $\text{Ga}(\text{NO}_3)_3 \cdot x\text{H}_2\text{O}$ also contains no evidence for bridging hydroxides that are observed in the cluster. Related Raman studies on synthetic nanorods

of GaO(OH) identify several strong low energy Ga-O stretching modes around 300 cm^{-1} that are not observed in the Ga₁₃ cluster.²⁹ Additionally, a signature at 605 cm^{-1} in the spectrum of the GaO(OH) species represents a Ga-O stretch of tetrahedral coordination, which is predictably absent in the cluster.²⁵⁻²⁶ Since the Ga-O bonds in the Ga₁₃ cluster spectrum are of pseudo-octahedral coordination, this confirms this distinct coordination geometry of the Ga₁₃ cluster.

2.4.2. Infrared Results: Solid Phase. To complement the results gathered by Raman, IR spectroscopy was also performed on the Ga₁₃ cluster in the solid state. Congruent to what was observed by Raman, a broad water absorption that is associated with bulk water occurs at 3359 cm^{-1} (see Figure S3 in the Appendix). The mode at 1620 cm^{-1} in the IR spectrum of Ga₁₃ (Figure 2.5) is also consistent with the same water out of plane bending mode observed in the Al₁₃ IR spectrum (Figure 2.2) and in the Raman spectra of both clusters (Figures 2.1 and 2.4), suggesting that the water in Ga₁₃ is interacting with nitrate as previously described for the Al₁₃ cluster. The peaks at 824 cm^{-1} and $\sim 1381\text{ cm}^{-1}$ are indicative of the asymmetric and symmetric stretching vibrations of the nitrate ion. The bending and stretching vibrational modes of Ga-O in the exterior shell vibrations are detected at 560 cm^{-1} , 620 cm^{-1} , and 687 cm^{-1} .

Similar to Al(NO₃)₃, Ga(NO₃)₃ only contains one weak Ga-O IR signal at 560 cm^{-1} , while none of the modes for the hydroxide bridges are present. Smaller weak modes of the μ_x -OH ($x = 2$ or 3) bridges are observed at 906 cm^{-1} and 1102 cm^{-1} . As shown with the Al₁₃ cluster, vibrational spectroscopy and computational analysis have given us insight into the vibrational characteristics of the cluster that show Ga₁₃ is structurally unique when compared to the parent monomeric gallium nitrate and several

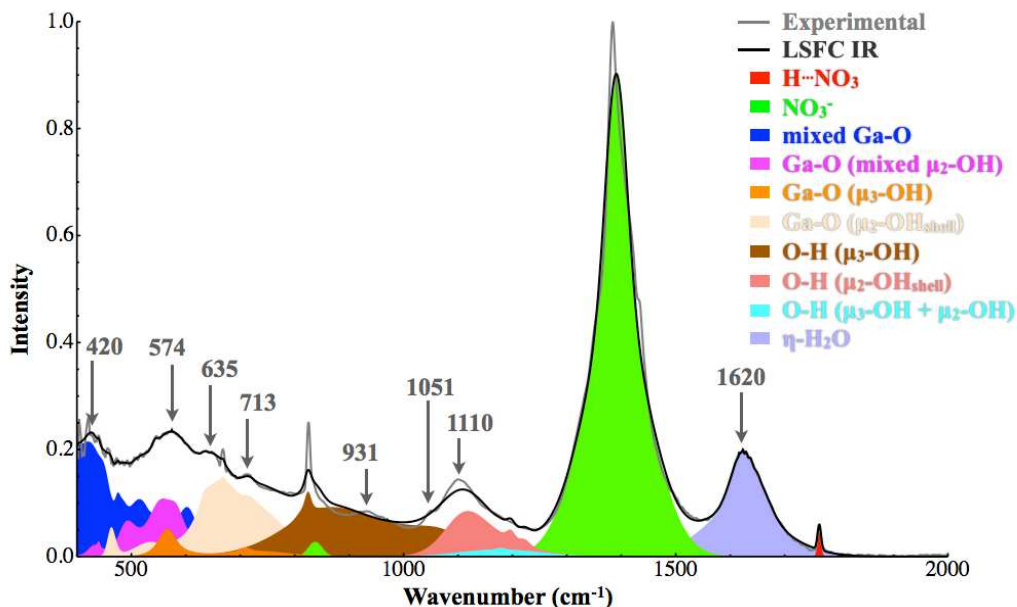


Figure 2.5. Experimental and simulated IR spectra of Ga_{13} in the solid phase from 400-2000 cm^{-1} with computational peak analysis shown. The RMSD for this LSFC IR spectrum is 1.7%.

oligomeric/polymeric species. However, because of the low intensity of the IR signals for the Ga-O stretch in the Ga_{13} cluster, it may not be the most ideal tool to identify this cluster. In spite of this, it is clear that with the use of vibrational spectroscopy and quantum mechanical calculations, we can characterize the Ga_{13} cluster and distinguish it from similar species in solution and the solid state.

2.4.3. Raman Spectra Analysis: Solution Phase. Upon dissolution, the peaks observed in the solid state decrease and appear as a broad Ga-O stretching vibration centered at 507 cm^{-1} and a shoulder at 450 cm^{-1} (Figure 2.6). This broadening phenomenon is very similar to what was observed for the Al_{13} . With increasing dilution, the overall relative intensity of the peaks at 507 cm^{-1} decrease linearly, however, the peak shape remains the same, suggesting the dominant species in solution does not change with serial dilution. In comparison to the Ga-O stretch of $\text{Ga}(\text{H}_2\text{O})_6^{3+}(\text{aq.})$ at 525 cm^{-1} , the Ga-O stretch of the

cluster at 507 cm^{-1} still vibrates at a slightly lower energy, suggesting that Ga_{13} is still present in aqueous solution. This is supported by a previous report showing that the cluster has a size of 5.6 ± 1.8 angstroms in aqueous solution via Small Angle X-ray scattering.⁷ As observed with Al_{13} , this feature does not change over the period of a month, suggesting potential long term stability of this species in solution.

2.5. Al_{13} vs Ga_{13} : DISCUSSION

In a direct comparison of the Raman spectra of each cluster from $300\text{-}600\text{ cm}^{-1}$, the relative intensities of the M-O vibrations in the Ga_{13} cluster spectra are far more intense in the solid state than Al_{13} . In addition, the Al-O bonds in Al_{13} cluster give stronger infrared absorptions as well as more discrete peaks in relation to Ga_{13} . The origins of this phenomenon are complex and could arise from several different factors. One possibility is due to the phenomenon of d-block contraction, Gallium (1.81χ) is more electronegative (Pauling's scale) than Aluminum (1.61χ) and the dipole moment (μ) experienced by any specified M-O bond would be greater for Al, which results in greater IR activity. The opposite effect is shown to be true for Ga_{13} in that it is more susceptible to being distorted by an applied electric field (more polarizable), favoring Raman activity. In the solution phase, both polymeric species lose features that are prominent in the crystalline phase resulting in one broad feature because of the additional degrees of vibrational freedom. With dilution, it appears that the Ga_{13} cluster remains present in solution over a wide variety of concentrations and it remains persistent in solution over extended periods of time. However, dilution studies of the Al_{13} cluster were inconclusive due to the weak signal shown in the Raman spectrum.

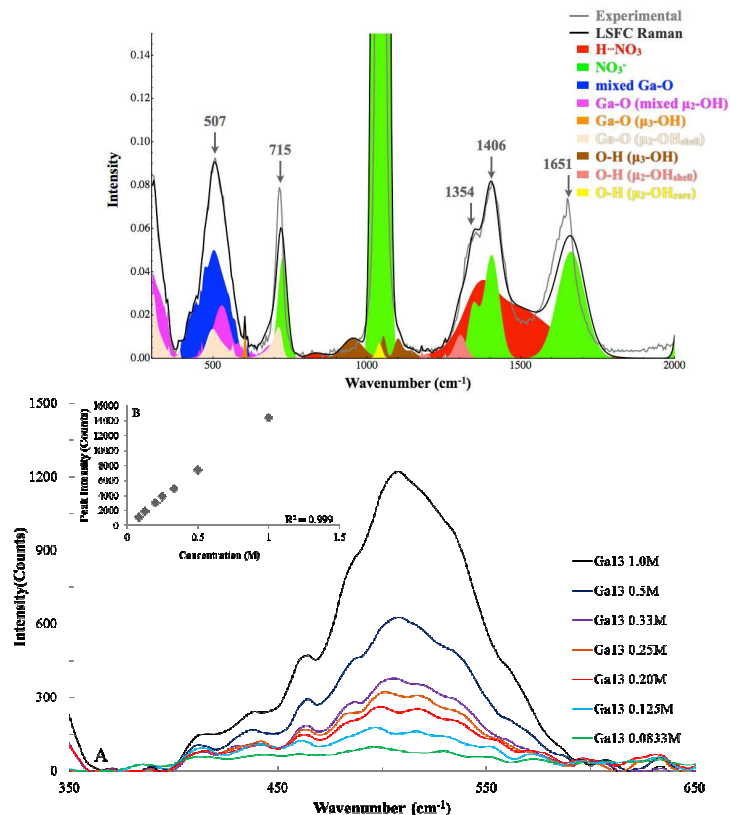


Figure 2.6. Simulated (top) and experimental (bottom) Raman spectra of the Ga_{13} cluster in solution phase from $350\text{-}650\text{ cm}^{-1}$. The RMSD for this LSFC Raman spectrum is 0.57 %. The Ga-O modes coalesce into a broad feature at 502 cm^{-1} . Upon dilution, only the peak intensity changes with dilution suggesting that the species remains persistent in solution (bottom insert). A plot of the intensity of the peak at 502 cm^{-1} versus concentration shows a linear decrease with dilution. In spite of the limitations observed with IR, it is clear that with the use of vibrational spectroscopy, particularly Raman in conjunction with quantum mechanical calculations, we can characterize and identify the Ga_{13} cluster and distinguish it from similar species in solution and the solid state.

2.6. CONCLUSIONS

Raman and infrared spectroscopy, as well as quantum mechanical calculations have been used to characterize Al_{13} and Ga_{13} clusters in the solid and solution phases. Our findings show that these clusters exhibit unique vibrational characteristics that differ from the parent monohydrate salts as well as natural and synthetic minerals that have comparable bonding arrangements. We have also shown that even though these clusters are analogous to each other, they have very different vibrational characteristics from each

other and their parent nitrate salt starting materials. The Al_{13} cluster exhibited several Al-O modes in both Raman and IR spectra, but showed more prominent IR activity. The Ga_{13} cluster had more intense Ga-O Raman signals, but was not as resolved in the IR spectrum. In solution, both clusters experienced an apparent break in symmetry and many of the peaks observed in the solid phase are no longer observable. The M-O mode for each cluster remains constant over an extended period of time, suggesting that both clusters remain the predominant species in solution. In summary, this report reveals that both Al_{13} and Ga_{13} can be identified in the solid state and aqueous solution by vibrational spectroscopy and shows that these clusters are present in H_2O over a long time period, suggesting that vibrational spectroscopy is an effective complementary technique to more “modern” approaches aimed at probing nanoscale structure in solution.²³

2.7. CHAPTER III BRIDGE

Chapter III focuses on a facile method to directly transmetalate In^{3+} on to the aluminum tridecamer to produce heterometallic aluminum-indium tridecamer clusters. Additionally, a thin film of aluminum indium oxide (AIO) was prepared from the aforementioned clusters to show its utility as a precursor ink for device applications.

CHAPTER III

TRANSMETALLATION OF AQUEOUS INORGANIC CLUSTERS: A USEFUL ROUTE TO THE SYNTHESIS OF HETEROMETALLIC ALUMINUM AND INDIUM HYDROXO-AQUO CLUSTERS

3.1. INTRODUCTION

My contributions as co-author included Raman spectroscopy on the solid $f\text{-Al}_7\text{In}_6$ tridecamer and Dynamic Light Scattering (DLS) experiments on the $f\text{-Al}_7\text{In}_6$ and $f\text{-Al}_{13}$ solutions. I also solution processed the amorphous thin film of $f\text{-Al}_7\text{In}_6$ from which transmission electron microscopy (TEM), energy dispersive X-ray spectroscopy (EDX), and atomic force microscopy (AFM) were used to determine film composition and roughness. Dr. Lev N. Zakharov collected all single-crystal X-ray data. Maisha Devonish invaluable contributions to this work were in developing the actual facile synthetic method for producing $f\text{-Al}_7\text{In}_6$ and performing $^1\text{H-NMR}$ and $^1\text{H-DOSY}$ experiments with $f\text{-Al}_7\text{In}_6$. The results presented in this chapter were published in 2014 in *Inorganic Chemistry* and received the ACS editor's choice award.

$[\text{Al}_x\text{In}_y(\mu_3\text{-OH})_6(\mu\text{-OH})_{18}(\text{H}_2\text{O})_{24}](\text{NO}_3)_{15}$ hydroxy-aquo clusters ($\text{Al}_x\text{In}_{13-x}$) are synthesized through the evaporation of stoichiometrically varied solutions of Al_{13} and $\text{In}(\text{NO}_3)_3$ using a transmetalation reaction. Several spectroscopic techniques ($^1\text{H-NMR}$, $^1\text{H-DOSY}$, DLS, and Raman) are used to compare $\text{Al}_x\text{In}_{13-x}$ to its Al_{13} counterpart. A thin

film of aluminum indium oxide was prepared from an **Al₇In₆** cluster ink showing its utility as a precursor for materials.

Transparent electronics and devices have emerged as one of the most promising developments for next generation technologies. Solution-processed multi-component materials such as indium gallium oxide (IGO) and aluminum indium oxide (AIO) offer routes to enable new or enhanced performance levels in large area electronics and energy devices such as flat-panel displays, solar cells, and LEDs.¹⁻⁶ Here we present a transmetalation process that yields the new hydroxy-aquo cluster $[\text{Al}_7\text{In}_6(\mu_3\text{-OH})_6(\mu\text{-OH})_{18}(\text{H}_2\text{O})_{24}](\text{NO}_3)_{15}$ (**Al₇In₆**) (Figure 3.1) by direct treatment of the related **Al₁₃** cluster with indium nitrate. To the best of our knowledge this is the first instance of direct transmetalation of metal ions into the exterior shell of such hydroxy/aquo cluster species. We show that this route not only enables the synthesis of previously reported heterometallic Ga/In clusters, but is the most reliable route to form Al/In congeners.

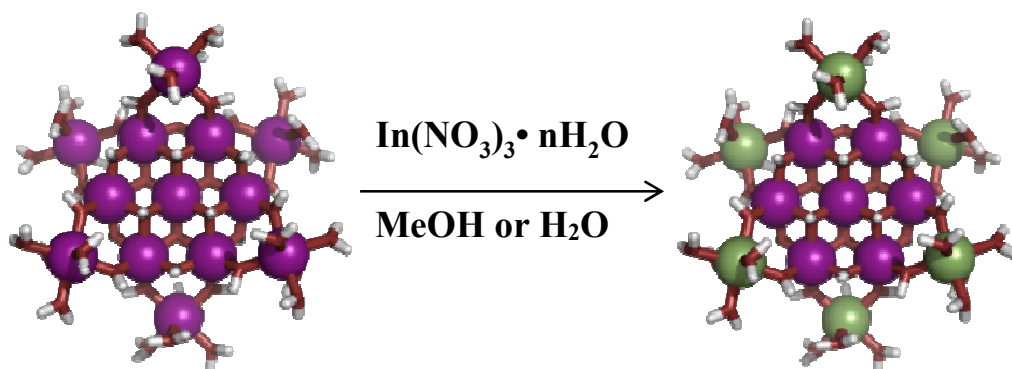


Figure 3.1. Simple representation of the transformation from **Al₁₃** to **Al₇In₆** upon addition of $\text{In}(\text{NO}_3)_3$. In^{3+} ions (green) displace Al^{3+} ions (purple) on the labile outer shell of the cluster. Images are wireframe and ball structures generated from the crystal structures of **Al₁₃** and **Al₇In₆**.

We have reported the synthetic route to an array of nanoscale Group 13 tridecameric hydroxy/aquo clusters composed of gallium and indium.^{7,8} The utility of these clusters as

precursors/inks for metal oxide semiconductors was previously demonstrated in an IGO thin film device formed from **Ga₇In₆**.⁸ The resulting dense, uniform, and pinhole-free film represents an emergent example of low-temperature solution processing of thin film transistors (TFTs) in which a completely inorganic cluster was used as a precursor material. This process provides a low temperature alternative for producing thin films as compared to the deposition and sputtering techniques traditionally used to create similar devices.⁶ As a result, we have begun to explore the use of other inorganic aqueous precursor solutions for materials applications.

Aluminum-containing materials in particular show promise as precursor candidates in several applications including dielectric layers and capacitors.⁹⁻¹³ However, the current number of soluble, dynamic precursors for low temperature aqueous processing is limited to [Al₁₃(μ₃-OH)₆(μ-OH)₁₈(H₂O)₂₄](NO₃)₁₅ (**Al₁₃**),¹³⁻¹⁵ [Al₈(OH)₁₄(H₂O)₁₈](SO₄)₅•16H₂O (**Al₈**),¹⁶ and [Al₄(OH)₆(H₂O)₁₂][Al(H₂O)₆]₂(Br)₁₂ (**Al₄**).^{17,18} The synthesis of Al₁₃ originally required the addition of a base (NaOH or NH₄OH) and the carcinogenic additive dibutylnitrosoamine (DBNA).¹⁴ In the case of the heterometallic Al/In clusters, the product was difficult to reproduce under the same conditions. Transmetalation eliminates the need for base and organic reagents as well as provides a reliable synthesis for preparing these otherwise inaccessible heterometallic clusters, in particular **Al₇In₆**. Furthermore, we show that the resulting clusters can be used as precursors for smooth, amorphous aluminum indium oxide (AIO) thin films that are comparable to films of similar content produced by atomic layer deposition or sputtering deposition.^{9,10,19} In addition, transmetalation is an unusual reaction for aqueous coordination clusters.

The metal exchange phenomenon has been exhibited in several examples of polyoxometalate structures.²⁰⁻²³ Electrospray Ionization Mass Spectroscopy (ESI-MS) characterization was used to identify mixed-metal phosphate-centered Keggin ions in aqueous tungsten and phosphododecametalate solutions.^{20,21} Similar experiments for niobate/tantalate²² and Mo/V-selenite²³ systems showed additional mixed-metal species. Altering the pH conditions of monomeric salt solutions has led to the substitution of the central metal ion of Keggin-Al₁₃ by Ga, Fe, or Ge as well as a variety of di- and trivalent metal ions into the Anderson cluster [Mo₇O₂₄]⁶⁻.²⁴⁻²⁹ We explored the potential for metal exchange in tridecameric clusters and discovered that such a process occurs when mixing **Al₁₃** and In(NO₃)₃. As a result indium ions substitute into the exterior metal sites of the cluster to produce **Al₇In₆** (Figure 3.1). The ability of **Al₁₃** to easily convert into **Al₇In₆** hints at dynamic metal and ligand exchange that might occur in solution and influence speciation of **Al₁₃** and related Al clusters.

While this report focuses on the Al derivatives,³⁰ related studies reveal that the previously described **Ga₇In₆** cluster⁸ can also be synthesized via transmetalation. For example, a 1:12 ratio of Ga₁₃:In(NO₃)₃ produces **Ga₇In₆** (see experimental section). The reverse reaction is also possible: when excess Ga(NO₃)₃ is added to **Ga₇In₆**, **Ga₁₃** forms. This provides further evidence of a dynamic equilibrium between the M₁₃ (M = Al or Ga) cluster and M(NO₃)₃ monomer. Nuclear Magnetic Resonance (NMR) spectroscopy, Diffusion Ordered Spectroscopy (¹H-DOSY), Dynamic Light Scattering (DLS) and Raman spectroscopy have been used to provide valuable information in the characterization of these inorganic cluster species.³¹⁻³³ We have specifically used these

techniques in tandem to identify size and structural differences between **Al₁₃** and **Al₇In₆** in solution.

3.2. EXPERIMENTAL

3.2.1. General Methods. All reagents were purchased from commercial sources and used as received. Aluminum nitrate nonahydrate (99.0%-Al), indium nitrate hydrate (99.999%-In), and gallium nitrate hydrate (99.99%-Ga) were purchased from Strem Chemicals. Methanol (MeOH) was used as received. Unless specified, all reactions were conducted in standard 20-mL scintillation vials. ¹H-NMR and ¹H-DOSY spectra were obtained on a Varian INOVA-500 MHz NMR Spectrometer. The Bipolar Pulse Pair Stimulated Echo (Dbppste) pulse sequences was used to acquire diffusion data with a 50 ms diffusion delay, 200 ms gradient length, 20 gradient levels, and nt = 16 scans. The Varian DOSY package was used for processing and measuring the diffusion coefficient (D_t). The hydrodynamic radius (R_h) was calculated using the Einstein-Stokes equation

$$(R_h = \frac{K_b T}{6\pi\eta D_t})$$

where K_b = Boltzmann's constant, T = temperature in kelvin, η = viscosity, and D_t = translational diffusion coefficient.³¹ Percent error was calculated using measured values for ferrocene in DMSO.^{34,35} DLS measurements were taken using the Mobius from Wyatt technologies. The samples were filtered using a 0.1 μ m PTFE syringe tip to remove any particulate matter followed by immediate analysis ($t < 1$ minute). Dynamics software and averaged over 20 measurements with a 5 second integration time per acquisition. Raman spectra of the **Al₇In₆** single crystals were collected using an Alpha 300S SNOM confocal Raman microscope. The spectra from each sample were averaged over 2000 accumulations at 0.5 second exposure time per scan. Thin films were fabricated via spin

coating (3000 rpm for 30 seconds) a 0.2 M aqueous solution of **Al₇In₆** onto a p-type Si wafer pre-treated with a piranha solution (7:3 v/v ratio of concentrated H₂SO₄ and 35% H₂O₂). Prior to spin coating, the solutions were filtered through a 0.1 μm PTFE syringe tip to remove any particulate matter and/or potential agglomerates. The subsequent films were then annealed at 300 °C for 30 minutes prior to analysis.

3.2.2. General Procedure for the Synthesis of Al₇In₆ and Ga₇In₆. A solution of **Al₁₃** (0.078 g, 0.037 mmol)^{14b} and In(NO₃)₃ (0.27 g, 0.90 mmol) in MeOH (10 mL) was left to evaporate open to air. After several days crystals of **Al₇In₆** formed (10% product yield with respect to starting amount of **Al₁₃**). Single crystal X-ray diffraction reveals a structure identical in geometry to the previously reported heterometallic clusters.⁸ **Ga₇In₆** was synthesized following the same method as for **Al₇In₆**. A solution of **Ga₁₃** (0.100 g, 0.037 mmol) and In(NO₃)₃ (0.27 g, 0.90 mmol) in MeOH (10 mL) was left to evaporate open to air. **Ga₇In₆** crystals formed after several days (20% yield with respect to the amount of **Ga₁₃**). Both **Al₁₃** and **Ga₁₃** were used as is following a wash with acetone. See ESI for specific spectral details.

3.3. RESULTS AND DISCUSSION

The ¹H-NMR spectra of Al₁₃ and Al₇In₆ reveal several differences between the compounds (Figure 3.2). The peaks between 9.10 ppm and 9.32 ppm in Al₁₃ (A) that are indicative of Al(NO₃)₃ (inset, C) are mostly absent from B. It appears that the species present in the ¹H-NMR spectrum of Al(NO₃)₃ remains once the crystallization of Al₁₃ occurs. Subsequent recrystallization to produce Al₇In₆ removes this species. Another set of peaks are observed between 7.04 ppm and 7.21 ppm. The observed 1:1:1 triplet is associated with a spin ½ nucleus (such as ¹H) coupling to an S = 1 nucleus (such as ¹⁴N).

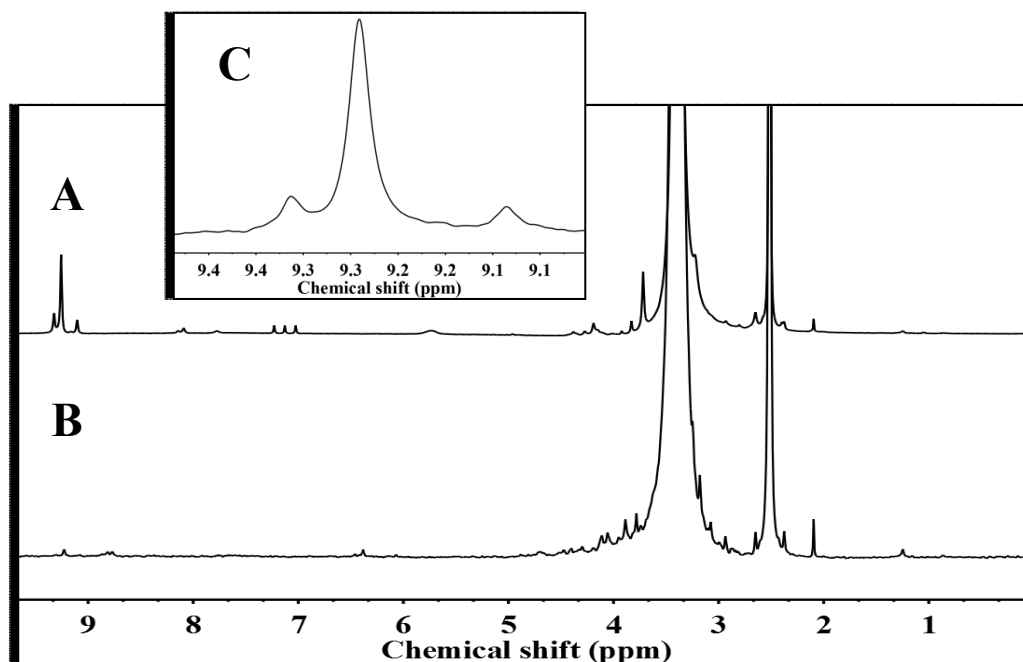
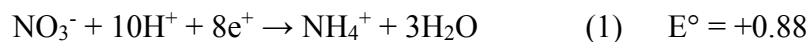


Figure 3.2. $^1\text{H-NMR}$ of Al_{13} (A), Al_7In_6 (B), and $\text{Al}(\text{NO}_3)_3$ (C).

Al_{13} is produced by the reduction of $\text{Al}(\text{NO}_3)_3$ by zinc powder.¹⁴ The reduction of nitrate ions by zinc metal is thermodynamically feasible (equations 1-3), particularly in acidic environments.³⁶ Therefore, it seems reasonable that the triplet is a result of that reduction process of nitrate to ammonium at an acidic pH. Again, as a consequence of recrystallization, those peaks disappear when Al_7In_6 is formed and isolated.



$^1\text{H-DOSY}$ was performed to compare the sizes of Al_{13} and Al_7In_6 in solution. The hydrodynamic radii (R_h) of Al_{13} and Al_7In_6 were essentially equivalent ($R_h = 1.1 \text{ nm} \pm 0.3 \text{ nm}$ and $1.0 \text{ nm} \pm 0.3 \text{ nm}$, respectively) in d_6 -DMSO although we expected the R_h for Al_7In_6 to be slightly larger than that of Al_{13} based upon the size of the atomic radii for Al

(1.431 Å) and In ($1.65 \text{ Å} \pm 0.03 \text{ Å}$)³⁷ and the average calculated Al-O (1.839 Å) and In-O (2.086 Å) bond lengths.

Utilizing dynamic light scattering (DLS) as a corroborative technique to DOSY, we have also determined the size of both the **Al₁₃** and **Al₇In₆** clusters in *d*₆-DMSO as well as in aqueous solutions. In a direct solvent comparison with the DOSY experiment, the R_h of **Al₁₃** and **Al₇In₆** in *d*₆-DMSO is very close to that measured with DOSY at $1.0 \text{ nm} \pm 0.3 \text{ nm}$ and $0.9 \text{ nm} \pm 0.4 \text{ nm}$, respectively (Figure 3.3). In water, DLS shows that the **Al₁₃** cluster is $1.0 \text{ nm} \pm 0.1 \text{ nm}$ (Figure 3.3). By comparison, the measured R_h for **Al₇In₆** is $15.7 \text{ nm} \pm 2.0 \text{ nm}$, roughly an order of magnitude larger in water than its homometallic counterpart, suggesting that the discrete **Al₇In₆** cluster is not a stable species in water, but rather aggregates favoring the formation of larger, apparently stable nanoparticles.

The R_h of **Al₁₃** in water is the same as in *d*₆-DMSO, suggesting the cluster is stable in both solvents. However, the autocorrelation function suggests higher polydispersity for the cluster in *d*₆-DMSO than in H₂O. This difference is likely due to the viscosity effects of *d*₆-DMSO (2.0 cP vs. 0.89 cP for DMSO and H₂O, respectively, at 25 °C) that would cause fluctuations in cluster rates of diffusion in solution. Solution studies are currently in progress to fully understand the solution speciation and other dynamic characteristics of these clusters in various solvents. Nevertheless, it is clear that the two clusters behave differently in aqueous solution and these techniques can provide a routine platform for understanding the solution chemistry of hydroxo-aquo clusters in general.

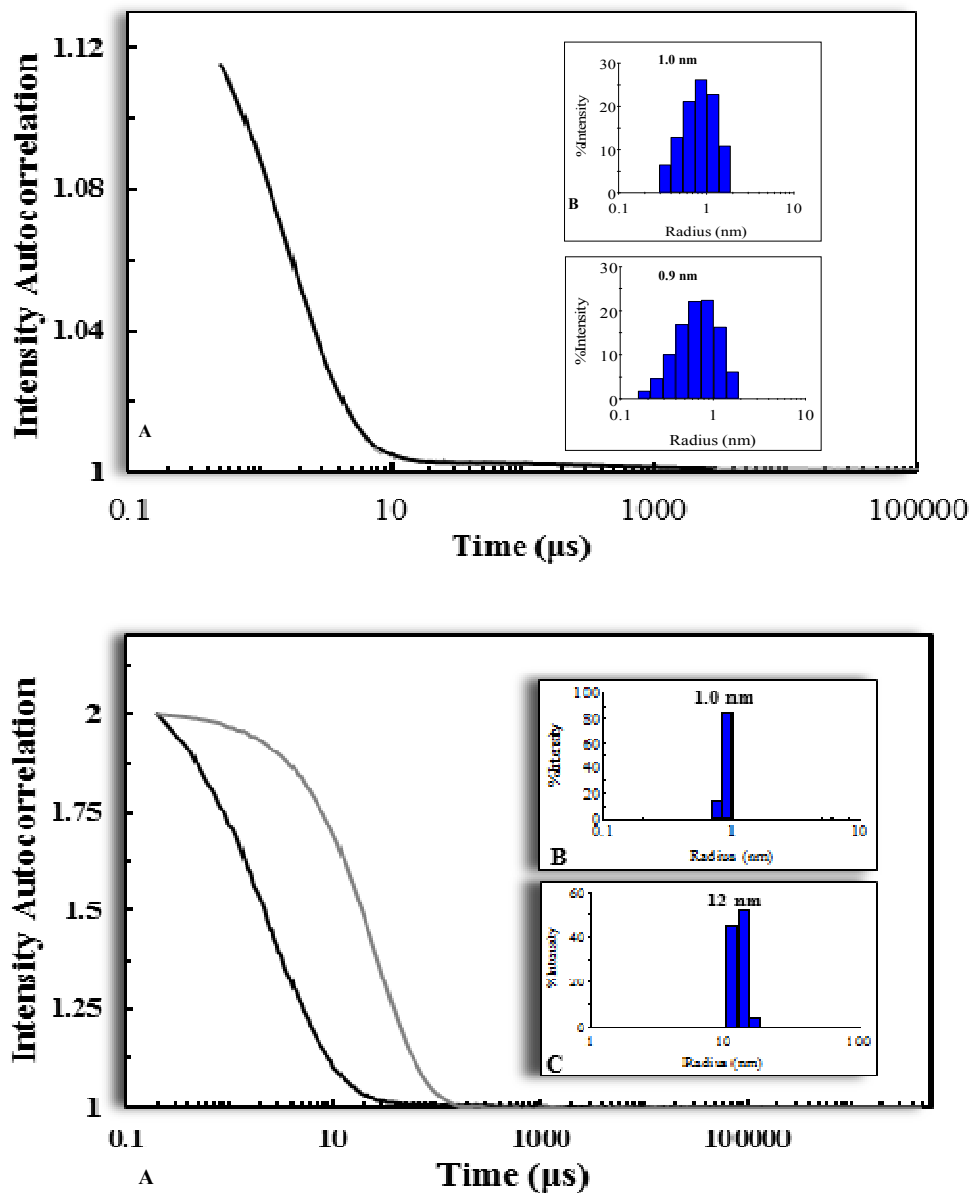


Figure 3.3. *Top:* (A) Autocorrelation function of 2 mM Al_{13} (black) and 2 mM Al_7In_6 (grey) in d_6 -DMSO (traces stack on top of each other). Hydrodynamic radii of Al_{13} (B) and Al_7In_6 (C) in d_6 -DMSO are displayed in the insets. *Bottom:* (A) Autocorrelation function of 0.2 M Al_{13} (black) and 0.2 M Al_7In_6 (grey) in H_2O . Hydrodynamic radii of Al_{13} (B) and Al_7In_6 (C) in H_2O are displayed in the insets.

Solid state Raman spectroscopy is a valuable technique for characterizing single crystals of this cluster type. In previous work, quantum mechanical computations were used to identify the various vibrational modes associated with Al_{13} .³³ Upon investigation

of Al_7In_6 , the incorporation of indium into the cluster changes the vibrational features of the cluster, and therefore each cluster has its own unique Raman signature (Figure 3.4).

The spectrum of Al_7In_6 reveals several new modes that distinguish it from Al_{13} (Figure 3.4). The most significant difference between the two clusters is the disappearance of the breathing mode of Al_{13} at 478 cm^{-1} in the spectrum for Al_7In_6 . The broad peak with medium relative intensity at 428 cm^{-1} can be attributed to Al-OH-In stretching vibrations.

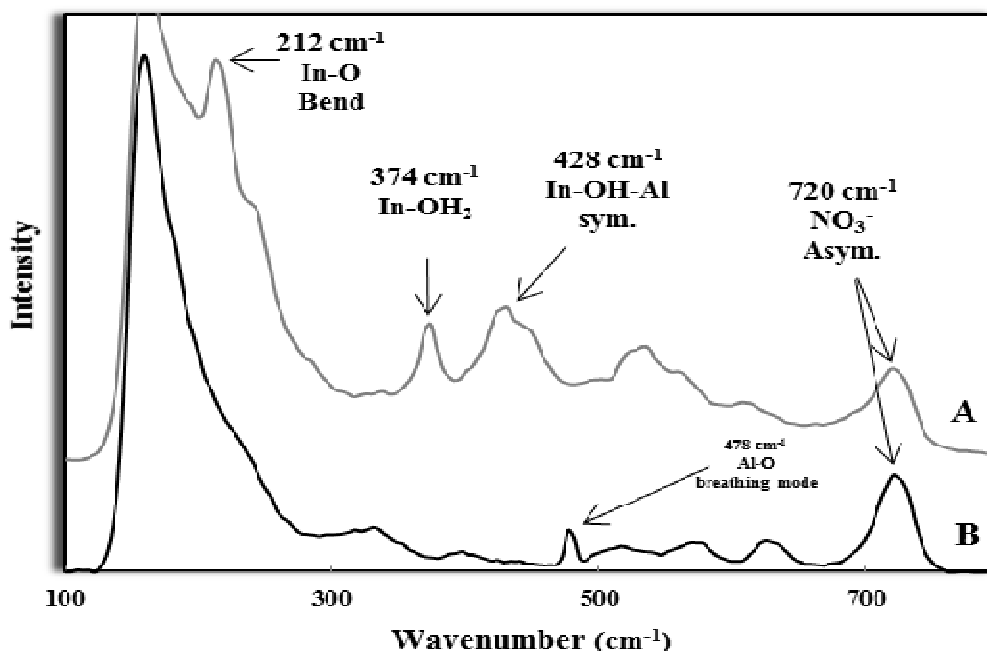


Figure 3.4. Solid state Raman spectra of Al_{13} (black) and Al_7In_6 (grey) between 100 cm^{-1} and 800 cm^{-1} .

A narrower band with slightly less intensity at 374 cm^{-1} corresponds to the vibrations of In and the coordinated waters (In-OH_2) of the exterior cluster shell. The lower wavenumber peak at 212 cm^{-1} can also be assigned as an In-O bending mode due to the lack of spectral evidence for a bound nitrate to the cluster.³⁸ More specifically, there are no signs of peak splitting in the anti-symmetric and symmetric NO_3^- peaks (720 cm^{-1}

and 1048 cm^{-1} , respectively) that denote the existence of an indium nitrate species ($\text{In}(\text{NO}_3)(\text{H}_2\text{O})_5^{2+}$).³⁸ The vibrational modes typically associated with the free NO_3^- ions in **Al₇In₆** are consistent with those observed in **Al₁₃** (721 cm^{-1} , 1048 cm^{-1} , 1350 cm^{-1} , and 1411 cm^{-1}) suggesting that the nitrates behave similarly in the two clusters. There are also several weaker modes present between $450\text{-}650\text{ cm}^{-1}$ that are attributed to the Al-O vibrations, similar to what has been previously reported for **Al₁₃**.³³

Thin films were prepared as a single layer from an aqueous solution at 0.2 M total metal concentration of the **Al₇In₆** cluster. Both transmission electron microscopy (TEM) and X-ray reflectivity (XRR) measurements show a film thickness of close to 6 nm (5.7 nm for SEM and $5.5\text{ nm} \pm 0.2\text{ nm}$ for XRR). TEM and atomic force microscopy (AFM) images reveal that **Al₇In₆** produces uniform and atomically smooth thin films from spin-coating when used as a solution precursor (Figure 3.5).

As compared to the indium gallium oxide (IGO) solution-processed film formed from **Ga₇In₆**, we see with TEM that the AIO film surface morphology is also dense and pinhole-free with minimal signs of inhomogeneity.⁸ The $16\text{ }\mu\text{m}^2$ AFM image shows that the **Al₇In₆** film is very smooth across the surface (RMS roughness = 0.145 nm), despite film thinness. Energy dispersive x-ray spectroscopy (EDX) analysis confirms the existence of an oxide composed of Al and In in the film (aluminum indium oxide, AIO). The relative composition measurements show a ratio of $\text{Al}_{1.02}\text{In}_{0.98}\text{O}_{2.95}$, close in comparison to the aforementioned IGO thin film device.⁸ Device performance and applications will be reported in due course.

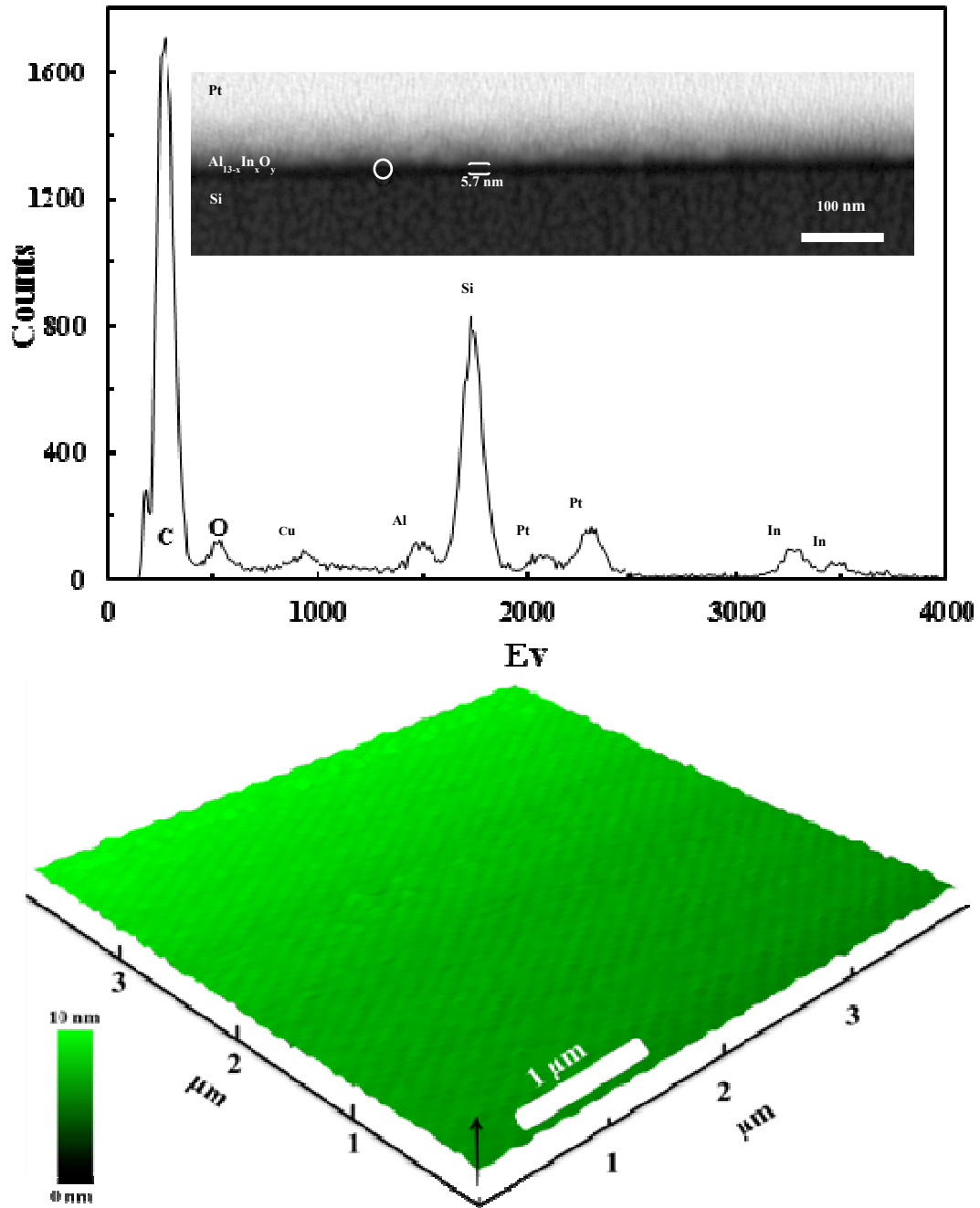


Figure 3.5. Top: EDX analysis of the solution processed Al_7In_6 precursor and cross-sectional TEM (top insert) of the $\text{Al}_{13-x}\text{In}_x\text{O}_y$ thin film. The white circle represents the spot on which the EDX scan was performed. **Bottom:** AFM 3D side view of $\text{Al}_{13-x}\text{In}_x\text{O}_y$ thin film ($16 \mu\text{m}^2$).

3.4. CONCLUSIONS

In summary, we have been able to synthesize the heterometallic **Al₇In₆** hydroxo-aquo cluster via a transmetalation reaction. ¹H-NMR and Raman spectroscopies reveal that in the solution and solid states, respectively, **Al₇In₆** cluster has distinct spectral features in relation to the **Al₁₃** cluster. ¹H-DOSY and DLS show that these clusters persist in solution as multiple discrete species. In addition a dense, smooth, uniform, thin film of AIO was fabricated using **Al₇In₆**. By utilizing these techniques to identify **Al₇In₆** in the solid and solution phases, we are better equipped to explore and understand the complex solution dynamics and exchange reactions of these clusters. These clusters also serve as potential precursors for solution deposition of metal oxide thin films. Heterometallic clusters also provide the additional advantage of tuning the metal ratios at the molecular level in spin-coating applications.

3.5. CHAPTER IV BRIDGE

The next chapter entails some preliminary investigation into the effects that non-aqueous solvent have on the solution dynamics of the aluminum tridecamer cluster.

CHAPTER IV

INVESTIGATION OF THE PROTON EXCHANGE RATE KINETICS OF AQUEOUS $[\text{Al}_{13}(\mu_3\text{-OH})_6(\mu_2\text{-OH})_{18}(\text{H}_2\text{O})_{24}]^{15+}$

4.1. INTRODUCTION

Christopher A. Colla (University of California, Davis) computed all proton rate exchange and energy parameters. I performed dynamic light scattering, phase analysis light scattering, and AT-IR spectroscopy for $f\text{-Al}_{13}$. I also helped to write the corresponding portions of the manuscript from which this work was based. Maisha Devonish performed all variable temperature ^1H -NMR experiments in addition to ^1H and ^{27}Al NMR titrations. She was also the first author of the manuscript that is being submitted to *Dalton Transaction*.

The reaction between copper (II) sulfate pentahydrate, nickel (II) sulfate, and pyridine in DMF yields green crystals of $\{(\text{C}_5\text{H}_6\text{N})_2[\text{Cu}_4(\text{OH})_2(\text{SO}_4)_4(\text{H}_2\text{O})_4]\}_n$ at room temperature. This anionic 1-D chain structure contains two different Cu centers and is composed of the repeating tetrameric copper clusters. The octahedral CuO_6 metal ions form a $\{\text{M}-(\mu_2\text{-OH})_2\text{-M}\}$ rhombus core that is linked to trigonal bipyramidal CuO_5 metal ions through bridging sulfate groups. Rather than direct copper coordination by free-base pyridine ligands, the negative charge of the tetrameric structure is balanced by pyridinium counter-cations arranged in a π - π stacking motif that also hydrogen bonds to the chains of cluster anions. This is a new example of an inorganic transition metal 1-D polymer containing rhombus building blocks.

Aluminum is the most abundant metal and third most abundant element in the earth's crust behind oxygen and silicon. Its ubiquitous nature has led to an encyclopedic catalogue of the hydrolytic behaviour of aluminum ions: in mineral surface-water reactions, in coordination complexes, in organic media, etc.¹⁻⁵ There has been particular attention paid to specific hydrolysis products such as the Keggin structure $[\text{AlO}_4\text{Al}_{12}(\text{OH})_{24}(\text{H}_2\text{O})_{12}]^{7+}$ ($\kappa\text{-Al}_{13}$), which was first structurally characterized in 1960.^{6,7} This molecule was identified as the major component of flocculants in several streams where the exposure of neutral waters to acidic mining run-off resulted in localized regions at pH values between 4.2 and 4.9.⁸ The strong heavy metal affinity of these flocculants leads to environmental ramifications that include water contamination and phytotoxicity. Since then $\kappa\text{-Al}_{13}$ has intentionally been used as a molecular-scale model to study the formation of polymeric flocculants as well as the surface chemistry reactivity of metal-oxide minerals.⁹ More recently, other tridecameric aluminium species $[\text{Al}_{13}(\mu_3\text{-OH})_6(\mu_2\text{-OH})_{18}(\text{H}_2\text{O})_{24}]^{15+}$ (referred to herein as " $f\text{-Al}_{13}$ ") have been synthesized and crystallographically confirmed.¹⁰⁻¹² Early synthetic methods utilized base (i.e. NaOH, NH_4OH and $\text{Al}(\text{OH})_3$) hydrolysis to form the polynuclear species.¹¹ A pH gradient resulted from the addition of base and subsequently lead to co-crystallization of both $\kappa\text{-Al}_{13}$ and $f\text{-Al}_{13}$, thus indicating that both can condense under the same conditions within the same pH regime. In addition, evidence of a penta-coordinated aluminum complex in the aforementioned flocculants suggested that more polycations were present as either solid intermediates or soluble species. Therefore aluminum speciation in aqueous media becomes more interesting and piecing together the composition of aluminium formations in the environment becomes more complex.

The residency times for protons bound to the hydroxy-aquo ligands of $f\text{-Al}_{13}$. These studies serve as a preliminary comparison between $f\text{-Al}_{13}$ and $\kappa\text{-Al}_{13}$ that could help to inform how structural variability is related to reactivity.¹³ This information will be useful as geochemical reactions become important in the development of functional materials for electronics applications.¹⁴

4.2. EXPERIMENTAL

4.2.1. Materials and Methods. Aluminum nitrate nonahydrate (99.0%-Al) and zinc powder were obtained from the University of Oregon chemical reuse facility through the reclamation of material originally purchased from Baker and Adamson and an as yet unknown source, respectively. Methanol (MeOH) was purchased from Macron Fine Chemicals. All starting materials were used as received from commercial sources. ^1H -NMR and single crystal X-ray diffraction (XRD) were used to confirm the composition of the final product.¹⁵ Reactions were set up in standard 20-mL scintillation vials to amass a bulk quantity.

4.2.2. General Procedure for the Synthesis of $f\text{-Al}_{13}$. Al_{13} was prepared using a previously published synthesis.¹⁰ Zn powder (87 mg, 1 mmol) was added to a scintillation vial containing $\text{Al}(\text{NO}_3)_3$ (100 mg, 2 mmol) dissolved in MeOH (10 mL). The vial was capped loosely and the resulting mixture was left to stir overnight until Zn dissolved completely. Once the final solution was transparent and particulate-free the vial was uncapped and the solution was left to evaporate. Within five days colorless, block crystals formed.

4.2.3. ^1H -NMR Spectroscopy. Variable-temperature NMR experiments were conducted using a Bruker Avance III-HD 600 NMR spectrometer. 16 scans were

recorded over a sweep width of 20.0 KHz. Sample temperature was determined using low-temperature (4% MeOH in MeOD) and high-temperature (80% EG in 20% DMSO- d_6) standards. VT NMR experiments were also performed on $\text{Al}(\text{NO}_3)_3$ as controls.

4.2.4. Dynamic Light Scattering. Two mL solution of 50 mM Al_{13} were dissolved in varying H_2O :acetone mol ratios (See SI table for further details). Prior to analysis, each sample was filtered into the cuvette with a 0.1 PTFE μm syringe filter to remove any potential particulate matter. The following dynamic light scattering (DLS) and phase analysis light scattering (PALS) measured using the Mobius from Wyatt technologies. DLS was used to measure changes in the hydrodynamic radius (R_h) of the alumina species in solution. The Dynamics software uses the Einstein-Stokes equation ($R_h = K_b T / 6\pi\eta D_t$) where K_b = the Boltzmann constant, T = temperature in kelvin, η = viscosity, and D_t = translational diffusion coefficient to solve for the R_h value. Viscosity measurements of the $f\text{-Al}_{13}$ and H_2O :acetone mixtures were consistent with previously measured results.^[ref] Phase analysis light scattering (PALS) was then ran subsequently to measure the change in conductivity and zeta potential as a function of acetone equivalents to water. The samples were measured under an electric field frequency of 10 Hz, a voltage amplitude of 3.0 V and the values were averaged over a collection period of 20 seconds.

4.2.5. Infrared Spectroscopy. Infrared spectra for both clusters were collected with a Nicolet 6700 ATR-IR spectrometer. Spectra spanning the range of 650 cm^{-1} - 4000 cm^{-1} were obtained with 64 scans at a resolution of 4 cm^{-1} .

4.2.6. Rate Equations. Although there are several proton sites that could exchange with solution on the $f\text{-Al}_{13}$ molecule, it is undoubtedly true that exchange between these

sites is via the reservoir of bulk water and not intramolecular exchange. Thus we can treat the system with a two-site exchange model. The NMR lineshape for the exchanging two-site system is calculable from the Bloch-McConnell equations, but a more useful approximation is possible here because the mole fraction of protons in water is much larger than the mole fraction of protons in the exchange site on the $f\text{-Al}_{13}$, and because exchange is in the slow regime where two peaks can be resolved. Under these conditions the lifetime of a particular proton and activation parameters can be gauged from the variation of the linewidth with temperature.

$$\frac{1}{\tau} = \pi \cdot (FWHM_i - FWHM_o) \quad (1)$$

In this equation, the $FWHM_i$ corresponds to the measured linewidth; the $FWHM_o$ is the linewidth in the absence of exchange. The $FWHM_o$ is probably on the order of 2-3 Hz by analogy to the $^1\text{H-NMR}$ signals assigned to methyl groups in similar solutions. These widths are negligible given that the experimental peaks showing evidence of exchange broadening are over a hundred Hz in linewidth.

To test the accuracy of the approximation, six sets of data ($0.02 \leq \tau \leq 0.0008$ s) were generated by solving the Bloch-McConnell equations for two-site exchange and for two cases where $|v_w - v_{Al}| = 2000$ and 5000 Hz, where $|v_w - v_{Al}|$ is the difference in Hertz of the resonance of the $^1\text{H-NMR}$ signals from water and sites on the Al_{13} , respectively. In the simulations, the intensity of the $f\text{-Al}_{13}$ signal was set 0.0005 that of the proton signals, to approximate our case where the concentrations of protons in exchanging sites differ by a large amount. The synthetic data were then treated as experiment results. In each case, the approximation was found to be appropriate and leads to estimates of τ that are

accurate to within a factor of two. This variation is within the uncertainties given by errors in the activation parameters that are exponentiated (see below).

The temperature dependence of $k_{ex}(s^{-1})$, the first-order rate coefficient for exchange of water molecules from the inner-coordination sphere to the bulk solution, takes the form of the Eyring equation:

$$\frac{1}{\tau} = k_{ex} = \frac{k_b \cdot T}{h} e^{\frac{\Delta S^\ddagger}{R}} e^{\frac{-\Delta H^\ddagger}{RT}} \quad (2)$$

where k_b is Boltzmann's constant and the exponential terms include the activation entropy $[\Delta S^\ddagger]$ and activation enthalpy $[\Delta H^\ddagger]$ for chemical exchange. The parameters T , R , and h are absolute temperature, the gas constant, and Planck's constant, respectively. In one case only, the linewidths reached a minimum with temperature and began to reverse, suggesting that very low temperatures were causing the tumbling of the molecule to slow appreciably and that this slower tumbling were broadening the linewidths. For this spectrum alone (3.6 ppm in the DMSO solution), an Arrhenius-like relation was added to Eqn. (X) to approximate the increased broadening because of increased viscosity:

$$\frac{1}{\tau} = k_{ex} = \frac{k_b \cdot T}{h} e^{\frac{\Delta S^\ddagger}{R}} e^{\frac{-\Delta H^\ddagger}{RT}} + W_{298} e^{\frac{E}{RT}} \quad (3)$$

Where E and W are fitting parameters only and are not essential to the analysis.

4.3. RESULTS AND DISCUSSION

4.3.1. *H₂O/Acetone-d₆*. At -20°C and below four resonances at 9.8 ppm (D), 7.8 ppm (C), 4.5 ppm (B), and 3.8 ppm (A) are observed in the spectra for **f-Al₁₃** (Figure 4.1). The peak at 9.8 ppm is also present in the spectrum for Al(NO₃)₃ and is assigned to the aluminum hexaaqua complex [Al(H₂O)₆]³⁺ (see the Appendix).

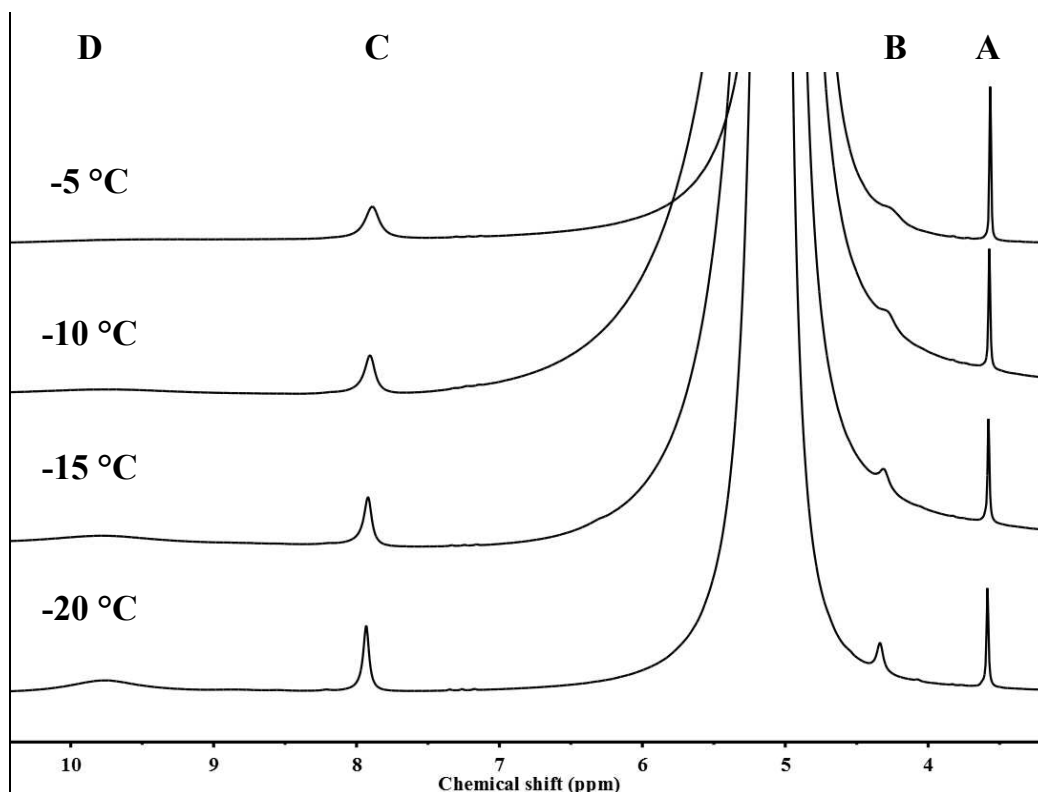


Figure 4.1. $^1\text{H-NMR}$ spectra ($-5\text{ }^\circ\text{C}$ to $-20\text{ }^\circ\text{C}$) of $f\text{-Al}_{13}$ in a 2.5:1 (v/v) mix of $\text{H}_2\text{O}/\text{acetone-d}_6$. The peak centered at 5.2 ppm is associated with bulk water in the solution. The peak at 9.8 ppm represents the hexaaqua $[\text{Al}(\text{H}_2\text{O})_6]^{3+}$ complex seen in the spectra for $\text{Al}(\text{NO}_3)_3$. Peaks A, B, and C integrate to 1:1:2, respectively.

Over the entire temperature range the chemical shifts and integration values for $f\text{-Al}_{13}$ and $\kappa\text{-Al}_{13}$ signals are very similar.¹³ Three proton resonances exist for $\kappa\text{-Al}_{13}$: $\mu_2\text{-OH}$, $\mu_2\text{-OH}'$, and H_2O . $f\text{-Al}_{13}$ contains three types of hydroxide protons in addition to the protons associated with water (Figure 4.2). The first group of hydroxide protons ($\mu_3\text{-OH}$, green) connect the core aluminium ion to the middle ring of aluminium ions. The second group of protons ($\mu_2\text{-OH}$, purple) coordinate the middle ring of aluminium ions to one another. The third group ($\mu_2\text{-OH}'$, yellow) links the middle and outer rings of aluminium

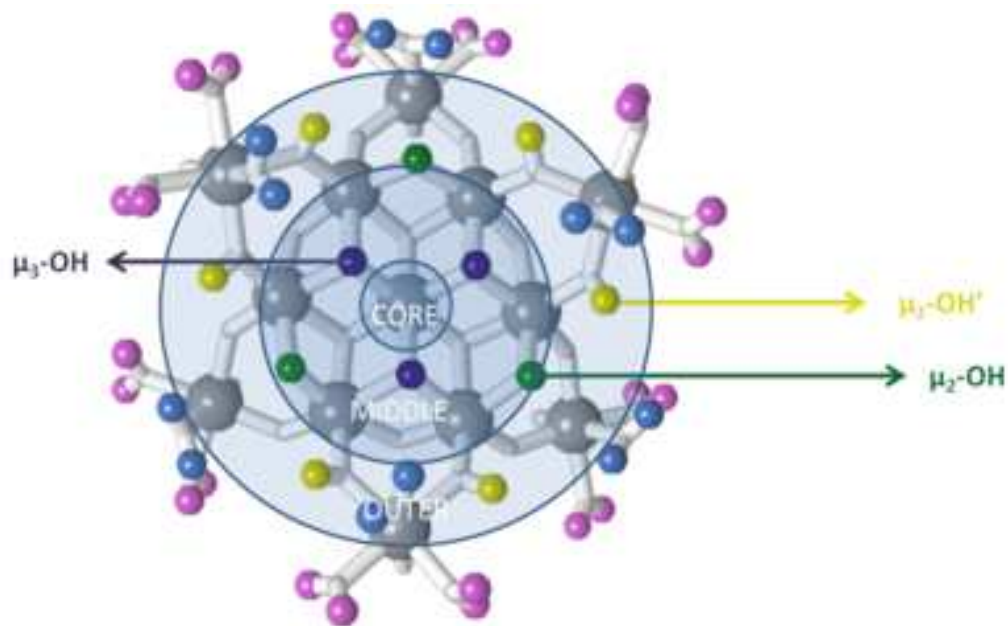


Figure 4.2. Diagram of $f\text{-Al}_{13}$ showing the different types of protons coordinated to the core ($\mu_3\text{-OH}$, purple), middle ($\mu_2\text{-OH}$, green), and outer ($\mu_2\text{-OH}'$, yellow) shells of aluminium metal ions. Water molecules are color-coded to reflect differences based upon symmetry, not coordination.

ions. Four water molecules fill the remaining coordination sites for each outer shell metal ion. If all proton resonances for $f\text{-Al}_{13}$ are accounted for, the integrations based upon chemical shifts equate to 1:1:2:4 respectively. However, the number of resonances and the expected chemical shifts do not reflect this. Therefore two possibilities exist: 1) the chemical shifts for H₂O ligands on flat- Al_{13} are not visible due to rapid proton exchange on the NMR timescale, or 2) $f\text{-Al}_{13}$ is rearranging to form $\kappa\text{-Al}_{13}$. Dynamic and phase analysis light scattering were used to investigate this potential rearrangement further (Table 4.1).

Table 4.1. Diagram of $f\text{-Al}_{13}$ showing the different types of protons coordinated to the core ($\mu_3\text{-OH}$, purple), middle ($\mu_2\text{-OH}$, green), and outer ($\mu_2\text{-OH}'$, yellow) shells of aluminium metal ions. Water molecules are color-coded to reflect differences based upon symmetry, not coordination.

% acetone (V/V)	$f\text{-Al}_{13}$ (mL)	H ₂ O (mL)	Acetone (mL)
0	1.0	1.0	0.0
5	1.0	0.9	0.1
10	1.0	0.8	0.2
15	1.0	0.7	0.3
20	1.0	0.6	0.4
25	1.0	0.5	0.5
30	1.0	0.4	0.6
35	1.0	0.3	0.7
40	1.0	0.2	0.8
50	1.0	0.0	1.0

Results show that the hydrodynamic radius (R_h) of $f\text{-Al}_{13}$ decreases from $1.00 \text{ nm} \pm 0.05 \text{ nm}$ to approximately half its original size at $0.55 \text{ nm} \pm 0.09 \text{ nm}$ with increasing mol % of acetone (Figure 4.3). Since R_h is influenced by the overall charge of a molecule, it is easy to speculate that the resultant species is $\kappa\text{-Al}_{13}$ based upon the decreased charge of $\kappa\text{-Al}_{13}$ (+7) compared to $f\text{-Al}_{13}$ (+15). ^1H -DOSY experiments where $R_h = 0.6 \text{ nm} \pm 0.4 \text{ nm}$ and $1.2 \text{ nm} \pm 0.3 \text{ nm}$ for $\kappa\text{-Al}_{13}$ and $f\text{-Al}_{13}$, respectively.¹⁵ Viscosity effects can be ruled out due to the fact that the measured diffusion coefficients readily increase even though the viscosities at lower acetone percentages ($\eta < 5\%$ acetone) are higher relative to water ($\eta = 1.019 \text{ cP}$ at $20 \text{ }^\circ\text{C}$).

A similar trend is also observed with conductivity (σ) and zeta potential (ζ) measurements. The conductivity drops to half of its original value from 5.0 mS/cm to 2.5 mS/cm as acetone is added to the solution (Figure 4.4). The zeta potential decreases sharply from +54 mV to +0.5 mV at 10 mol % acetone before levelling out. Previous studies have indicated that such a drop off in overall charge and conductivity while the concentration is constant is very indicative of cation aggregation and eventual precipitation. However, since there is no observable increase in size or precipitation over time, ion association is not likely. The most probable scenario is that acetone is replacing nitrate ions and acting as the dominant counterion in solution. It has been shown that the analogous flat $[\text{Ga}_{13}(\mu_3\text{-OH})_6(\mu_2\text{-OH})_{18}(\text{H}_2\text{O})_{24}]^{15+}$ (**f-Ga₁₃**) has a radius of gyration (R_g) (core size without the influence of the counterion) of $0.6 \text{ nm} \pm 0.2 \text{ nm}$ and an R_h of $0.90 \text{ nm} \pm 0.08 \text{ nm}$.¹⁶ Assuming **f-Al₁₃** has a similar core size as that of **f-Ga₁₃**, what one is actually observing via DLS is the core size of the cluster. This is possible because the hydrogen bonding interactions between the acetone carbonyl group and **f-Al₁₃** water ligands of the clusters are greater than the $\text{NO}_3^- : \text{H}_2\text{O}$ interactions. The overall size of the ionic sphere surrounding the cluster shrinks as the acetone is continuously added, resulting in a smaller R_h .

ATR-IR spectra of a 1 M **f-Al₁₃** solution (14% acetone content) was compared to 14% acetone in water and pure acetone (Figure 4.5). The spectra reveal that the C=O stretching vibration at 1711 cm^{-1} for acetone red shifts to 1698 cm^{-1} while the C—H deformation mode (1355 cm^{-1}) and C—C (1219 cm^{-1}) blue shifts to 1362 cm^{-1} and 1234 cm^{-1} respectively. These observed spectral shifts are common and a well-studied

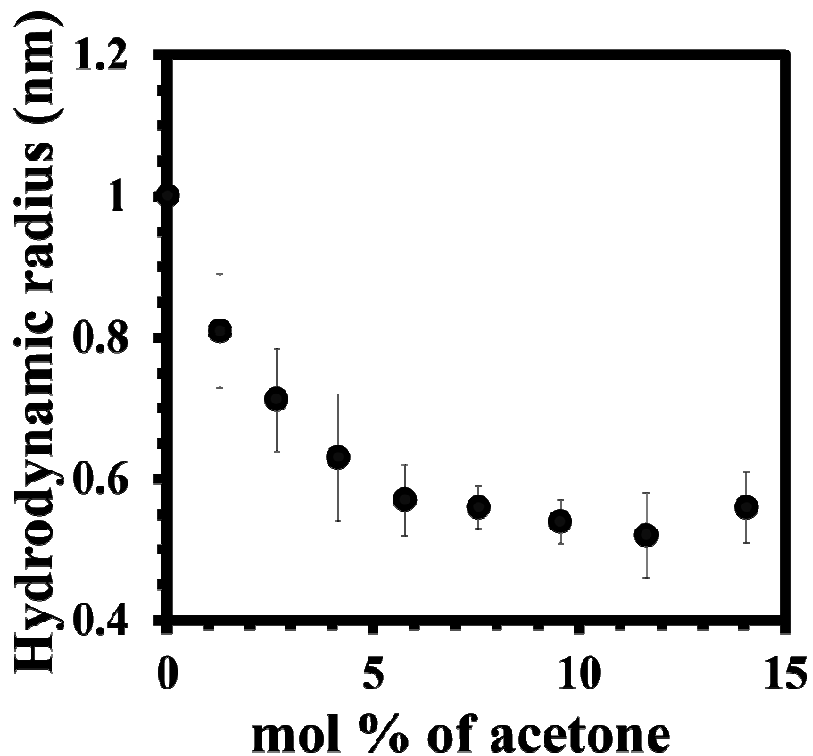


Figure 4.3. Hydrodynamic radius of *f*-Al₁₃ as a function of mol % acetone.

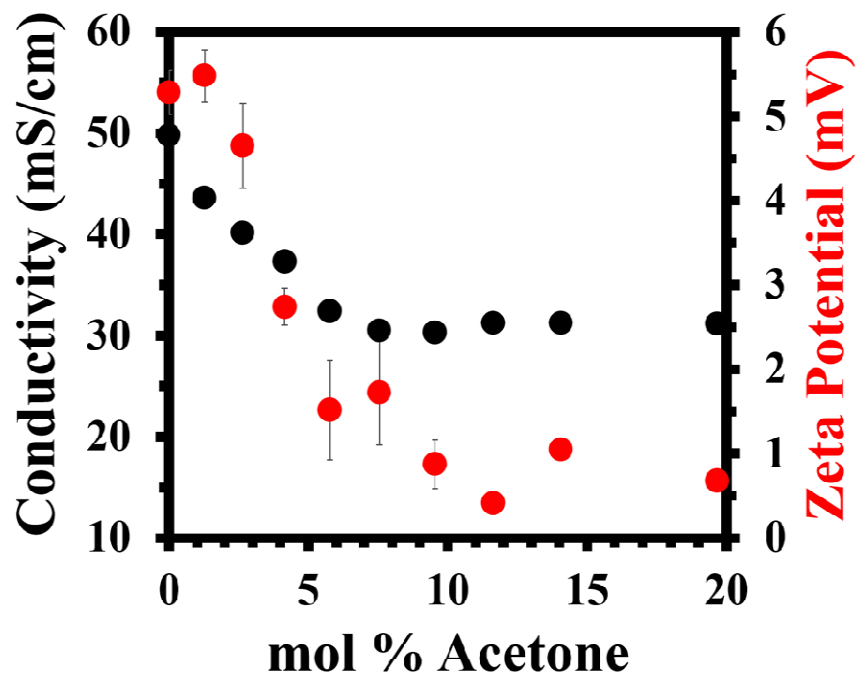


Figure 4.4. Conductivity and zeta potential measurements for *f*-Al₁₃.

interaction between the C=O...H—OH bonding interactions. The red shifting of the C=O bond is due the elongation of this bond while the blue shifts are from the shortening of the C—H and C—C bonds. These interactions are pronounced at lower acetone quantities (mol % \leq 15) and this phenomena is most likely occurring with the water molecules on the cluster as well.

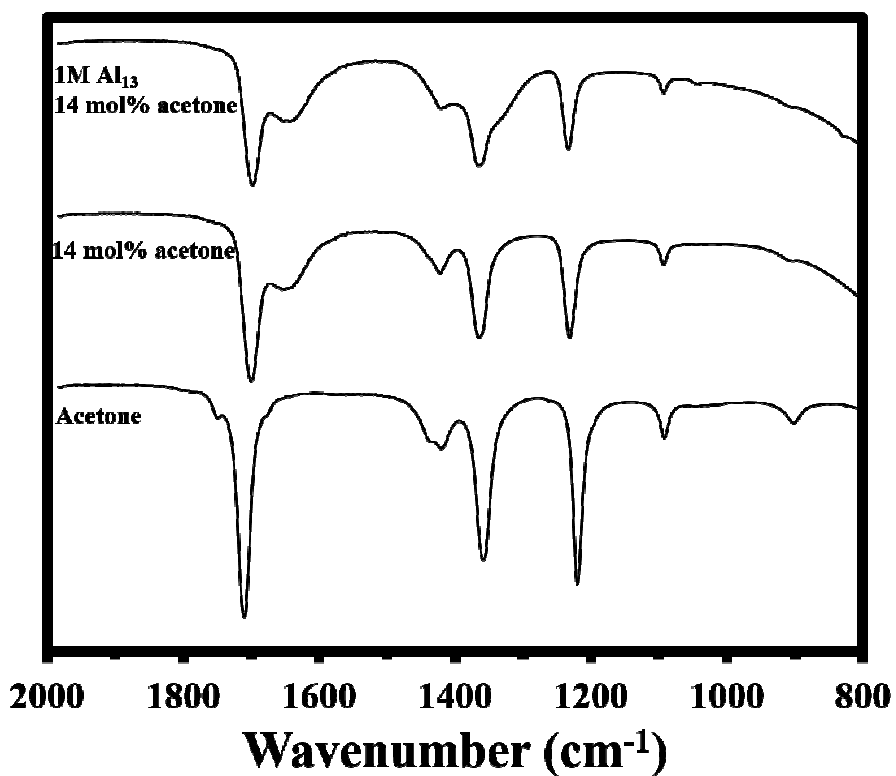


Figure 4.5. Stacked ATR-IR spectra of 1M *f*-Al₁₃ at 14 mol% acetone, 14% acetone in water mixture, and pure acetone.

¹H and ²⁷Al-NMR experiments were used to further probe this event. The conditions used for DLS and PALS analysis were duplicated and the spectra were taken at room temperature. Once enough acetone is present in solution, the spectra were also collected at -20 °C where more resonances can be observed.

At -10°C , the incremental addition of acetone to a solution of $f\text{-Al}_{13}$ in D_2O produced a ^1H -NMR spectrum similar to that observed at low temperatures for $\kappa\text{-Al}_{13}$, although the chemical shifts of the proposed $\mu_2\text{-OH}$ and $\mu_2\text{-OH}'$ protons were slightly upfield by comparison. The resonance for $f\text{-Al}_{13}$ observed via ^{27}Al -NMR also becomes smaller as the percentage of acetone in solution increases. All together this leads us to believe that a molecular rearrangement has occurred.

4.3.2. D_2O . Two peaks are present for $f\text{-Al}_{13}$ at 7.6 ppm and 3.6 ppm near 0°C (Figure 4.6). This is different for $\text{Al}(\text{NO}_3)_3$ for which one peak at 9.5 ppm is observed. Based upon observations the peak at 3.6 ppm is likely the resonance of a set hydroxyl protons for $f\text{-Al}_{13}$. Two peaks are present for $f\text{-Al}_{13}$ at 7.6 ppm and 3.6 ppm near 0°C (Figure 4.7). This is different for $\text{Al}(\text{NO}_3)_3$ for which one peak at 9.5 ppm is observed (see SI). Based upon observations the peak at 3.6 ppm is likely the resonance of a set hydroxyl protons for $f\text{-Al}_{13}$. Several ^1H -NMR peaks assigned to bound hydroxyls conspicuously broaden with increased temperature (Table 4.2), suggesting that the bound protons are in dynamic equilibrium with water in the solvent (Figure 4.8). Proton transfer must be in the slow-exchange regime because the frequency separation is large between the proton signals corresponding to the $f\text{-Al}_{13}$ and the peak centered at 5.2 ppm that is assigned to bulk water in the solvent.^{13,17}

The results are compiled in Table 4.3 where the fitted activation parameters and the logarithms of estimated lifetimes $(\frac{1}{\tau} = k_{ex})$ of protons on various $f\text{-Al}_{13}$ oxygens are estimated.

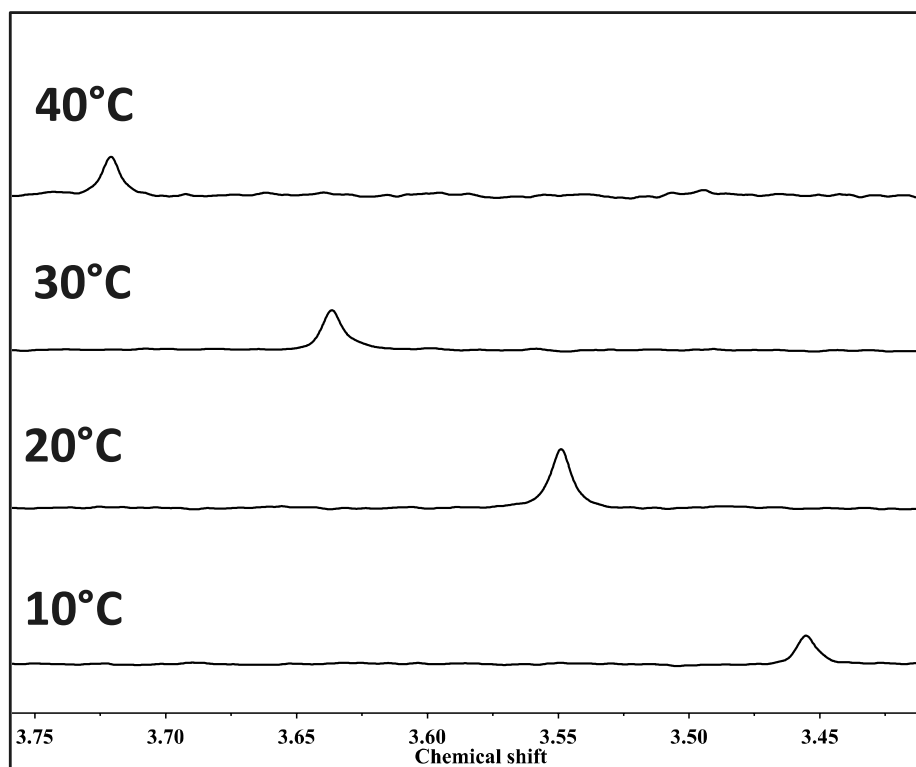


Figure 4.6. ^1H -NMR spectra of variable-temperature experiment for $f\text{-Al}_{13}$ in D_2O . $\text{H}_2\text{O}/\text{DMSO-}d_6$.

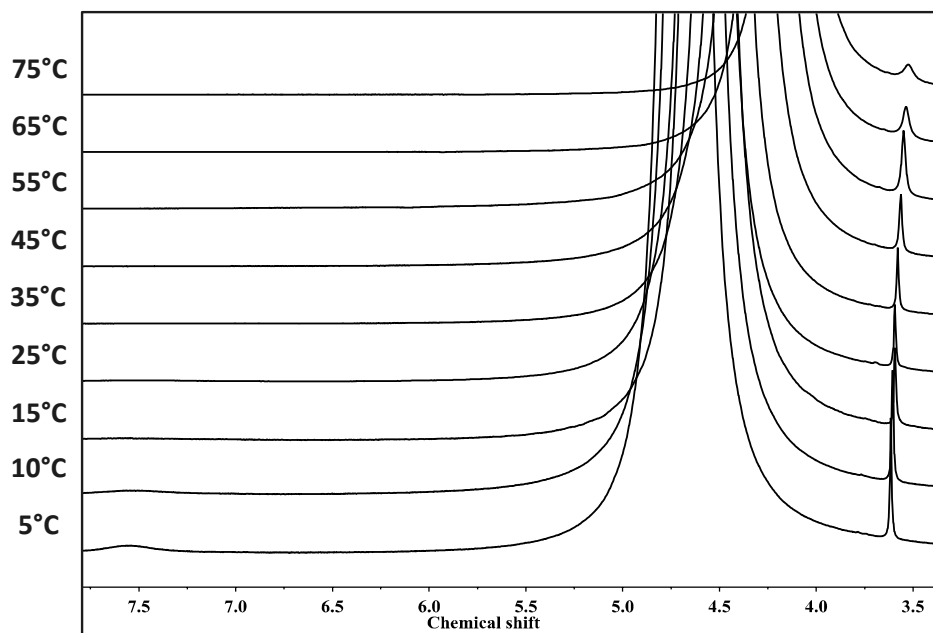


Figure 4.7. ^1H -NMR spectra of variable-temperature experiment for $f\text{-Al}_{13}$ in 1:2 (v/v) solution of $\text{H}_2\text{O}/\text{DMSO-}d_6$.

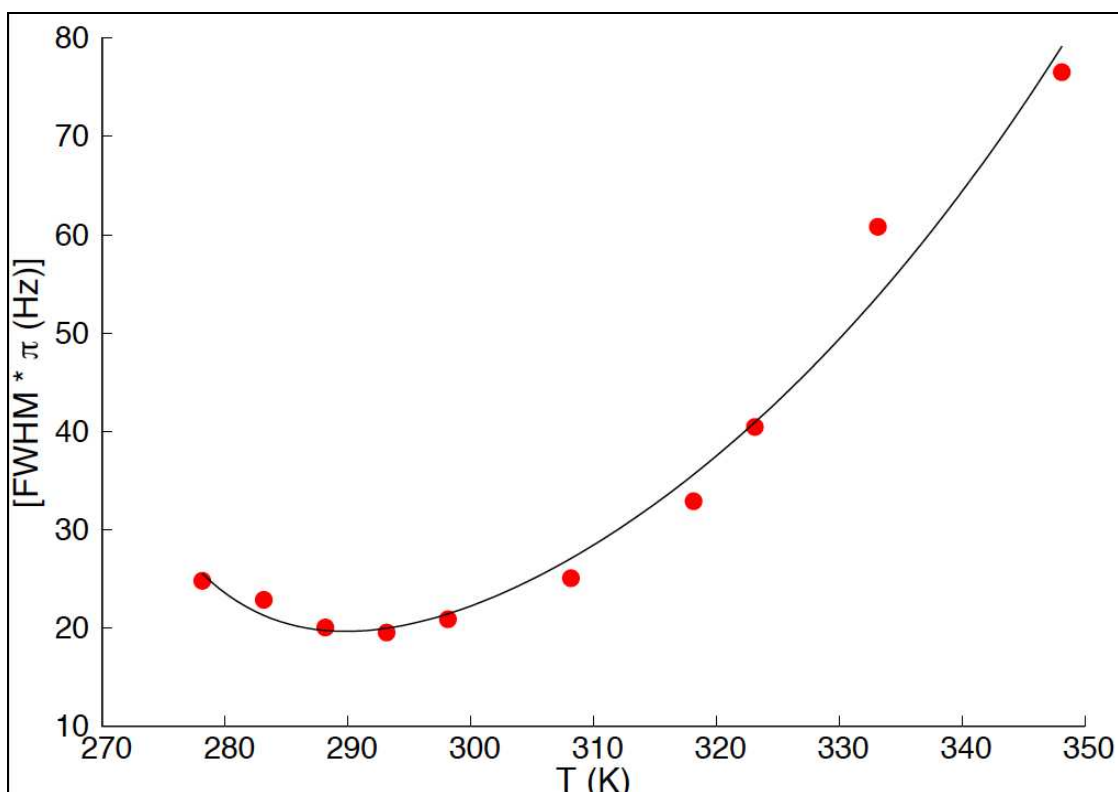


Figure 4.8. Plot of the kinetics data for the μ_2 -OH proton of $f\text{-Al}_{13}$ in 1:2 (v/v) solution of $\text{H}_2\text{O}/ \text{DMSO-}d_6$.

Table 4.2. Full-width half-max (FWHM) values for the peaks of $f\text{-Al}_{13}$ at 3.61 ppm in 1:2 (v/v) solution of $\text{H}_2\text{O}/ \text{DMSO-}d_6$.

Temp (°C)	FWHM (Hz)
3.61 - 3.52 (C)	
0	9.12
5	9.98
15	11.64
35	14.05
45	18.03
50	41.17
60	72.13

Table 4.3. Residency times and activation parameters for proton sites on **f-Al₁₃**. Standard errors are in parentheses.

Proton site	log (k_{298}/s^{-1})	ΔH^\ddagger (kJ·mol ⁻¹)	ΔS^\ddagger (J·mol ⁻¹ ·K ⁻¹)
H ₂ O/acetone- <i>d</i> ₆			
μ_2 -OH	4(1)	44 (8)	-30(30)
μ_2 -OH'	3.0(0.2)	32.8(0.7)	-78(3)
μ_3 -OH			
H ₂ O/DMSO- <i>d</i> ₆			
μ_2 -OH'	3.0(0.6)	39(3)	-60(10)
μ_2 -OH	1.4(0.5)	22(3)	-146(8)
D ₂ O			
μ_2 -OH			

The logarithms of the exchange coefficients are compiled because the uncertainties are large and derive largely from the ~10% standard errors assigned to the ΔH^\ddagger values, which are exponentiated to get k_{ex} . The uncertainties are only normally distributed in $\log(k_{ex})$, not k_{ex} . The key point to derive from Table 4.3 is that the lifetimes are on the order of milliseconds ($k_{ex} \approx 10^3 s^{-1}$), which compares well with previous work on the [AlO₄Al₁₂(OH)₂₄(OH₂)₁₂]⁷⁺ Keggin ion.¹³ The average lifetimes at 298K for protons on the two sets of μ_2 -OH bridges in a 2:1 H₂O:DMSO solution were estimated at: 0.013 and 0.2 s⁻¹, within uncertainties to the values estimated here for **f-Al₁₃**. What we cannot evaluate in this study is whether or not there are proton-enhanced pathways for exchange

of the protons on μ_2 -OH bridges, as was detected for one site in the $[\text{AlO}_4\text{Al}_{12}(\text{OH})_{24}(\text{OH}_2)_{12}]^{7+}$ Keggin ion.

4.4. CONCLUSIONS

The increasing linewidths with temperature were fit to version of the Eyring equation. Implicit in this fitting is the assumption of a two-site exchange. Uncertainties are normally distributed for $\log(k_{298})$, not k_{298} , and were estimated by Monte Carlo propagation from uncertainties in the activation enthalpies derived from the Eyring equation.

4.5. CHAPTER V BRIDGE

Chapter V continues the investigations on the effects solvents may have on cluster speciation. This chapter specifically explores how the unique properties that other protic solvents like alcohols influences and promotes cluster agglomeration in solution.

CHAPTER V

FORMATION OF ALUMINIUM NANO-AGGLOMERATES FROM

AQUEOUS FLAT- $\text{Al}_{13}(\mu_3\text{-OH})_6(\mu_2\text{-OH})_{18}(\text{H}_2\text{O})_{24}(\text{NO}_3)_{15}$:

INVESTIGATIONS OF SOLVENT EFFECTS ON SOLUTION

DYNAMICS

5.1. INTRODUCTION

For this work, I was the main contributor with regards to the initial project conception, experimental design, data collection, and authorship for this piece that is being submitted to the Journal of American Chemical Society. My lab mate Susan Cooper warrants great recognition for her critical DOSY NMR analysis of the cluster size in methanol. My two undergraduates Alexia Smith and Dolly Zhen also deserves much credit for carrying out experiments pertaining towards understanding the nanoagglomerates' speciation in solution as a function of solvent composition and time.

We have qualitatively investigated the chemical speciation and interactions of flat- $\text{Al}_{13}(\text{OH})_{12}(\text{H}_2\text{O})_{24}(\text{NO}_3)_{15}$ (**f-Al₁₃**) dissolved in alcoholic solutions via **DLS**, **PALS**, **DOSY-NMR**, electrolytic conductivity, and Raman spectroscopy. Upon immediate dissolution of **f-Al₁₃** in methanol, dynamic light scattering reveals the existence of aluminum-based nanoparticles ranging from approximately 6 nm – 20 nm in radius. The size of the nanoparticles derived from **f-Al₁₃** was found to dependent on several factors including the Al^{3+} concentration, water/alcohol ratio, and the dielectric constant of the solvent system. However, the nanoagglomerates do not persist in alcoholic solution.

Additionally, Raman spectroscopy reveals that the formation of methyl nitrate (CH_3NO_3 , C—O stretch at 816 cm^{-1}) in solution also plays a significant role in facilitating the growth and breakdown of aluminum nanoagglomerates.

As the most abundant metal in the Earth's crust (~8% of the Earth's solid weight), aluminum has been revered throughout human history for being one of the most utilized elements ever discovered.¹ Its impact on modern society is ubiquitous as it has been heavily integrated into numerous areas including but not limited to transportation, ceramics, absorbents, waste remediation, semiconductors, medicine, aerospace, etc.² However, although aluminum is commonly found in the environment, a full understanding of the complexity of aluminum chemistry continues to be a grand challenge. In particular, understanding the mechanisms at which several intricate and highly complex aluminum species that have been isolated in aqueous solution form continues to be one of the most investigated aspects regarding aluminum chemistry.^{3,4} For instance, it is well-understood that depending on the pH environment, aluminum can adopt many different structural motifs. Within a given pH regime, species such as $\text{Al}(\text{H}_2\text{O})_6^{3+}$ ion, extended polymeric networks [Gibbsite: $\gamma\text{-Al}(\text{OH})_3$], and discrete, nanoscale clusters including $\text{Al}_8(\text{OH})_{14}(\text{H}_2\text{O})_{18}^{8+}$ (**Al₈**), keggin- $\text{NaAl}_{13}\text{O}_4(\text{OH})_{24}(\text{H}_2\text{O})_{12}(\text{SO}_4)_8$ (**k-Al₁₃**), flat- $\text{Al}_{13}(\text{OH})_{12}(\text{H}_2\text{O})_{24}^{15+}$ (**f-Al₁₃**), and $\text{Al}_2\text{O}_8\text{Al}_{28}(\text{OH})_{56}(\text{H}_2\text{O})_{18}^{26+}$ (**Al₃₀**) have all been observed.^{3, 5-7}

A number of recent and emerging studies have focused on the understanding the dynamic interactions for many of the aforementioned aluminum clusters (e.g. formation, energetics, exchange kinetics, and stability) in aqueous solution that have allowed for a better fundamental understanding of aluminum speciation.⁸⁻¹³ However, there have been

very few direct studies regarding the solution chemistry of polymeric aluminum species in other protic solvents, particularly alcohols.¹⁴ Fundamentally, understanding the dynamic interactions solvents can have on solution speciation is been of interest by scientist across many disciplines. Solvents interactions with a host compound are well-known to affect chemical reactivity, solubility, and equilibrium. From an environmental prospective, aqueous aluminum waste matter has been a long-standing concern. Largely due to acidic rain and industrial processing, vast quantities of polymeric aluminum species (flocs) often accumulate in the soil and wash away in wastewater where alcohols such as methanol, ethanol, and isopropanol are among some the most commons protic compounds present.^{15,16} As such, understanding how some of the aforementioned alcohols may interact with aqueous aluminum species is paramount towards ultimately determining the overall impact this have on the environment.

Herein we present a unique example of the effects that alcohols can have on the solution speciation of aluminum. For this particularly study, we have limited the scope to focus on the dissolution products of **f-Al₁₃** in various alcoholic solutions (i.e. methanol, ethanol, and isopropanol). These targets were selected because **f-Al₁₃** is soluble in a wide concentration range in both water and alcohols (particularly in methanol). Additionally, alcohols are among some of the most common solvents in waste areas, where they could interact with aluminum flocs. Dynamic light scattering (**DLS**), phase analysis light scattering (**PALS**), diffusion-ordered spectroscopy (**DOSY**), and electrolytic conductivity measurements, and Raman spectroscopy are used to explore and further understand the solution speciation of **f-Al₁₃** in the presence of alcohols.

5.2. EXPERIMENTAL

5.2.1. Materials and Sample Preparation. Crystalline $\text{Al}(\text{NO}_3)_3 \cdot 9\text{H}_2\text{O}$ (Sigma Aldrich 98%) was used without further purification to synthesize the **f-Al₁₃** cluster via zinc reduction and confirmed with Raman spectroscopy prior to solution preparation and analysis. Reagent grade methanol (Sigma Aldrich 99.8%) and deionized water was used as the solvent media for each set of experiments.

5.2.2. Dynamic and Phase Analysis Light Scattering. Prior to analysis, each sample was filtered into the cuvette with a 100 nm PTFE syringe filter to remove any potential unwanted particulate matter. The following dynamic light scattering (DLS) and phase analysis light scattering (PALS) measured using the Mobius from Wyatt technologies. DLS was used to measure changes in the hydrodynamic radius (R_h) of the alumina species in solution. For each data point collected, 20 acquisition were average over a 10 second scan rate. The Dynamics software uses the Einstein-Stokes equation ($R_h = K_b T / 6\pi\eta D_t$) where K_b = the Boltzmann constant, T = temperature in kelvin, η = viscosity, and D_t = translational diffusion coefficient to solve for the R_h value.

Phase analysis light scattering (PALS) was ran simultaneously with DLS to measure the conductivity and zeta potential. The samples were measured under an electric field frequency of 10 Hz, a voltage amplitude of 3.0 V and the values were averaged over a collection period of 20 seconds. **Note:*** To ensure that no appreciable changes occurred under the influence of the applied potential, each DLS experiment was also performed sans the applied potential. The error between each comparison was less than 1%.

5.2.3. NMR spectroscopy. All ^1H -NMR data and ^1H -DOSY experiments were collected on an INOVA-500 MHz spectrometer. An ampule of methanol- d_4 from Cambridge

Isotope Laboratories (DLM-51) was used and spectra were taken with 5mm NMR tubes. Al_{13} at a concentration of 7 mM of was mixed with methanol- d_4 right before the samples were taken. DOSY data was collected using the pulsed field gradient double stimulated echo pulse sequence with convection compensation (Dpfdgste). The diffusion delay was 100 ms, diffusion gradient was 3 ms, the number of increments was 50 and the number of scans was 32. The lowest gradient value was set to 1000 and the highest gradient value was set to 20000. Both alternate gradient sign and lock gating were selected during the data acquisition. In order to determine the diffusion coefficient the Varian software package was used. The hydrodynamic radius was determined by using the Einstein-Stokes Equation.

5.2.4. Raman Spectroscopy. Raman spectra were collected using an Alpha 300S SNOM confocal Raman microscope in a 180° backscattering configuration. A continuous wave pump laser at an excitation wavelength of 532 nm provided 60 mW of power. A 0.3 m spectrometer equipped with 600 grooves/mm grating was used to detect stokes Raman scattering and provided a resolution of 1 cm^{-1} . The spectra from each sample were averaged over 100 accumulations at an exposure time of 0.5 s per acquisition.

5.3. RESULTS AND DISCUSSION

The hydrodynamic radius (R_h) of **f-Al₁₃** was measured in water and methanol at a concentration of 100 mM to illustrate the initial effects methanol has on **f-Al₁₃** speciation. The R_h after immediate dissolution for the **f-Al₁₃** cluster was $6.0 \text{ nm} \pm 1.2 \text{ nm}$ (polydispersity % = 21%), which was a six times larger relative to **f-Al₁₃** in water ($1.0 \text{ nm} \pm 0.1 \text{ nm}$, polydispersity % = 10%) (Figure 5.1). Such a stark contrast in size and particle distribution between each solvent environment suggests that the cluster is agglomerating

in methanol. To further investigate the cause of this phenomenon, we conducted a series of experiments that focused on understanding the effects of concentration, time, charge, and counterion on influencing **f-Al₁₃** nanoparticle formation and stability. Solid **f-Al₁₃** was dissolved into pre-mixed solutions of water and methanol with varying volume % of methanol to determine the minimal amount of methanol required to promote agglomeration. DLS measurements revealed that the formation of the **f-Al₁₃** nanoagglomerates is gradual, requiring a significant amount of methanol (~0.3 mol eq., 40 - 60% by volume) was required before agglomeration was statistically significant (Figure 5.1).

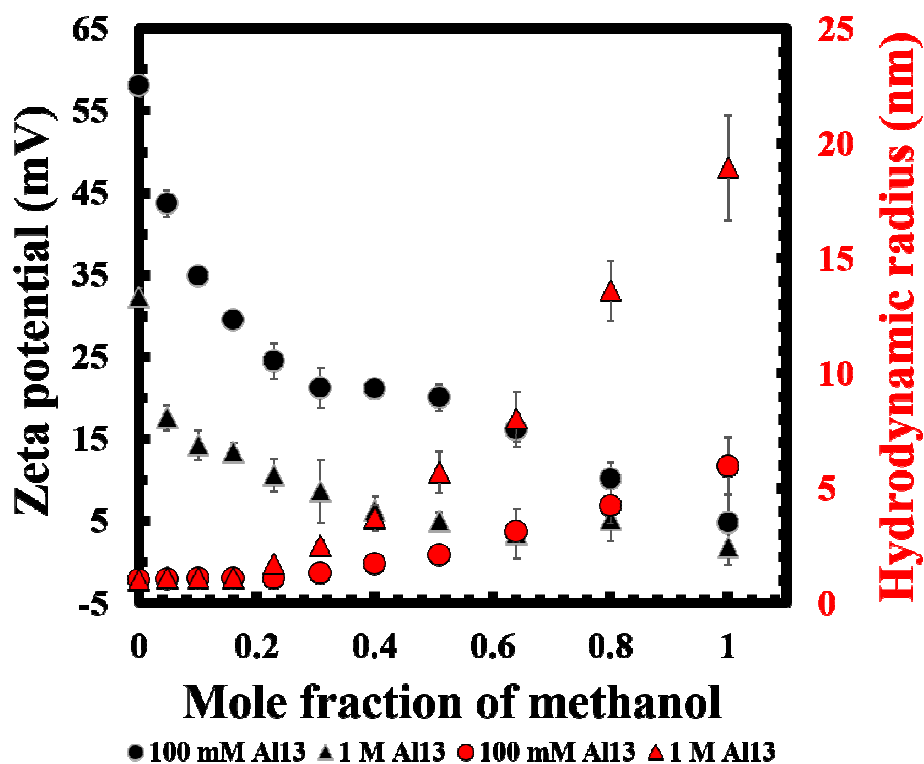


Figure 5.1. Hydrodynamic radius and ζ -potential of **f-Al₁₃** as a function of the mole fraction of methanol and Al^{3+} concentration. The molarity for **f-Al₁₃** was held constant throughout each solvent mixture. Each point in the figure were collected upon immediate dissolution of **f-Al₁₃**.

Beyond 0.3 mol eq. methanol, the **f-Al₁₃** nanoparticles continue to grow exponentially in size until reaching a maximum at 100% methanol content. The increase in particle size is also concentration-dependent based on the DLS data at different concentrations of **f-Al₁₃**. 1 M **f-Al₁₃** in methanol has a maximum size of 19 nm ± 2.4 nm (polydispersity % = 13%) while 0.1 M **f-Al₁₃** is approximately a third in size at 6.0 nm ± 1.2 nm (polydispersity % = 21%). It should be noted that this process is also reversible in that the titration of methanol into a aqueous solution of **f-Al₁₃** cluster will cause agglomeration to occur while the titration of water to **f-Al₁₃** in methanol causes the solution to dissociate similarly to what is observed by pre-mixing the solvents.

Interestingly, similar trends were observed when other alcohols are used, such as ethanol and propanol (Figure 5.2). As seen with the methanol:H₂O mixtures, significant agglomeration for both ethanol:H₂O and isopropanol:H₂O mixtures occurred when the alcohol content exceeded 0.4 mol eq. in solution. However, the degree of agglomeration was far more pronounced in at that 0.73 mol eq. ethanol and 0.49 mol eq. n-propanol the size of the agglomerates are 12 nm ± 0.47 nm and 13 nm ± 0.1 nm respectively. Also, it should be noted that the reversibility of the ethanol:H₂O and isopropanol:H₂O mixtures were limited due to solubility limits at higher alcohol concentrations.

Zeta potential is was collected along with the R_h to investigate the how the growth of the **f-Al₁₃** nanoagglomerates would affect the overall charge speciation and stability of the system (Figure 5.1). The sharp decline in the magnitude of the zeta potential (ζ) suggests a significant decrease in overall charge repulsion at higher methanol content. This increase in attractive forces can be explained by the difference in dielectric constants (ϵ_r) between water (80 at 20 °C) and methanol (33 at 20 °C). Although the dipole

moments (μ) of water ($\mu = 1.85$) and methanol ($\mu = 1.7$) are relatively similar, the large gap in ϵ_r means that methanol is reducing the transmission of repulsive forces of **f-Al₁₃** in aqueous solution (ζ of 0.1 M **f-Al₁₃** in H₂O = 58 mV \pm 1.4 mV). As such, this attenuation of the electrostatic interactions most likely plays a key role in causing the **f-Al₁₃** cluster to agglomerate. It should be noted that at 100% methanol, the value for ζ -potential drops below 5 mV at all concentrations studied. Such a low value for ζ -potential predicts that these nano-agglomerates will not persist in solution over time. The agglomerates will either precipitate out of solution or dissociate in solution to more stable species until a dynamic equilibrium is reached.

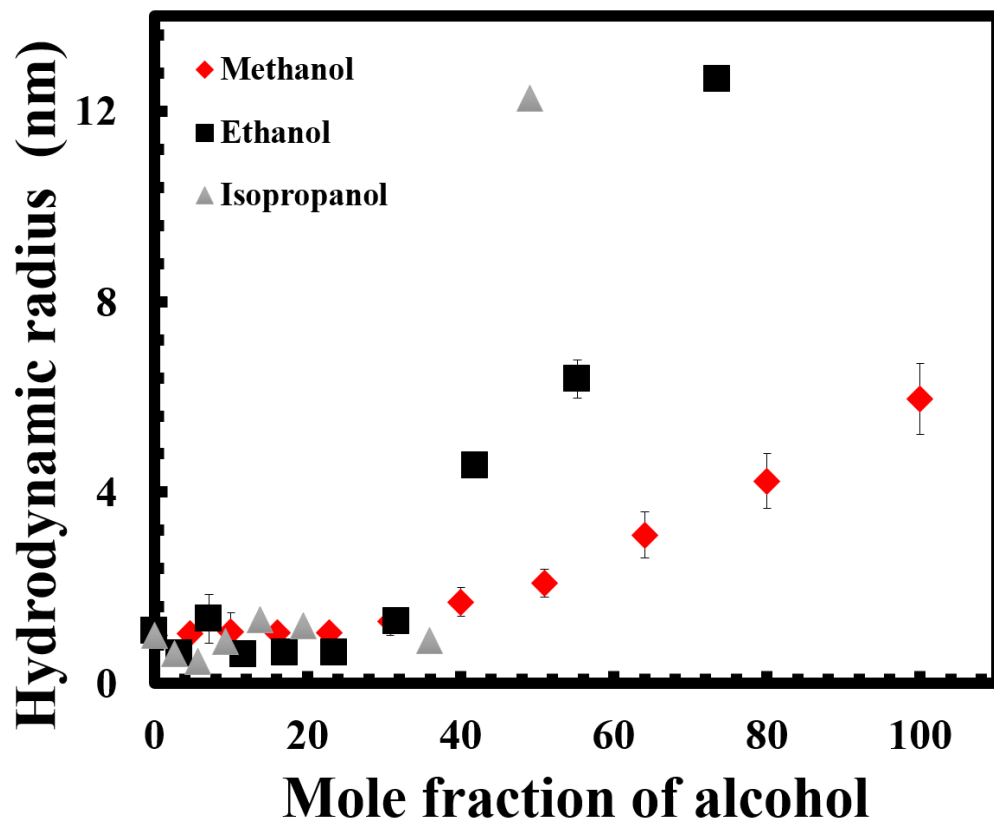


Figure 5.2. Hydrodynamic radius as a function of mole fraction of alcohol for three different alcohols. Each solution mix was prepared at 100 mM Al³⁺ concentration.

To determine which scenario was more likely, the hydrodynamic radius and ionic conductivity of 0.1 M **f-Al₁₃** in methanol was monitored over a 24 hr. time period (Figure 5.3). With no visible signs of precipitation, the R_h of the **f-Al₁₃** nanoagglomerates decrease from 6 nm to 4.0 within the first 10 hours and continued to breakdown until an equilibrium was reached at $2.0 \text{ nm} \pm 0.3 \text{ nm}$. The change in conductivity under the same time frame was shown to be inversely related to the size decrease of the agglomerates. Such an increase in conductivity over time points to an increasing number ions in solution, further suggesting that ion dissociation is a key contributor to the decrease in size of the **f-Al₁₃** nano-agglomerates.

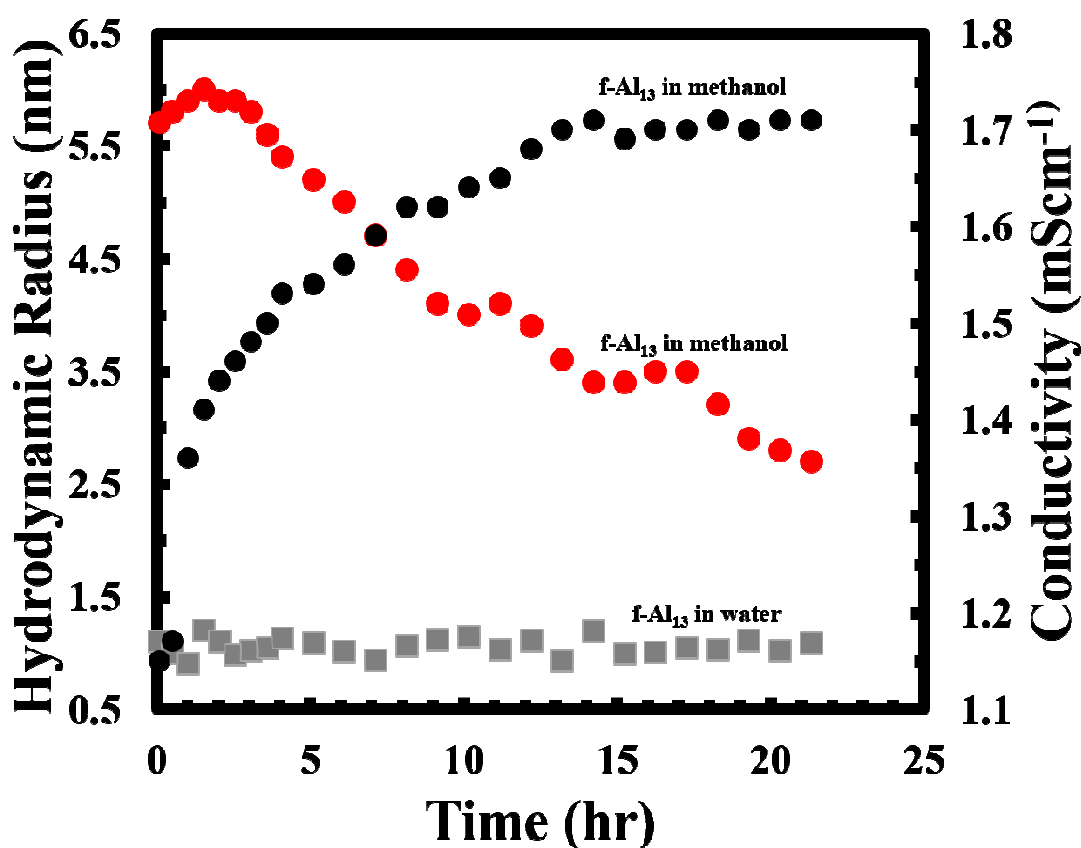


Figure 5.3. Size (red) and conductivity (black) plot of 0.1 M **f-Al₁₃** in methanol as a function of time compared to 0.1 M **f-Al₁₃** in water (grey).

DOSY-NMR was performed on 100 mM **f-Al₁₃** in methanol to corroborate with the initial results shown earlier (Figure 5.4). The ¹H-NMR spectra of **f-Al₁₃** in methanol yielded one peak at 1.3 ppm which had a diffusion coefficient of $2.3 \times 10^{-12} \text{ m}^2\text{s}^{-1}$ ($R_h = 1.6 \text{ nm}$) immediately after the sample was made and $2.5 \times 10^{-12} \text{ m}^2\text{s}^{-1}$ ($R_h = 1.8 \text{ nm}$) after 24 hrs. Although the size of the agglomerates after equilibrium was reached agreed well in value measured by **DLS**, the initial value was less than what was measured by **DLS**.

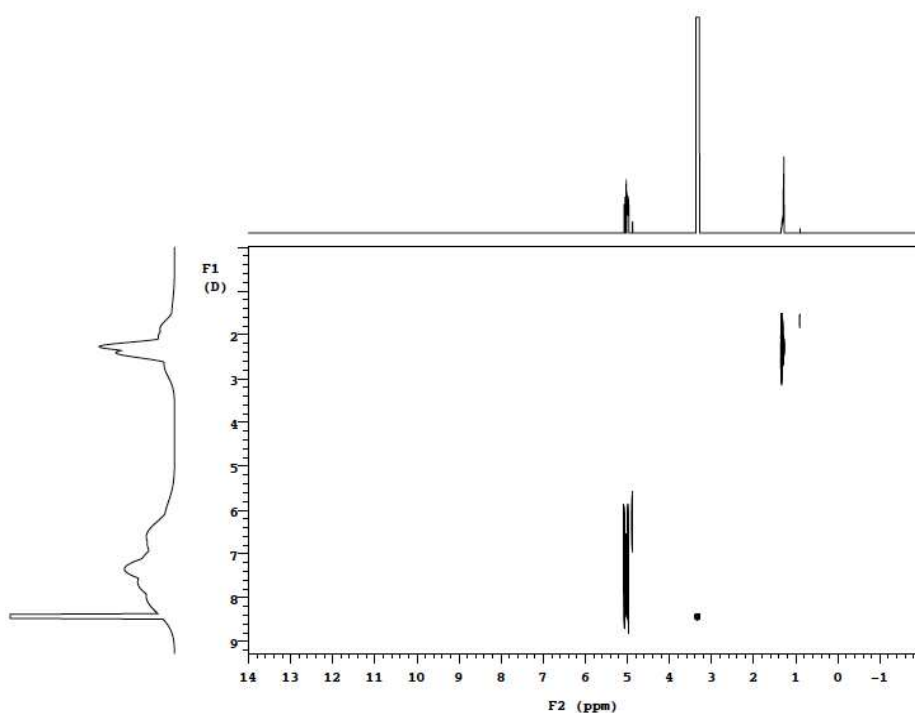


Figure 5.4. DOSY-NMR spectra of 100 mM **f-Al₁₃**.

The discrepancy in values may be explained through the inherent nature of each technique. **DLS** is uniquely sensitive towards detecting larger species in solution while **DOSY-NMR** normally detects the species that has the most significant concentrations. This is significant in that this suggests that even though larger agglomerates are present, they are not the dominant species at any point in solutions.

In attempts to understand the agglomeration from a structural prospective, the Raman spectrum of the **f-Al₁₃** in methanol was compared to the spectra of methanol, HNO₃, and a 1:1 methanol:HNO₃ ratio mix. A methanolic solution of **f-Al₁₃** showed a sharp, distinct peak at 816 cm⁻¹. This same peak is present in the methanol:HNO₃ mix sans **f-Al₁₃** and thus these peaks can be assigned to be C—O stretching vibration unique to aqueous methyl nitrate (CH₃ONO₂).¹⁷

The presence of peaks attributable to methyl nitrate in the **f-Al₁₃** spectrum strongly suggests that the nitrate counterions are not tightly bound to cluster in solution and can readily associate with methanol (Equation 5.1). Control measurements of 0.1 M, 1.0 M, or 2.0 M Al(NO₃)₃ in methanol do not show any signs of the formation of CH₃ONO₂, which further supports this idea



The formation of CH₃ONO₂ is significant because it can be linked to the formation and decomposition of the **f-Al₁₃** nanoagglomerates. In addition to a lower ϵ_r value for methanol affecting charge repulsion, the formation of CH₃ONO₂ likely plays a significant role in the of **f-Al₁₃** agglomeration through the removal of acidic protons (H⁺) from the **f-Al₁₃** cluster in solution. Additionally, the area intensity of C—O stretching vibration at 816 cm⁻¹ for methyl nitrate decreases on a similar time scale to the disappearance of the **f-Al₁₃** agglomerates (Figure 5.5). This further suggests that methyl nitrate plays a role in the agglomeration and dissolution of **f-Al₁₃**. As such, we postulate that the decrease in particle size is dependent on the amount of water and the amount of CH₃ONO₂ is present in solution.

Under the same experimental conditions described in Figure 5.1, **f-Al₁₃**, the Raman data reveals that the intensity of C—O stretching vibrations at 816 cm⁻¹ decreases significantly at higher ratios of water. Additionally, the data showed the symmetric C—O stretching vibration of methanol at 1024 cm⁻¹ and a slight blue shifting of the N—O symmetric stretch of nitrate ion from 1043 cm⁻¹ to 1048 cm⁻¹, signifying the weakening of the C—O bonds and release of the “free” nitrate ions as the CH₃ONO₂ hydrolyzed.

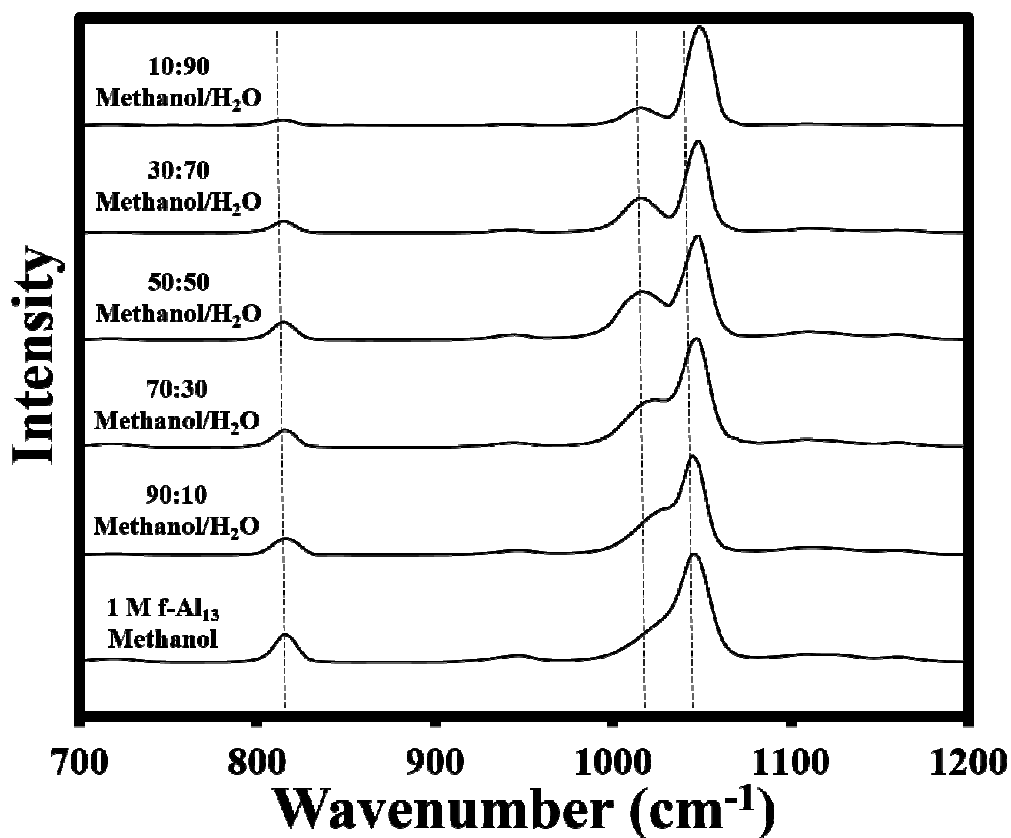


Figure 5.5. Stacked Raman from 700 cm⁻¹ to 1200 cm⁻¹ spectra various MeOH:H₂O mixtures of 1 M **f-Al₁₃**.

We can now attribute the slow breakdown of the **f-Al₁₃** agglomerates in 100% methanol (Figure 5.3) to the presence of a large number of water molecules in the solid

state **f-Al₁₃** prior to dissolution. In addition to this, significantly more water is produced as a byproduct of the reaction (equation 5.1). The excess water that is created over time pushes back the equilibrium (Le Chatelier's principle) by protonating the CH₃ONO₂, converting it into CH₃OH and HNO₃ and affecting the breakdown of the **f-Al₁₃** agglomerates.

5.4. CONCLUSIONS

We have shown that a subtle change in solvent environments can have significant effects on the speciation dynamics of aluminum chemistry. With this study we seek to bring more attention to an area of aluminum chemistry that is lacking a significant fundamental knowledge base. More importantly however, we hope that this study will bring more awareness of the impact that aluminum speciation in non-aqueous media can potentially have on our environment.

5.5. CHAPTER VI BRIDGE

The next discusses the work published on the electrochemical titration of gallium and gallium-indium tridecamer cluster that spawned from a graduate level laboratory immersion course.

CHAPTER VI

ELECTROCHEMICAL SYNTHESIS OF FLAT-[Ga_{13-x}In_x(μ₃-OH)₆(μ-OH)₁₈(H₂O)₂₄(NO₃)₁₅] CLUSTERS AS AQUEOUS PRECURSORS FOR SOLUTION-PROCESSED SEMICONDUCTORS

6.1. INTRODUCTION

We acknowledge Jeffrey Ditto and Josh Razink for assistance in electron beam imaging. Additional acknowledgements go to the student participants as well as co-instructors Matt Carnes and Chris Knutson for making significant contributions towards designing the project for this class project and publishing this chapter manuscript in the *Journal of Materials Chemistry*. My role as the third instructor focused on the following: developing functional uses of the analytical techniques used by the students in class as well as data interpretation and collection.

Flat-[Ga₁₃(μ₃-OH)₆(μ-OH)₁₈(H₂O)₂₄](NO₃)₁₅ (Ga₁₃) and heterometallic [Ga_{13-x}In_x(μ₃-OH)₆(μ-OH)₁₈(H₂O)₂₄](NO₃)₁₅ (x = 5, 4) clusters were synthesized by the electrolysis of metal nitrate salt solutions to directly form, without purification, aqueous precursor inks for In_xGa_{13-x}O_y semiconducting films in < 2 hr. Raman spectroscopy and ¹H-NMR spectroscopy confirm the presence of [Ga_{13-x}In_x(μ₃-OH)₆(μ-OH)₁₈(H₂O)₂₄(NO₃)₁₅]. Bottom-gated thin-film transistors were fabricated using ~16 nm-thick Ga_{13-x}In_xO_y films as an active channel layer, displaying turn-on voltages of -2 V, and on/off current ratios

greater than 10^6 . The channel-average mobility of the transistors fabricated from the cluster solutions generated by electrolysis was $\sim 5 \text{ cm}^2 \text{ V}^{-1}\text{s}^{-1}$ which was more than twice that of transistors fabricated from control solutions with the simple nitrate salt precursors of $\sim 2 \text{ cm}^2 \text{ V}^{-1}\text{s}^{-1}$. Electrochemical cluster synthesis thus provides a simple and direct route to aqueous precursors for solution-processed inorganic electronics.

Thin film deposition using aqueous inorganic-cluster precursors provides an alternative to traditional vacuum processing techniques for thin-film manufacture.^{1,2} As one example, “flat” Group 13 $[\text{M}_{13}(\mu_3\text{-OH})_6(\mu\text{-OH})_{18}(\text{H}_2\text{O})_{24}(\text{NO}_3)_{15}]$, homo- and heterometallic clusters (Figure 6.1) have been used to deposit high-performance semiconductor³ and dielectric films⁴. Because of this, significant effort has been aimed at improving Group-13 cluster synthesis. Early syntheses took two weeks and used dibutylnitrosamine (DBNA), a known carcinogen.^{3,5} Wang *et al.* showed that the addition of Zn powder to acidic $\text{Al}(\text{NO}_3)_3$ solutions results in condensation of $[\text{Al}_{13}(\mu_3\text{-OH})_6(\mu\text{-OH})_{18}(\text{H}_2\text{O})_{24}(\text{NO}_3)_{15}]$ (Al_{13}) clusters via a gradual pH increase of the solution through nitrate reduction. The reaction is complete in approximately two days and the carcinogenic DBNA is no longer needed.⁶ A disadvantage to this method is that extensive purification is required to remove Zn^{2+} from the precursor solution. The preferential solubility of zinc nitrate in alcohol is used to purify the clusters, as M_{13} clusters are negligibly soluble in many organic solvents. In contrast, electrochemistry provides a direct mechanism to drive reduction reactions without the use of chemical reagents that must be later removed. Recently, both flat⁷ and Keggin⁸ Al_{13} clusters have been electrochemically synthesized.

Here we report the electrochemical synthesis of $[\text{Ga}_{13-x}\text{In}_x(\mu_3\text{-OH})_6(\mu\text{-OH})_{18}(\text{H}_2\text{O})_{24}]^{15+}$ ($x = 0, 4, 5$) clusters and show that the aq. solutions obtained can be used, without purification, to deposit Ga-In-O channel layers with good thin-film transistor (TFT) performance. The elimination of secondary reagents and purification steps is beneficial for mass production, sustainability, and cost. Films can be cast directly from the modified salt solutions, making this a direct method for obtaining various homo- and heterometallic Group 13 oxide thin films with a variety of applications.

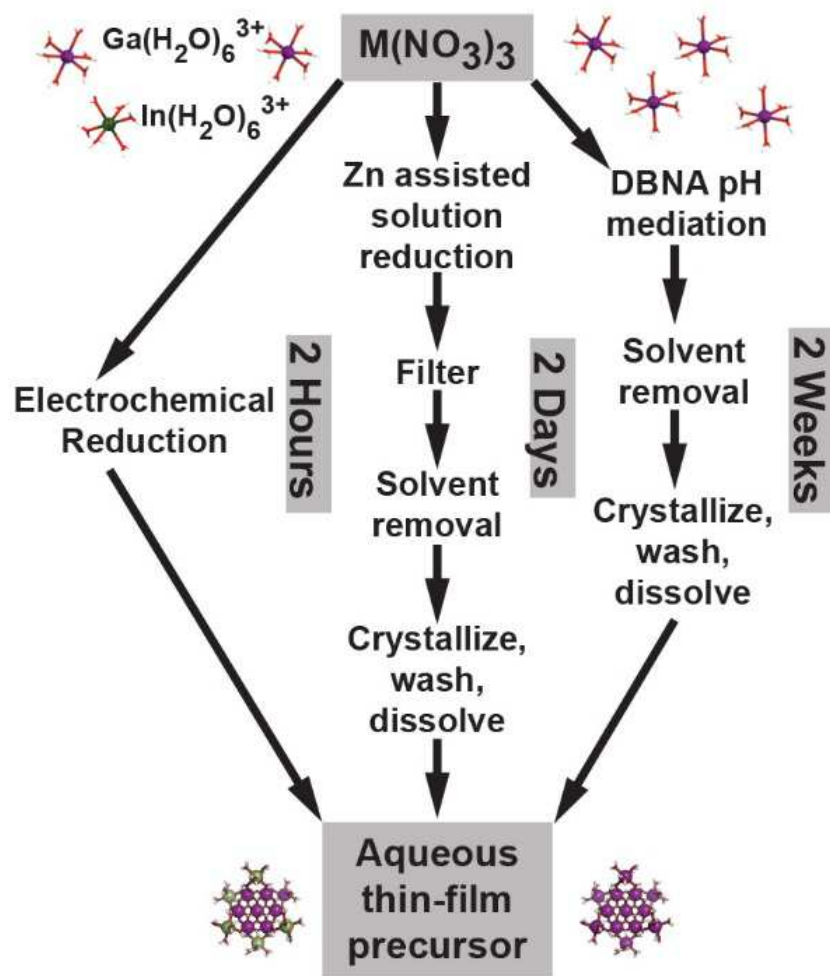
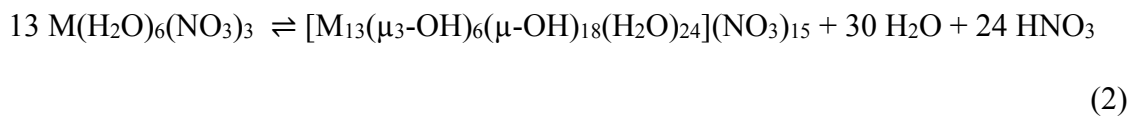
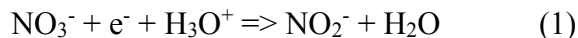


Figure 6.1. Comparison of M_{13} cluster synthesis routes.

6.2. RESULTS AND DISCUSSION

The synthesis is performed in a two-compartment electrochemical cell comprising 1) a beaker housing the Pt working electrode, a Ag/AgCl reference electrode, and pH probe and 2) a medium fritted tube, inside the beaker, containing a Pt counter electrode (Figure S1). Experimental details are provided in the Supplemental Information in the Appendix. The applied working electrode potentials were chosen to be slightly negative of the reduction potential of the metal cations at the pH of interest as described by their Pourbaix diagrams.⁹ Potentials of -1.00 V vs. Ag/AgCl for Ga and -0.49 V vs. Ag/AgCl for Ga-In mixtures were used to generate the desired products with the given apparatus. The voltage of -1.00 V for aq. solutions of gallium nitrate caused a change in the luster of the Pt surface which could be seen by eye.¹⁰ Yields of washed product show this plating results in a relatively small amount of Ga loss overall (< 2%).

The primary mechanism of this reaction appears to be the removal of nitrate from the solution via its reduction to ammonium, NO_x, and potentially other species. The removal of nitrate counter anions from the solution raises the pH of the solution by consuming protons as in (1) and thus drives the formation of the cluster via LeChatelier's Principle as it acts on the reaction as given in (2).



Analysis of an air-dried aliquot of the crude reaction by ¹H-NMR shows a prominent triplet peak with equal peak heights corresponding to the ¹H-¹⁴N coupling of ammonium ions centered at 7.1 ppm¹¹ (Figure S6.3). This indicates that nitrate is reduced to

ammonium as a part of one pathway in which counterions are removed from solution and the pH is raised. Although the presence of ammonium ions indicates that nitrate reduction is involved in raising the pH of the cluster solution and forcing plating of the metal aqua species, it does not rule out other contributing mechanisms. We find that electrolysis at sufficiently high current results in evolution of a brown gas. This is likely due to the reduction of NO_3^- to NO_x gases.¹² We performed the electrochemical synthesis of Ga_{13} and $\text{Ga}_{13-x}\text{In}_x$ mixed clusters at a constant applied voltage which was high enough to reduce small amounts of metal but low enough to prevent large losses of material to plating. We believe that some metal plating onto the electrode is important to condition the Pt toward nitrate reduction. Nitrate can undergo a number of reduction processes to form species including N_2O_4 , HNO_2 , NO , and NH_4^+ . The standard reduction potentials are similar, between +0.8-1.0 V vs. NHE,^{13a} and all much more positive than the hydrogen reduction potential. At a clean Pt electrode, however, H_2 generation might be expected to dominate given the fast kinetics relative to nitrate reduction. We did not observe significant bubbles (that would be associated with H_2 formation) on the Pt electrode surface. After Pt is modified by Ga/In plating it likely becomes poisoned for hydrogen evolution and thus kinetically preferences the nitrate reduction reaction.^{13b} These data support the hypothesis that nitrate reduction is the predominate electrochemical reaction. Regardless of the cathode reaction, charge balance requires additional positively charged species (e.g. $\text{In}(\text{H}_2\text{O})_6^{3+}$ or $\text{Ga}(\text{H}_2\text{O})_6^{3+}$) to migrate from the counter electrode compartment into the working electrode compartment or negatively charged species (e.g. NO_3^-) to migrate the opposite direction. Both migration processes serve to lower the nitrate-to-metal-ion ratio in the working-electrode-compartment film-precursor solution.

Proton NMR provides useful information for the identification and determination of the degree of substitution by indium in heterometallic clusters. Analysis of aq. inorganic clusters by ^1H -NMR spectroscopy is traditionally challenging in protic solvents, however, due to acidic proton exchange with the solvent. In most aprotic solvents, analysis of inorganic clusters by ^1H NMR spectroscopy is made difficult by the low solubility of highly-charged clusters. These obstacles are overcome by using d_6 -DMSO, which allows for the detection of signals arising from water molecules and hydroxide bridges of the cluster. To confirm the presence of clusters, a portion of the electrochemically generated samples was air dried and then dissolved in d_6 -DMSO. These samples were allowed to equilibrate overnight to ensure even DMSO exchange at the outer hydroxyl shell of the clusters.¹⁴ The ^1H -NMR spectra of the reduced $\text{Ga}(\text{NO}_3)_3$ product is consistent with that of flat- Ga_{13} clusters previously reported (Figure S6.3).¹⁵

Using ^1H -NMR, we are able to distinguish between differently substituted heterometallic clusters once they have been dried and isolated. After equilibrating in d_6 -DMSO for 24 hr the clusters for each Ga:In ratio gives rise to a distinctive spectrum with a clearly developed fingerprint region (S. I. Figure S4). Although we can identify the Ga:In ratio from this signature, we are still unable to distinguish between positional isomers of the In at the exterior of the clusters. Crystals were grown of each of the isomers independently and their spectra taken to calibrate our results.¹⁶ The ^1H -NMR spectra obtained for the product of the mixed metal nitrate reduction, starting with a 6:7 ratio of Ga to In, is consistent with the Ga_9In_4 cluster synthesized independently (S.I. Figure S6.4). After washing the product of the electrochemical reaction with isopropanol, this product appears to have exchanged some of the external metal ions to form Ga_8In_5

clusters as is evident by the change in their distinctive $^1\text{H-NMR}$ spectra. This suggests that the clusters may be dynamic in the presence of the washing solvent and that In readily substitutes for Ga within the cluster (Figure 6.2). Exchange of In atoms around flat M_{13} has recently been observed in solution to be a reversible, equilibrium process.¹⁶

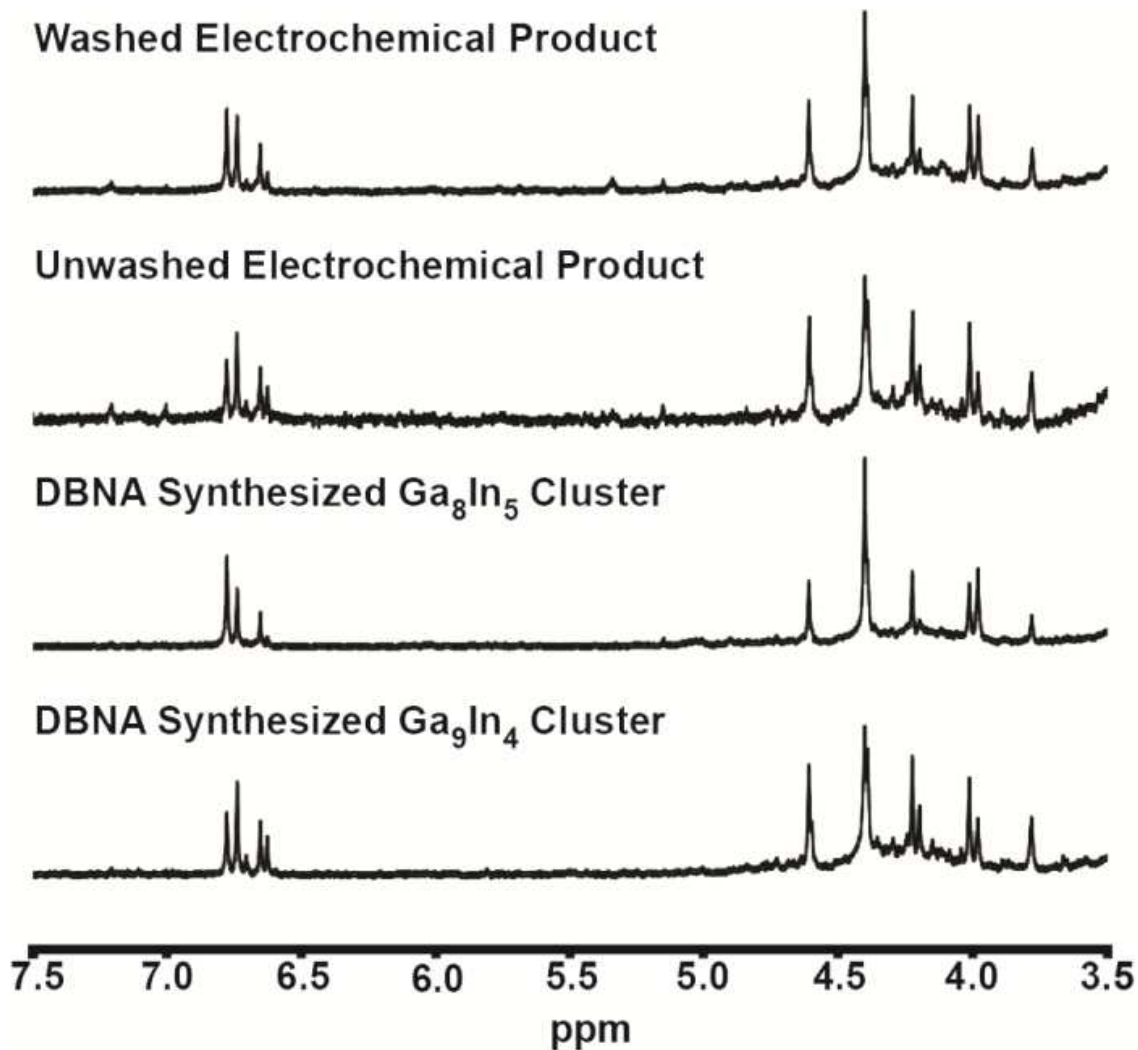


Figure 6.2. $^1\text{H-NMR}$ (d_6 -dmsO) spectra of washed and unwashed precipitated cluster products from DBNA and electrochemical syntheses. Based on comparison to the DBNA-derived control samples, the unwashed electrochemical product is assigned the composition Ga_9In_4 , while the washed electrochemical product is assigned the composition Ga_8In_5 .

We find evidence for M_{13} species forming with fewer reducing equivalents than that reported for the Zn-based synthesis of $[Al_{13}(\mu_3-OH)_6(\mu-OH)_{18}(H_2O)_{24}(NO_3)_{15}]$.^{6a} Ga_{13} clusters are observed after passing a cathodic charge of 0.7-0.8 electrons per Ga, and 0.4-0.5 electrons per metal in the case of the $Ga_{13-x}In_x$ clusters. The Zn-based synthesis of Al_{13} used 1.0 reducing equivalents per Al (1:2 Zn:Al as Zn is a $2e^-$ reductant). The synthesis of a related Sc_2 cluster used 0.75 reducing equivalents per Sc.^{6b} Our hypothesis to explain such behavior is that if hydroxyl-bridged metal cluster formation is under equilibrium control, not all of the excess nitrate counterions need to be consumed for clusters to form. Our analysis does not however exclude the possibility that the reaction does not go to completion under the conditions used. Nitrate ions can also be effectively removed from association with the growing clusters by counterbalancing the positive charge associated with newly formed ammonium ions, leaving this new ammonium nitrate salt in solution but allowing ions to diffuse away from clustering species.

Raman spectroscopy has also been shown to be a useful technique for identifying M_{13} clusters.¹⁷ The Raman spectra of aliquots from the electrochemical synthesis agree with previous reports of Ga_{13} clusters, highlighted by the ν_1 Ga-O symmetric stretch, or breathing mode at $464 \pm 1 \text{ cm}^{-1}$ (Figure 6.3).¹⁷ The Raman spectra of the structurally analogous $Ga_{13-x}In_x$ cluster reveal similar vibrational features to those observed in Ga_{13} clusters, with the ν_1 breathing mode slightly red-shifted to $449 \pm 1 \text{ cm}^{-1}$. This shift is consistent with the substitution of the larger In for Ga, and with the observed difference between the vibrational modes of In and Ga hexa-aqua salts (Figure 6.3).

The class of flat M_{13} Group 13 clusters prepared previously have been shown to be effective precursors for high-quality thin films.^{3,4} In this study, aq. cluster-containing

solutions with an In:Ga ratio of 6:7 produced by the electrochemical synthesis were directly spin-cast onto thermally grown SiO₂ on Si wafers and annealed at 550 °C. This process circumvents the recrystallization step and the need to wash and dissolve the solid products in another solvent, thus reducing the time and solvent needed for synthesis. Heterometallic clusters were used to generate channel layers within TFTs. A TEM image of a device cross-section confirms the uniform morphology of thin films processed from the electrochemically-synthesized precursor (Figure 6.4a). EDX measurements of the films (Figure S5) confirmed the presence of both In and Ga in the films.

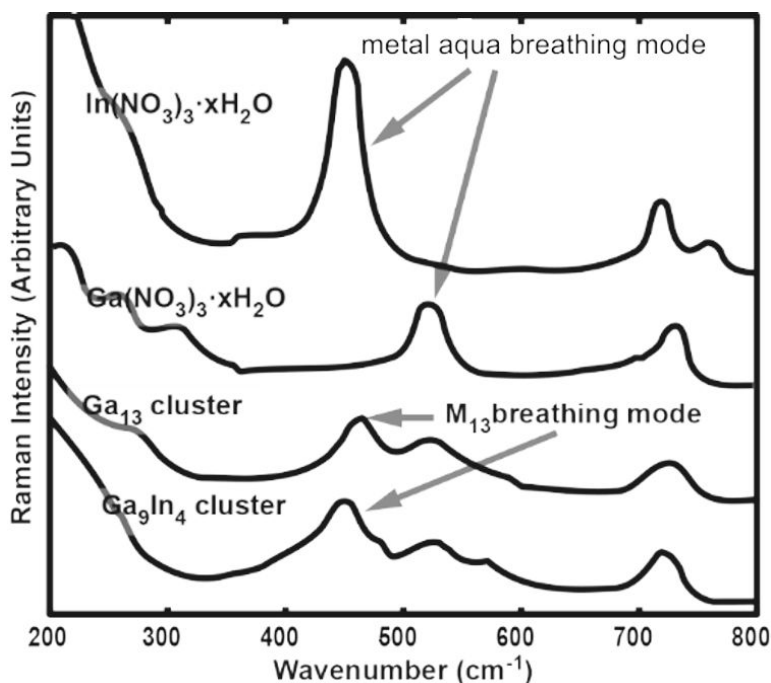


Figure 6.3. Solid-state Raman spectra of nitrate salts and electrochemically generated cluster samples. Spectra for cluster compounds were collected on a single crystal using a Raman microscope and are largely free of metal nitrate impurities. Note the red-shift in the ν_1 breathing mode center for the In-substituted cluster ($449 \pm 1 \text{ cm}^{-1}$) when compared to that for the Ga cluster ($464 \pm 1 \text{ cm}^{-1}$). The uncertainties given are associated with the error in fitting the peak center.

Figures 6.4b, c, and d show the device properties of the heterometallic cluster channel layer in TFTs processed from the electrochemically generated cluster solutions and

compares them to those made using a starting nitrate salt solution. The devices derived from electrochemically-synthesized precursors are comparable to previously reported devices using DBNA-derived precursors.³ Devices obtained from cluster precursors show on-to-off current ratios of greater than 10^6 and turn-on voltages near -2 V whereas the devices made from starting salt solution show slightly negative turn-on voltages of ~ -3 V and on-to-off ratios greater than 10^5 (Figure 6.4c).

The average channel mobility of cluster films are greater than those obtained from starting salt solution films by at least a factor of two (Figure 6.4d). These values for mobility were calculated by the method of Wager *et al.*¹⁸ Compared to the mixed salt solutions of $\text{In}(\text{NO}_3)_3$ and $\text{Ga}(\text{NO}_3)_3$, the $\text{Ga}_{13-x}\text{In}_x$ clusters have fewer nitrate counter ions per active metal because the nitrates are consumed electrochemically during the cluster synthesis. This decrease in nitrate concentration drives olation and preorganization of the metal hydroxides into clusters.¹⁹ Because nitrates are removed during the annealing step to give an oxide thin film, we attribute the enhanced performance of the electrolyzed solution to reduced porosity in the final semiconductor channel that would be caused by decomposing counter ions.

Although the goal of this work is to show the new electrochemical synthesis route yields cluster precursors whose TFT performance is similar to clusters made by conventional methods, it is also useful to compare the performance to other solution-derived oxide thin films. Kim *et. al.* reported the use of “combustion processing” to deposit related In-Zn-O films at temperatures as low as 200 °C from methoxyethanol solutions.^{20a} Composition-optimized $\text{In}_{0.7}\text{Zn}_{0.3}\text{O}_{1.35}$ devices fabricated with a SiO_2 gate dielectric (as is done here) had saturation mobilities (μ_{sat}) of $10 \text{ cm}^2 \text{ V}^{-1} \text{ s}^{-1}$ after annealing

at 400 °C. Hwang et. al. reported μ_{sat} of $8 \text{ cm}^2 \text{ V}^{-1} \text{ s}^{-1}$ for $\text{In}_{0.7}\text{Zn}_{0.3}\text{O}_{1.35}$ after annealing at 300 °C when $\text{Zn}(\text{NO}_3)_2$ and $\text{In}(\text{NO}_3)_3$ were deposited from an aqueous solution.^{20b} The $\text{In}_{0.46}\text{Ga}_{0.53}\text{O}_{1.5}$ studied here had average channel mobilities of $5 \text{ cm}^2 \text{ V}^{-1} \text{ s}^{-1}$. Studies of vapor-deposited films show that mobility increases sharply with higher In concentration.^{20c} Increasing the In:Ga ratio in the clusters would be expected to further increase TFT performance. Alternative gate dielectrics (e.g. amorphous alumina^{20a}), and surface/interface passivation layers,²¹ also dramatically improve the TFT performance of films made from other solution precursors. These strategies can directly be used to improve the performance of the cluster precursors reported here.

6.3. CONCLUSIONS

In summary, an alternate synthetic method is reported for the synthesis of flat homo- and heterometallic Group 13 cluster precursor solutions that can be directly used in the fabrication of thin-film transistors. This new method reduces the processing time to generate M_{13} cluster solutions from two days to two hours. The synthesis is carried out electrochemically so as to reduce protons and nitrate ions in a controlled fashion. Heterometallic clusters synthesized using this method are functionally similar in transistor applications to previously synthesized and characterized clusters.³ These films are capable of being spin-cast directly from unpurified reaction solutions into high-quality thin films. The films are dense, smooth, and processable at relatively moderate temperatures under ambient atmospheric conditions. This reagent-free, electrochemical synthesis may also find application in future mechanistic studies of cluster formation and speciation.

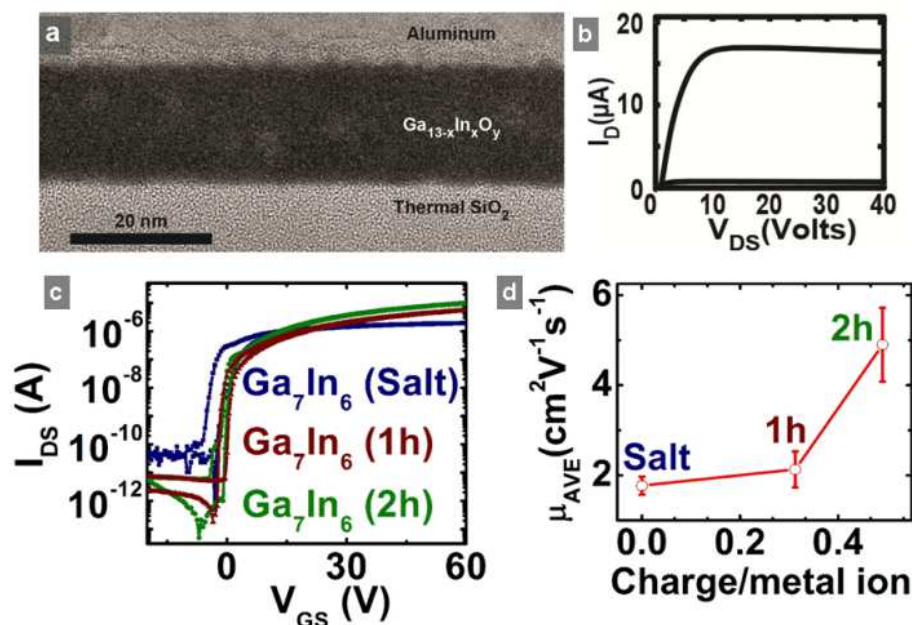


Figure 6.4. (a) Transmission electron microscopy image demonstrating the uniform morphology of thin films processed from the electrochemically-synthesized precursor. (b) Average transfer curve compiled from five bottom-gate TFTs processed using the electrochemically synthesized $\text{Ga}_{13-x}\text{In}_x$ heterometallic clusters to generate channel layers. (c) Representative transfer plots for 550 °C air-annealed In-Ga-O films created using the electrochemically synthesized $\text{Ga}_{13-x}\text{In}_x$ heterometallic cluster and starting salt solution precursors. (d) Average channel mobility determined at $V_{GS} = 40$ V for films made at various electrolyzed time intervals (and thus different average numbers of electrons passed into the solution per metal ion). Device performance is increased with longer electrolysis, consistent with removal of nitrate and formation of clusters. The devices consist of the following structures: Al/Si (p+)/ SiO_2 (100 nm)/In-Ga-O(15 nm)/Al, length = 150 μm , width = 1000 μm , and $V_{DS} = 0.1$ V (V_{DS} = drain source voltage; V_{GS} = gate source voltage; I_D = drain current).

6.4. CHAPTER VII BRIDGE

The following chapter discusses how the immersion course in cluster chemistry was designed and how we utilized this format to generate publication quality research within the timeframe of a ten-week course.

CHAPTER VII

MENTORING GRADUATE STUDENTS IN RESEARCH AND TEACHING BY UTILIZING RESEARCH AS A TEMPLATE

7.1. INTRODUCTION

Special acknowledgements must go to Dr. Christopher Knutson, Dr. Matthew Beekman, and Dr. Matt Carnes for their contributions as well as acting as superb mentors and guiding me through the process of starting and finish this particular project. I wrote the “graduate student reflection” portion and was a key editor of this article that was published in the *Journal of Chemical Education*.

We have designed a unique guided-inquiry-inspired course for entry-level graduate students using chemical research as a mechanism to teach research-oriented problem-solving skills. The course has been designed for flexibility around a shared research experience. The curriculum can be modified each year by incorporating a new research project into the framework of the course. Advanced graduate students and postdoctoral scholars serve as course instructors, providing significant teaching and mentoring opportunities for them. The benefits of the inquiry-driven approach have been reinforced through careful selection of instructors and students. We have been able to create a positive learning environment and a highly beneficial award system for students and instructors by offering an opportunity to publish class results in a scholarly journal. The

course serves as a template for the implementation of similar graduate coursework at comparable research institutions.

The primary goal of graduate education is to prepare students as researchers for careers in either academic or industrial environments.¹ Generally, an integral part of research training at the graduate level occurs through peer-guided osmosis; namely, knowledge flows in a rather unstructured way from senior graduate students or postdoctoral associates to new graduate students. We have recently introduced a new graduate-level course to examine and augment this research training via a guided-inquiry-inspired approach. In this contribution, we outline the structure and set of methods that we have used to build a flexible and adaptive offering. We also briefly discuss the perspectives of the participants, the initial outcomes of the course, and some of the evolution the course has undergone. Although standardized, expository laboratories are common in most entry-level chemistry courses, such preset laboratories do not satisfy the need for the high-order cognitive training required in graduate-level research.² Many institutions currently offer guided-inquiry-based classes to their upper division students, and some institutions have begun to adopt such classes at the first-year level.³⁻⁷ However, the majority of existing classes have established project schemes that only skim the surface of a research experience. Consequently, students are rarely expected to independently develop a project beyond a set of historically accomplished tasks that clearly demonstrate curricular keystones.⁵ We actively utilize many of the positive aspects of inquiry^{8,9} by providing a controlled environment and controlled student body to facilitate students' transitions into graduate research. Students enter our class with a well-developed knowledge of chemical principles, allowing them to effectively formulate

complete hypotheses and solve chemical problems. It can be argued that students at the post-baccalaureate level are in the perfect phase of education for inquiry-inspired classes because they are not subject to the cognitive overload associated with having to learn new techniques while exploring. In addition, to maintain enthusiasm throughout the course without giving answers to students,¹⁰ the prestigious goal of journal publication is offered as motivation. In turn, the instructors are given a chance to improve their instructional skills and lead a research group. Hence, the class provides both the students and the instructors a constructive, inquiry-driven experience that is crucial to training the next generation of researchers and educators.⁸ Historically, guided inquiry has been the basis for the majority of graduate-level education, particularly in doctoral programs. Professors, as mentors and advisors, facilitate the research of beginning students, who in turn must actively inquire about common practices and develop methods to solve novel problems.¹¹ As graduate students progress through their respective programs, approaching doctoral or even postdoctoral levels, they must make another transition from being the agent of exploration to the manager of others' exploration. This transition often lacks guidance and formal training. In most cases, it is assumed that the graduate will quickly transition between the role of research assistant to industrial researcher or assistant professor on the basis of proven aptitude in research. Multiple recent studies have shown that graduates are more employable, successful in their respective programs, and ultimately capable of teaching when given mentorship and opportunity to teach.¹²⁻¹⁵ Peer-level instruction has been shown to be useful in the presentation of chemical laboratory information;⁷ therefore, a pairing of graduate students at disparate levels has the potential to be a successful mechanism for instruction and learning for all

participants. The class's instructors are Ph.D. candidates and postdoctoral researchers with strong interests in collegiate teaching. Instructors are selected from the Center for Sustainable Materials Chemistry (CSMC), a National Science Foundation Phase II Center for Chemical Innovation. Graduate students who are generally in their first year of study are offered the class as an extension of M.S. degree programs in semiconductor processing or polymer chemistry through the Master's Industrial Internship Program at the University of Oregon.¹⁶ These seemingly diverse programs, semiconductors and polymers, are both relevant to the field of inorganic solution processing of thin films, which is the primary focus of the CSMC.¹⁷⁻²² Students enter the class with a skill set that can leverage the opportunities provided by the instructors. The course is carried out in the Center for Advanced Materials Characterization in Oregon (CAMCOR), a shared-user facility. CAMCOR contains extensive state-of-the-art materials characterization equipment, which is made available for the students. Considering the construct, the class's primary research projects have been designed to address three major criteria. First, the class must conduct new, pertinent research. Incorporating research as a model for education is an excellent method for defining problems and developing methods for seeking solutions.²³ This method offers the challenges of learning how to approach research problems and offers "on-the-job" training for incoming graduate students with a grade and a potential journal publication as incentive. The process involves higher cognitive development and skills carrying real-world significance, which increases retention of acquired information. Second, the class is designed to address major criteria of graduate education in materials chemistry, including characterization and synthesis. Recent work by Ellis, Widstrand, and Nordell shows this method to be promising for

increasing both interest in and retention of subject matter presented in coursework.²⁴ Training to use necessary instrumentation for future research is incentivized scholastically and structured as a peer-based activity with review of performance and understanding. This method lessens the burden on other members of the graduate students' future research groups and offers the students an ability to report information taken from pertinent instrumentation with confidence, even as beginning researchers. Third, the class offers students a rare opportunity to learn how to produce a journal publication as a function of coursework. This approach allows students to have comprehensive exposure to the job activities of a graduate researcher: planning, researching, and writing for publication. Early exposure to professional responsibilities has been shown to be a successful educational method.²⁴ Though the third criterion is a lofty goal, we subscribe to the belief that setting high goals is a precursor to student success.

7.2. ROLE OF INSTRUCTORS

Instructors are tasked with establishing curricula, evaluation criteria, and budgets for the class. These tasks were chosen to acclimate the future collegiate educators to their coming duties. Attention to these factors has been shown to be important in graduate preparation for successful teaching and research,^{8,25,26} making this an opportunity for professional growth while enhancing employability. Students are expected to actively participate in research and laboratory activities. Faculty members within the CSMC make themselves available to provide mentoring for both instructors and students alike.

7.3. COURSE OBJECTIVES FOR STUDENTS

The course is designed to address six major objectives associated with the success of researchers at the graduate level: 1. Introducing the students to research-group dynamics

by imitating a research-group format. 2. Exposing the students to new chemistry and technologies through guided reading assignments. 3. Using inquiry to establish standardized, best-practice laboratory standard operating procedures in small groups. 4. Exposing students to experimenting in cutting-edge, shared-use facilities. 5. Using peer review in grading of presentations and formulation of manuscripts. 6. Writing a manuscript covering the research carried out in the class. We elaborate on each of these objectives in the following sections of the paper. We have successfully run a course at University of Oregon based on these criteria and objectives twice. The first iteration used early center chemistries to produce nanoscale capacitive devices with tuned dielectric constants; the second iteration of the class refined methods used to produce and evaluate group 13 metal hydroxide precursor materials for solution-processing nanoscale electronic devices. Both classes have produced manuscripts, with the first currently in publication²⁷ and the second currently submitted.

Introducing Students to Group-Research Dynamics Though research groups are an integral part of the graduate-level research experience, their unique functional aspects are rarely addressed in undergraduate laboratory courses. Traditional laboratory classes tend to pair students of equal experience for individual experiments that take little more than hours to complete. Graduate research often involves projects shared among collaborators with diverse backgrounds for weeks, months, and even years. Productive insights, project standardization, and success of projects are typically contingent on open communication among researchers. In this class, a “research group meeting” format is used for information exchange, which mirrors the prevalent form of communication in graduate study. Because the students come from diverse backgrounds, the approach brings

beneficial insights to the surface. For instance, the first iteration of the class generated values for the morphology of thin films by X-ray reflectometry (XRR) and atomic force microscopy (AFM) that did not agree. These data were opened to inquiry-based interpretation and the students were better able to understand that XRR probes both interfaces of a film, whereas AFM only investigates surface topography. By starting each class period with a group discussion, best practices are standardized via thoughtful discussion. Daily group meetings also allow students an opportunity to defend their ideas and collectively decide how to progress by evaluating which tasks should continue and which to abandon in order to achieve the class goals. In this way, inquiry is promoted and students learn to lead when they have insights toward solutions. At the same time, the emphasis on direct experimentation emulates a true research format.

Introducing Students to New Chemistry and Technology through Guided Reading Assignments The class has no formal text just as true research has no formal text. Samples of pertinent literature are provided to the students as a basis for initiating a project, as lead references for an ongoing literature search, and for writing an introduction to their paper. Quizzes based upon the assigned literature are administered to ensure that the students stay up to date on required class reading and to encourage students to actively discuss the contents of what they have read. Finally, literature review offers a clear visual of what publication-quality figures are and how to use data to bolster a story. Further literature searching on the state-of-the-art is encouraged to hone the students' understanding of the context of the class's experiments. Using Inquiry To Establish Standardized, Best-Practice Laboratory Standard Operating Procedures in Small Groups With some literature background, students formulate hypotheses,

procedures, and practices to complete the class project. There are many instances in which standardization has been necessary for group success, including but not limited to solution formulations, synthetic procedures, dilution and titration mechanisms, material separations, and characterization techniques. The group is allowed to decide how to use a limited budget to plan instrument usage and ultimately provide pertinent figures for their paper. Emulating standard research practice, the course instructors are encouraged to offer guidance about budgets and time management if the students are not advancing as necessary. Using group discussion generates a streamlined equipment scheduling and training regimen. When given the task of deciding how much time to spend on individual and group training for facilities, the students quickly go about defining roles for themselves and taking on the associated responsibilities. Use of instrumentation is facilitated by students readily asking each other about previous training from their prerequisite polymer or semiconductor coursework and then organizing accordingly. Small group work allows for concurrent scheduling via guidance of the inquiry into training and scheduling of experiments in the shared-user facility. Exposing Students to Experimenting in Cutting-Edge, Shared-Use Facilities The CAMCOR facility has a variety of advanced materials characterization equipment.²⁸ Students have access to all equipment in CAMCOR with the only limit being the budget. Upon completion of required training, access is provided to instrument calendars, allowing students to directly schedule time for their measurements. During group meetings, the class carries out budgetary analysis to determine whether it is more cost beneficial for the class to train in a technique or simply have a trained technician do the evaluation. For instance, because of the low number of samples evaluated using AFM, students opted to have technicians

provide those measurements, but the students trained to do spectroscopic precursor evaluation owing to the high volume of spectroscopic data required for the project. As part of the standard curriculum, each student in the class is required to formulate a presentation about one of the characterization techniques available in CAMCOR. The presentations include the fundamentals of the measurement, best practices in sample preparation, and the applicability to the overall project.

Grades for the presentations are assessed on the basis of responses to peer review. Utilizing Peer Review in Grading and Formulation of Manuscripts Unlike most conventional courses, this class features a significant amount of peer review. In a well-functioning research group, there is extensive discourse and review. Properly managed discourse among graduate students can provide for a highly productive research environment. As research centers and educational institutions, we strive to produce skilled skeptics who are capable of defending good ideas with logic and evaluating the scientific merits of others' ideas critically and fairly. As previously mentioned, each student in the class gives a presentation about a characterization technique that is peer reviewed. Instructors also offer grades for the presentations. Criteria for grading include the following: (i) Were the principles of the measurement clearly defined? (ii) Did the presenter clearly demonstrate the applicability of the technique to the project? (iii) Would you be likely to commission this person to have these tests done on your samples? Students are encouraged to ask questions until they feel comfortable that the grading criteria are addressed. Reviews are given anonymously. In the history of the course, only one student out of fifteen opted out of the review exercise by assigning full credit to the rest of the class despite performance. The student was later questioned about the behavior

and viewed the practice of reviewing peers as being outside of the responsibilities of a student. Aside from this single student, the peer-review method rendered evaluations of presentations surprisingly similar to those assessed by the instructors (within one standard deviation). Because of the small sample sizes, it had been expected that interpersonal feelings would influence grading among students; however, we have found that not to be the case in our two iterations thus far. Finally, participation grades for the entire course are assessed via peer review. A sample assessment rubric can be found in the Supplemental Information in the Appendix. Each member of the class assigns numerically scaled grades to all other members of the class according to five basic criteria listed below:

1. Did the individual provide regular and pertinent input during group discussions?
2. Did the individual listen and consider the ideas of others during decision making?
3. Did the individual exhibit professionalism and respect for his or her colleagues?
4. Did the individual contribute significantly to the overall success of the group?
5. Would you seek out this individual for future collaboration?

We believe that these questions are important reflections of research performance. The most interesting anecdotal findings from this exercise are that the peer reviews consistently reflected distaste and disdain for minimally participating students. In contrast, students who worked toward their abilities, though varied, had positive reviews. Even the aforementioned student who assigned full credit to all other students on the presentation reviews docked points from the idle student in that cohort on reliability-related criteria. One of the major challenges presented to the instructors is the task of mentoring students so that they see why participation is critical not only in this class but

also in their education and their future careers. It was observed that students tended to express a great deal of generosity toward their peers upon assessment, with strengths being addressed in greater numbers than weaknesses. In the second iteration of the course, the list was appended to include a prompt for students to indicate the importance of their peers to the overall project. This change was made to generate a better, more democratic method of determining authorship for the final class paper but was not used in overall grading of the students. The necessity of this sixth prompt will be discussed later. Writing a manuscript about the research carried out in the class from the beginning, the students in each class are motivated to write a manuscript covering the findings of the class. To accomplish this grand goal, students are encouraged to set up online document sharing and bibliography management. In the first iteration of the class, active writing and review were undertaken immediately by all but one member of the class. The manuscript was written, reviewed, and iteratively edited by the majority of the class and then submitted to the instructors. Instructors were then tasked with reviewing the article and providing feedback to the students. Following minor grammatical and graphical modification, the article was submitted to the journal *Solid State Sciences* and subsequently accepted for publication.²⁷ The second iteration of the class had more stringent individual writing requirements, with each student being assigned sections of the paper to write for the instructors' review. Writing began immediately after the midterm examination was completed.

7.4. GRADUATE INSTRUCTOR REFLECTIONS

From teaching this class, we (the instructors) learned a great deal about research group management. Leading the group through the entirety of a research project provided

a great deal of insight into team management and teaching through doing. We also learned a great deal about conflict management, as each iteration had at least one set of incompatible student personalities and relatively stressful situations to manage and overcome. Our involvement in conflict resolution, and our assistance in moving the project along, endeared us to the students. In the months since the class, it has become clear to us that we are now regarded as trusted peers and mentors by many of the participants who still seek us out to discuss data and experiments unrelated to the class. We have found that the experience of leading this class reflects positively upon us in applications for academic positions. The initial postdoctoral instructor is currently working as an assistant professor at a primarily undergraduate institution. The initial senior graduate student enjoyed the experience so much that he returned as a postdoctoral scholar to lead a new group by teaching the class for a second iteration. After teaching the second iteration, he secured a position as an instructor at a large state school. The last postdoctoral instructor involved in the course is actively applying to academic positions and using the class as an example of his teaching and leadership abilities. Overall, this has been a quite beneficial experience that has helped us develop our teaching philosophies and instructional abilities. Upon reflection, we are all more likely to use inquiry in future instruction because of our favorable experience with intensive inquiry-based exercises and our observations of the positive value of the exercises.

7.5. FORMER STUDENT REFLECTIONS

A statement from one of the former students offers a student perspective on the experience: During the summer of 2010, I was one of six students who participated in the first iteration of the class. Although I had little familiarity with the class format, I felt that

it was an opportunity to learn about graduate-level research and journal publication. Initially, I struggled to keep up with the frantic pace of class, project management, group organization, and the intensive research involved. After expressing my concerns to my instructors, they helped me realize that the cause of the class's struggles stemmed from a lack of leadership. As a result, I volunteered to take on the responsibility of leadership by becoming a project manager. By doing so, I began to excel, receive accolades from the instructors and my peers for my efforts. In the end, our hard work and diligence translated into a published journal article [see ref 27] despite the early struggles. Current Instructor Reflection This statement from a current course instructor provides an instructor's perspective on the experience: Due to my experience, I was granted the opportunity to be one of the instructors in the second iteration. As an aspiring professor, I took advantage of the opportunity to develop instructional skill that will be useful in my future career. Due to previously being a student in the class, the students were quite open and responsive to my suggestions. As the course progressed, the students began to take ownership of the project as I had taken ownership of my own, which was very rewarding to witness. For me, knowing that my guidance was having a positive impact on these students was the greatest form of satisfaction during the course. I learned a great deal from the challenges that developed during the class, particularly how to improve student–student and student– instructor interactions. Overall, my experiences as a student and an instructor in this class have allowed to me to grow academically and professionally in ways I would not have envisioned prior to this experience.

7.6. EVALUATION AND EVOLUTION

The effectiveness of the course was metered through final publication as well as in-class assessments. Assessments, such as weekly quizzes, were used to keep students up to date on the literature. Although quizzes were used as a prompt for student action and as study guides for students to prepare for examinations, midterm examinations were used to determine whether students understood the experiments and the reasoning behind the research in which they were actively involved. Midterm examinations were generated to achieve the goals of evaluating student understanding. These exams required students to generate process flows and answer intricate questions pertinent to interpreting data for their respective project. The first cohort of six students did extremely well on the processing midterm exam, with mean scores of 96% and a standard deviation of 5%. The second iteration of the class, with nine students and two midterms, had a broader-reaching project, and that fact was reflected by the lower class averages on the processing midterm ($86 \pm 7\%$). The lower average grades for the processing midterms in the second cohort likely are due to the greater experimental specificity of the individual students in that iteration of the class. For example, one group of students concentrated on Raman spectroscopy and another concentrated on synthesis. This led to comprehensive exams reflecting a strong understanding of the specific topic and a weaker understanding of broad application. It should be noted that with such small sample sizes and the requirement for project-specific exams, these data are correlational at best. Because writing a research paper for a scholarly journal is a backbone of the course, assigning authorship fairly is of utmost importance. In the first iteration of the class, order of authorship was determined solely by alphabetical order. This method was problematic because it did not reflect the amount of work each student put into the project. That is to

say, minimally participating students received higher billing than key experimenters and writers. The system was abandoned because it was unfair, nondemocratic, and arguably not representative of common authorship practices. During the class's second iteration, a great deal of importance was put into rectification of the issues involving authorship. Although both iterations had significant use of peer review in the grading of the class, the second iteration used the peer-review process to generate a democratic basis for order of authorship. In the peer-review section, students were asked to rank their co-workers' importance based upon the prompt: "This individual contributed significantly to the overall success of the group." The rankings provided by the class allowed authorship to be assigned both fairly and democratically. We suggest using a similar method for those pursuing a similar course at their institution. Issues also emerged with the writing assessment in the first iteration of the course. The paper was primarily generated by two of the students who took leadership roles. It was difficult to do a writing assessment on the other four class participants because of the level of editing that was going on between the students within the class. In the second iteration, the group meeting was used as an opportunity for the students to split the paper into sections and assign the sections to individuals. This simplified the writing assessment for instructors and also provided the students with tangible measurements of their peers for utilization in review. Student course evaluations indicated that a majority of the class felt that the guided-inquiry experience was appropriate for their level of education. Many also indicated that the course provided their first opportunity to generate published research results. Some students equated the class to an internship-type experience for research. Anecdotal class reviews showed that students recognized the utility and philosophy of the research in

both the assessment and their own reviews of the class. Generally, negative reviews were registered about time constraints, interactions with other students, and the lack of standardization. As a group, students reported having a fruitful exercise in discovery that developed skills that helped them have successful internships as researchers and engineers in companies. Two students who entered the Ph.D. program at the University of Oregon have described a smooth transition to the research environment, taking knowledge and skills from the class to advance their research projects.

7.7. CONCLUSIONS

This paper outlines an inquiry-based graduate course in which both instructors and students gain experience by carrying out some the roles of professors and graduate students, respectively. The instructors of the class gained valuable experience teaching at the graduate level and managing a small research group with a designated goal of their own design. Instructors also gained experience in the practical matters of generating curriculum, quizzes, tests, readings, and grades. The instructors have validated their abilities to teach and conduct cutting-edge research with a small, diverse group of students; these experiences have supported academic applications and subsequent employment. We are continuing to track the progress of the careers of both the participating students and the instructors via social networking web sites as part of a longitudinal study of the impact of the class on career choices and career trajectories. To date, the success of this inquiry-inspired class has been directly related to the abilities, subject expertise, and motivation of the students and instructors. As evidenced previously, the class has been a useful introduction to the realities of graduate scholarship for post-baccalaureate students. It is also an excellent introduction to the academic

instructional setting for circa- doctoral students who rarely have the opportunity to lead their own classes. We believe that similar programs can and should be implemented in other areas of chemistry at the graduate level. The underlying challenges that the course addresses, as well as the implemented methods, have the potential to considerably enhance graduate education. By using active apprenticeship models and learning-through-doing exercises, students and instructors are simultaneously able to learn valuable lessons about research, group dynamics, and leadership that will carry through to their chosen careers.

7.8. CHAPTER VIII BRIDGE

The next subsequent chapters diverges from the group 13 polycations and focuses on characterizing transition metal-based clusters in the solid-state and solution. Chapter VIII introduces several techniques and experiments used to further understand the chemical properties of a hafnium sulfate cluster and how these properties affect thin film formation and nanopatterning.

CHAPTER VIII

MECHANISMS DIRECTING THE NANOSCALE

PATTERNING OF THIN FILMS OF HAFNIUM CLUSTERS

8.1. INTRODUCTION

This chapter stems from large collective project effort from multiple research groups and therefore the following individuals must be acknowledged: Feixiang Luo, Rose E. Ruther, Richard P. Oleksak, Jennie M. Amador, Shawn R. Decker, Joshua R. Motley, Darren W. Johnson, Gregory S. Herman, Eric L. Garfunkel, and Douglas A. Keszler. My contribution to this research consisted of designing and performing a three-month DLS study on monitor the stability of the tetrameric hafnium cluster in solution as well as being a co-author and editor for the manuscript that is being submitted for publication to *Langmuir*.

Polyoxometalates and related metal oxide clusters offer an especially promising approach to very high resolution lithography. The small cluster size effectively decreases the minimum pixel size of the pattern compared to approaches based on nanoparticles or even polymers. Under acidic conditions, hafnium forms very small clusters (radius ≤ 1 nm). By controlling the assembly of clusters into thin films and introducing radiation sensitive ligands, very high resolution patterns can be written with UV photons or electron beams. Here we elaborate on the mechanisms which control the thermal and radiation chemistry of these materials and ultimately the sensitivity and resolution which can be obtained. Raman and X-ray photoelectron spectroscopies are used to follow the

coordination of sulfate and peroxide ligands in films as a function of thermal processing and radiation exposure. Results from the spectroscopic studies are correlated with direct measurements of film solubility and resist sensitivity. Small changes in the solution chemistry of the film precursors yield significant differences in the patterning properties of the final films. The ability to control condensation chemistry is critical to further developing cluster based materials which can be directly patterned at the nanoscale.

The ability to pattern materials at ever smaller length scales has driven advances in electronics, photonics, plasmonics, micro/nano-electromechanical systems, and sensor technologies. However, further refinements in photon and electron beam resists are necessary to continue decreasing feature sizes that can be achieved with lithographic patterning. Chemically amplified resists have become the standard in industry since they were first introduced by IBM in the 1980's. While these resists have excellent sensitivity, acid diffusion and statistical dose fluctuations contribute to line edge roughness (LER) and limit resolution in these materials.¹ Very high resolution has been achieved with non-chemically amplified resists such as a poly(methyl-methacrylate) (PMMA)^{2,3} and hydrogen silsesquioxane (HSQ),^{4,5} but conversely these materials require large exposure doses. As pattern dimensions continue to shrink, the molecular structure of the resist itself becomes increasingly important. Large LER in polymeric resists has been attributed to the formation of polymer aggregates with sizes on the order of tens of nanometers.⁶⁻⁸ Low LER in resists of calixarene⁹, molecular glasses¹⁰, HSQ¹¹, and nanoparticles¹² have been attributed to the small size and uniformity of the fundamental units which make up these materials.

Polyoxometalates (POMs) and similar metal oxide clusters offer a very promising approach to nanoscale patterning. Clusters may be highly mono-disperse with sizes below what is typically achieved with polymeric or nanoparticle systems. Many metal oxides have relatively high absorbance for EUV (13.5 nm) lithography.¹³ Additionally, inorganic materials offer very high etch resistance which enables thinner films and prevents pattern collapse of high aspect ratio features.¹² In addition, thinner films also reduce proximity effects and enable higher resolution.⁴ Recently, we showed that metal oxide sulfates (MSO_x) demonstrate very high resolution, moderately high sensitivity, and exceptionally low LER.¹⁴⁻¹⁶ The resist chemistry is based on the controlled condensation of metal oxide clusters which are deposited from aqueous solutions using simple techniques such as spin-coating.

In this contribution, we elaborate on the thermal and radiation chemistry of the hafnium based system. Under acidic conditions in the absence of strongly complexing anions, hafnium forms tetranuclear clusters with formula [Hf₄(OH)₈(H₂O)₁₆]⁸⁺ as shown in Figure 8.1a.^{17, 18} Both sulfate and peroxide are known to coordinate strongly to hafnium (IV).¹⁹ Near atomically smooth, amorphous films can be deposited from hafnium sulfate solutions (HafSO_x),²⁰ while the addition of radiation-sensitive peroxide ligands yields a film that can be directly patterned using UV light or electron beams.¹⁴⁻¹⁶ By monitoring the chemical changes that occur in the film as a function of annealing temperature and radiation exposure, a more mechanistic understanding of the role these coordinating ligands play in determining film properties emerges. The sensitivity and resolution of the resist is strongly dependent on the composition of the films precursors. The results presented here are an important step towards understanding and controlling

condensation chemistry in resists formed from metal oxide clusters and will help to advance the development of all classes of inorganic resists.

8.2. EXPERIMENTAL

8.2.1. Solution Precursor Preparation. A hafnium stock solution was prepared from $\text{HfOCl}_2 \cdot 8\text{H}_2\text{O}$ (98+%, Alfa Aesar) and 18.2 M Ω purified water at approximately 1 M concentration. The exact concentration was determined gravimetrically by conversion of a known volume of solution to solid hafnium oxide. 1 M H_2SO_4 (BDH Chemicals) and 30 wt% H_2O_2 (Macron) were used as received. All HafSO_x solutions were prepared by mixing HfOCl_2 , H_2O_2 , and H_2SO_4 solutions and diluting with 18.2 M Ω purified water to the appropriate concentration. The sulfate to hafnium molar ratio varied from 0.1 to 2. The H_2O_2 to hafnium molar ratio varied from 0 to 7. The molarity of the precursor solution is given with respect to hafnium.

8.2.2. Film Deposition. For experiments using quartz crystal microbalance (QCM), thin HafSO_x films were deposited on QCM crystals with SiO_x coating designed for liquid applications (Inficon). Prior to deposition the QCM crystals were cleaned with a UV/ozone treatment to generate a hydrophilic surface. For Raman spectroscopy, films were deposited on sapphire or aluminum substrates (80 nm Al/200 nm thermal SiO_2/Si). For all other experiments films were deposited on silicon < 100 > substrates with native oxide. Prior to deposition the silicon substrates were rinsed with deionized water, acetone, and isopropanol and treated with an oxygen plasma etch for 5 – 10 minutes. All films were deposited via spin coating at 3000 rpm for 30 s followed by a thermal anneal on a hotplate at temperatures from 70 – 300 °C.

8.2.3. *Dynamic Light Scattering (DLS)*. DLS data for a 150 mM HafSO_x solution were taken using the Mobius from Wyatt technologies. The samples were filtered using a 0.1 µm PTFE syringe tip to remove any particulate matter that may be present in solution. The sample was kept refrigerated at 5 °C and aliquots were taken periodically for size analysis over the course of several months. The hydrodynamic radius (R_h) and polydispersity were determined using Dynamics software where the data was averaged over 20 measurements with 5 second integration time per acquisition.

8.2.4. *Microscopy*. Transmission electron microscopy (TEM) imaging was performed using an FEI Titan 80-200 TEM operating at 200 kV. For cluster images, a surface functionalized TEM grid (NanoPlus, Dune Sciences) was placed face down on a drop of 150 mM HafSO_x solution. The grid was then placed face down on deionized water to rinse off excess material. TEM cross sections were prepared via the focused ion beam lift out method on a Quanta 3D Dual Beam scanning electron microscope and imaged using an FEI Titan 80-200 TEM operating at 200 kV. Atomic force microscopy (AFM) images were acquired with a Bruker Innova AFM in intermittent contact (tapping) mode using silicon probes with a resonance frequency of 300 kHz and a force constant of 40 N/m (Budget Sensors). To correct for sample tilt and scanner bow, images were leveled by polynomial background subtraction. Scanning electron microscopy (SEM) imaging was performed on an FEI Nova NanoSEM 230 operating at 5 kV.

8.2.5. *Raman Spectroscopy*. Solution Raman spectra (500-3000 cm⁻¹) were collected on a Thermo Scientific DXR SmartRaman spectrometer with a 780 nm laser source. Thin film Raman spectra were collected using a Horiba LabRAM 800 equipped with a 532 nm

laser source, 300 lines/mm grating, and a 100x objective. The energy scale was calibrated using a SiO₂ standard.

8.2.6. Quartz Crystal Microbalance (QCM). QCM measurements of film etch rate were measured with an RQCM (research quartz crystal microbalance) and PLO-10i (phase lock oscillator) system from Inficon. QCM crystals were placed in a crystal holder designed for contact with liquids. Crystals were immersed in tetramethylammonium hydroxide solutions (electronic grade, Alfa Aesar) and the change in resonance frequency was monitored with a frequency counter (Keithley) and recorded using custom software.

8.2.7. X-ray Photoelectron Spectroscopy (XPS). XPS spectra were acquired with a Thermo Scientific K-alpha X-ray photoelectron spectrometer with an Al K-alpha (1486 eV) micro-focused monochromatic X-ray source and ultra-low energy electron flood gun. A pass energy of 50 eV was used for high-resolution element specific XPS spectra and a pass energy of 200 eV was used for lower resolution survey spectra. All spectra were analyzed with the Advantage software package from Thermo Scientific. Peak widths were constrained to the same value for deconvolution of oxygen 1s spectra. Peak positions were constrained to within a narrow window of values. The binding-energy scale was calibrated with the adventitious carbon 1s peak at 284.8 eV.

8.2.8. Peroxide analysis. The peroxide content of the thin films was measured using standard permanganate titrations and compared to the hafnium content measured by inductively coupled plasma optical emission spectrometry (ICP-OES). Samples were prepared by stripping films from silicon wafers with 1 M sulfuric acid. A portion of the sample was titrated with KMnO₄ for peroxide analysis and the remainder was diluted with 1% nitric acid for ICP analysis. The hafnium concentration was determined using a

Teledyne Leeman Prodigy ICP-OES in axial mode at spectral lines of 277.33 and 239.33. Standards were made by diluting a 1000 ppm hafnium standard (Inorganic Ventures) with 1% nitric acid.

8.3. RESULTS AND DISCUSSION

First, we establish that the HafSO_x precursor (Figure 8.1a) solutions consist of discrete nano-sized clusters. Upon first inspection, DLS results (Figure 8.1b) reveals that clusters have a hydrodynamic radius of approximately 1 nm. Over the course of several months no appreciable change in size is observed, suggesting that the combination of lower temperatures and the addition of peroxide provide for better long term storage. The size was also measured directly with TEM. Clusters with a radius of ~ 1 nm are resolved in Figure 8.1c. The size measured by TEM is slightly larger than by DLS, likely due to small amounts of aggregation that occur when the samples are dried on the TEM grid. The size from DLS is also larger than would be expected for the hafnium tetramer.²¹ The addition of sulfate and peroxide ligands results in more highly polymerized species consistent with prior work on zirconium sulfate solutions.^{22,23} The cross-sectional TEM image of a HafSO_x film (Figure 8.1d) reveals nearly atomic-level smoothness of the film, which can be attributed to the small size of the clusters in the precursor solution. Surface roughness is directly correlated with sidewall roughness in fully developed patterns.^{7,8,11} The exceptional smoothness of HafSO_x films results in very low LER.^{14,15}

The coordination of sulfate and peroxide ligands to the clusters was studied using Raman spectroscopy. Figure 8.2 a shows the Raman spectra of the precursor solution, as well as sulfuric acid and hydrogen peroxide for comparison. The $\nu_1(\text{O-O})$ vibration in free (uncoordinated) peroxide appears at 876 cm^{-1} as seen in the spectrum of aqueous

hydrogen peroxide. The coordination of peroxide to the hafnium clusters results in a new stretch at 834 cm^{-1} consistent with what has been observed previously for hafnium peroxo complexes.²⁴⁻²⁶ Typically a large excess of peroxide is added to the precursor solutions to stabilize the small hafnium clusters and prevent further polymerization. Peroxide acts a capping ligand which prevents olation and condensation similar to acetylacetonate or carboxylate ligands commonly used in sol gel chemistry.²⁷ While a significant amount of free peroxide is typically present in the solutions, only bound peroxide is present in the final films (Figure 8.2 a). Similarly, the coordination of sulfate to the hafnium clusters can be followed in the Raman spectra. Free sulfate (SO_4^{2-}) and bisulfate (HSO_4^-) appear at 982 and 1050 cm^{-1} respectively²⁸ as seen in the spectrum of aqueous sulfuric acid (Figure 8.2a). At least two new vibrational modes appear for sulfate coordinated to hafnium, with peaks at 967 and 1004 cm^{-1} . Similar spectra have been reported for other sulfate complexes.^{29,30} Both free and bound sulfate are present in the precursor solution, but films contain primarily bound sulfate.

As a radiation sensitive ligand, peroxide plays an important role in the patterning chemistry (vide infra). The number of peroxide ligands that can bind to each cluster is an important factor that influences the sensitivity of the final resist. We therefore sought to characterize the relative amount of bound peroxide in the precursor solutions and resulting films. Figure 8.2b shows Raman spectra of HfOCl_2 solutions with increasing amounts of hydrogen peroxide. For low peroxide concentrations, all of the peroxide coordinates to the cluster and only the stretch at 834 cm^{-1} is observed. With increasing amounts of peroxide, the free peroxide stretch at 876 cm^{-1} appears and grows in intensity, while the intensity of the bound peroxide stretch saturates. The free peroxide stretch first

appears when the peroxide to hafnium molar ratio reaches 0.5, indicating that approximately 2 peroxide ligands can coordinate to each hafnium tetrameric unit. This is consistent with prior investigations which propose that two peroxide groups replace four hydroxyl groups in the tetramer to form $[\text{Hf}_4(\text{O}_2)_2(\text{OH})_4(\text{H}_2\text{O})_{16}]^{8+}$.³¹ The peroxide to hafnium ratio was also measured in films. As deposited, the films are soluble and can be rinsed from the substrates for analysis using standard wet chemical techniques. The peroxide to hafnium molar ratio was determined to be 0.67 ± 0.09 from permanganate titration and ICP-OES analysis. Both the solution and thin film analysis indicate that the number of peroxide ligands that are able to bind to each hafnium cluster is relatively small with less than one peroxide group per hafnium ion.

Figure 8.2c shows Raman spectra of thin films annealed at increasingly high temperatures for three minutes. The peroxide group is remarkably thermally stable and shows only a 20% loss in intensity in the Raman spectrum when annealed to 125 °C. Figure 8.2d shows Raman spectra for a film soft-baked at 80 °C that has been exposed to an electron beam dose of 800 $\mu\text{C}/\text{cm}^2$. The peroxide group is completely decomposed by electron beam exposure. Thus, the peroxide group exhibits relatively high thermal stability, but is easily decomposed by other forms of radiation. This selectivity is an important factor in its selection as a contrast mechanism in inorganic resists.

The decomposition of peroxide groups was explored further using XPS. Figure 8.3a shows a typical O 1s spectrum obtained after a relatively long x-ray exposure (> 30 mins). The O 1s peak can be resolved into two components. The higher binding energy (BE) O 1s peak at 532.0 eV (peak A) is assigned to oxygen in hydroxyl and sulfate groups.³²⁻³⁶ The lower BE O 1s peak at 530.2 eV (peak B) can be attributed to oxygen in

the Hf-O-Hf network similar to hafnium oxides.³⁴⁻³⁷ Figure 8.3b shows the evolution of the O 1s spectrum with increasing number of scans and exposure to X-rays. The rise in the lower BE peak is consistent with the growth of the oxide network with continued exposure to radiation. Figure 8.3 c plots the atomic percent of peak B out of the total oxygen (peak A + peak B), which provides a quantitative method to monitor the dynamic formation of the Hf-O-Hf network. In the unexposed films, peroxide groups prevent condensation and very little of peak B can be resolved. Radiation-induced decomposition of peroxide groups leads to oxide network formation which saturates around 30 scans.

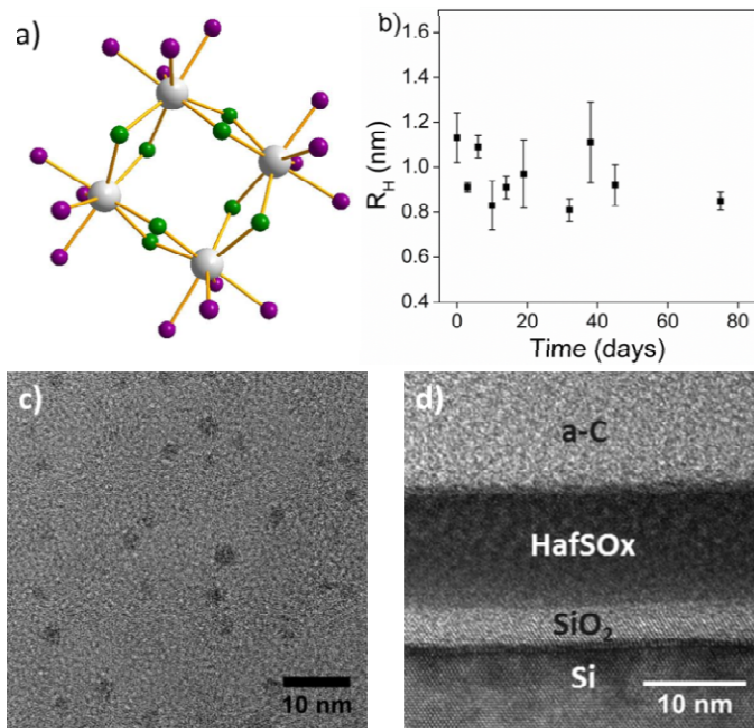


Figure 8.1. (a) Structure of hafnium tetramer. White: hafnium; Green: hydroxyl oxygen; Purple: oxygen in bound water. (b) DLS size analysis for a 150 mM HafSO_x solution as a function of solution age. (c) TEM image of hafnium sulfate clusters. (d) Cross-sectional TEM image of a spin-coated HafSO_x film on a Si/SiO₂ substrate with amorphous carbon protecting layer.

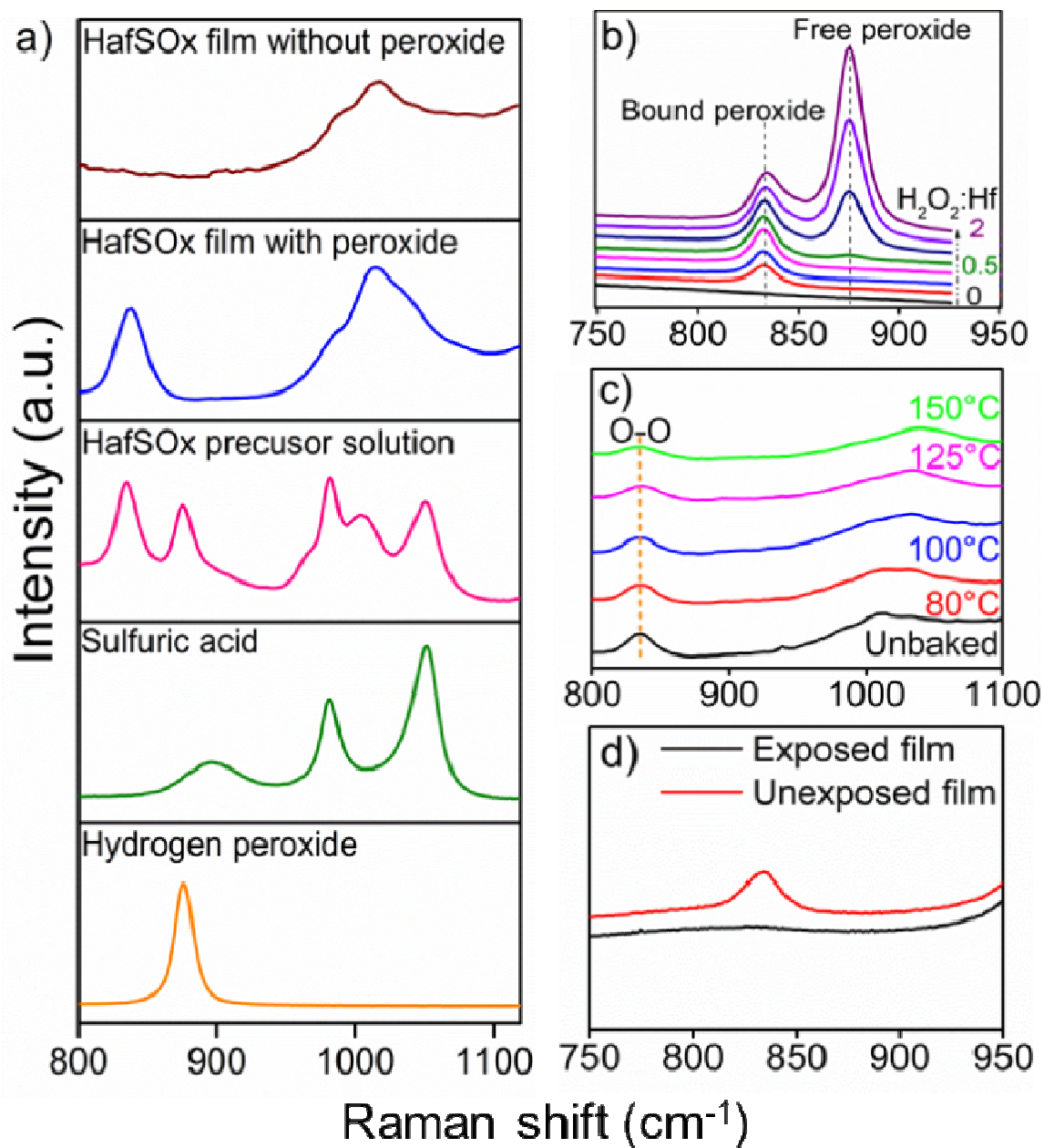


Figure 8.2. Raman spectra of (a) hydrogen peroxide, sulfuric acid, the HafSO_x precursor solution, and HafSO_x films made with and without peroxide. (b) HfOCl₂ solutions with increasing concentrations of hydrogen peroxide. (c) HafSO_x films annealed at increasingly high temperatures. (d) a HafSO_x film before and after exposure to electron beam radiation.

Film condensation was also followed in XPS for films spun from solutions with different amounts of peroxide (Figure 8.3c). HafSO_x films made without H₂O₂ show significant oxide network formation initially and no increase is observed with increasing

scans. Films made with different amounts of peroxide in the precursor solution show very similar behavior with respect to condensation. This is consistent with results from Raman spectroscopy and wet chemical analysis which indicate that the amount of peroxide in the films saturates at less than one peroxide group per hafnium ion. Increasing the amount of peroxide in the solutions above a molar ratio of 0.5 does not cause further changes in the radiation chemistry of the films. Together, the XPS results provide further evidence that oxide network formation is driven by the decomposition of peroxide groups.

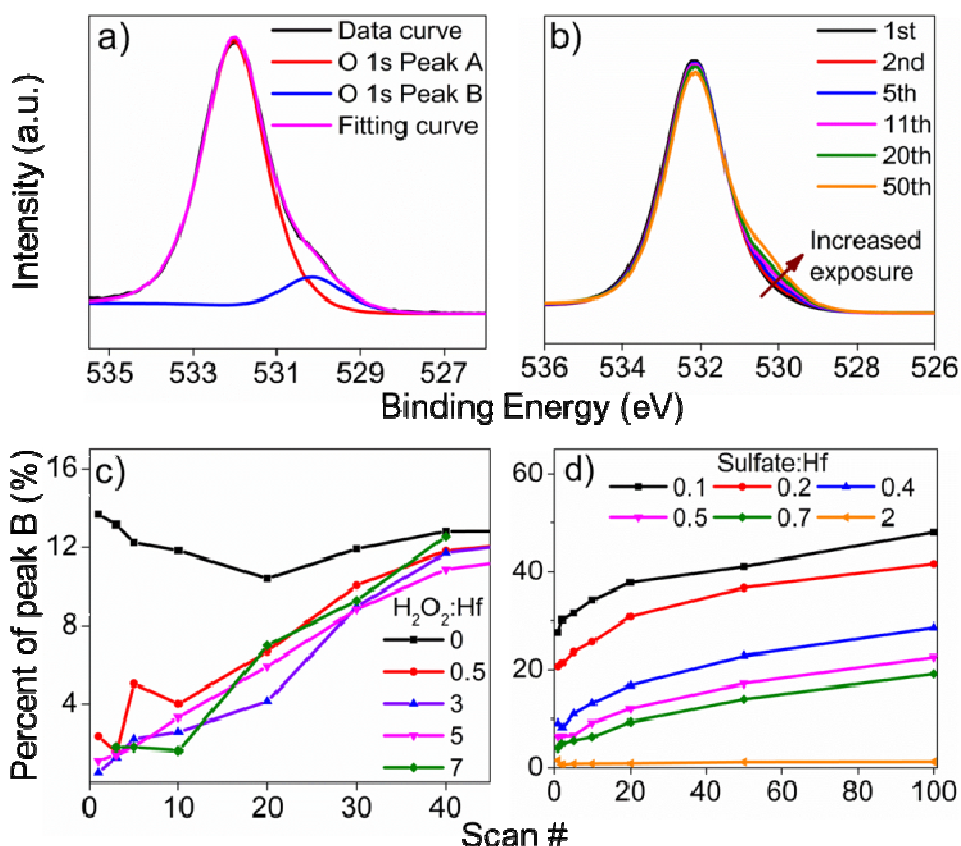


Figure 8.3. (a) XPS O1s spectra of a HafSO_x film collected after a long X-ray exposure time (> 30 mins). (b) XPS O1s peak evolution with increasing number of scans. (c) Quantitative comparison of O 1s peak evolution for HafSO_x films with increasing amounts of peroxide. (d) Quantitative comparison of O 1s peak evolution for HafSO_x films with increasing amounts of sulfate.

Film condensation is also controlled by the concentration of sulfate groups. The amount of sulfate in the films is easily changed by varying the relative amount of sulfuric acid in the precursor solutions. Figure 8.3d plots the atomic percent of peak B out of the total oxygen for films made with different amounts of sulfate. Films with fewer sulfates have a higher percentage of oxygen coordinated as oxide initially. All films with the sulfate to hafnium ratio < 2 show increasing oxide formation with longer X-ray exposure. The curves also follow the same slope, which confirms that similar amounts of peroxide are present in the films to drive further condensation. When the hafnium to sulfate ratio is equal to 2, no measurable oxide is present. Since the stoichiometry of the film is close to $\text{Hf}(\text{SO}_4)_2$, no additional oxide or hydroxide ligands are needed for charge balance.

The condensation reactions that occur upon exposure to radiation result in a decrease in solubility of the exposed regions. To further understand how changes in processing conditions influence film solubility, film dissolution was monitored using QCM. Films were deposited on QCM crystals, and the change in mass was monitored as the films were dissolved in tetramethylammonium hydroxide (TMAH) solutions.^{38, 39} Figure 8.4 a shows results for the dissolution of films made with and without peroxide. The films made with peroxide are significantly more soluble as seen by the much larger loss in mass. These results provide even further evidence that peroxide acts as a capping ligand, preventing oligation and oxide network formation. Annealing temperature is another important factor that changes solubility. Figure 8.4 b show that films quickly transition from soluble to insoluble with only a 20 °C increase in the soft bake temperature. The minimal amount of energy required to significantly change the solubility of HfSO_x explains the high sensitivity of this material relative to other non-chemically amplified

resists.¹⁴⁻¹⁶ Figures 8.4c and 8.4d present data for films made with different amounts of sulfate. Films with more sulfate etch more quickly while films with too little sulfate are largely insoluble. This is consistent with the XPS results and the solubility trends of hafnium sulfate salts. Neutral hafnium sulfates (salts without hydroxyl groups with a sulfate to hafnium ratio of 2) such as $\text{Hf}(\text{SO}_4)_2 \cdot n\text{H}_2\text{O}$ are highly soluble whereas the basic salts (salts with hydroxyl groups with a sulfate to hafnium ratio less than 2) such as $\text{Hf}(\text{OH})_2\text{SO}_4 \cdot n\text{H}_2\text{O}$ tend to be less soluble. Comparing figures 8.4c with 8.4d indicates that films are also more soluble in more concentrated TMAH developer.

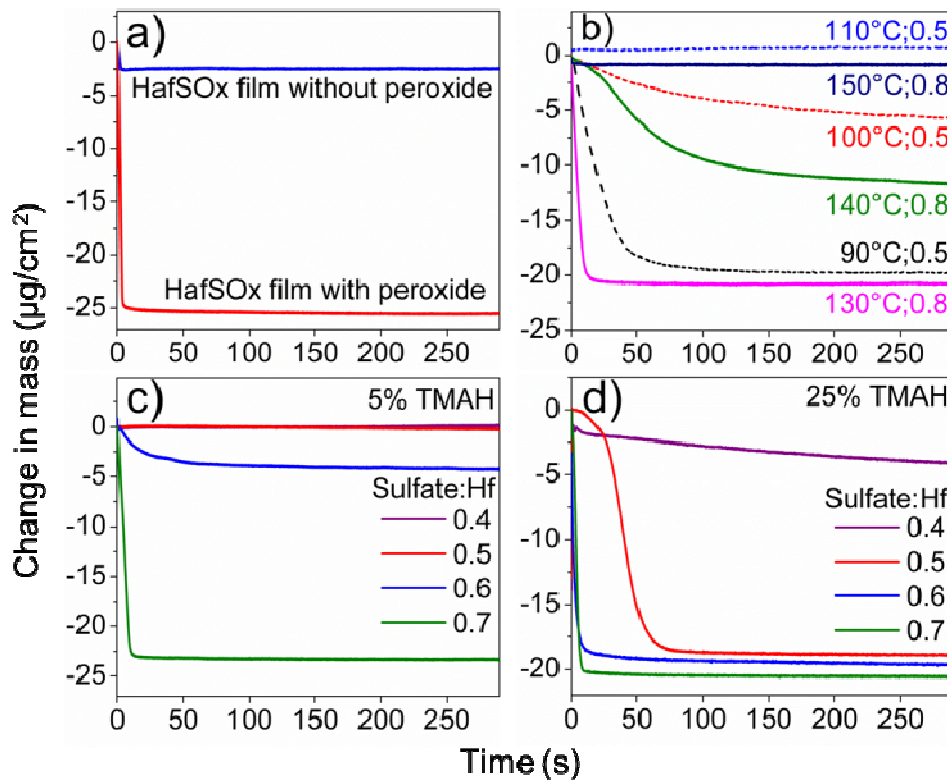


Figure 8.4. QCM measurements of the dissolution of (a) HafSOx films with and without peroxide developed in 5% TMAH. (b) HafSOx films with sulfate: Hf ratio of 0.5 and 0.8 annealed at increasing temperatures and developed in 25% TMAH. (c) HafSOx films with increasing sulfate: Hf ratio developed in 5% TMAH. (d) HafSOx films with increasing sulfate: Hf ratio developed in 25% TMAH.

The results from the XPS and QCM studies indicate that the solubility of HafSO_x films is controlled by a number of variables including the addition of peroxide, amount of sulfate, annealing temperature, and concentration of the TMAH developer. Important resist properties such as resolution and sensitivity can also be optimized by controlling these same variables. Figures 8.5a and 8.5b show SEM images of arrays that were patterned into a HafSO_x film using electron beam lithography. The squares are patterned using an electron beam dose which increases from 100 to 1500 $\mu\text{C}/\text{cm}^2$ in increments of 40 μC . Similar arrays were imaged by AFM to produce the contrast curve shown in Figure 8.5c. For low doses, the films remain soluble. The dose at which the films become insoluble (resist sensitivity) is easily tuned by changing the amount of sulfate in the resist. The film with less sulfate (Figure 8.5a) is more sensitive than the film with more sulfate (Figure 8.5b) but this increase in sensitivity comes at the expense of resolution.

Table 8.1 summarizes the XPS analysis of HafSO_x films made with different amounts of sulfate and presents an approximate film stoichiometry. The stoichiometry is derived from the XPS composition and the requirement for overall charge balance. 0.5 peroxide groups are assigned to each hafnium in agreement with the results of Raman spectroscopy. Film condensation is governed by two competing mechanisms. Condensation can occur thermally through the hydroxyl groups or it can proceed via a radiation stimulated pathway through the decomposition of peroxide groups. While the number of peroxide groups is fixed, the amount of sulfate can be adjusted over a wide range. Increasing the amount of sulfate in the films reduces the number of oxide and hydroxide groups which drive condensation. Changing the amount of sulfate in the films is, therefore, one means to control film solubility and resist sensitivity. Similarly,

resolution and other resist properties can be optimized through careful control of the coordination of the different ligands (peroxide, sulfate, oxide, and hydroxide). One limitation of the HafSO_x system is the relatively small number of peroxide groups that can coordinate to hafnium. This likely limits the sensitivity which can be achieved with this material. Metal ions which can coordinate to multiple peroxide ligands such as chromium, molybdenum, or tungsten may be of interest for increasing the sensitivity of this family of inorganic resists.

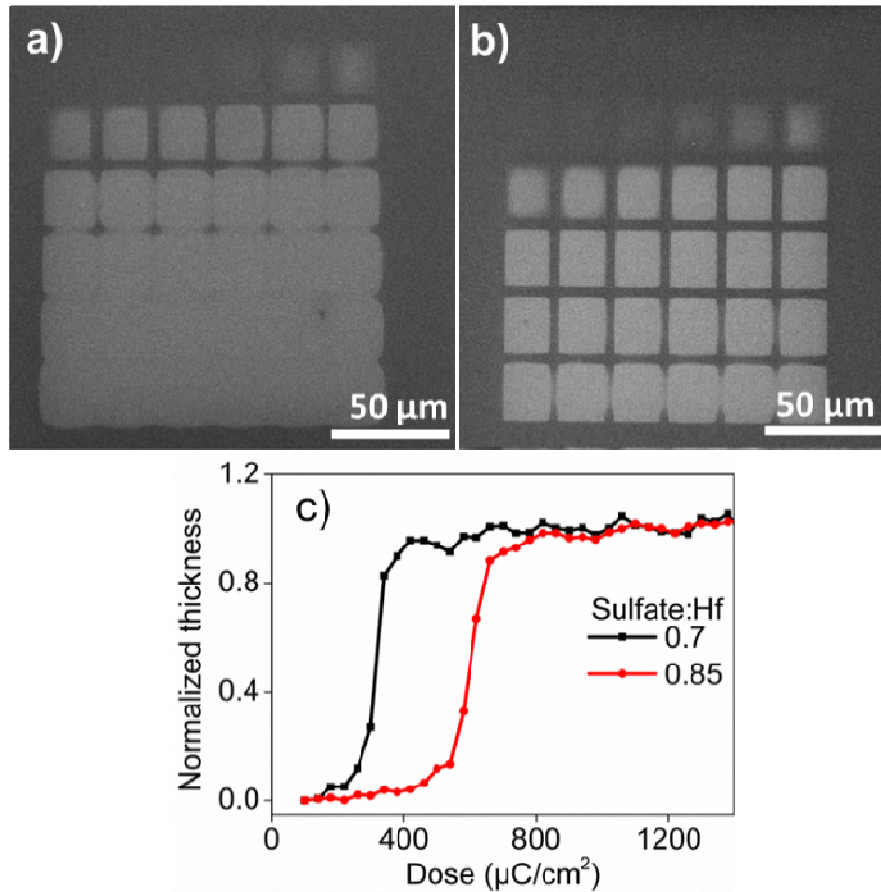


Figure 8.5. (a-b) SEM images of contrast arrays generated by patterning films at increasing electron beam exposure doses. The HafSO_x films have sulfate: Hf ratios of (a) 0.7 (b) 0.85. (c) Contrast curve generated from AFM images of contrast arrays similar to those shown in (a-b).

Table 8.1. Normalized atomic percent of Hf, O, S for HafSO_x films with increasing SO₄²⁻:Hf molar ratios from XPS analysis. An approximate film stoichiometry derived from the XPS composition is also shown.

Sulfate: Hf ratio in precursor solution	Hf (at.%)	O (at.%)	S (at.%)	approximate stoichiometry
0.10	23	74	3	Hf(O ₂) _{0.5} (SO ₄) _{0.14} (OH) _{0.56} O _{1.04}
0.20	20	75	5	Hf(O ₂) _{0.5} (SO ₄) _{0.25} (OH) _{0.90} O _{0.89}
0.40	17	74	9	Hf(O ₂) _{0.5} (SO ₄) _{0.51} (OH) _{0.64} O _{0.67}
0.50	16	73	11	Hf(O ₂) _{0.5} (SO ₄) _{0.65} (OH) _{0.20} O _{0.75}
0.70	14	73	13	Hf(O ₂) _{0.5} (SO ₄) _{0.86} (OH) _{0.14} O _{0.57}

8.4. CONCLUSIONS

Peroxo hafnium sulfate clusters offer a promising approach to nanoscale patterning because the small cluster size enables high resolution and low line edge roughness. Peroxide groups are effective capping ligands which limit condensation in the films and increase solubility prior to exposure. Peroxide ligands are decomposed by photon and electron radiation, resulting in controlled condensation in exposed regions and formation of an insoluble hafnium oxide network. The resolution and sensitivity of the HafSO_x system are easily tuned by changes in the sulfate content of the films, annealing temperature, and concentration of the basic developer.

8.5. CHAPTER IX BRIDGE

Chapter IX continues on the trend of investigating transition metal-based clusters. In particular, we have synthesized and characterized of a unique class of rhomb-centered copper tetranuclear subunits.

CHAPTER IX

SYNTHESIS AND STRUCTURAL DETERMINATION OF 1-D CHAIN COORDINATION POLYMER COMPOSED OF $\{M(\mu\text{-OH})_2M\}$ RHOMB-CENTERED TETRANUCLEAR COPPER SUBUNITS GRADUATE STUDENTS IN

9.1. INTRODUCTION

Dr. Lev N. Zakharov performed single-crystal XRD while I performed Raman spectroscopy and subsequently wrote that portion of this work. Maisha synthesized of the Copper (II) sulfate cluster and served as the main author of the manuscript from which this chapter is derived. This work as a result was submitted to *Acta Cryst C*.

The reaction between copper (II) sulfate pentahydrate, nickel (II) sulfate, and pyridine in DMF yields green crystals of $\{(C_5H_6N)_2[Cu_4(OH)_2(SO_4)_4(H_2O)_4]\}_n$ at room temperature. This anionic 1-D chain structure contains two different Cu centers and is composed of the repeating tetrameric copper clusters. The octahedral CuO_6 metal ions form a $\{M-(\mu_2\text{-OH})_2\text{-}M\}$ rhombus core that is linked to trigonal bipyramidal CuO_5 metal ions through bridging sulfate groups. Rather than direct copper coordination by free-base pyridine ligands, the negative charge of the tetrameric structure is balanced by pyridinium counter-cations arranged in a π - π stacking motif that also hydrogen bonds to the chains of cluster anions. This is a new example of an inorganic transition metal 1-D polymer containing rhombus building blocks.

Simple copper salts have garnered interest for a variety of applications including the use of copper (II) sulfate pentahydrate as an herbicide and copper (II) arsenate as a wood preservative. More complex structures that incorporate copper into molecules containing multi-dentate oxygen and nitrogen-donating ligands have been developed and studied for a variety of applications such as molecular magnetism and gas adsorption.¹⁻⁴ Notable studies of polynuclear copper structures have focused on compounds that function as catalysts and mimics for biological processes.⁵⁻⁷ An interesting feature of a number of these species is the rhomb, or “diamond core” structure that is proposed to play a role in many metalloenzymatic processes. Several discrete high valent oxo compounds (composed of Ni^{III}, Co^{III}, and Cu^{III} metal ions) have been reported in the literature that contain a {M-(μ -O)₂-M} rhomb core.⁸⁻¹¹ However, these complexes typically experience thermal instability at room temperature. The metal-oxo rhomb core is also found in transition metal coordination polymers with greater thermal stability, but the discrete {M-(μ -OH)₂-M} core is rarely observed.^{12,13}

The preparation and crystal structure of $\{(C_5H_6N)_2[Cu_4(OH)_2(SO_4)_4(H_2O)_4]\}_n$, a new inorganic coordination cluster linked together in the crystalline state through hydrogen bonds, is reported herein. This anionic species is composed of tetranuclear divalent Cu metal ion subunits that each contain a {M-(μ -OH)₂-M} rhomboid core. The subunits are connected in a 1-D array through hydrogen bonds between the pyridinium counteranions and the sulfato ligands. Surprisingly, in the presence of an excess of pyridine, the tetramer prefers to hydrogen-bond with the pyridinium ion as opposed to coordinate to pyridine, a typical interaction seen with related structures crystallized from other organic

solvents.¹³ This structure also represents a new contribution to the small but growing class of all-inorganic Cu-based cluster compounds.

9.2. EXPERIMENTAL

9.2.1. Materials and methods. All chemicals were used as received from commercial sources. Pyridine and dimethylformamide (DMF) were purchased from Mallinckrodt. Copper (II) sulfate was obtained from our reuse facility and manufactured by Mallinckrodt. Methanol (MeOH) was used as received from Macron chemicals. The synthesis of $\{(C_5H_6N)_2[Cu_4(OH)_2(SO_4)_4(H_2O)_4]\}_n$ was inspired by a previously reported procedure of a series of unrelated Pb clusters.⁷

9.2.2. Synthesis of $\{(C_5H_6N)_2[Cu_4(OH)_2(SO_4)_4(H_2O)_4]\}_n$. A 0.05 M solution of pyridine in MeOH (1 mL) was layered onto a solution of 0.05 M CuSO₄ and 0.05 M Ni(NO₃)₂ (50:50 v/v, 1 mL total, both in DMF) in a test tube. Ethyl acetate (EtOAc) was added to the solution using vapor diffusion and after several weeks light green crystals formed (9% isolated yield).

9.2.3. Crystal Structure determination. Single-crystal x-ray diffraction was performed on a Bruker Smart Apex diffractometer 173 K (2) using Mo K α radiation ($\lambda = 0.71073$ Å). Adsorption corrections were applied by SADABS. The structure was solved by direct methods completed by subsequent difference Fourier syntheses, and refined by full-matrix least-squares procedures on F². Highly disordered solvent molecules in the crystal structure were treated by SQUEEZE. Correction of X-ray data by SQUEEZE is 353 electrons/shell. All non-hydrogen atoms were refined with anisotropic thermal parameters. All calculations were performed by the Bruker SHEXTL package. Full

crystallographic details are available in the Supplemental Information in the Appendix. Selected bond lengths and angles are summarized in Table 1.

9.2.4. Raman Spectroscopic Analysis. Raman spectra of the single crystal of $\{(C_5H_6N)_2[Cu_4(OH)_2(SO_4)_4(H_2O)_4]\}_n$ were collected using an Alpha 300S SNOM confocal Raman microscope in a 180° backscattering configuration. A continuous wave pump laser provided ~ 60 mW of power with an excitation wavelength of 532 nm. A 0.3 m spectrometer equipped with 600 grooves/mm grating was used to detect Raman scattering with a spectral resolution of 2.5 cm^{-1} . The spectra from the copper cluster were averaged over 500 accumulations at 0.75 s exposure time per scan. The intense Si signature at 520.5 cm^{-1} was used as an internal reference.

9.3. RESULTS AND DISCUSSION

$\{(C_5H_6N)_2[Cu_4(OH)_2(SO_4)_4(H_2O)_4]\}_n$ is comprised of two distinct Cu centers. The distorted octahedral copper (II) ions (Cu1, Figure 9.1) are bridged by two μ_3 -OH groups to form a $\{Cu(\mu\text{-OH})_2\text{-Cu}\}$ rhomb core. The core is connected to the trigonal bipyramidal copper (II) ions (Cu2) by four μ_3 -sulfato ligands; water fills the remaining coordination sites of each CuO_6 site. Each sulfato ligand bridges three Cu ions creating two $Cu_3(\mu_3\text{-OH})$ edge-shared tetrahedra.

The inversion center about the central $Cu_2(OH)_2$ rhomb establishes a symmetry that leads to two dimeric units bridged by the rhomb core. The chemical formula of this structure is closely related to that of the natrochalite-type mineral $[NaCu_2(SO_4)_2(OH)\cdot H_2O]$ although natrochalite only has octahedral Cu ions and no $\{M(\mu\text{-OH})_2\text{-M}\}$ bridging sites.

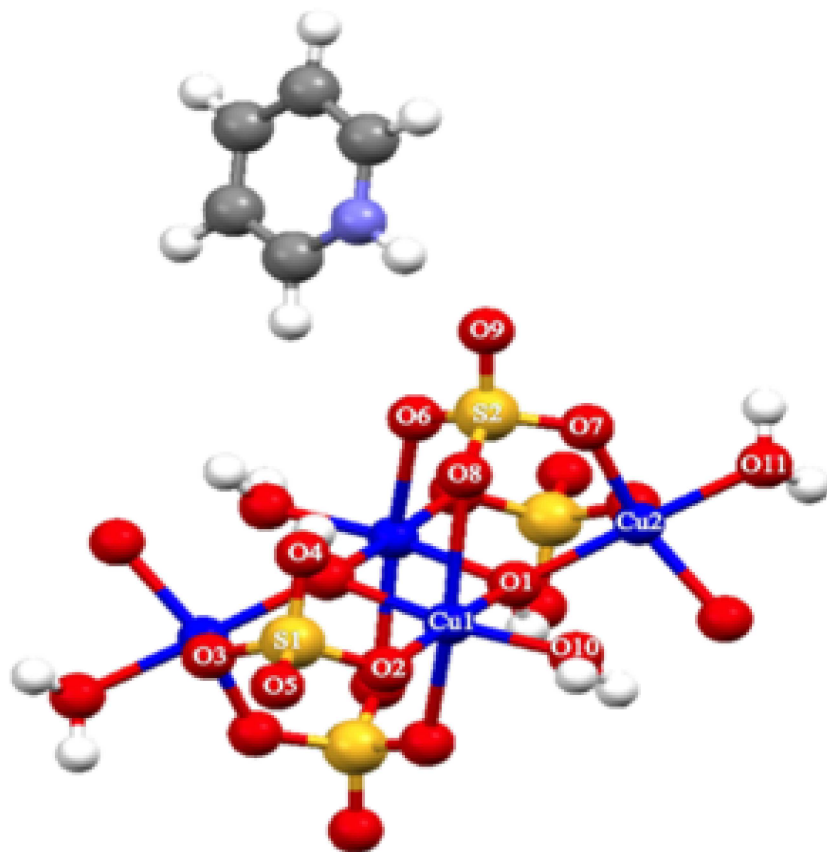


Figure 9.1. Ball and stick representation of the $\{(C_5H_6N)_2[Cu_4(OH)_2(SO_4)_4(H_2O)_4]\}_n$ tetramer. The pyridinium cation hydrogen bonds to the μ_3 -sulfato ligand and water ligand of two adjacent Cu_4 subunits. The oxygen and sulfur atoms neighboring Cu1 and Cu2 are labeled (hydrogen labels omitted for clarity).

$\{(C_5H_6N)_2[Cu_4(OH)_2(SO_4)_4(H_2O)_4]\}_n$ (Figure 9.2) is linked to form an anionic chain that propagates along the a-axis in similar manner to $\{(C_5H_7N_2)[Cu_2(OH)(SO_4)(H_2O)]\}_n$ that was recently reported by Lah and coworkers.¹⁴ The polymer forms an extended 1-D network charge balanced by pyridinium ions held within the structure by hydrogen bonding to the Cu chains. The subunits are coordinated to one another through the μ_3 -sulfato ligands coordinated to the copper centers. The cations are arranged in a slight offset; however, they feature significant π - π stacking and are arranged with the ring plane parallel to the [1,0,0] direction.

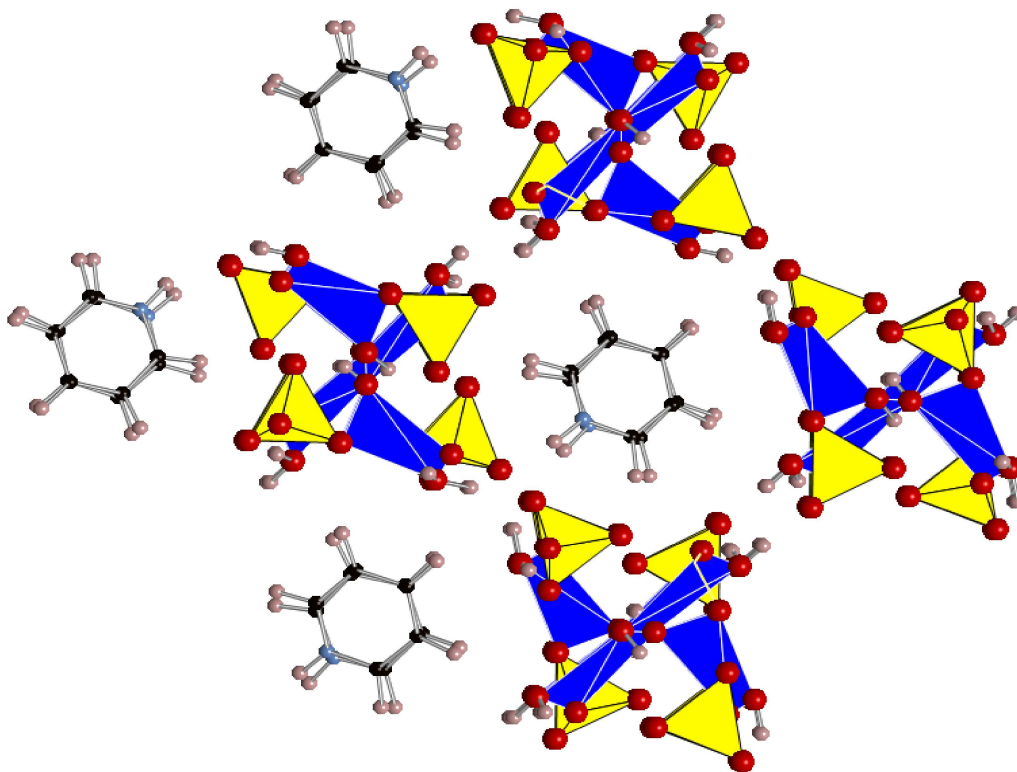


Figure 9.2. Polyhedral representation of $\{[(C_5H_6N)_2[Cu_4(OH)_2(SO_4)_4(H_2O)_4]]_n\}$ along the a axis. The Cu subunits hydrogen-bond to pyridinium cations that π - π stack to form a 1-D chain. Copper metal ions are blue, sulfur atoms are yellow, and oxygen atoms are red.

The role of $Ni(NO_3)_2$ in the reaction is not clear; however in its absence the resulting product is the previously published $\{[H_2N(CH_3)_2][Cu_2(OH)(SO_4)_2(H_2O)_2]\}_n$ coordination polymer.¹⁵ In that structure dimethylammonium cations form hydrogen bonds within the polymer network, linking the dimeric chains into 2-D sheets. The variations observed between these two extended structures are proposed to be due to the presence of dimethylamine, a product of DMF hydrolysis. In addition, several related Cu polynuclear compounds with similar structural features to $\{[(C_5H_6N)_2[Cu_4(OH)_2(SO_4)_4(H_2O)_4]]_n\}$ have been reported in the literature that contain organic ligands such as tetrazole, pyridine, and other N-donating ligands directly coordinated to the Cu cluster core.^{16–19} The all-inorganic Cu tetramer reported herein is a new structure type in that regard, and given the

interest in purely inorganic clusters as precursors for metal oxide and related functional films, this cluster type provides a new addition to the field.²¹⁻²⁰ The bond lengths and angles of the $\{M-(\mu-OH)_2-M\}$ motif for $\{(C_5H_6N)_2[Cu_4(OH)_2(SO_4)_4(H_2O)_4]\}_n$ fall within the range observed for other complexes featuring the $\{M-(\mu-O)_2-M\}$ rhomb core (Figures 9.3 and 9.4).²¹

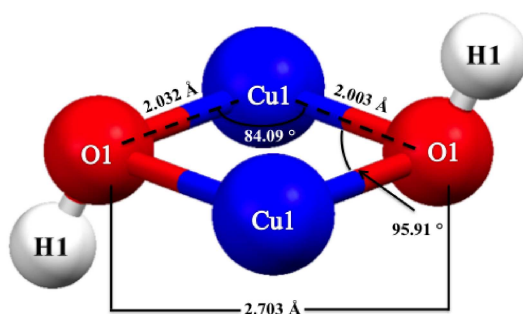


Figure 9.3. Selected bond lengths and angles for the rhomboid $\{M-(\mu-OH)_2-M\}$ core of $\{(C_5H_6N)_2[Cu_4(OH)_2(SO_4)_4(H_2O)_4]\}_n$. For clarity, atoms are not shown to scale.

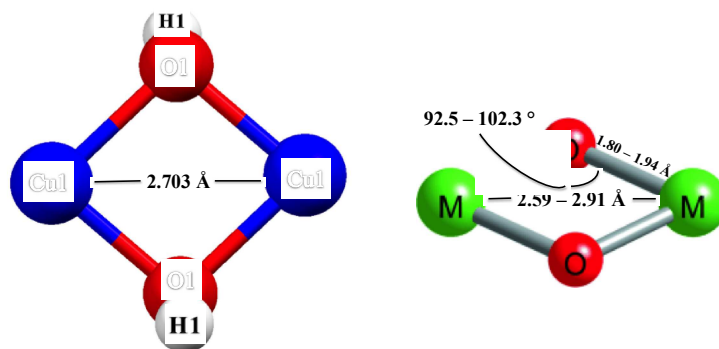


Figure 9.4. Bond lengths and angles for $\{(C_5H_6N)_2[Cu_4(OH)_2(SO_4)_4(H_2O)_4]\}_n$ (left) and ranges observed for the rhomboid core in related $M(\mu-O)_2$ sites (right). Image on the right from Que, et. al.²⁵ Atoms are not shown to scale.

Raman spectroscopy provides additional information about the coordination and bonding environment of the Cu cluster. A spectral comparison between liquid pyridine, cupric sulfate, and single crystalline $\{(C_5H_6N)_2[Cu_4(OH)_2(SO_4)_4(H_2O)_4]\}_n$ is shown in

Figure 9.5. An expanded inset of the copper cluster Raman spectrum (Figure 9.5c) reveals several weak modes between 2800 cm^{-1} - 3700 cm^{-1} , most notably the weak, narrow O-H stretching vibration of the bridging metal center $\{\text{M}-(\mu\text{-OH})_2\text{-M}\}$ at 3572 cm^{-1} . In addition, the intense C-H symmetric stretching band at 3052 cm^{-1} for pyridine (Figure 9.5b) is not present in the copper cluster spectrum, signifying an overall lowering in C_{2v} symmetry of pyridine due to its interaction with the copper cluster. This loss of symmetry is further suggested by the disappearance of the ring bending modes at 978 cm^{-1} and 1022 cm^{-1} , respectively (Figure 9.5a).²⁶

The doubly degenerate sulfato symmetry stretching modes of cupric sulfate at 1016 cm^{-1} and 1045 cm^{-1} are not present in the copper cluster. This symmetric stretching mode of sulfate is observed as a sharp intense peak at 979 cm^{-1} , a very common feature among many similar copper-based minerals with sulfate as a counterion.^{26,27} Several weak features are present from 100 cm^{-1} - 600 cm^{-1} which can be ascribed to various Cu-O and sulfato bending and anti-symmetric stretching modes. Three weaker modes also appear at 832 cm^{-1} , 866 cm^{-1} , and 883 cm^{-1} in the copper cluster that can be assigned to the $\{\text{M}-(\mu\text{-OH})_2\text{-M}\}$ anti-symmetric stretching vibrations.

9.4. CONCLUSIONS

$\{(\text{C}_5\text{H}_6\text{N})_2[\text{Cu}_4(\text{OH})_2(\text{SO}_4)_4(\text{H}_2\text{O})_4]\}_n$ has been synthesized and characterized using single crystal X-ray diffraction and Raman spectroscopy. The $\{\text{Cu}-(\mu\text{-OH})_2\text{-Cu}\}$ rhomboid core of each tetramer is coordinated to an adjacent tetramer to form 1-D networks linked to planar pyridinium countercations arranged in π - π stacking motifs and hydrogen bonded to the sulfato ligands of the tetramers. The unique anionic nature and rhomboid features of this structure add a new compound to a small class of all inorganic copper structures.

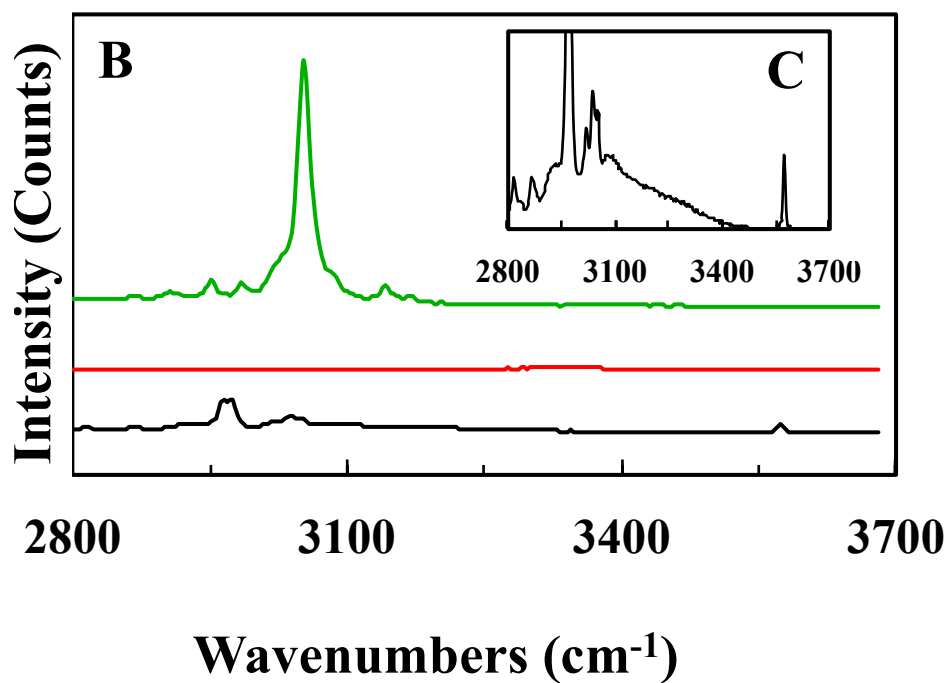
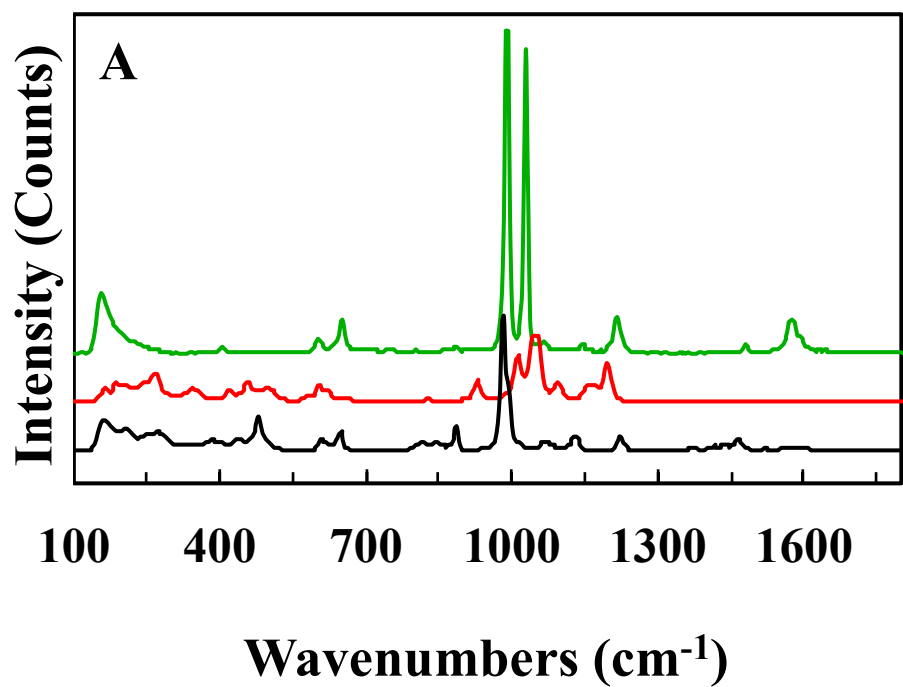


Figure 9.5. Stacked Raman spectra of pyridine (green), cupric sulfate (red), and $\{(C_5H_6N)_2[Cu_4(OH)_2(SO_4)_4(H_2O)_4]\}_n$ (black). A) $100\text{ cm}^{-1} - 1700\text{ cm}^{-1}$ B) $2800\text{ cm}^{-1} - 3700\text{ cm}^{-1}$. C) Inset of the copper cluster from 2800 cm^{-1} to 3700 cm^{-1} .

9.5. CHAPTER X BRIDGE

The last chapter provides my brief concluding remarks about my thesis work on a whole.

CHAPTER IX

CLOSING REMARKS

Within the confines of my dissertation work, I was able to make significant contributions towards establishing an overall better understanding of the basic chemistry associated with many classes of aqueous inorganic clusters. With regards to their solution dynamics and speciation, utilizing many of the aforementioned techniques ascribed throughout my thesis has allowed for several advanced studies, many of which have been published, journal recognition/awards, and a model framework for future investigations. Although many challenges still remain towards aqueous inorganic cluster characterization, what this work reveals is that there what we are now far better equipped to solve such advanced problems that were previous inaccessible prior to me enrolling into the program. With that being said, there are still many innovative techniques and methods yet to be designed that will be eventually be used to delved even further than what I was able to do so in my short time here. As such, I greatly look forward to reading what the next great scientific breakthroughs that many of my colleagues will discover in the future.

APPENDIX

SUPPLEMENTAL INFORMATION

Chapter II Supplemental Information

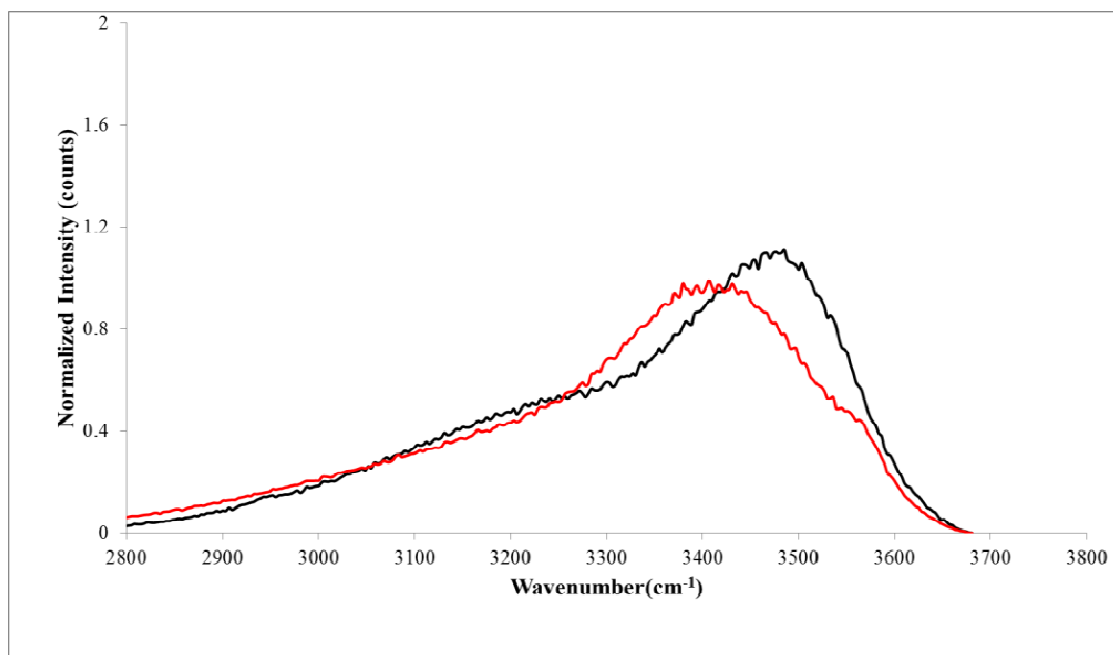


Figure S1. From 2600-3800 cm^{-1} displays the different types of waters associated with each of the cluster. Red = Ga_{13} ; Black = Al_{13}

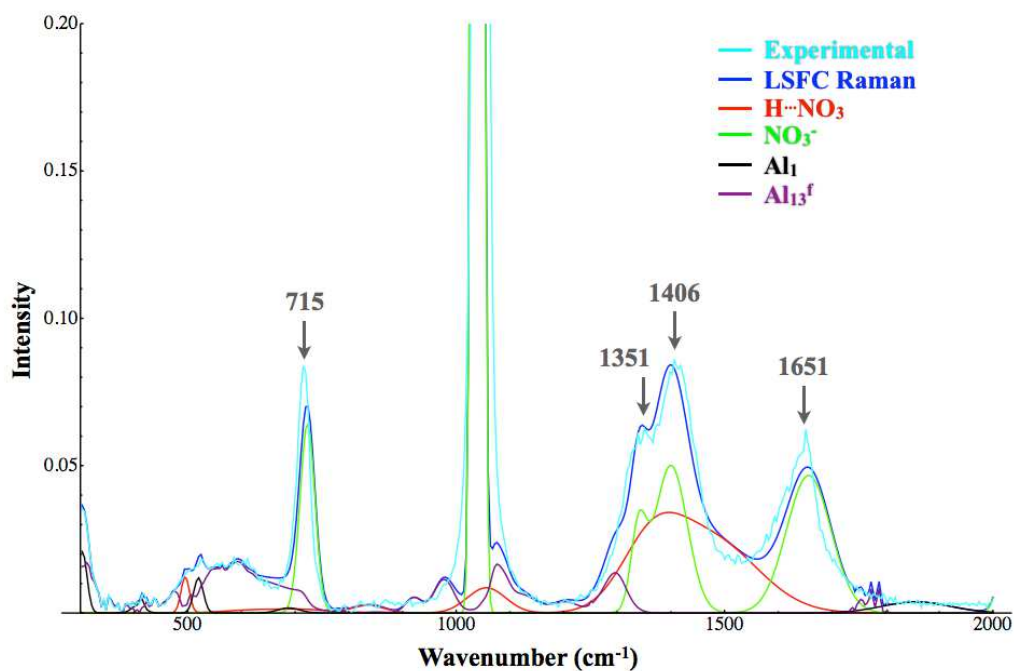


Figure S2. Solution phase Raman of the flat Al_{13} cluster. Top: LSFC Raman spectrum computed using the aluminum monomer (Al_1). This LSFC spectrum has an RMSD of 0.64 %. Bottom: LSFC Raman spectrum computed using Al_1 and the aluminum tridecamer (Al_{13}^f). This LSFC spectrum has an RMSD of 0.48 %.

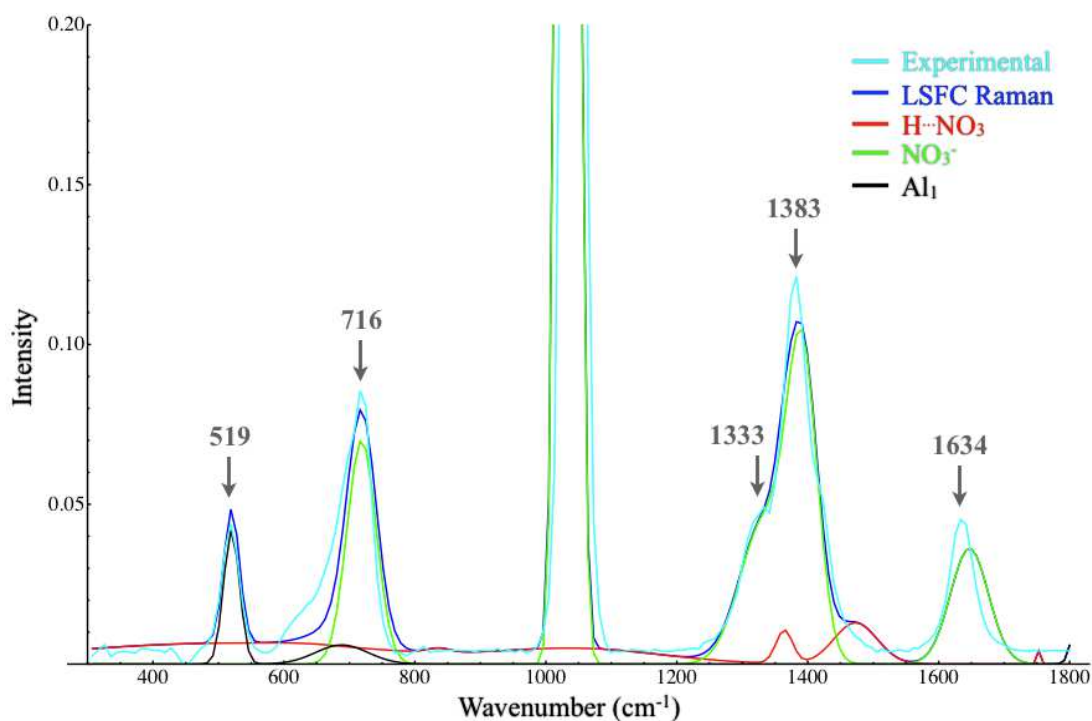


Figure S3. Solid State Raman spectrum of aluminum nitrate hydrate salt. LSFC Raman spectrum was computed using aluminum monomer (Al_1) and nitrate vibrational modes, and was used to determine the computed frequency scaling factor for the monomer. The LSFC Raman spectrum has an RMSD of 0.574 %.

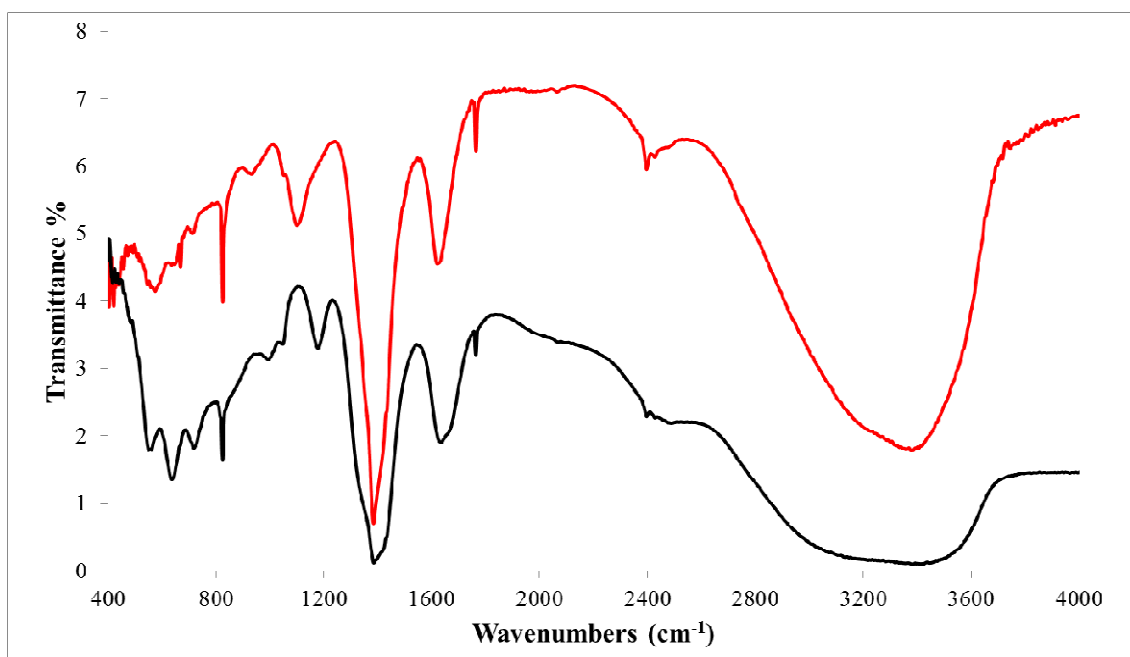


Figure S4. IR overlay of Al₁₃ (black) and Ga₁₃ (red) clusters

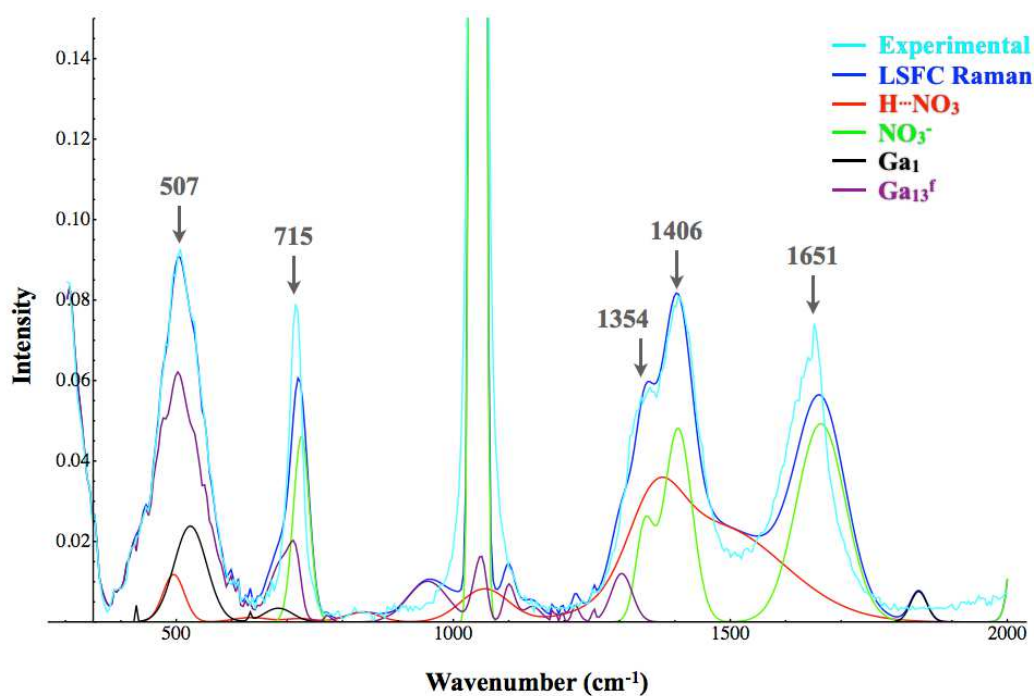
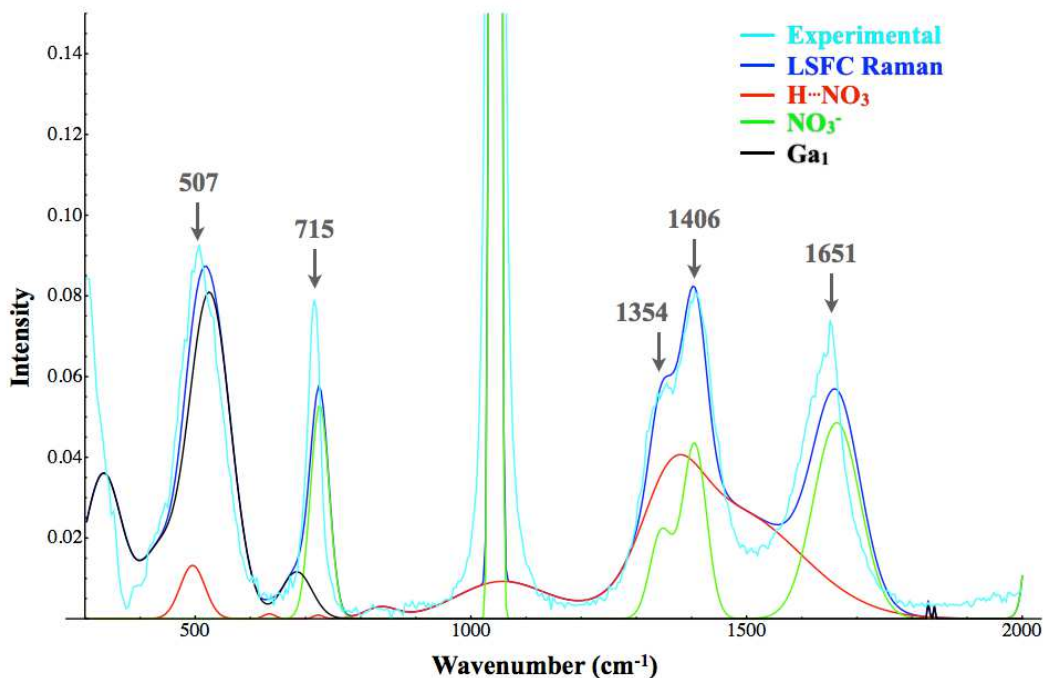


Figure S5. Solution phase Raman of the flat Ga_{13} cluster. Top: LSFC Raman spectrum computed using the gallium monomer (Al_1). This LSFC spectrum has an RMSD of 0.92 %. Bottom: LSFC Raman spectrum computed using Ga_1 and the gallium tridecamer (Ga_{13}^f). This LSFC spectrum has an RMSD of 0.48 %.

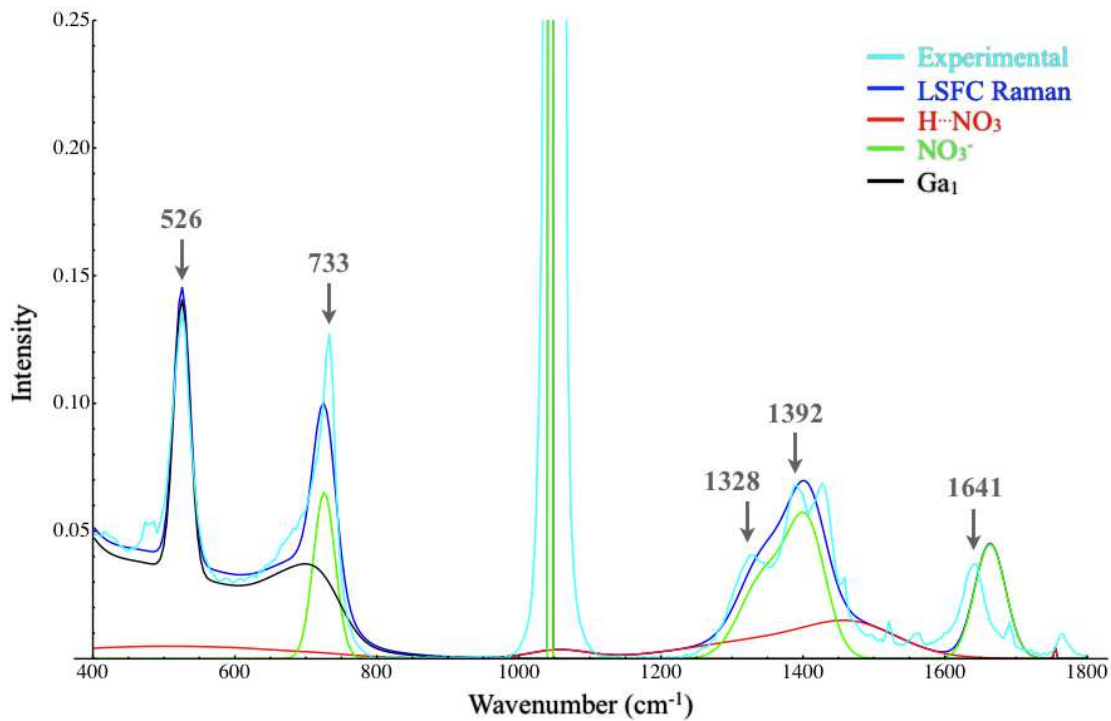


Figure S6. Solid State Raman spectrum of gallium nitrate hydrate salt. LSFC Raman spectrum was computed using gallium monomer (Ga₁) and nitrate vibrational modes, and was used to determine the computed frequency scaling factor for the monomer. The LSFC Raman spectrum has an RMSD of 0.76 %.

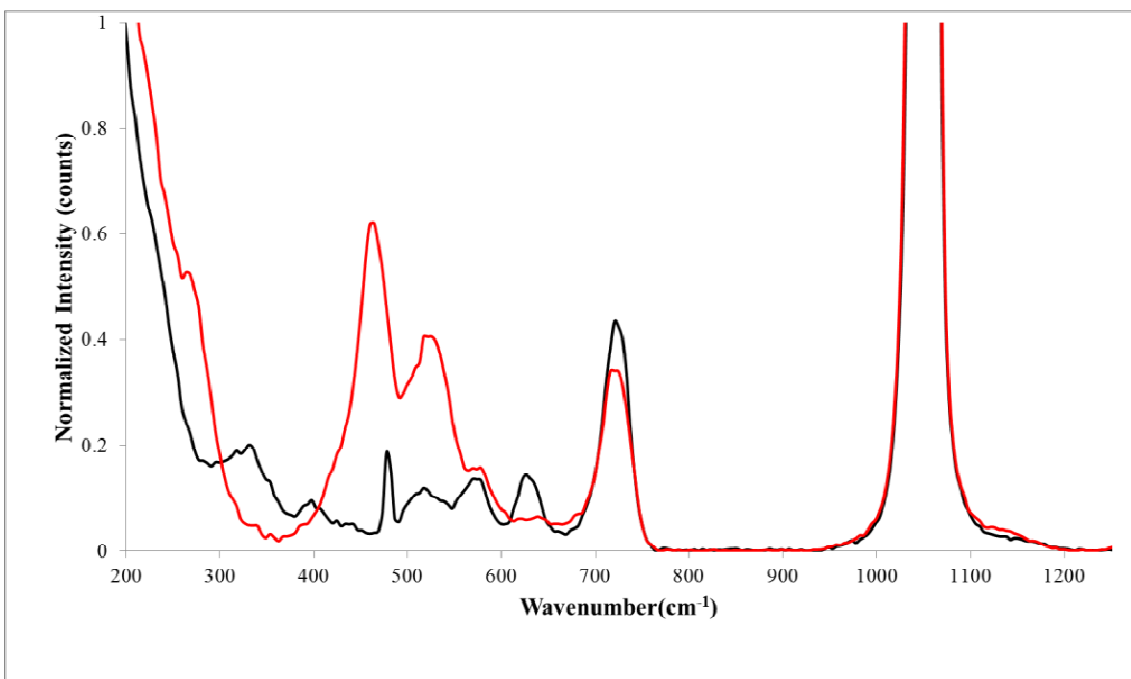


Figure S7. Raman overlay of Al₁₃ (black) and Ga₁₃ (red) clusters with normalized intensity

Table S6. Raman and IR spectral data for Al₁₃ in the solid state and aqueous solution at 25 °C

Raman Table		
Al ₁₃ Solid	Al ₁₃ (0.1M)	Peak Assignments
		Computational Analysis
313, w	-	Al-O
380, w	-	Al-O
424, w	-	Al-O
478, w	-	Al-O
517, w	-	Al-O
-	525, v, br	Al-O
574, w	-	Al-O
626, w	-	Al-O
725, m	715, m	NO₃⁻¹, asy
1048, vs	1048, vs	NO₃⁻¹, sym
1101, vw, sh	-	μ₂-OH
1340, m	1341, m	NO₃-1 asy
1401, m	1400, m	NO₃-1 asy
1637, m	1626, m	H₂O•••NO₃⁻¹, d
3271, s, br	-	OH
3455, s, br	-	OH

Infrared Table

Al ₁₃ Solid	Peak Assignments
	Computational Analysis
550, w	Al-O
636, m	Al-O
717	Al-O•••ηH ₂ O
824	NO ₃ ⁻¹ , sym
994	μ ₃ -OH
1048	μ ₃ -OH core
1178	μ ₃ -OH and μ ₂ -OH shell
1380, vs	NO ₃ ⁻¹ , asy
1634, m, br	H ₂ O•••NO ₃ ⁻¹ , d
1657, m, br	H ₂ O•••NO ₃ ⁻¹ , d
3291	OH

S = strong, m = medium, w = weak, v = very, br = broad, sh = shoulder, asy. = asymmetric, sym = symmetric, b = bend, d = deformation, str = stretch; The numbers in table are in wavenumbers (cm⁻¹)

Table S7. Raman and IR data of Ga₁₃ in Solid and Solution phase at 25 °C

Raman Table		
Ga ₁₃	Ga ₁₃	Peak Assignments
Single Crystal	0.1M	Computational Analysis
420,w, sh	-	Ga-O
464, s	-	Ga-O, sym
	507, m, br	Ga-O, sym
525,m	-	Ga-O
574,w	-	Ga-O
630, vw	-	Ga-O
716, s	716, m	NO ₃ ⁻¹ asy
1048, vs	1048, vs	NO ₃ ⁻¹ sym
1110, w,sh	-	μ2-OH
1330, m	1330m	NO ₃ ⁻¹ asy
1395, m	1394,m	NO ₃ ⁻¹ asy
1621, m	1621, m	H ₂ O•NO ₃ ⁻¹ , d
3234, br	-	OH
3388, br	-	OH
3533, sh	-	OH

Infrared Table

Ga ₁₃	Peak Assignments
Single crystal	Computational Analysis
420	Ga-O
574	Ga-O
635	Ga-O
713	Al-O••ηH ₂ O
824	NO ₃ ⁻¹ , sym
913	μ ₃ -OH core
1051	μ ₃ -OH and μ ₂ -OH shell
1101	μ ₂ -OH shell
1381	NO ₃ ⁻¹ , asy
1620	H ₂ O••NO ₃ ⁻¹ , d
3359	OH

S = strong, m = medium, w = weak, v = very, br = broad, sh = shoulder, asy = asymmetric, sym = symmetric, b = bend, d = deformation, str = stretch; The numbers in table are wavenumbers (cm⁻¹)

Full authorship of Gaussian 09

Gaussian 09, Revision B.01, M. J. Frisch, G. W. Trucks, H. B. Schlegel, G. E. Scuseria, M. A. Robb, J. R. Cheeseman, G. Scalmani, V. Barone, B. Mennucci, G. A. Petersson, H. Nakatsuji, M. Caricato, X. Li, H. P. Hratchian, A. F. Izmaylov, J. Bloino, G. Zheng, J. L. Sonnenberg, M. Hada, M. Ehara, K. Toyota, R. Fukuda, J. Hasegawa, M. Ishida, T. Nakajima, Y. Honda, O. Kitao, H. Nakai, T. Vreven, J. A. Montgomery, Jr., J. E. Peralta, F. Ogliaro, M. Bearpark, J. J. Heyd, E. Brothers, K. N. Kudin, V. N. Staroverov, R. Kobayashi, J. Normand, K. Raghavachari, A. Rendell, J. C. Burant, S. S. Iyengar, J. Tomasi, M. Cossi, N. Rega, J. M. Millam, M. Klene, J. E. Knox, J. B. Cross, V. Bakken, C. Adamo, J. Jaramillo, R. Gomperts, R. E. Stratmann, O. Yazyev, A. J. Austin, R. Cammi, C. Pomelli, J. W. Ochterski, R. L. Martin, K. Morokuma, V. G. Zakrzewski, G. A. Voth, P. Salvador, J. J. Dannenberg, S. Dapprich, A. D. Daniels, Ö. Farkas, J. B. Foresman, J. V. Ortiz, J. Cioslowski, and D. J. Fox, Gaussian, Inc., Wallingford CT, 2009.

Cartesian coordinates of Al and Ga tridecamers.

Structures and thermodynamic energies were computed by HF/6-31G(d,p)/PCM-UFF (H₂O, Gaussian 09).

1. [Al₁₃(OH)₂₄(H₂O)₂₄]¹⁵⁺

Supporting Information: Al13p.log

Using Gaussian 09: AM64L-G09RevB.01 12-Aug-2010
=====

HF 6-31G** OPT(CalcFC,maxcycles=200,RFO) SCRF=(Solvent=water)

Freq

#N Geom=AllCheck Guess=TCheck SCRF=Check GenChk RHF/6-31G(d,p) Freq

Pointgroup= C1 Stoichiometry= Al13H72O48(15+) C1[X(Al13H72O48)]
#Atoms= 133

Charge = 15 Multiplicity = 1

SCF Energy= -6781.56580449 Predicted Change= -2.727151D-04
=====

Optimization completed. {Found 1 times}
Item Max Val. Criteria Pass? RMS Val. Criteria Pass?
Force 0.00034 || 0.00045 [YES] 0.00005 || 0.00030 [YES]
Displ 0.12275 || 0.00180 [NO] 0.12275 || 0.00180 [NO]

Atomic Coordinates (Angstroms)
Type X Y Z

Al 0.000629 0.001954 -0.026546
Al 2.746024 -1.274422 -0.050675
Al 0.267732 -3.018799 0.010024
Al -2.473543 -1.729653 -0.023126
Al -2.750355 1.282771 -0.011175
Al -0.266430 3.018938 0.012138
Al 2.479910 1.743342 -0.045983
Al 3.038684 -4.212797 1.665169
Al -2.223941 -4.752552 -1.585280
Al -5.214107 -0.467639 1.590330
Al -3.001083 4.298917 -1.605450
Al 2.205697 4.699589 1.673805
Al 5.193599 0.437309 -1.695401
O -0.691254 -1.493431 -0.959471
O 0.709174 1.482791 0.921906

O	1.630782	0.159395	-0.982676
O	0.944998	-1.343706	0.915906
O	-1.642830	-0.149574	0.921277
O	-0.940473	1.364872	-0.948487
O	1.807037	-2.600343	-0.948801
O	-1.348536	-2.869871	0.921586
O	-3.161299	-0.262826	-0.959164
O	-1.830278	2.590284	0.939658
O	1.329388	2.914040	-0.928946
O	3.173142	0.281186	0.874692
O	3.474309	-2.478504	1.162596
O	1.244825	-4.115369	1.175415
O	-0.476566	-4.318363	-1.115760
O	-2.928873	-3.065088	-1.240291
O	-3.952858	-1.743811	1.109919
O	-4.147767	1.006635	1.185116
O	-3.440785	2.532774	-1.201315
O	-1.209821	4.158174	-1.123137
O	0.459779	4.200310	1.262170
O	3.000376	3.116599	1.115831
O	3.945115	1.729255	-1.209210
O	4.113290	-1.021461	-1.285300
O	2.626281	-3.734532	3.505123
O	3.582066	-5.015742	-0.003509
O	4.882904	-4.421583	2.283886
O	2.779055	-6.041522	2.312953
O	-1.889432	-4.361873	-3.457921
O	-2.696799	-5.492607	0.130127
O	-1.676318	-6.566646	-2.067795
O	-4.002726	-5.305961	-2.178187
O	-4.672969	-0.525583	3.454587
O	-6.116709	-0.529780	-0.112653
O	-6.457708	-1.882559	2.117019
O	-6.603031	0.763385	2.184188
O	-2.614488	3.918357	-3.470934
O	-3.524650	5.034948	0.096354
O	-4.844696	4.566523	-2.181317
O	-2.724411	6.159161	-2.145303
O	2.104853	4.050699	3.505270
O	2.520627	5.622399	0.008433
O	1.487669	6.368745	2.372466
O	3.956652	5.388670	2.219259
O	4.635614	0.512929	-3.557663
O	6.126256	0.423785	-0.004752
O	6.457032	1.828349	-2.220200
O	6.549065	-0.823399	-2.318463

H	-0.694077	-1.515960	-1.909015
H	0.725830	1.487854	1.871082
H	1.639607	0.147749	-1.932710
H	0.961931	-1.329525	1.865019
H	-1.656472	-0.151777	1.871066
H	-0.937840	1.381968	-1.897745
H	2.012693	-2.959871	-1.798049
H	-1.485221	-3.122061	1.822803
H	-3.398381	-0.271828	-1.874068
H	-1.988081	2.782876	1.851311
H	1.442051	3.227722	-1.814202
H	3.466204	0.327652	1.772222
H	4.101988	-2.062097	1.738329
H	0.756895	-4.855595	1.513863
H	0.143885	-4.957545	-1.443141
H	-3.477026	-2.755389	-1.949316
H	-4.207702	-2.616361	1.384174
H	-4.256484	1.728204	1.790796
H	-4.054678	2.148686	-1.813652
H	-0.698886	4.904588	-1.412937
H	-0.140868	4.423022	1.961461
H	3.900632	3.067748	1.410471
H	4.177791	2.582635	-1.552751
H	4.155869	-1.711542	-1.933985
H	1.763810	-3.517832	3.839272
H	3.278285	-3.549152	4.171478
H	4.485603	-5.080774	-0.291148
H	3.041481	-5.555445	-0.567630
H	5.182154	-5.217459	2.709896
H	5.643887	-3.927477	2.000684
H	2.993861	-6.840051	1.844934
H	2.527426	-6.255270	3.204203
H	-2.538060	-4.450629	-4.146921
H	-1.101237	-3.968358	-3.812339
H	-2.108018	-5.781148	0.816157
H	-3.583440	-5.751726	0.353226
H	-1.715431	-7.329277	-1.502124
H	-1.362188	-6.824362	-2.926681
H	-4.826914	-4.875050	-1.981781
H	-4.183120	-6.179200	-2.508771
H	-3.933733	-1.016476	3.793311
H	-4.987939	0.072680	4.122412
H	-6.732852	0.124380	-0.421304
H	-5.951961	-1.157189	-0.805325
H	-7.129694	-2.253748	1.557625
H	-6.515197	-2.262357	2.985944

H	-7.423455	0.457055	2.554930
H	-6.699647	1.677751	1.944923
H	-1.762984	3.683651	-3.820606
H	-3.277324	3.778850	-4.137683
H	-4.422813	5.166402	0.377054
H	-2.936455	5.285326	0.797225
H	-5.139769	5.382428	-2.570792
H	-5.605579	4.058516	-1.923921
H	-2.858121	6.914391	-1.584632
H	-2.464438	6.443991	-3.013532
H	1.733541	4.531987	4.235769
H	2.347005	3.178493	3.791521
H	2.140324	6.463849	-0.216546
H	3.126315	5.364041	-0.675596
H	2.035691	7.038015	2.767840
H	0.650946	6.757410	2.143006
H	4.347983	5.280992	3.078513
H	4.518436	5.935043	1.682087
H	3.890674	0.998214	-3.891705
H	4.958821	-0.071071	-4.234388
H	6.760160	-0.243914	0.230997
H	6.109827	1.086788	0.673311
H	7.147268	2.178399	-1.669507
H	6.512816	2.212631	-3.087443
H	7.378863	-0.546141	-2.691083
H	6.598847	-1.749816	-2.113502

Statistical Thermodynamic Analysis

Temperature= 298.150 Kelvin Pressure= 1.00000 Atm

SCF Energy=	-6781.56580449	Predicted Change=	-2.727151D-04
Zero-point correction (ZPE)=	-6780.4645	1.10130	
Internal Energy (U)=	-6780.3662	1.19959	
Enthalpy (H)=	-6780.3652	1.20053	
Gibbs Free Energy (G)=	-6780.5760	0.98970	

Frequencies -- 23.2052 27.2815 37.3857

2. [Ga₁₃(OH)₂₄(H₂O)₂₄]¹⁵⁺

Supporting Information: Ga13p.log

Using Gaussian 09: AM64L-G09RevB.01 12-Aug-2010
=====

=====

```
#HF/6-31G(d,p) scf=(maxcycle=300,direct,tight,xqc) density=current  
SCRF=(PCM,SOLVENT=H2O) opt=(maxcycle=250,RFO) IOp(1/8=5) freq  
#N Geom=AllCheck Guess=TCheck SCRF=Check Test GenChk RHF/6-31G(d,p)  
Freq
```

```
Pointgroup= C1   Stoichiometry= Ga13H72O48(15+)   C1[X(Ga13H72O48)]  
#Atoms= 133  
Charge = 15      Multiplicity = 1
```

```
SCF Energy= -28612.2252477   Predicted Change= -1.176400D-04  
=====
```

=====

```
Optimization completed.      {Found   1   times}  
Item  Max Val.  Criteria  Pass?  RMS Val.  Criteria  Pass?  
Force  0.00017 || 0.00045 [ YES ]   0.00002 || 0.00030 [ YES ]  
Displ  0.07657 || 0.00180 [ NO ]   0.07657 || 0.00180 [ NO ]
```

```
Atomic  Coordinates (Angstroms)  
Type   X           Y           Z
```

Ga	-0.000699	0.003284	-0.016475
Ga	2.730100	-1.367395	-0.020500
Ga	0.177154	-3.047913	0.005512
Ga	-2.549200	-1.671282	-0.015201
Ga	-2.734332	1.377315	-0.004388
Ga	-0.180474	3.052077	0.013545
Ga	2.550254	1.685257	-0.029783
Ga	2.942097	-4.398925	1.669558
Ga	-2.397170	-4.748206	-1.621657
Ga	-5.307081	-0.324095	1.624440
Ga	-2.915355	4.450783	-1.633809
Ga	2.377357	4.729846	1.680458
Ga	5.293636	0.286301	-1.685348
O	-0.750347	-1.504521	-0.976488
O	0.760178	1.500418	0.954062
O	1.674315	0.106597	-0.985081
O	0.925396	-1.400310	0.951860
O	-1.680256	-0.100633	0.949929
O	-0.923642	1.422947	-0.966215

O	1.765186	-2.696751	-0.981963
O	-1.455814	-2.878489	0.968136
O	-3.213583	-0.175721	-0.992713
O	-1.782694	2.692156	0.986557
O	1.439179	2.909115	-0.975538
O	3.222001	0.197023	0.947312
O	3.443242	-2.619363	1.232282
O	1.110808	-4.210870	1.211523
O	-0.596980	-4.344289	-1.177879
O	-3.084030	-3.011550	-1.268254
O	-4.050305	-1.666953	1.167583
O	-4.174642	1.153421	1.229089
O	-3.427987	2.662145	-1.234158
O	-1.089313	4.249821	-1.167202
O	0.575758	4.271523	1.279788
O	3.127915	3.064692	1.169158
O	4.047854	1.643002	-1.228253
O	4.147866	-1.174473	-1.281197
O	2.586370	-3.987458	3.586861
O	3.466702	-5.161218	-0.083167
O	4.813694	-4.747306	2.261249
O	2.618806	-6.274963	2.278252
O	-2.102974	-4.362495	-3.553568
O	-2.856596	-5.477177	0.161925
O	-1.884295	-6.604541	-2.150967
O	-4.219408	-5.339510	-2.172673
O	-4.787908	-0.371377	3.546408
O	-6.183994	-0.364221	-0.152713
O	-6.634009	-1.703624	2.198080
O	-6.724684	0.950730	2.194469
O	-2.565652	4.064282	-3.557711
O	-3.410952	5.193527	0.133406
O	-4.786039	4.822388	-2.205920
O	-2.587212	6.334759	-2.213091
O	2.271590	4.147405	3.582301
O	2.705650	5.601352	-0.066288
O	1.786606	6.511267	2.338393
O	4.189069	5.395930	2.206633
O	4.767720	0.345776	-3.606543
O	6.200517	0.260235	0.078617
O	6.639418	1.646604	-2.250564
O	6.687823	-1.011908	-2.277167
H	-0.758789	-1.533145	-1.928111
H	0.776337	1.505644	1.905482
H	1.687719	0.099805	-1.936881
H	0.943930	-1.409864	1.903607

H	-1.693840	-0.106038	1.901580
H	-0.928203	1.452637	-1.917966
H	1.961081	-3.047604	-1.838404
H	-1.617005	-3.170387	1.854219
H	-3.528928	-0.184614	-1.884462
H	-1.973867	2.956440	1.874500
H	1.572363	3.215767	-1.861434
H	3.570021	0.241452	1.826214
H	4.076082	-2.232235	1.823289
H	0.591136	-4.934115	1.540038
H	0.009796	-4.997825	-1.504132
H	-3.653581	-2.678362	-1.949720
H	-4.314397	-2.535388	1.447516
H	-4.254252	1.874952	1.839316
H	-4.064770	2.296973	-1.834683
H	-0.557589	4.986184	-1.445610
H	-0.049246	4.570915	1.927346
H	4.030326	2.986706	1.453115
H	4.312715	2.496389	-1.548405
H	4.176343	-1.877828	-1.916362
H	1.755887	-3.664055	3.916766
H	3.267675	-3.792831	4.221069
H	4.373259	-5.352759	-0.297408
H	2.905456	-5.642313	-0.679620
H	5.085453	-5.580027	2.632844
H	5.589888	-4.241160	2.049994
H	2.640103	-7.062838	1.746637
H	2.312374	-6.491313	3.151954
H	-2.799573	-4.339168	-4.200466
H	-1.336484	-3.925343	-3.907602
H	-2.260098	-5.840798	0.805222
H	-3.740436	-5.761333	0.367824
H	-1.834037	-7.363479	-1.580523
H	-1.531070	-6.828448	-3.004965
H	-5.043893	-4.886254	-2.037736
H	-4.398435	-6.218341	-2.489730
H	-4.022642	-0.826530	3.879885
H	-5.064123	0.279980	4.181604
H	-6.885515	0.227408	-0.401801
H	-6.135797	-1.070183	-0.787059
H	-7.272180	-2.138188	1.643954
H	-6.624728	-2.115063	3.055123
H	-7.556005	0.656434	2.551737
H	-6.787781	1.877933	1.995224
H	-1.740860	3.738977	-3.900021
H	-3.251787	3.896176	-4.194257

H	-4.298442	5.439806	0.369235
H	-2.807736	5.561486	0.768409
H	-5.053360	5.659931	-2.569935
H	-5.564714	4.318745	-1.997995
H	-2.605879	7.109559	-1.662563
H	-2.275162	6.569679	-3.079844
H	1.814783	4.618512	4.270387
H	2.427572	3.253985	3.867131
H	2.447122	6.497486	-0.251571
H	3.303401	5.305723	-0.742475
H	2.400462	7.147873	2.689166
H	0.923206	6.906149	2.299340
H	4.596771	5.242082	3.051998
H	4.810718	5.826612	1.631103
H	4.003682	0.804684	-3.937518
H	5.043775	-0.299927	-4.247584
H	6.889103	-0.366546	0.273400
H	6.235041	0.959331	0.720679
H	7.292892	2.061226	-1.699040
H	6.640827	2.058326	-3.107665
H	7.525825	-0.735392	-2.632895
H	6.714475	-1.949874	-2.125785

Statistical Thermodynamic Analysis

Temperature= 298.150 Kelvin Pressure= 1.00000 Atm

=====

=====

SCF Energy=	-28612.2252477	Predicted Change=	-1.176400D-04
Zero-point correction (ZPE)=	-28611.1378		1.08742
Internal Energy (U)=	-28611.0345		1.19065
Enthalpy (H)=	-28611.0336		1.19159
Gibbs Free Energy (G)=	-28611.2572		0.96794

Chapter III Supplemental Information

Experimental Section

A solution of Al_{13} (0.078 g, 0.037 mmol)^[14] and $\text{In}(\text{NO}_3)_3$ (0.27 g, 0.90 mmol) in MeOH (10 mL) was left to evaporate open to air. After several days crystals of Al_7In_6 formed (10% yield). Single crystal X-ray diffraction reveals a structure identical in geometry to the previously reported heterometallic clusters.^[9,10] Ga_7In_6 is synthesized following the same method as for Al_7In_6 . Ga_{13} (0.100 g, 0.037 mmol) and $\text{In}(\text{NO}_3)_3$ (0.27 g, 0.90 mmol) in MeOH (10 mL) was left to evaporate open to air. Ga_7In_6 crystals form after several days (20% yield). NMR and DOSY spectra were obtained on a Varian INOVA-500 MHz NMR Spectrometer. The Bipolar Pulse Pair Stimulated Echo (Dbppste) pulse sequences was used to acquire diffusion data with a 50 ms diffusion delay, 200 ms gradient length, 20 gradient levels, and $n_t = 16$ scans. The Varian DOSY package was used for processing and measuring. Percent error was calculated using measured values for ferrocene in DMSO.^[30,31] DLS measurements were taken using the Mobius from Wyatt technologies. The samples were filtered using a 0.1 μm PTFE syringe tip to remove any particulate matter. The R_h was calculated using Dynamics software and averaged over 20 measurements with 5 second integration time per acquisition. Raman spectra of the Al_7In_6 single crystals were collected using an Alpha 300S SNOM confocal Raman microscope. The spectra from each sample were averaged over 2000 accumulations at 0.5 s integration time per scan. Thin films were fabricated via spin coating (3000 rpm for 30 sec.) a 0.2 M solution of Al_7In_6 onto a p-type Si wafer pre-treated with a 7:3 v/v ratio of concentrated H_2SO_4 and 35% H_2O_2 (piranha). Prior to spin

coating, the solutions were filtered through a 0.1 μm PTFE syringe tip to remove any particulate matter and potential larger agglomerates. The films were then annealed at 300 $^{\circ}\text{C}$ for 30 minutes prior to analysis.

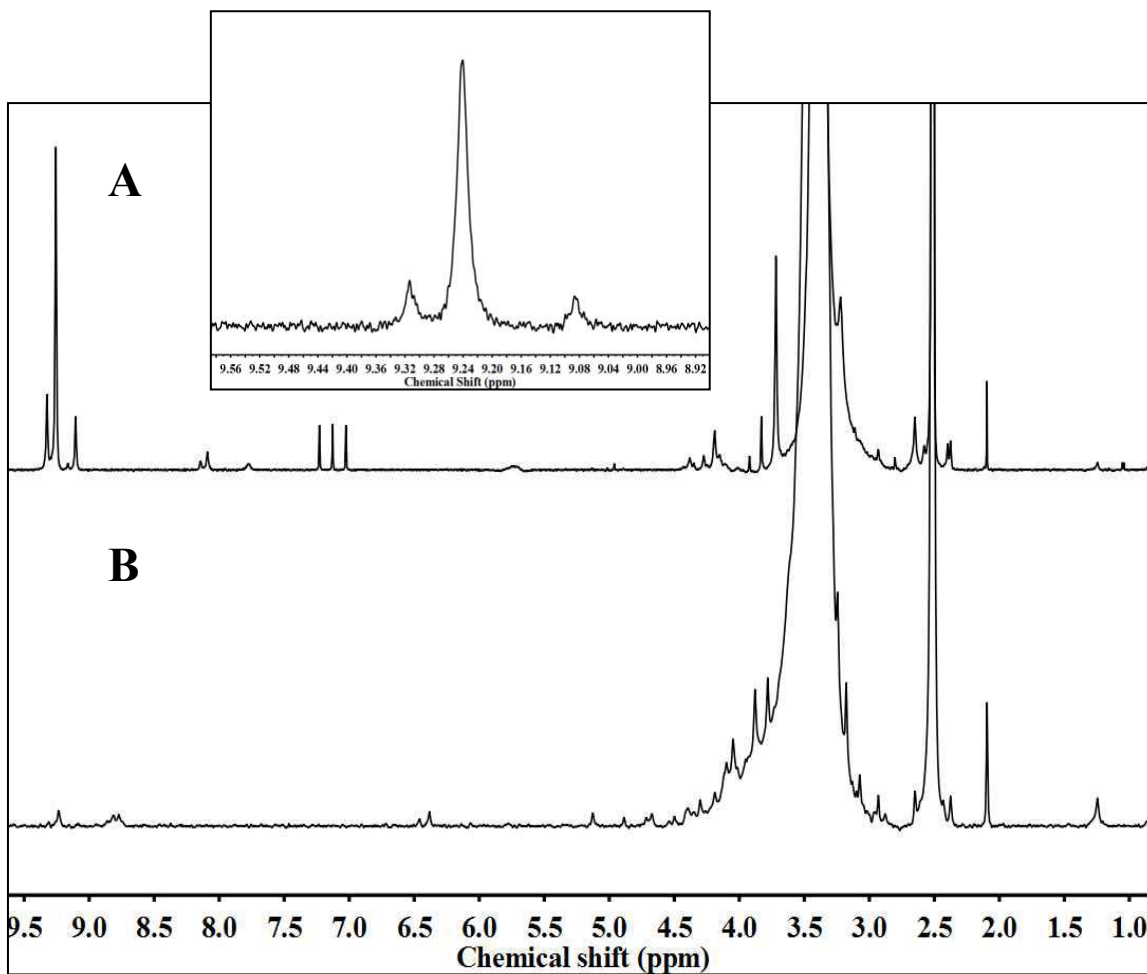


Figure S3. ^1H NMR of Al_{13} (A) and Al_7In_6 (B) in d_6 -DMSO. (Inset) the spectrum for $\text{Al}(\text{NO}_3)_3$ (C) in d_6 -DMSO.

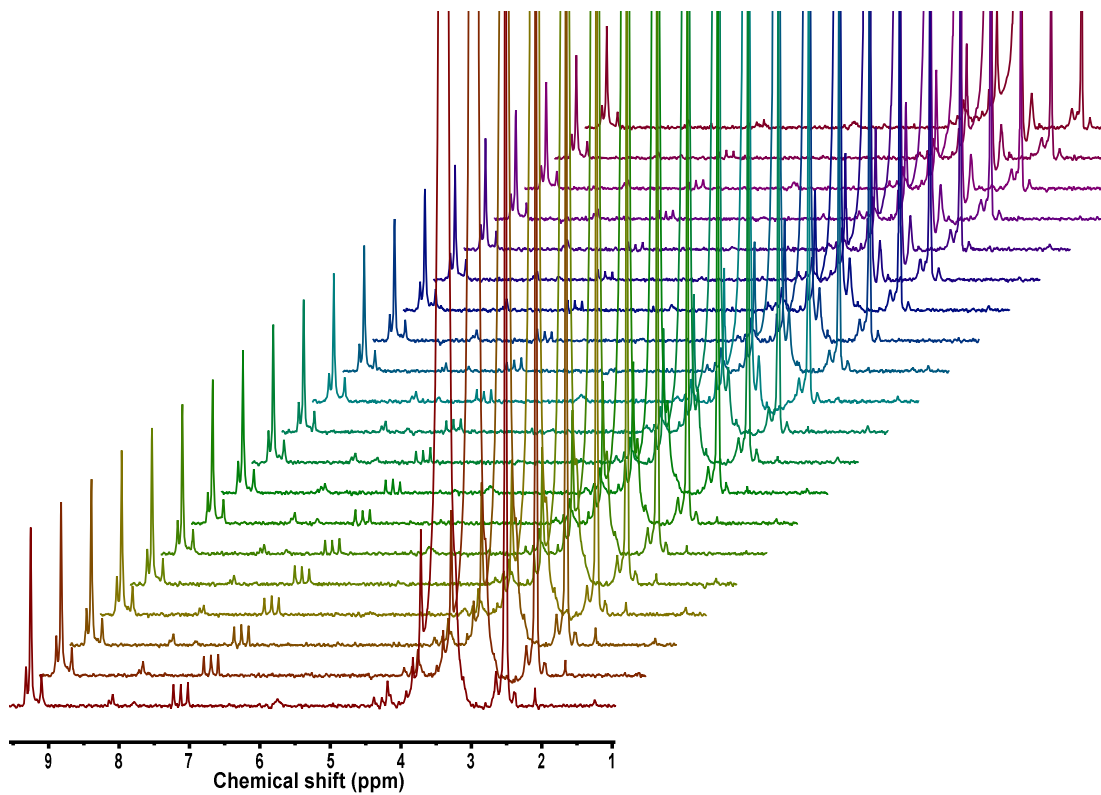


Figure S4. Stacked plot of Al_{13} DOSY in d_6 -DMSO.

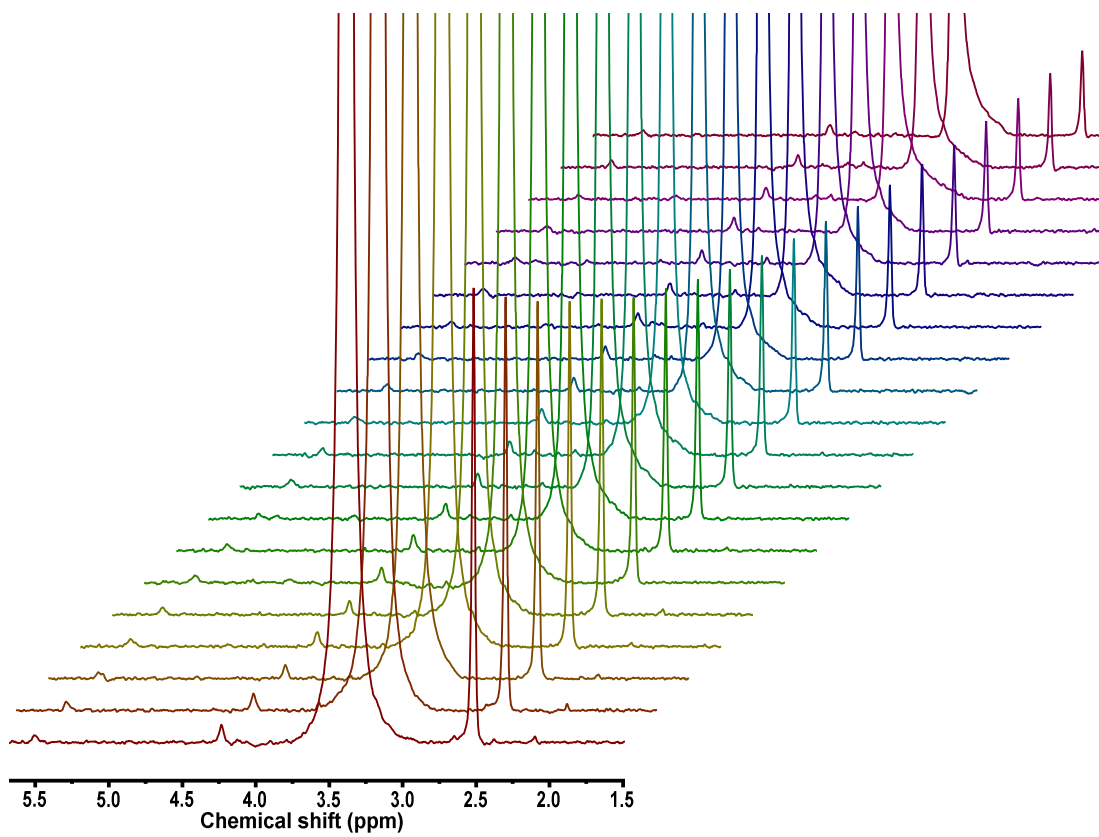


Figure S5. Stacked plot of Al₇In₆ DOSY in d₆-DMSO

Table S3. Diffusion coefficient (D) and hydrodynamic radius (R_h) values from Al₁₃ and Al₇In₆ DOSY in *d*₆-DMSO. The values for each peak associated with the clusters are averaged together (in bold) to give the overall D and R_h for each cluster. Values not corrected for DOSY software error.

Al ₁₃	Frequency (ppm)	Diffusion coefficient (m ² /s)	Standard error	Temperature (K)	η (Pa·s)	r (Å)
		8.06E-11	2.10E-11	298	2.03E-03	13.33
	8.0849	7.69E-11	2.92E-11	298	2.00E-03	14.223
	4.2745	6.47E-11	2.53E-11	298	2.00E-03	16.9
	4.2725	6.99E-11	1.75E-11	298	2.00E-03	15.643
	4.2686	9.78E-11	3.10E-11	298	2.00E-03	11.178
	4.1905	6.43E-11	9.72E-12	298	2.00E-03	17.013
	4.1876	6.89E-11	8.84E-12	298	2.00E-03	15.863
	4.1739	8.82E-11	2.36E-11	298	2.00E-03	12.393
	4.169	6.75E-11	2.53E-11	298	2.00E-03	16.192
	4.1602	6.44E-11	2.95E-11	298	2.00E-03	16.976
	4.1505	1.17E-10	2.05E-11	298	2.00E-03	9.3829
	4.1466	1.07E-10	3.17E-11	298	2.00E-03	10.233
	3.8292	7.24E-11	1.36E-11	298	2.00E-03	15.111
	3.7159	7.53E-11	6.35E-12	298	2.00E-03	14.521
	3.6963	9.47E-11	2.25E-11	298	2.00E-03	11.55
Al ₇ In ₆	Frequency (ppm)	Diffusion coefficient (m ² /s)	Standard error	Temperature (K)	η (Pa·s)	r (Å)
		8.83E-11	2.31E-11	298	2.03E-03	12.18
	4.239	8.58E-11	1.75E-11	298	2.03E-03	12.53
	4.235	9.26E-11	1.98E-11	298	2.03E-03	11.61
	4.234	8.15E-11	2.49E-11	298	2.03E-03	13.19
	4.231	9.43E-11	1.66E-11	298	2.03E-03	11.40
	3.237	9.84E-11	2.10E-11	298	2.03E-03	10.92
	3.228	9.06E-11	2.50E-11	298	2.03E-03	11.86
	3.226	9.83E-11	2.49E-11	298	2.03E-03	10.93
	3.220	9.43E-11	2.42E-11	298	2.03E-03	11.40
	3.210	8.29E-11	2.47E-11	298	2.03E-03	12.96
	3.207	9.13E-11	2.63E-11	298	2.03E-03	11.77
	3.205	8.88E-11	2.84E-11	298	2.03E-03	12.10
	3.182	8.61E-11	2.55E-11	298	2.03E-03	12.48
	3.177	7.47E-11	2.50E-11	298	2.03E-03	14.39
	3.171	7.62E-11	1.92E-11	298	2.03E-03	14.10

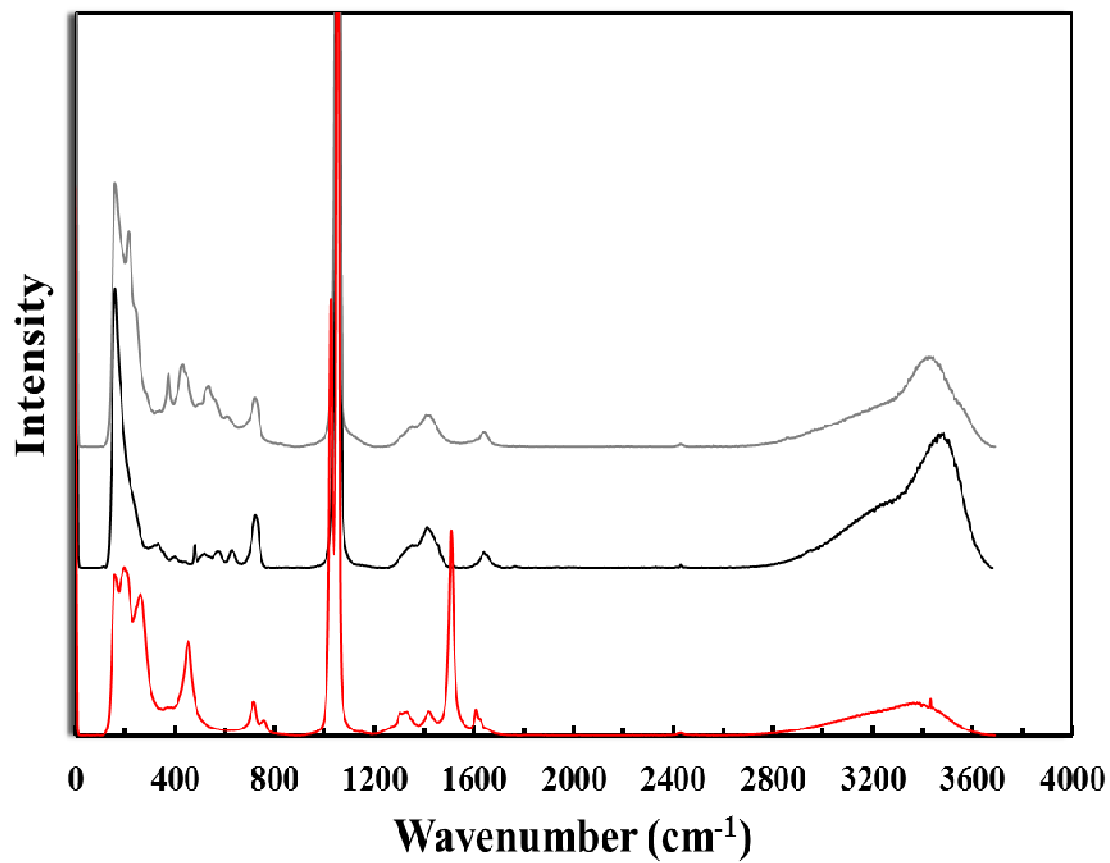


Figure S4. Stacked solid state Raman spectra of Al_7In_6 (grey), Al_{13} (black), and $\text{In}(\text{NO}_3)_3$.

Table S5. Raman of Solid state **Al₇In₆** at 25°C.

Peak Position (cm ⁻¹)	Peak Assignment
212	In-O, b
369	Al-O, str.
428	In-OH-Al, str, In-OH-Al, str.
594	Al-O, str
720	NO ₃ ⁻ , asym. str.
1048	NO ₃ ⁻ sym. str.
1334	NO ₃ ⁻¹
1401	NO ₃ ⁻¹
1627	H ₂ O•••NO ₃ ⁻¹ , d
3273	O-H, str.
3411	O-H, str.
3540	“Free” H ₂ O

S = strong, m = medium, w = weak, v = very, br = broad, sh = shoulder, asy = asymmetric, sym = symmetric, b = bend, d = deformation, str = stretch; The numbers in table are in wavenumbers (cm⁻¹)

Table S6. DLS data for the hydrodynamic radius of 2mM Al₁₃ in DMSO.

Data chart for 2 mM Al ₁₃ in DMSO								
	Peak1 Radius (0.1-10 nm)	Peak 1 %Pd	Peak 1 %Intensity	Peak 1 %Mass	Peak 2 Radius (10-100 nm)	Peak 2 %Pd	Peak 2 %Intens ity	Peak 2 %Mass
1	1.44	18.78	1.9	87.6	21.88	42.24	27. 48	0.99
2	1.69	19.56	2.15	82.52	24.28	45.48	29. 32	1.15
3	1.06	23.58	1.05	90.54	18.9	41.11	21. 56	0.77
4	1.38	20.54	1.38	83.7	22.04	44.75	25. 18	1.16
5	1.88	25.02	1.66	72.65	--	--	--	--
6	2.51	22.55	0.89	31.53	--	--	--	--
7	1.31	23.43	1.21	85.51	19.42	41.35	24. 92	1.42
8	1.33	22.75	1.78	89.52	22.34	44.43	28. 49	0.9
9	1.05	23.62	1.59	93.59	21.05	46.57	26. 89	0.58
10	1.39	19.55	1.79	86.86	21.87	42.39	27. 72	0.96
11	2.75	28.43	1.41	47.11	19.46	42.12	23. 9	6.17
12	1.54	14.91	1.77	83.29	21.67	42.34	28. 23	1.36
13	1.87	15.28	2.58	80.3	25.41	41.29	31. 26	1.14
14	1.27	23.17	1.99	91.61	23.2	41.85	28. 94	0.6
15	1.03	21.21	1.25	91.89	24.69	47.87	34. 32	0.63
Mean	1.57	21.49	1.63	79.88	22.02	43.37	27. 55	1.37
SD	0.51	3.55	0.44	17.55	2.03	2.21	3.2 7	1.47
SD %	32.37	16.52	27.26	21.97	9.21	5.1	11. 86	106.97
Min	1.03	14.91	0.89	31.53	18.9	41.11	21. 56	0.58
Max	2.75	28.43	2.58	93.59	25.41	47.87	34. 32	6.17

Table S7. DLS data for the hydrodynamic radius of 2 mM Al₇In₆ in DMSO.

Data chart for 2 mM Al₇In₆ in DMSO								
	Peak 1 Radius (0.1-10 nm)	Peak 1 %Pd	Peak 1 %Intensity	Peak 1 %Mass	Peak 2 Radius (10-100 nm)	Peak 2 %Pd	Peak 2 %Intensity	Peak 2 %Mass
1	0.68	10.43	0.02	50.71	72.17	48.74	97.23	28.94
2	1.3	25.35	0.4	88.78	72.31	51.31	99.24	10.4
3	9.04	10.19	4.48	17.25	62.81	17.44	95.52	82.75
4	0.59	13.25	0.35	98.31	10.37	20.57	2.26	0.14
5	0.62	10.52	0.24	95.99	66.69	41.29	94.49	2.52
6	4.89	11.91	1.48	27.26	65.55	40.47	94.99	52.4
7	1.26	14.58	0.52	85.94	71.34	57.04	98.99	8.88
8	0.68	11	0.25	96.53	10.98	18.11	3.46	0.38
9	--	--	--	--	12.01	8.12	5.96	10.99
10	1.83	9.92	0.64	74.75	75.84	67.28	99.16	20.46
Mean	2.32	13.02	0.93	70.61	52.01	37.04	69.13	21.79
SD	2.86	4.88	1.39	31.2	28.47	19.82	45.06	26.7
SD%	8.18	23.8	1.94	973.49	810.31	392.68	2030.24	713.08
Min	0.59	9.92	0.02	17.25	10.37	8.12	2.26	0.14
Max	9.04	25.35	4.48	98.31	75.84	67.28	99.24	82.75

Table S8. DLS data for the hydrodynamic radius of 0.1M Al₁₃ in H₂O.

Data Chart for 0.1M Al₁₃ in H₂O				
	Radius(nm)	Polydispersity (nm)	%PD	PD Index
	1	0.3	32.7	0.327
	1	0.4	37.8	0.378
	1	0.4	41.3	0.413
	1	0.4	42.6	0.426
	1	0.5	46.7	0.467
	1	0.4	36.6	0.366
	1	0.4	37.1	0.371
	1	0.5	45	0.45
	1.1	0.6	57.1	0.571
	0.9	0.5	57.1	0.571
	1.1	0.4	34.1	0.341
	1	0.4	44.2	0.442
	1	0.4	43.1	0.431
	1	0.5	52.8	0.528
	1.1	0.6	54.4	0.544
	1	0.6	54.7	0.547
	1	0.4	40.6	0.406
	1	0.4	41.1	0.411
	1	0.5	50.6	0.506
	1.1	0.6	55.2	0.552
Mean	1	0.5	45.2	0.452
SD	0.04	0.1	7.9	0.079
SD%	3.8	18.9	17.5	17.489
Min	0.9	0.3	32.7	0.327
Max	1.1	0.6	57.1	0.571

Table S9. DLS data for the hydrodynamic radii of 0.1 M Al₇In₆ in H₂O.

Data chart for 0.1M Al₇In₆ in H₂O								
Acq.	Peak Radius (0.1-10 nm)	Peak 1 %Pd	Peak 1 Intensity	Peak 1 %Mass	Peak 2 Radius (10-100 nm)	Peak 2 %Pd	Peak 2 Intensity	Peak 2 %Mass
1	--	--	--	--	13.69	59.93	98.75	99.36
2	--	--	--	--	13.87	53.57	99.95	99.49
3	1.45	37.14	1.85	87.74	12.9	43.46	97.73	11.54
4	0.74	23.61	0.88	92.95	12.45	48.18	98.59	6.61
5	1.3	24.73	1.11	75.03	14.05	52.64	98.89	24.97
6	1.89	24.86	2.06	71.31	13.97	49.19	97.94	28.69
7	1.39	27.5	1.54	82.17	14	49.58	98.46	17.3
8	--	--	--	--	14.33	57.24	100	100
9	--	--	--	--	14.76	59.46	100	100
10	1.45	14.45	2.3	85.87	13.7	49.91	97.61	13.86
11	2.13	24.96	4.54	84.75	14.24	43.75	95.46	15.25
12	0.68	18.92	0.63	91.58	14.52	59.41	99.37	8.42
13	1.1	29.96	1.09	85.61	14.03	53.24	98.91	14.39
14	1.99	30.21	2.8	81.73	13.97	43.74	97.2	18.27
15	--	--	--	--	13.89	50.86	100	100
16	0.96	15.15	1.26	91.72	12.35	43.68	95.05	8.16
17	1.34	20.97	0.39	46.57	14	53.15	99.61	53.43
18	1.48	29.79	1.46	78.13	14.16	52.87	98.48	21.68
19	--	--	--	--	14.55	56.05	100	100
20	1.81	27.94	3.18	85.68	14.45	46.07	96.82	14.32
Mean	1.41	25.01	1.79	81.49	13.89	51.3	98.44	42.81
SD	0.44	6.1	1.12	11.82	0.64	5.44	1.46	39.53
SD%	31.49	24.81	62.67	14.51	4.64	106	1.49	92.32
Min	0.68	14.45	0.39	46.57	12.35	43.46	95.05	6.61
Max	2.13	37.14	4.54	92.95	14.76	59.93	100	100

Chapter VI Supplemental Information

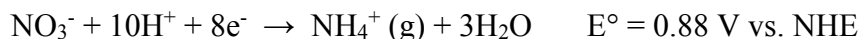
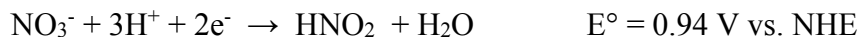
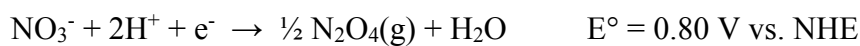
Experimental Methods

General: All chemicals were used as received, with no further purification: Zn (Alfa Aesar), Ga(NO₃)₃•xH₂O (Alfa Aesar), In(NO₃)₃•xH₂O (Johnson Matthey Materials Technology), Aluminum (Kurt J. Lesker, 99% Al), DMSO-*d*₆ (Cambridge Isotope Laboratories Inc). The degree of hydration of metal salts was determined by thermogravimetric analysis (TGA). Raman spectroscopic measurements were taken using a WITec alpha 300S. Raman spectra were averaged over 100 acquisitions using a 532 nm excitation wavelength laser that provided 40 mW of power. Samples for transmission electron microscope (TEM) analysis were prepared by focused ion beam milling of device structures utilizing an FEI Helios DualBeam system with a Ga-ion beam. Low-resolution TEM images were acquired using an FEI 80-300 Titan TEM and a 200 kV accelerating voltage. Energy dispersive X-ray spectroscopy (EDX) was taken from the film to confirm mixed-metal content. ¹H-NMR spectra were obtained on a Bruker 600 MHz spectrometer using Topspin Software. Data was processed in MestReNova. The experiments were run at 298 K in 5 mm tubes (2 mM in DMSO-*d*₆). Electrochemistry was carried out using an Autolab Nova potentiostat. All pH measurements were carried out *in-situ* using an IQ Instruments GLP series pH ISFET probe.

Electrochemical Synthesis: A three-electrode configuration (Figure S1) was used for the electrochemical cluster synthesis. The working electrode was composed of a Pt wire with a diameter of 0.60 mm and a length of 28.0 cm giving it an area of 5.28 cm². The counter electrode was composed of a Pt wire with a diameter of 0.60 mm and a length of

7.0 cm giving it an area of 1.32 cm². Typical current densities ranged from 7 to 15 mA cm⁻². A Ag/AgCl reference electrode was used for all syntheses.

The working and counter electrodes were placed in the same beaker with the counter electrode enclosed in a medium fritted glass tube (10-20 μm) to confine species generated at the counter electrode from the rest of the solution. The cathodic current passed at the working electrode was assumed to be largely associated with nitrate reduction as discussed in the text. Numerous reduction reactions are possible, given the range oxidation states accessible to N. The relevant reduction potentials are 0.8-1 V positive of the standard hydrogen electrode. Examples include:



From: *Standard Potentials in Aqueous Solutions*; Bard, A. J.; Parsons, R.; Jordan, J., Eds.; International Union of Pure and Applied Chemistry, 1985.

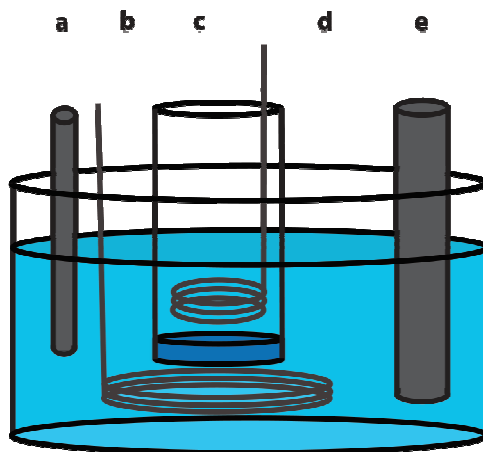
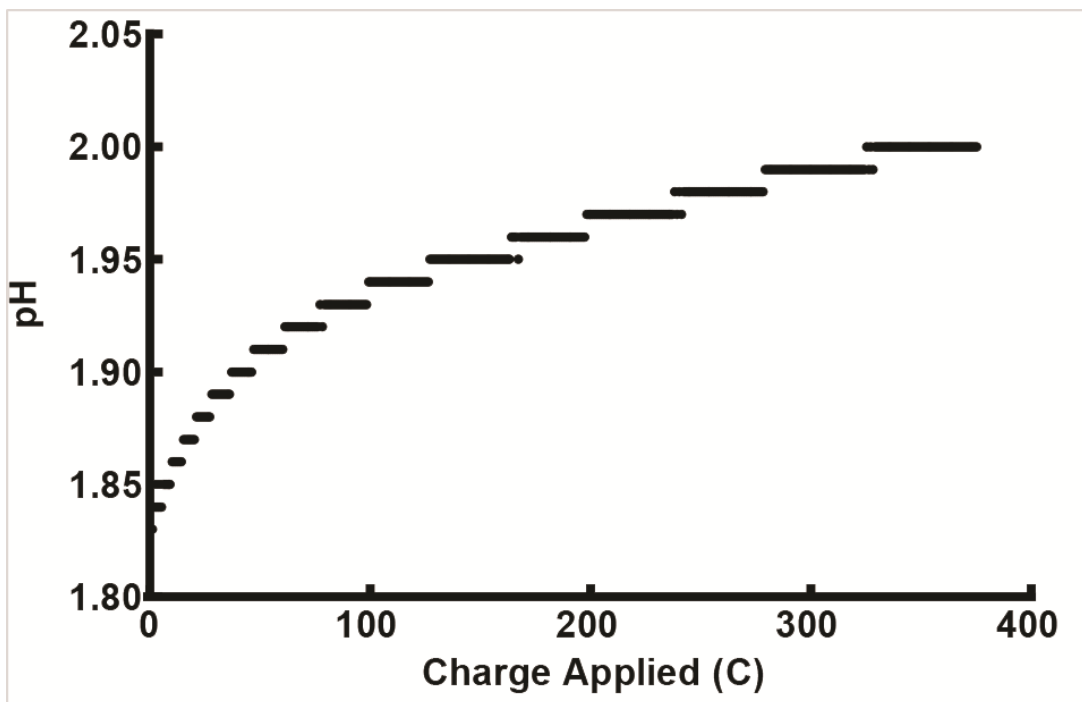


Figure S1. Sample image of the electrochemical cell used for the synthesis of clusters. a) Ag/AgCl reference electrode, b) Pt working electrode, c) Pt counter electrode, d) medium-fritted glass tube, e) pH probe. The reaction was performed in an open cell and any gaseous products that may have been formed were not collected.

Electrochemical Synthesis of flat-Ga₁₃: A 250 mM Ga cluster solution was prepared by dissolving 2.05 g Ga(NO₃)₃•4H₂O in 25 mL of 18.3 MΩ H₂O, and then applying a potential of -1.0 V vs. Ag/AgCl with the solution constantly stirring to remove products from the surface of the working electrode. A small amount of Ga was observed on the working electrode due to the potential being more negative than the Ga standard reduction potential. Electrolysis was terminated after ~2 hr after passing ~420 C of charge. At this point the solution could be used directly for film deposition. For analysis of the cluster solids, the reaction mixture was dried to a transparent glass over the course of 3 days in a watch glass. Scrapings of the dried reaction mixture were rinsed with isopropyl alcohol (IPA) to remove unreacted metal salts.

Electrochemical Synthesis of flat-Ga_{13-x}In_x (x = 5, 4): A 340 mM (total metal content) 6:7 In:Ga solution was prepared by dissolving appropriate amounts of Ga(NO₃)₃ and In(NO₃)₃ in 25 mL of 18.3 MΩ H₂O. The working electrode potential was set to -0.49 V vs. Ag/AgCl. The potential was less negative than in the case of the pure Ga cluster synthesis as the potential was practically

limited by the less-negative reduction potential of In (-0.58 vs Ag/AgCl) compared to Ga (-0.77 vs Ag/AgCl). The electrolysis was terminated after ~2 hr after passing ~390 C of charge. Aliquots of solution (3-4 mL) were placed in an evaporating dish (for analysis) while the remainder of the solution was used for thin-film deposition and processing. Drying and washing of the solid was carried out in the same manner as with Ga_{13}



clusters. $\text{Ga}_{13-x}\text{In}_x$ clusters were also synthesized using Zn metal as reductant, as reported previously,¹ and were used as standards for comparison with electrochemically produced clusters.

Figure S2. pH as a function of total cathodic charge passed through a 50 ml 0.34 M solution of 7:6 Ga:In nitrate in water. The starting salt solution has a pH of 1.83 and begins to buffer around a pH of 2 as cluster formation in the solution occurs.

Nuclear Magnetic Resonance: ^1H -NMR was conducted on the isolated products of both electrochemical syntheses (Figure S3). The spectra obtained from these experiments were compared to known samples (Figure S4). Similar to Ga_{13} , NMR data indicates that

the mixed clusters are dynamic in solution; however, one day after dissolution distinct “fingerprint” regions emerge for each species. Heterometallic clusters can most easily be differentiated by comparing the ^1H signals between 6.5 ppm and 6.8 ppm (Figure S4). Proton signals appear farther downfield with increased In:Ga ratios. This trend provides a simple tool for the determination of metal ratios in In:Ga heterometallic clusters.

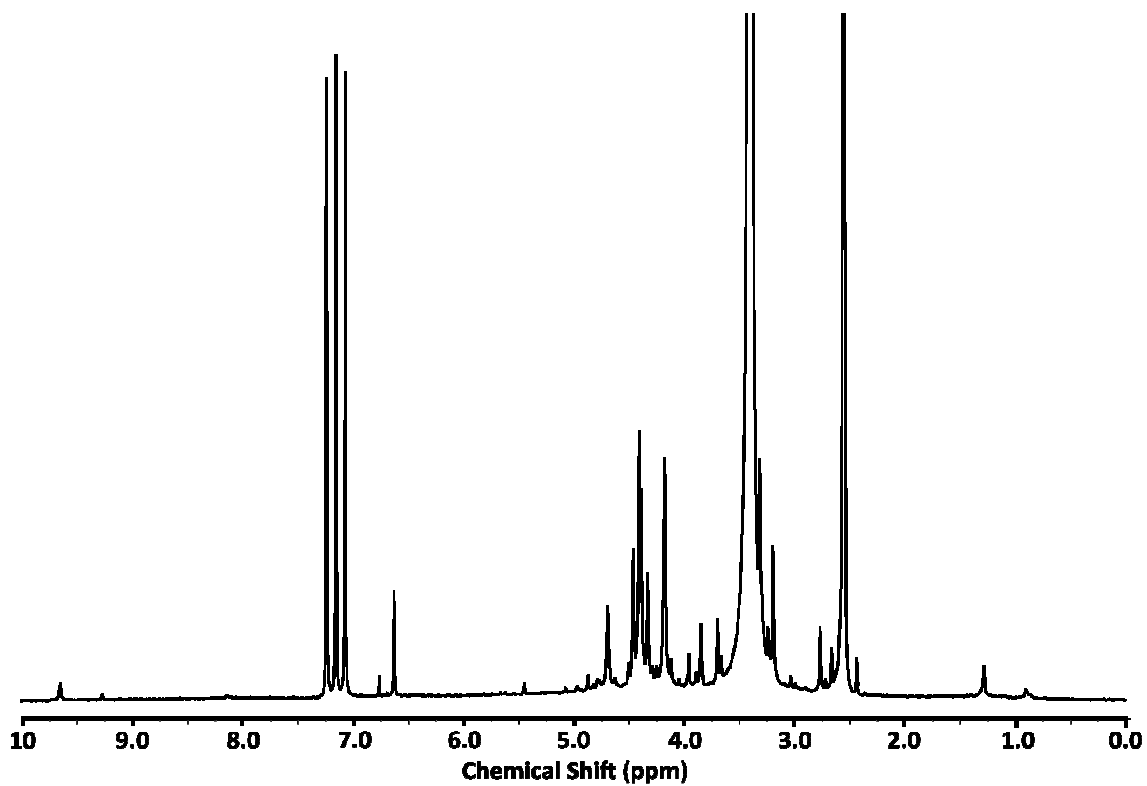


Figure S3. ^1H NMR spectrum of raw, electrochemically-synthesized Ga_{13} . Note the three large peaks at values just greater than 7 ppm correspond to ammonium ion being present in the sample. The fingerprint region is between 6.5 and 6.9 ppm.

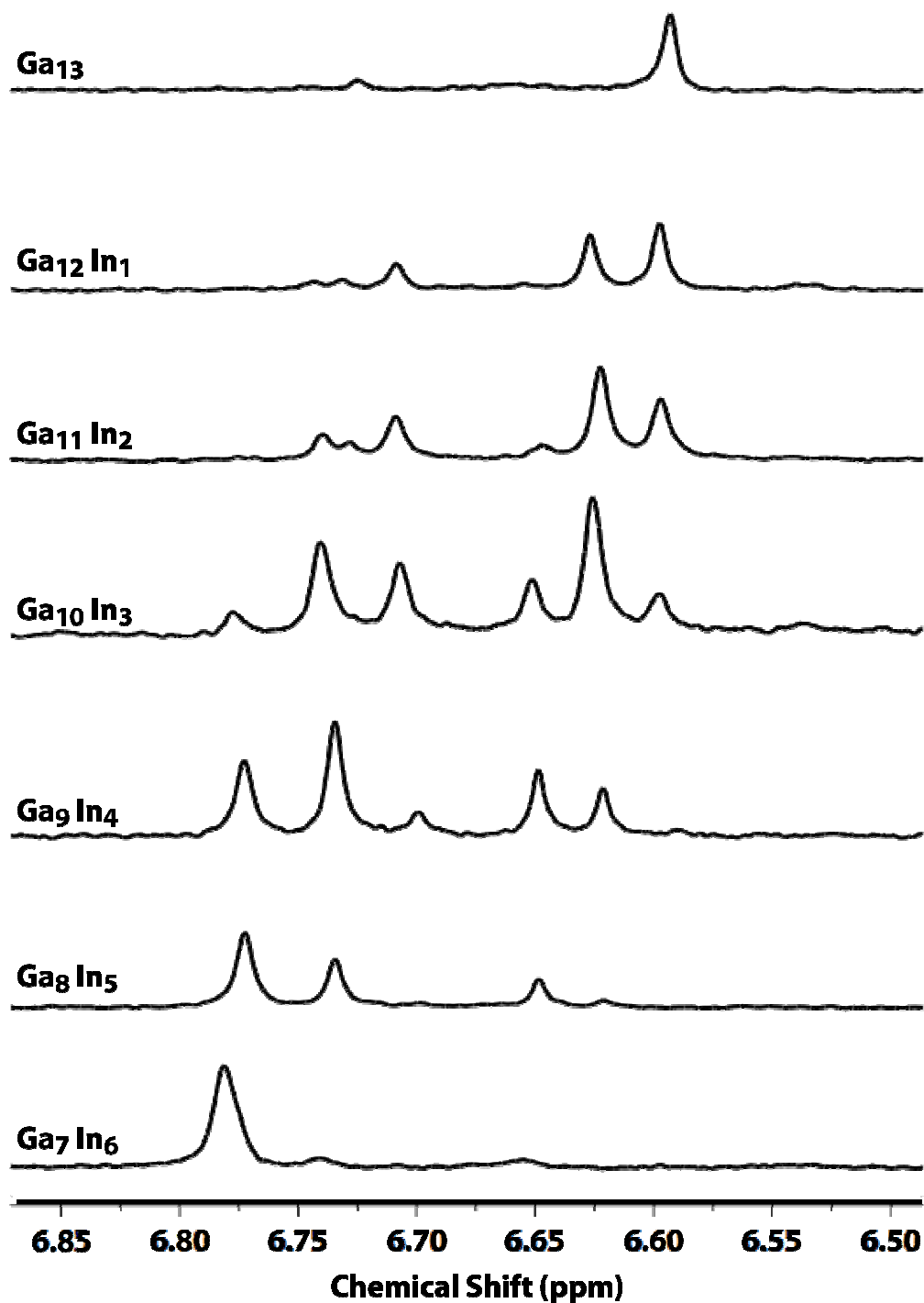


Figure S4. ^1H NMR fingerprint region of various M_{13} clusters synthesized by the Zn-reduction method, illustrating the definitive characteristics of each substitution (from Ref. S2). The composition was determined for each sample from the single-crystal structure also obtained. This data is included here to demonstrate that the fingerprint region of the ^1H NMR spectra are indeed indicative of the Ga-In ratio in the cluster.

Film and Electrical Characterization: Thin film transistors (TFTs) were fabricated by delivering the unpurified electrochemical solutions through a 0.45 μm PTFE filter onto 100 nm thermally grown SiO_2 on $\text{p}^+\text{-Si}$ (resistivity $\sim 0.007 \Omega \text{ cm}$) with a Cr/Au ohmic back contact (Hewlett Packard). Substrates were subjected to an oxygen plasma etch cleaning (150 W RF field, 120 s, 300 mTorr, 74.6 sccm O_2) in a March CS-1701 plasma etcher prior to solution deposition. Films were spin-cast at 3000 RPM for 30 s, and immediately transferred to a 300 $^\circ\text{C}$ hotplate for 1 min. The thin films were then annealed under air in a furnace at 550 $^\circ\text{C}$ for 2 hr. The TFT devices consist of the following structures: channel dimension = 1000 m x 500 m, channel width (W) = 1000 m, and channel length (L) = 150 m. Current-voltage behavior was measured with two Keithley 2400 SMUs joined via Labview using a 1 V step size and 200 ms dwell time. Device performance was assessed through analysis of channel average mobility (μ_{ave}), turn-on voltage (V_{on}), and drain current on-to-off ratio ($I_{\text{on}}/I_{\text{off}}$) measurements.

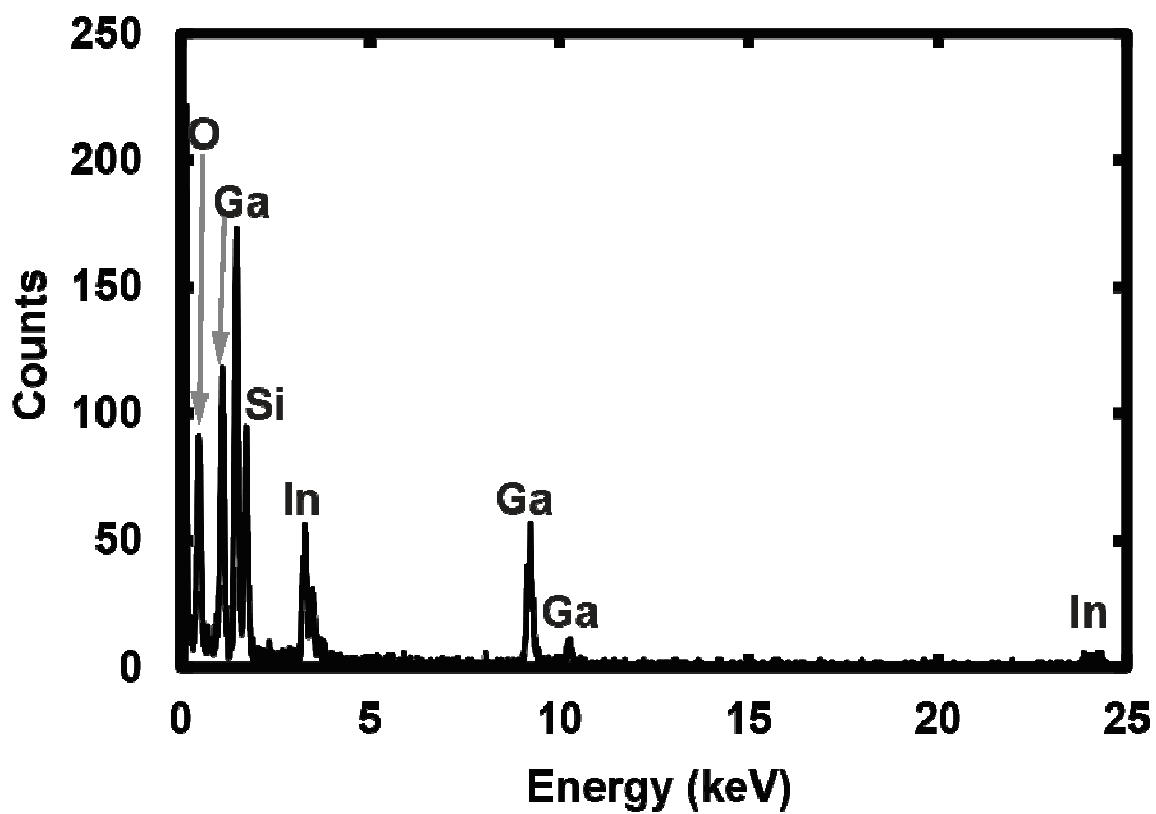


Figure S5. Energy dispersive x-ray spectroscopy measurements of the film presented in Figure 4a confirming the presence of Ga, In and O in the final material.

REFERENCES CITED

CHAPTER I

1. (a) S. L. Cumberland, K. M. Hanif, A. Javier, G. A. Khitrov, G. F. Strouse, S. M. Woessner, C. S. Yun, *Chem Mater*, 2002, **14**, 1576; (b) H. Ogino, S. Inomata, H. Tobita, *Chem Rev*, 1998, **98**, 2093; (c) S. Dehnen, M. Melullis, *Coordin Chem Rev*, 2007, **251**, 1259.
2. (a) G. E. Kostakis, A. M. Ako, A. K. Powell, *Chem Soc Rev*, 2010, **39**, 2238; (b) G. E. Kostakis, S. P. Perlepes, V. A. Blatov, D. M. Proserpio, A. K. Powell, *Coordin Chem Rev*, 2012, **256**, 1246.
3. (a) R. Sessoli, A. K. Powell, *Coordin Chem Rev*, 2009, **253**, 2328; (b) M. Viciano-Chumillas, S. Tanase, J.L. de Jongh, J. Reedijk, *Eur. J. Inorg. Chem.*, 2010, 3403.
4. (a) M. T. Pope, A. Muller, *Angew. Chem. Int. Edit.*, 1991, **30**, 34; (b) Baker, L. C. W.; Glick, D. C. *Chem. Rev.*, **1998**, **98**, 3; (c) A. Muller, P. Kogerler, A. W. M. Dress, *Coordin. Chem. Rev.*, 2001, **222**, 193; (d) M. Nyman, *Dalton T.*, 2011, **40**, 8049.
5. Z. L. Mensinger, W. Wang, D. A. Keszler, D. W. Johnson, *Chem. Soc. Rev.*, 2012, **41**, 1019.
6. (a) F. C. Meldrum, H. Cölfen, *Chem. Rev.* 2008, **108**, 4332; (b) A. Navrotsky, *Proc. Natl. Acad. Sci. U. S. A.* 2004, **101**, 12096; (c) L. Addadi, S. Raz, S. Weiner, *Adv. Mater.* 2003, **15**, 959; (d) A. Legg, M. Q. Zhu, L. R. Comolli, B. Gilbert, J. F. Banfield, *Langmuir* **2014**, **30**, 9931; (e) M. Q. Zhu, B. Legg, H. Z. Zhang, B. Gilbert, Y. Ren, J. F. Banfield, , G. A. Waychunas, *Environ. Sci. Technol.*, 2012, **46**, 8140.
7. D. Grandjean, A. M. Beale, A. V. Petukhov, B. M. Weckhuysen, *J. Am. Chem. Soc.*, 2005, **127**, 14454.
8. (b) A. Kalaji, S. Skanthakumar, M. G. Kanatzidis, J. F. Mitchell, L. Soderholm, *Inorg. Chem.* 2014, **53**, 6321; (c) L. A. Chivacci, C. Bourgaux, V. Briois, S. H.; Pulcinelli, C. V. Santilli, *J. Appl. Crystallogr.* 2000, **33**, 592; (d) L. A. Chivacci, S. H. Pulcinelli, C. V. Santilli, V. Briois, *Chem. Mat.* 1998, **10**, 986; (e) L. A. Chivacci, C. V. Santilli, S. H. Pulcinelli, C. Bourgaux, V. Briois, *Chem. Mat.* 2004, **16**, 3995; (f) L. A. Chivacci, C. V. Santilli, S. H. Pulcinelli, A. F. Craievich, *J. Appl. Crystallogr.* 1997, **30**, 750.
9. A. F. Oliveri, M. E. Carnes, M. M. Baseman, E. K. Richman, J. E. Hutchison, and D. W. Johnson, *Angew. Chemie Int. Ed.*, 2012, **51**, 10992.
10. A. F. Oliveri, E. W. Elliott, M. E. Carnes, J. E.; Hutchison, Johnson, D. W., *ChemPhysChem.*, 2013, **14**, 2655.

11. Z. L. Mensinger, J. T. Gatlin, S. T. Meyers, L. N. Zakharov, D. A. Keszler, D. W. Johnson, *Angew. Chem. Int. Ed.*, 2008, **47**, 9484.
12. M. Alemayehu, J. E. Davis, M. Jackson, B. Lessig, L. Smith, J. D. Sumega, C. Knutson, M. Beekman, D. C. Johnson, D. A. Keszler, *Solid State Sci.* 2011, **13**, 2037.
13. B. Bogdan Botar, A. Ellernb, P. Kögerler, *Dalton Trans.*, 2012, **41**, 8951.
14. L. Moreno-Real, E.R. Losilla, M.A. Aranda, M. Martinez-Lara, S. Bruque, M. Gabas, *J. Solid State Chem.* 1998, **137**, 289-294.
15. N. E. Jacobsen, *NMR Spectroscopy Explained: Simplified Theory, Applications and Examples for Organic Chemistry and Structural Biology*, John Wiley & Sons, Inc., 2007.
16. L. Ronconi and P. J. Sadler, *Coord. Chem. Rev.*, 2008, **252**, 2239.
17. R. V. Parish, *NMR, NQR, EPR, and mossbauer spectroscopy in inorganic chemistry*, Ellis Horwood Limited, Chichester, West Sussex, 1990.
18. Z. L. Ma, K. M. Wentz, B. A. Hammann, I.-Y. Chang, M. K. Kamunde-Devonish, P. H.-Y. Cheong, D. W. Johnson, V. V. Terskikh, and S. E. Hayes, *Chem. Mater.*, 2014, **26**, 4978.
19. L. Allouche, C. Huguenard, and F. Taulelle, *J. Phys. Chem. Solids*, 2001, **62**, 1525.
20. L. Allouche, C. Gerardin, T. Loiseau, G. Ferey, and F. Taulelle, *Angew. Chemie Int. Ed.*, 2000, **39**, 511.
21. L. Allouche and F. Taulelle, *Inorg. Chem. Commun.*, 2003, **6**, 1167.
22. W. H. Casey, *Chem. Rev.*, 2006, **106**, 1.
23. G. Fu, L. F. Nazar, and A. D. Bain, *Chem. Mater.*, 1991, **3**, 602.
24. G. Furrer, B. L. Phillips, K.U. Ulrich, and R. Pöthig, *Science*, 2002, **297**, 2245.
25. S. K. Lee, J. F. Stebbins, C. A. Weiss, and R. J. Kirkpatrick, *Chem. Mater.*, 2003, **15**, 2605.
26. L. J. Michot, E. Montargès-Pelletier, B. S. Lartiges, J.B. d’Espinose de la Caillerie, V. Briois, *J. Am. Chem. Soc.*, 2000, **122**, 6048.
27. W. O. N. Parker, R. Millini, and I. Kiricsi, *Inorg. Chem.*, 1997, **36**, 571.
28. B. L. Phillips, W. H. Casey, and M. Karlsson, *Nature*, 2000, 379.
29. J. W. Akitt, in *Multinuclear NMR*, ed. J. Mason, Springer US, 1987, 259.
30. J. W. Akitt, *Nuclear Magnetic Resonance Spectroscopy in Liquids containing Compounds of Aluminium and Gallium*, Elsevier, 1972, **vol. 5**.

31. F. W. Wehrli, in *Annual Reports on NMR Spectroscopy*, ed. G. A. Webb, Academic Press, 1979, **vol. 9**, 125.
32. www.webelements.com
33. A. F. Oliveri, L. A. Wills, C. R. Hazlett, M. E. Carnes, P. H-Y. Cheong, D. W. Johnson, **2014**, *manuscript in preparation*.
34. L. Helm and A. E. Merbach, *Chem. Rev.*, 2005, **105**, 1923.
35. Y. Cohen, L. Avram, and L. Frish, *Angew. Chemie Int. Ed.*, 2005, **44**, 520.
36. R. C. Hardy and R. L. Cottington, *J. Res. Natl. Bur. Stand.*, 1949, **42**, 573–578.
37. W. N. Baker, *J. Chem. Phys.*, 1936, **4**.
38. T. D. W. Claridge, *High-resolution NMR techniques in organic chemistry*, 1999.
39. (a) M. Nilsson, G.A. Morris, *Mag. Res. Chem.* 2006; **44**, 655; (b) G. A. Morris, Diffusion-ordered spectroscopy (DOSY). In: D.M. Grant, R.K. Harris, ed. *Encyclopedia of Nuclear Magnetic Resonance*. Wiley. 2002: 35; (c) M. Nilsson, M. A. Connell, A. L. Davis, G. A. Morris, *Anal. Chem.*, 2006, **78**, 3040.
40. J. Ling, et al., *J. Am. Chem. Soc.*, 2010, **132**, 13395.
41. R.L. Johnson, et al., *Angew. Chemie Int. Ed.*, 2013, **52**, 7464.
42. J.R. Rustad, and W.H. Casey, *Nat. Mater*, 2012, **11**, 223.
43. J.R. Rustad, J.S. Loring, and W.H. Casey, *Geochim. Cosmochim. Ac.*, 2004, **68**, 3011.
44. C.A. Ohlin, *Chemistry-An Asian Journal*, 2012. **7**, 262.
45. C.A. Ohlin, et al., *Dalton Trans.*, 2009, **27**, 5278.
46. Villa, E.M., et al., *J. Am. Chem. Soc.*, 2010, **132**, 5264.
47. C.J. Besecker, *Inorg. Chem.*, 1985. **24**, 1027.
48. M. Filowitz, *Inorg. Chem.*, 1979, **18**, 93.
49. M. Filowitz, *J. Am. Chem. Soc.*, 1976. **98**, 2345.
50. W.G. Klemperer, *NATO ASI Series, Series C: Mathematical and Physical Sciences*, 1983, **103**, 245.
51. W.H. Casey, et al., *Geochim. Cosmochim. Ac.*, 2000, **64**, 2951.
52. E.M. Villa, *Angew. Chem. Int. Ed.*, 2008. **47**, 4844.
53. E.M. Villa, et al., *J. Am. Chem. Soc.*, 2009. **131**, 16488.

54. J.R. Black, M. Nyman, and W.H. Casey, *J. Am. Chem. Soc.* 2006. 128, **45**, 14712.
55. Ohlin, C.A., *Chem. Eur. J.*, 2011, **17**, 4408.
56. J.R. Houston, and W.H. Casey, *Dalton Trans.* 2005, **22**, 3667.
57. Houston, J.R., B.L. Phillips, and W.H. Casey, *Geochimica et Cosmochimica Acta*, 2006. **70**, 1636-1643.
58. W.H. Casey, and B.L. Phillips, *Geochim. Cosmochim. Ac.*, 2001, **65**, 705.
59. S.J. Harley, C.A. Ohlin, and W.H. Casey, *Geochim. Cosmochim. Ac.*, 2011, **75**, 3711.
60. B. Bureau, G. Silly, J.Y. Buzaré, C. Legein, D. Massiot, *Solid State Nucl. Magn. Reson.* 1999, **14**, 181.
61. (a) K. J. D. MacKenzie; M. E. Smith. *In Multinuclear Solid-State NMR of Inorganic Materials*; R.W. Cahn. Ed.; (b) *Pergamon Materials Series*, Elsevier Science Ltd, 2002, 653.
62. D. Massiot; I. Farnan; N. Gautier; D. Trumeau; A. Trokiner; J.P. Coutures. *Solid State Nucl. Magn. Reson.* 1995, **4**, 241.
63. T. Vosegaard; D. Massiot; N. Gautier; H. Jakobsen. *J. Am. Chem. Soc.*, 1998, **120**, 8184.
64. E. Rather, J.T. Gatlin, P.G. Nixon, T. Tsukamoto, V. Kravtsov, D.W. Johnson, *J. Am. Chem. Soc.* 2005, **127**, 3242.
65. M.K. Kamunde-Devonish, M.N. Jackson, Jr., Z.L. Mensinger, L.N. Zakharov, D.W. Johnson, *Inorg. Chem.* 2014, **53**, 7101.
66. D. Massiot, F. Fayon, M. Capron, I. King, S. Le Calvé, B. Alonso, J.-O. Durand, B. Bujoli, Z. Gan, G. Hoatson. *Mag. Reson. Chem.*, 2002, **40**, 70.
67. R.E. Wasylishen, S.E. Ashbrook, S. Wimperis, *NMR of Quadrupolar Nuclei in Solid Material*, Ed.; John Wiley & Sons Ltd., United Kingdom, 2012.
68. S.J. Clark, M.D. Segall, C.J. Pickard, P.J. Hasnip, M.J. Probert, K. Refson, M. Z. Payne., *Kristall.* 2005, **220**, 567.
69. C. D. Putnam, M. Hammel, G. L. Hura, and J. a Tainer, *Q. Rev. Biophys.*, 2007, **40**, 191.
70. H. Schnablegger and Y. Singh, *The SAXS Guide*, Anton Paar, Second Rev., 2011.
71. O. Glatter and O. Kratky, *Small Angle X-ray Scattering*, Academic Press Inc, New York, 1982.
72. P. B. Moore, *J. Appl. Crystallogr.*, 1980, **13**, 168.

73. Y. Hou, D. B. Fast, R. E. Ruther, J. M. Amador, L. B. Fullmer, S. R. Decker, L. N. Zakharov, M. Dolgos, and M. Nyman, *J. Solid State Chem.*, 2014, **Accepted**.
74. Y. Hou, L. N. Zakharov, and M. Nyman, *J. Am. Chem. Soc.*, 2013, **135**, 16651.
75. R. E. Ruther, B. M. Baker, J.-H. Son, W. H. Casey, and M. Nyman, *Inorg. Chem.*, 2014, **53**, 4234.
76. V. W. Day, W. G. Klemperer, and D. J. Maltbie, *J. Am. Chem. Soc.*, 1987, **109**, 299.
77. T. Kojima, M. R. Antonio, and T. Ozeki, *J. Am. Chem. Soc.*, 2011, **133**, 7248.
78. M. Nyman, T. M. Alam, F. Bonhomme, M. a. Rodriguez, C. S. Frazer, and M. E. Welk, *J. Clust. Sci.*, 2006, **17**, 197.
79. M. Nyman, F. Bonhomme, T. M. Alam, M. a. Rodriguez, B. R. Cherry, J. L. Krumhansl, T. M. Nenoff, and A. M. Sattler, *Science*, 2002, **297**, 996.
80. F. Bonhomme, J. P. Larentzos, T. M. Alam, E. J. Maginn, M. Nyman, F. Hall, and N. Dame, *Inorg. Chem.*, 2005, **44**, 1774.
81. M. Nyman, J. P. Larentzos, E. J. Maginn, M. E. Welk, D. Ingersoll, H. Park, J. B. Parise, I. Bull, and F. Bonhomme, *Inorg. Chem.*, 2007, **46**, 2067.
82. Z. Zhang, Q. Lin, D. Kurunthu, T. Wu, F. Zuo, S. Zheng, C. J. Bardeen, X. Bu, and P. Feng, *J. Am. Chem. Soc.*, 2011, **2**, 6934.
83. R. P. Oleksak, R. E. Ruther, F. Luo, K. C. Fairley, S. R. Decker, W. F. Stickle, D. W. Johnson, E. L. Garfunkel, G. S. Herman, and D. A. Keszler, *Appl. Mater. Interfaces*, 2014, **6**, 2917.
84. G. M. Muha and P. a. Vaughan, *J. Chem. Phys.*, 1960, **33**, 194.
85. M. Aberg, *Acta Chem. Scand.*, 1977, **31**, 171.
86. D. M. Tiede, R. Zhang, L. X. Chen, L. Yu, and J. S. Lindsey, *J. Am. Chem. Soc.*, 2004, **126**, 14054.
87. R. Zhang, P. Thiyagarajan, and D. M. Tiede, *J. Appl. Crystallogr.*, 2000, **33**, 565.
88. J. Lim, S. P. Yeap, H. X. Che, S. C. Low, *Nanoscale Res. Lett.*, 2013, **8**, 1.
89. S. E. Harden, *Biotechnol. Appl. Biochem.* 1986, **8**, 489.
90. T. Jian, S. H. Anastasiadis, A. K. Rizos, G. Fytasc, *J. Chem. Phys.*, 1994, **101**, 3222.
91. <http://www.intechopen.com/books/proteininteractions/characterization-of-protein-proteininteractions-via-static-and-dynamic-light-scattering>
92. <http://www.wyatt.com>

93. J. A. Dieringer et. al., *Faraday Discuss.*, 2006, **132**, 9.
94. M. E. Keating, H. J. Byrne, *Int. J. Nanomedicine*, 2013, **8**, 1335.
95. Mason, T.G.; Gang, H.; Weitz, D.A., *J. Opt. Soc. Am. A*, 1997, **14**, 139.
96. W. Wang, W. Liu, I.-Y. Chang, L. A. Wills, L. N. Zakharov, S. W. Boettcher, P. H.-Y. Cheong, C. Fang, D. A. Keszler, *PNAS* 2013, **110**, 1839.
97. M. N. Jackson Jr, L. A. Willis, I.-Y. Chang, M. E. Carnes, L. Scatena, P. H.-Y. Cheong, D. W. Johnson, *Inorg. Chem.*, 2013, **52**, 6187.
98. W. W. Rudolph, R.; Mason, C. C. Pye, *Phys. Chem. Chem. Phys.* 2000, **2**, 5030.
99. X. López, J. J. Carbó, C. Bo, J. M. Poblet, *Chem. Soc. Rev.*, 2012, **41**, 7537.
100. A. J. Bridgeman, *Chem. Eur. J.* 2004, **10**, 2935.
101. X. López, J. M. Poblet, *Inorg. Chem.* 2004, **43**, 686.
102. H. El Moll, et al., *Chem. Eur. J.*, 2011, **17**, 14129.
103. R. Carr, I. A. Weinstock, A. Sivaprasadarao, A. Müller, *Nano Lett.*, 2008, **8**, 3916.
104. L. Vilà-Nadal, et al. *Phys. Chem. Chem. Phys.*, 2011, **13**, 20136.
105. J. Gao, P. Amara, C. Alhambra, M. J. Field, *J. Phys. Chem. A.*, 1998, **102**, 4714.
106. A. Tongraar, K. R. Liedl, B. M. Rode, *J. Phys. Chem. A.*, 1998 **102**, 10340.
107. L. Kronik, T. Stein, *J. Chem. Theory Comput.*, 2012, **8**, 1515.
108. F. De Angelis, S. Fantacci, A. Selloni, M. K. Nazeeruddin, M. Grätzel, *J. Am. Chem. Soc.*, 2007, **129**, 14156.
109. J. F. Parker, K. A. Kacprzak, O. Lopez-Acevedo, H. Häkkinen, R. W. Murray, *J. Phys. Chem. C*, 2010, **114**, 8276.
110. X. López, C. Bo, J. M. Poblet, *J. Am. Chem. Soc.* 2002, **124**, 12574.
111. J. M. Maestre, X. Lopez, C. Bo, J.M. Poblet, C. A. Daul, *Inorg. Chem.*, 2002, **41**, 1883.
112. W. B. Kim, T. Voitl, G. J. Rodriguez-Rivera, J. A. Dumesic, *Science* 2004, **305**, 1280.
113. D. G. Truhlar, C. J. Cramer, A. Lewis, J. A. Bumpus, *J. Chem. Ed.* 2004, **81**, 596.

CHAPTER II

1. G.D. Wilk, R.M. Wallace, J.M. Anthony, *J. Appl. Phys.* **2001**, *89*, 5243.
2. Mensinger, Z. L.; Wang, W.; Keszler, D. A.; Johnson, D. W. *Chem. Soc. Rev.* **2012**, *41*, 1019.
3. E.; Gatlin, J. T.; Nixon, P. G.; Tsukamoto, T.; Kravtsov, V.; Johnson, D. W. *J. Am. Chem. Soc.* **2005**, *127*, 3242.
4. Mensinger, Z. L.; Gatlin, J. T.; Meyers, S. T.; Zakharov, L. N.; Keszler, D. A.; Johnson, D. W. *Angew. Chem Int. Ed.* **2008**, *47*, 9484.
5. Bi, Z.; Feng, C.; Wang, D.; Ge, X.; Tang, H. *Colloid Surf, A.* **2012**, *407*, 91.
6. Bi, Z.; Feng, C.; Wang, D.; Ge, X.; Tang, H. *Colloid Surf, A.* **2012**, *416*, 73.
7. Oliveri, A. F.; Carnes, M. E.; Baseman, M. M.; Richman, E. K.; Hutchison, J. E.; Johnson, D. W. *Angew. Chem Int. Ed.* **2012**, *51*, 10992.
8. Alemayehu, M.; Davis, J. E.; Jackson, M.; Lessig, B.; Smith, L.; Sumega, J. D.; Knutson, C.; Beekman, M.; Johnson, D. C.; Keszler, D. A. *Solid State Sci.* **2011**, *13*, 2037.
9. Piszczek, P.; Radtke, A.; Grodzicki, A.; Wojtczak, A.; Chojnacki, J. *Polyhedron.* **2007**, *26*, 679.
10. Wang, W.; Wentz, K. M.; Hayes, S. E.; Johnson, D. W.; Keszler, D. A. *Inorg. Chem.* **2011**, *3*, 9
11. Frisch, M. J. *et al. Gaussian 09.* (Gaussian, Inc.: Wallingford, CT).
12. Waterland, M.R.; Kelley, A.M., *J. Chem. Phys.* **2000**, *113*, 6760.
13. Wang, W.; Chang, I.-Y.; Zakharov, L.; Cheong, P. H.-Y.; Keszler, D.A. *Inorg. Chem.* **2013**, *52*, 1807.
14. Rudolph, W. W.; Masonb, R.; Pyec, C. C. *Phys. Chem. Chem. Phys.* **2000**, *2*, 5030.
15. Klopprogge, J. T.; Frost, R. L. *J. Mater. Sci.* **1999**, *34*, 4199.
16. Klopprogge, J. T.; Frost, R. L. *Spectrochim. Acta. A.* **1999**, *55*, 163.
17. Klopprogge, J. T.; Frost, R. L. *J. Mater. Sci.* **1999**, *4*, 4367.
18. Frost, R. L. *Clays Clay Miner.* **1998**, *46*, 280.
19. Brühne, S.; Gottlieb, S.; Assmus, W.; Alig, E.; Schmidt, M. U. *Cryst. Growth Des.* **2008**, *8*, 489.

20. Frenzel, J.; Oliveira, A. F.; Duarte, H.; Heine, T.; Seifert, G. *Z. Anorg. Allg. Chem.* **2005**, *631*, 1267.
21. Noel, Y.; Demichelis, R.; Pascale, F.; Ugliengo, P.; Orlando, R.; Dovesi, R. *Phys. Chem. Miner.* **2008**, *36*, 47.
22. Frost, R.; Ruan, H.; Klopogge, T. *J. Raman. Spectrosc.* **2001**, *32*, 745.
23. Baschenko, S. M.; Marchenko, L. S. *Semicond. Phys. Quantum Electron. Optoelectron.* **2011**, 77.
24. Oliveri, A. F.; Elliott III, E. W.; Carnes, M. E.; Hutchison, J. E.; Johnson, D. W. *ChemPhysChem* **2013**, *manuscript submitted*.
25. Wang, W.; Liu, W.; Chang, I.-Y.; Wills, L. A.; Zakharov, L. N.; Cheong, P. H.-Y.; Boettcher, S. W.; Fang, C.; Keszler, D. A. **2013**, *manuscript submitted*.
26. Scatena, L.F.; Richmond, G.L.; *J. Phys. Chem. B* **2001**, *105*, 11240.
27. Rudolph, W. W.; Pye, C. C.; Irmer, G. *J. Raman. Spectrosc.* **2002**, *33*, 177.
28. Rudolph, W. W.; Pye, C. C. *Phys. Chem. Chem. Phys.* **2002**, *4*, 4319.
29. Zhao, Y.; Yang, J.; Frost, R. L. *J. Raman. Spectrosc.* **2008**, 1327.

CHAPTER III

1. Anderson, J.T.; Munsee, C.L.; Hung, C.M.; Phung, T.M.; Herman, G.S.; Johnson, D.C.; Wager, J.F.; Keszler, D.A., *Adv. Funct. Mater.*, **2007**, *17*, 2117.
2. Meyers, S.T.; Anderson, J.T.; Hong, D.; Hung, C.M.; Wager, J.F.; Keszler D.A., *Chem. Mater.*, **2007**, *19*, 4023.
3. Keszler, D.A., *Nature Mater.*, **2011**, *10*, 9.
4. Wager, J.F.; Yeh, B.; Hoffman, R.L.; Keszler, D.A., *Curr. Opin. Solid State Mater. Sci.*, **2013**, *in press*, <http://dx.doi.org/10.1016/j.cossms.2013.07.002>.
5. Mitzi, D. *Solution Processing of Inorganic Materials*; John Wiley & Sons: New Jersey, 2009.
6. (a) Presley, R. A.; Hong, D.; Chiang, H.Q.; Hung, C.M.; Hoffman, R.L.; Wager, J.F., *Solid-state Electronics.*, **2006**, *50*, 500; (b) Bloor, L. G.; Carmalt, C. J.; Pugh, D. *Coord. Chem. Rev.* **2011**, *255*, 1293.
7. Rather, E.; Gatlin, J. T.; Nixon, P. G.; Tsukamoto, T.; Kravtsov, V.; Johnson, D. W. *J. Am. Chem. Soc.* **2005**, *127*, 3242

8. Mensinger, Z. L.; Gatlin, J. T.; Meyers, S. T.; Zakharov, L. N.; Keszler, D. A.; Johnson, D. W., *Angew. Chem. Int. Ed.*, **2008**, *47*, 9484.
9. Hwang, Y.H.; Jeon, J.H.; Seo, S.J.; Bae, B.S., *Electrochem. Solid-State Lett.*, **2009**, *12*, 336.
10. Hwang, Y.H.; Bae, B.S., *J. Display Technol.*, **2013**, *9*, 704.
11. Kim, H.J.; No, S.Y.; Eom, D.; Hwang, C.S., *J. Kor. Phys. Soc.* **2006**, *49*, 1271.
12. Silva, R.; Zaniquelli, M.E.D., *Thin Film Solids.*, **2004**, *449*, 86.
13. Fan, G.; Sun, W.; Wang, H.; Feng, L., *Chem. Eng. J.*, **2011**, *174*, 467.
14. (a) Gatlin, J. T.; Mensinger, Z. L.; Zakharov, L. N.; MacInnes, D.; Johnson, D. W., *Inorg. Chem.*, **2008**, *47*, 1267. (b) Wang, W.; Wentz, K. M.; Hayes, S.E.; Johnson, D.W.; Keszler, D.A., *Inorg. Chem.*, **2011**, *50*, 4683.
15. Sun, Z.; Zhao, H.D.; Tong, H.G.E.; Wang, R.F.; Zhu, F.Z., *Chin. J. Struct. Chem.*, **2006**, *25*, 1217.
16. Casey, W.H.; Olmstead, M.M.; Phillips, B.L., *Inorg. Chem.*, 2005, *44*, 4888.
17. Sun, Z.; Wang, H.; Feng, H.; Zhang, Y.; Du, S., *Inorg. Chem.*, **2011**, *50*, 9238.
18. Mensinger, Z. L.; Wang, W.; Keszler, D. A.; Johnson, D. W., *Chem. Soc. Rev.*, **2012**, *41*, 1019.
19. Socol, G.; Socol, M.; Stefan, N.; Axente, E.; Popescu-Pelin, G.; Craciun, D.; Duta, L.; Mihailescu, C.N.; Mihailescu, I.N.; Stanculesu, A.; Visan, D.; Sava, V.; Galca, A.C.; Luculescu, C.R.; Craciun, V., *Appl. Surf. Sci.*, **2012**, *260*, 42.
20. Deery, M.J.; Howarth, O.W.; Jennings, K.R., *J. Chem. Soc. Dalton Trans.*, **1997**, 4783.
21. Spyratou, A.; Clifford, S.; Melich, X.; Deville, C.; Tissot, M.; Bonvin, G.; Perrottet, P.; Williams, A., *Aust. J. Chem.*, **2009**, *62*, 1291.
22. Sahureka, F.; Burns, R.C.; Nagy-Felsobuki, E.I., *Inorg. Chim. Acta*, **2003**, *351*, 69.
23. Corella-Ochoa, M.N.; Miras, H.N.; Long, D.L.; Cronin, L., *Chem. Eur. J.*, **2012**, *18*, 13743.
24. Lee, A. P.; Phillips, B. L.; Olmstead, M. M.; Casey, W. H., *Inorg. Chem.*, **2001**, *40*, 4485.
25. Lee, A. P.; Furrer, G.; Casey, W. H., *J. Colloid Interface Sci.*, **2002**, *250*, 269.
26. Parker, W. O., Jr.; Millini, R.; Kiricsi, I., *Inorg. Chem.*, **1997**, *36*, 571.
27. Keggin, J. F., *Proc. Roy. Soc. A.*, **1934**, *144*, 75.

28. Mensinger, Z. L.; Zakharov, L. N.; Johnson, D. W., *Acta Crystallogr. Sect. E: Struct. Rep. Online*, **2008**, E64, i8.
29. Gili, P., Nunez, P.; Lorenzo-Luis, P. A., *Acta Cryst. C: Cryst. Struct. Commun.*, **2006**, 56, E441.
30. Mensinger, Z. L.; Gatlin, J. T.; Meyers, S. T.; Zakharov, L. N.; Keszler, D. A.; Johnson, D. W. *Angew. Chem Int. Ed.* **2008**, 47, 9484.
30. Oliveri, A.F.; Carnes, M.E.; Baseman, M.M.; Johnson, D.W., *Angew. Chem. Int. Ed.*, **2012**, 51, 10992.
31. Oliveri, A. F.; Elliott, E. W.; Carnes, M. E.; Hutchison, J. E.; Johnson, D. W., *ChemPhysChem.*, **2013**, 14, 2655.
32. Jackson Jr, M. N. J.; Willis, L. A.; Chang, I.-Y.; Carnes, M. E.; Scatena, L.; Cheong, P. H.-Y.; Johnson, D. W., *Inorg. Chem.*, **2013**, 52, 6187.
33. Vorotyntsev, M.A.; Zinovyeva, V.A.; Picquet, M., *Electrochimica Acta.*, **2010**, 55, 5063.
34. Tsierkezos, N.G., *J. Solution Chem.*, **2007**, 36, 289.
35. Cheng, I.F.; Muftikian, R.; Fernando, Q.; Korte, N., *Chemosphere*, **1997**, 35, 2689.
36. Aldridge, S.; Downs, A.J. *The Group 13 Metals Aluminum, Gallium, Indium, and Thallium: Chemical Patterns and Peculiarities*; John Wiley & Son, Ltd.: United Kingdom, 2011.
37. Rudolph, W.W.; Fischer, D.; Tomney, M.R.; Pye, C.C., *Phys. Chem. Chem. Phys.*, **2004**, 6, 5145.

CHAPTER IV

1. D. P. Olander, R. S. Marianelli, and R. C. Larson, *Anal. Chem.*, 1969, **41**, 1097–1099.
2. J. Y. Bottero, J. M. Cases, F. Flessinger, and J. E. Poirier, *J. Phys. Chem.*, 1980, **84**, 2933–2939.
3. R. E. Schuster and A. Fratiello, *J. Chem. Phys.*, 1967, **47**, 1554–1555.
4. A. Fratiello, R. E. Lee, V. M. Nishida, and R. E. Schuster, *J. Chem. Phys.*, 1968, **48**, 3705–3711.
5. R. E. Connick and D. N. Fiat, *J. Chem. Phys.*, 1963, **39**, 1349–1351.
6. G. Johansson, G. Lundgren, L. G. Sillén, and R. Söderquist, *Acta Chem. Scand.*, 1960, **14**, 769–771.

7. G. Johansson, G. Lundgren, L. G. Sillén, and R. Söderquist, *Acta Chem. Scand.*, 1960, **14**, 771–773.
8. G. Furrer, B. L. Phillips, K.-U. Ulrich, and R. Pöthig, *Science (80-.)*, 2002, **297**, 2245–2247.
9. W. H. Casey, *Chem. Rev.*, 2006, **106**, 1–16.
10. W. Wang, K. M. Wentz, S. E. Hayes, D. W. Johnson, and D. A. Keszler, *Inorg. Chem.*, 2011, **50**, 4683–4685.
11. J. T. Gatlin, Z. L. Mensinger, L. N. Zakharov, D. MacInnes, and D. W. Johnson, *Inorg. Chem.*, 2008, **47**, 1267–1269.
12. W. Wang, W. Liu, I.-Y. Chang, L. A. Wills, L. N. Zakharov, S. W. Boettcher, P. H.-Y. Cheong, C. Fang, and D. A. Keszler, *Proc. Natl. Acad. Sci.*, 2013, **110**, 18397–18401.
13. J. R. Houston, B. L. Phillips, and W. H. Casey, *Geochim. Cosmochim. Acta*, 2006, **70**, 1636–1643.
14. A. Putnis, *Sci.*, 2014, **343**, 1441–1442.
15. M. K. Kamunde-Devonish, M. N. Jackson Jr., Z. L. Mensinger, L. N. Zakharov, and D. W. Johnson, *Inorg. Chem.*, 2014, **53**, 7101–7105.
16. A. F. Oliveri, M. E. Carnes, M. M. Baseman, E. K. Richman, J. E. Hutchison, and D. W. Johnson, *Angew. Chemie Int. Ed.*, 2012, **51**, 10992–10996.
17. J. Sandström, *Dynamic Nmr Spectroscopy*, Academic Press, 1982.

CHAPTER V

1. Rabinovich, D. *Nature Chem* 2013, 5, 67.
2. Mertens, J.; Casentin, B.; Masion, A.; Pothig, R.; Wehrli, B.; Furrer, G. *Water Res.* 2012, 46 53-62.
3. Casey, W.H. *Chem. Rev.* 2006, 106, 1-16.
4. Casey, W.H., *Review of Geophysics* 2003, 41, 1-20.
5. Casey, W.H.; Olmstead, M.M.; Phillips, B.L., *Inorg. Chem.* 2005, 44, 4888-4890.
6. Wang, W.; Wentz, K. M.; Hayes, S. E.; Johnson, D. W.; Keszler, D. A., *Inorg. Chem.* 2011, 50, 4683-4685.

7. Wang, W.; Liu, W.; Chang, I.-Y.; Wills, L. A.; Zakharov, L. N.; Boettcher, S. W.; Cheong, P. H.-Y.; Fang, C.; Keszler, D. A., *PNAS* 2013, 110, 18397-18401.
8. Jackson, M. N., Jr.; Wills, L. A.; Chang, I. Y.; Carnes, M. E.; Scatena, L. F.; Cheong, P. H.; Johnson, D. W., *Inorg Chem* 2013, 52, 6187-6192.
9. Armstrong, C.R.; Casey, W.H.; Navrotsky, A., *PNAS* 2011, 108, 14775-14779.
10. Ghosh, S.; Mashagekhi, H.; Pan, B.; Bhowmik, P.; Xing, B., *Lang-muir* 2008, 24, 12385-12391.
11. Li, H.; Addai-Mensah, J.; Thomas, J.C.; Gerson, A.R., *Colloid Sur-faces A: Physiochem. Eng. Aspect* 2003, 223, 83-94.
12. Mookherjee, M.; Keppler, Hans. B.; Manning, G.E.; *Geochemica et Cosmochimica Acta* 2014, 133, 128-141.
13. Bi, Z.; Feng, G.; Wang, D.; Ge, X.; Tang, H., *Colloid and Surfaces A: Physicochem. Eng. Aspects* 2012, 407, 91-98.
14. Richardson, D.; Alger, T.D., *J. Phys. Chem.* 1975, 79, 1773-1739.
15. Wang, W.; Yang, H.; Wang, X.; Jiang, J.; Wi, J., *J. Environmental Sciences* 2010, 22, 211-217.
16. "Aluminum in Drinking Water" World Health Organization, 2003, 2, 1-9.
17. Brand, J.C.; Cawthon, T.M., *Contribution from the James Forrestal Research Center, Princeton University* 1954, 77, 319-323.

CHAPTER VI

1. a) Jiang, K.; Zakutayev, A.; Stowers, J.; Anderson, M. D.; Tate, J.; McIntyre, D. H.; Johnson, D. C.; Keszler, D. A. *Solid State Sci.* 2009, **11**, 1692–1699. b) Jiang, K.; Anderson, J. T.; Hoshino, K.; Li, D.; Wager, J. F.; Keszler, D. A. *Chem. Mater.* 2011, **23**, 945–952. c) Meyers, S. T.; Anderson, J. T.; Hong, D.; Hung, C. M.; Wager, J. F.; Keszler, D. A. *Chem. Mater.* 2007, **19**, 4023–4029. d) Meyers, S. T.; Anderson, J. T.; Hung, C. M.; Thompson, J.; Wager, J. F.; Keszler, D. A. *J. Am. Chem. Soc.* 2008, **130**, 17603–9. e) Anderson, J. T.; Munsee, C. L.; Hung, C. M.; Phung, T. M.; Herman, G. S.; Johnson, D. C.; Wager, J. F.; Keszler, D. A. *Adv. Funct. Mater.* 2007, **17**, 2117–2124. f) Alemayehu, M.; Davis, J. E.; Jackson, M.; Lessig, B.; Smith, L.; Sumega, J. D.; Knutson, C.; Beekman, M.; Johnson, D. C.; Keszler, D. A. *Solid State Sci.* 2011, **13**, 2037–2040. (g) Nadarajah, A.; Carnes, M. E.; Kast, M. G.; Johnson, D. W.; Boettcher, S. W. *Chem. Mater.* 2013, **25**, 4080.
2. a) Murugavel, R.; Walawalkar, M. G.; Dan, M.; Roesky, H. W.; Rao, C. N. R. *Acc. Chem. Res.*, 2004, **37**, 763–774. b) Furdala, K. L.; Tilley, T. D. *J. Am. Chem. Soc.*

- 2001, **123**, 10133-10134. c) Sekar, P.; Greyson, E. C.; Barton, J. E.; Odom, T. W. *J. Am. Chem. Soc.*, 2005, **127**, 2054–2055. d) Kim, H. S.; Byrne, P. D.; Facchetti, A.; Marks, T. J. *J. Am. Chem. Soc.*, 2008, **130**, 12580–12581.
3. Mensinger, Z. L.; Gatlin, J. T.; Meyers, S. T.; Zakharov, L. N.; Keszler, D. A.; Johnson, D. W. *Angew. Chem. Int. Ed.* 2008, **47**, 9484–6.
 4. Smith, S. W.; Wang, W.; Keszler, D. A.; John F. Conley Jr. *J. Vac. Sci. Technol. A*, 2014, **32**, 041501.
 5. a) Gatlin, J. T.; Mensinger, Z. L.; Zakharov, L. N.; Macinnes, D.; Johnson, D. W. *Inorg. Chem.* 2008, **47**, 1267–9. b) Mensinger, Z. L.; Wang, W.; Keszler, D. A.; Johnson, D. W. *Chem. Soc. Rev.* 2012, **41**, 1019–30.
 6. a) Wang, W.; Wentz, K. M.; Hayes, S. E.; Johnson, D. W.; Keszler, D. A. *Inorg. Chem.* 2011, **50**, 4683–4685. b) Wang, W.; Chang, I. Y.; Zakharov, L.; Cheong, P. H.-Y.; Keszler, D.A., *Inorg. Chem.* 2013, **52**, 1807-1811.
 7. Wang, W.; Liu, W.; Chang, I.-Y.; Willis, L. A.; Zakharov, L. N.; Boettcher, S. W.; Cheong, P. H.-Y.; Fang, C.; Keszler, D. A. *Proc. Natl. Acad. Sci. USA* 2013, **110**, 18397.
 8. Hu, C.; Liu, H.; Qu, J. *Colloid Surface A*. 2005, **260**, 109-117.
 9. Pourbaix, M., *Atlas of electrochemical equilibria in aqueous solutions*. 2nd English Ed.: National Association of Corrosion Engineers, Houston, 1974.
 10. Saltman, W. M.; Nachtrieb, N. H. *J. Electrochem. Soc.* 1953, **100**, 126-130.
 11. Pretsch, E.; Bühlmann, P.; Badertscher, M. *Structure Determination of Organic Compounds: Tables of Spectral Data*, 4th Ed. Springer-Verlag, Berlin, 2009.
 12. da Cunha, M. C. P. M.; De Souza, J. P. I.; Nart, F. C. *Langmuir*, 2000, **16**, 771-777.
 13. a) *Standard Potentials in Aqueous Solutions*; Bard, A. J.; Parsons, R.; Jordan, J., Eds.; International Union of Pure and Applied Chemistry, 1985. b) Mahle, T. "*Metallic and bimetallic catalysts for electrochemical reduction of problematic aqueous anions*", Thesis, University of Illinois, Urbana-Champaign, 2012.
 14. Oliveri, A. F.; Carnes, M. E.; Baseman, M. M.; Richman, E. K.; Hutchison, J. E.; Johnson, D. W. *Angew. Chem. Int. Ed.* 2012, **51**, 10992-10996.
 15. Oliveri, A. F.; Elliott, E. W.; Carnes, M. E.; Hutchison, J. E.; Johnson, D. W., *ChemPhysChem.*, **2013**, *14*, 2655
 16. Kamunde-Devonish, M. K.; Jackson, Jr., M. N.; Mensinger, Z. L.; Zakharov, L. N.; Johnson, D. W. *Inorg. Chem.* 2014, *Article ASAP* (DOI: 10.1021/ic403121r).

17. Jackson, Jr, M. N.; Willis, L. A.; Chang, I.-Y.; Carnes, M. E.; Scatena, L.; Cheong, P. H.-Y.; Johnson, D. W. *Inorg. Chem.* 2013, **52**, 6187-6192.
18. Hong, D.; Yerubandi, G.; Chiang, H. Q.; Spiegelberg, M. C.; Wager, J. F. *Crit. Rev. Solid State Mater. Sci.* 2008, **33**, 101-132.
19. Henry, M.; Jolivet, J. P.; Livage, J.; “Aqueous Chemistry of Metal Cations: Hydrolysis, Condensation and Complexation”, *Structure and Bonding* 77, Springer-Verlag, Berlin, 1992.
20. (a) Kim, M.-G.; Kanatzidis, M. G.; Facchetti, A.; Marks, T. J. *Nat. Mater.* 2011, **10**, 382. (b) Hwang, Y. H.; Seo, J.-S.; Yun, J. M.; Park, H.; Yang, S.; Park, S.-H. K.; Bae, B.-S. *NPG Asia Mater.* 2013, **5**, e45. (c) Kamiya, T.; Hosono, H. *NPG Asia Mater.* 2010, **2**, 15.
21. (a) Rim, Y. S.; Chen, H.; Kou, X.; Duan, H.-S.; Zhou, H.; Cai, M.; Kim, H. J.; Yang, Y. *Adv. Mater.* 2014, **26**, 4273. (b) Street, R. A.; Ng, T. N.; Lujan, R. A.; Son, I.; Smith, M.; Kim, S.; Lee, T.; Moon, Y.; Cho, S. *ACS Appl. Mater. Interfaces* 2014, **6**, 4428.

CHAPTER VII

1. C. Aronica, G. Pilet, G. Chastanet, W. Wernsdorfer, J.-F. Jacquot, and D. Luneau, *Angew. Chem. Int. Ed. Engl.*, 2006, **45**, 4659–62.
2. X.-H. Bu, M.-L. Tong, H.-C. Chang, S. Kitagawa, and S. R. Batten, *Angew. Chem. Int. Ed. Engl.*, 2004, **43**, 192–5.
3. E. Q. Procopio, T. Fukushima, E. Barea, J. A. R. Navarro, S. Horike, and S. Kitagawa, *Chemistry*, 2012, **18**, 13117–25.
4. V. Tangoulis, C. P. Raptopoulou, S. Paschalidou, A. E. Tsohos, E. G. Bakalbassis, A. Terzis, and S. P. Perlepes, *Inorg. Chem.*, 1997, **36**, 5270–5277.
5. E. M. Johnston, S. Dell’Acqua, S. Ramos, S. R. Pauleta, I. Moura, and E. I. Solomon, *J. Am. Chem. Soc.*, 2014, **136**, 614–617.
6. D.-D. Li, F.-P. Huang, G.-J. Chen, C.-Y. Gao, J. L. Tian, W. Gu, X. Liu, and S.-P. Yan, *J. Inorg. Biochem.*, 2010, **104**, 431–441.
7. D.-D. Li, J. L. Tian, W. Gu, X. Liu, and S.-P. Yan, *J. Inorg. Biochem.*, 2010, **104**, 171–179.
8. T. C. Brunold, *Proc. Natl. Acad. Sci.*, 2007, **104**, 20641–20642.

9. S. Hikichi, M. Yoshizawa, Y. Sasakura, M. Akita, and Y. Moro-oka, *J. Am. Chem. Soc.*, 1998, **120**, 10567–10568.
10. S. Kundu, F. F. Pfaff, E. Miceli, I. Zaharieva, C. Herwig, S. Yao, E. R. Farquhar, U. Kuhlmann, E. Bill, P. Hildebrandt, H. Dau, M. Driess, C. Limberg, and K. Ray, *Angew. Chem. Int. Ed. Engl.*, 2013, **52**, 5622–6.
11. P. L. Larsen, T. J. Parolin, D. R. Powell, M. P. Hendrich, and A. S. Borovik, *Angew. Chemie Int. Ed.*, 2003, **42**, 85–89.
12. T. Jia, S. Zhu, M. Shao, Y. Zhao, and M. Li, *Inorg. Chem. Commun.*, 2008, **11**, 1221–1223.
13. Y.-Q. Zheng, D.-Y. Cheng, B.-B. Liu, and W.-X. Huang, *Dalt. Trans.*, 2011, **40**, 277–286.
14. N. Lah, I. Leban, and G. Giester, *Acta Crystallogr. Sect. C*, 2007, **C63**, m222–m224.
15. R. Cejudo, G. Alzuet, J. Borrás, M. Liu-González, and F. Sanz-Ruiz, *Polyhedron*, 2002, **21**, 1057–1061.
16. A. D. Burrows, M. F. Mahon, V. M. Sebestyen, Y. Lan, and A. K. Powell, *Inorg. Chem.*, 2012, **51**, 10983–10989.
17. G. Li, S. Song, N. Xu, X. Liu, and Z. Su, *J. Solid State Chem.*, 2008, **181**, 2406–2411.
18. K. Darling, W. Ouellette, A. Prosvirin, S. Freund, K. R. Dunbar, and J. Zubieta, *Cryst. Growth Des.*, 2012, **12**, 2662–2672.
19. J. Chen, T.-W. Wang, Z. Zhang, Y. Song, Q. Zhao, J. Ni, and Z.-L. Wang, *J. Mol. Struct.*, 2006, **794**, 154–159.
20. E. Rather, J. T. Gatlin, P. G. Nixon, T. Tsukamoto, V. Kravtsov, and D. W. Johnson, *J. Am. Chem. Soc.*, 2005, **127**, 3242–3243.
21. L. Que Jr. and W. B. Tolman, *Angew. Chem. Int. Ed. Engl.*, 2002, **41**, 1114–1137.
22. R.L. Frost, P.A. Williams, W. Martens, P. Leverett, J.T. Klopogge, *AM Mineral*, 2004, **89**, 1130-1137.
23. W. Marten, R.L. Frost, J.T. Klopogge, P.A. Williams, *J Raman Spectrosc*, 2003, **34**, 145-151.

CHAPTER VIII

1. Ito, H., Chemical amplification resists for microlithography. In *Microlithography - Molecular Imprinting*, Ito, H.; Marty, J. D.; Mauzak, M., Eds. Springer-Verlag Berlin: Berlin, 2005; Vol. 172, pp 37-245.
2. Yasin, S.; Hasko, D. G.; Ahmed, H., *Appl. Phys. Lett.* **2001**, 78, 2760-2762.
3. Duan, H. G.; Winston, D.; Yang, J. K. W.; Cord, B. M.; Manfrinato, V. R.; Berggren, K. K., *Journal of Vacuum Science & Technology B* **2010**, 28, C6C58-C56C62
4. Grigorescu, A. E.; Hagen, C. W., *Nanotechnology* **2009**, 20
5. Manfrinato, V. R.; Zhang, L. H.; Su, D.; Duan, H. G.; Hobbs, R. G.; Stach, E. A.; Berggren, K. K., *Nano Lett.* **2013**, 13, 1555-1558
6. Yoshimura, T.; Shiraishi, H.; Yamamoto, J.; Okazaki, S., *Appl. Phys. Lett.* **1993**, 63, 764-766
7. Nagase, M.; Namatsu, H.; Kurihara, K.; Iwadate, K.; Murase, K.; Makino, T., *Microelectronic Engineering* **1996**, 30, 419-422
8. Yamaguchi, T.; Namatsu, H.; Nagase, M.; Yamazaki, K.; Kurihara, K., *Appl. Phys. Lett.* **1997**, 71, 2388-2390
9. Fujita, J.; Ohnishi, Y.; Ochiai, Y.; Matsui, S., *Appl. Phys. Lett.* **1996**, 68, 1297-1299
10. Dai, J. Y.; Chang, S. W.; Hamad, A.; Yang, D.; Felix, N.; Ober, C. K., *Chem. Mat.* **2006**, 18, 3404-3411
11. Namatsu, H.; Takahashi, Y.; Yamazaki, K.; Yamaguchi, T.; Nagase, M.; Kurihara, K., *Journal of Vacuum Science & Technology B* **1998**, 16, 69-76
12. Trikeriotis, M.; Krysak, M.; Chung, Y. S.; Ouyang, C.; Cardineau, B.; Brainard, R.; Ober, C. K.; Giannelis, E. P.; Cho, K., *J. Photopolym Sci. Technol.* **2012**, 25, 583-586
13. Neisser, M.; Cho, K.; Petrillo, K., *J. Photopolym Sci. Technol.* **2012**, 25, 87-94
14. Stowers, J.; Keszler, D. A., *Microelectronic Engineering* **2009**, 86, 730-733
15. Telecky, A.; Xie, P.; Stowers, J.; Grenville, A.; Smith, B.; Keszler, D. A., *Journal of Vacuum Science & Technology B* **2010**, 28, C6S19-C16S22
16. Stowers, J. K.; Telecky, A.; Kocsis, M.; Clark, B. L.; Keszler, D. A.; Grenville, A.; Anderson, C. N.; Naulleau, P. P. In *Directly patterned inorganic hardmask for EUV lithography*, Proc. SPIE 7969, Extreme Ultraviolet (EUV) Lithography II, 2011; 2011; pp 796915-796915

17. Muha, G. M.; Vaughan, P. A., *The Journal of Chemical Physics* **1960**, 33, 194-199
18. Aberg, M., *Acta Chemica Scandinavica Series A-Physical and Inorganic Chemistry* **1977**, 31, 171-181
19. Connick, R. E.; McVey, W. H., *J. Am. Chem. Soc.* **1949**, 71, 3182-3191
20. Anderson, J. T.; Munsee, C. L.; Hung, C. M.; Phung, T. M.; Herman, G. S.; Johnson, D. C.; Wager, J. F.; Keszler, D. A., *Advanced Functional Materials* **2007**, 17, 2117-2124
21. Pappas, I.; Fitzgerald, M.; Huang, X. Y.; Li, J.; Pan, L., *Crystal Growth & Design* **2009**, 9, 5213-5219
22. Chiavacci, L. A.; Santilli, C. V.; Pulcinelli, S. H.; Craievich, A. F., *J. Appl. Crystallogr.* **1997**, 30, 750-754
23. Hu, Y.-J.; Knope, K. E.; Skanthakumar, S.; Kanatzidis, M. G.; Mitchell, J. F.; Soderholm, L., *J. Am. Chem. Soc.* **2013**, 135, 14240-14248
24. Dengel, A. C.; Griffith, W. P., *Polyhedron* **1989**, 8, 1371-1377
25. Tarafder, M. T. H.; Miah, M. A. L., *Inorg. Chem.*, **1986**, 25, 2265-2268
26. Tarafder, M. T. H.; Bhattacharjee, P.; Sarkar, A. K., *Polyhedron* **1992**, 11, 795-798
27. Piquemal, J. Y.; Briot, E.; Bregeault, J. M., *Dalton Transactions* **2013**, 42, 29-45
28. Malinowski, E. R.; Cox, R. A.; Haldna, U. L., *Anal. Chem.* **1984**, 56, 778-781
29. Rudolph, W. W.; Brooker, M. H.; Tremaine, P. R., *J. Solut. Chem.* **1999**, 28, 621-630
30. Szilagyi, I.; Konigsberger, E.; May, P. M., *Inorganic Chemistry* **2009**, 48, 2200-2204
31. Thompson, R. C., *Inorganic Chemistry* **1985**, 24, 3542-3547
32. Vasquez, R. P., *J. Electron Spectrosc. Relat. Phenom.* **1990**, 50, 167-170
33. Colon, J. L.; Thakur, D. S.; Yang, C. Y.; Clearfield, A.; Martin, C. R., *J. Catal.* **1990**, 124, 148-159
34. Barreca, D.; Milanov, A.; Fischer, R. A.; Devi, A.; Tondello, E., *Surface Science Spectra* **2007**, 14, 34-40
35. Shimizu, H.; Sato, T.; Konagai, S.; Ikeda, M.; Takahashi, T.; Nishide, T., *Jpn. J. Appl. Phys. Part 1 - Regul. Pap. Brief Commun. Rev. Pap.* **2007**, 46, 4209-4214
36. Flynn, B.; Kim, D.; Clark, B. L.; Telecky, A.; Arnadottir, L.; Szanyi, J.; Keszler, D. A.; Herman, G. S., *Surface and Interface Analysis* **2013**

37. Sarma, D. D.; Rao, C. N. R., *J. Electron Spectrosc. Relat. Phenom.* **1980**, *20*, 25-45
38. Hinsberg, W. D.; Willson, C. G.; Kanazawa, K. K., *J. Electrochem. Soc.* **1986**, *133*, 1448-1451
39. Hinsberg, W.; Houle, F. A.; Lee, S. W.; Ito, H.; Kanazawa, K., *Macromolecules* **2005**, *38*, 1882-1898

CHAPTER IX

1. C. Aronica, G. Pilet, G. Chastanet, W. Wernsdorfer, J.-F. Jacquot, and D. Luneau, *Angew. Chem. Int. Ed. Engl.*, 2006, **45**, 4659–62.
2. X.-H. Bu, M.-L. Tong, H.-C. Chang, S. Kitagawa, and S. R. Batten, *Angew. Chem. Int. Ed. Engl.*, 2004, **43**, 192–5.
3. E. Q. Procopio, T. Fukushima, E. Barea, J. A. R. Navarro, S. Horike, and S. Kitagawa, *Chemistry*, 2012, **18**, 13117–25.
4. V. Tangoulis, C. P. Raptopoulou, S. Paschalidou, A. E. Tsohos, E. G. Bakalbassis, A. Terzis, and S. P. Perlepes, *Inorg. Chem.*, 1997, **36**, 5270–5277.
5. E. M. Johnston, S. Dell'Acqua, S. Ramos, S. R. Pauleta, I. Moura, and E. I. Solomon, *J. Am. Chem. Soc.*, 2014, **136**, 614–617.
6. D.-D. Li, F.-P. Huang, G.-J. Chen, C.-Y. Gao, J. L. Tian, W. Gu, X. Liu, and S.-P. Yan, *J. Inorg. Biochem.*, 2010, **104**, 431–441.
7. D.-D. Li, J. L. Tian, W. Gu, X. Liu, and S.-P. Yan, *J. Inorg. Biochem.*, 2010, **104**, 171–179.
8. T. C. Brunold, *Proc. Natl. Acad. Sci.*, 2007, **104**, 20641–20642.
9. S. Hikichi, M. Yoshizawa, Y. Sasakura, M. Akita, and Y. Moro-oka, *J. Am. Chem. Soc.*, 1998, **120**, 10567–10568.
10. S. Kundu, F. F. Pfaff, E. Miceli, I. Zaharieva, C. Herwig, S. Yao, E. R. Farquhar, U. Kuhlmann, E. Bill, P. Hildebrandt, H. Dau, M. Driess, C. Limberg, and K. Ray, *Angew. Chem. Int. Ed. Engl.*, 2013, **52**, 5622–6.
11. P. L. Larsen, T. J. Parolin, D. R. Powell, M. P. Hendrich, and A. S. Borovik, *Angew. Chemie Int. Ed.*, 2003, **42**, 85–89.
12. T. Jia, S. Zhu, M. Shao, Y. Zhao, and M. Li, *Inorg. Chem. Commun.*, 2008, **11**, 1221–1223.

13. Y.-Q. Zheng, D.-Y. Cheng, B.-B. Liu, and W.-X. Huang, *Dalt. Trans.*, 2011, **40**, 277–286.
14. N. Lah, I. Leban, and G. Giester, *Acta Crystallogr. Sect. C*, 2007, **C63**, m222–m224.
15. R. Cejudo, G. Alzuet, J. Borrás, M. Liu-González, and F. Sanz-Ruiz, *Polyhedron*, 2002, **21**, 1057–1061.
16. A. D. Burrows, M. F. Mahon, V. M. Sebestyen, Y. Lan, and A. K. Powell, *Inorg. Chem.*, 2012, **51**, 10983–10989.
17. G. Li, S. Song, N. Xu, X. Liu, and Z. Su, *J. Solid State Chem.*, 2008, **181**, 2406–2411.
18. K. Darling, W. Ouellette, A. Prosvirin, S. Freund, K. R. Dunbar, and J. Zubieta, *Cryst. Growth Des.*, 2012, **12**, 2662–2672.
19. J. Chen, T.-W. Wang, Z. Zhang, Y. Song, Q. Zhao, J. Ni, and Z.-L. Wang, *J. Mol. Struct.*, 2006, **794**, 154–159.
20. E. Rather, J. T. Gatlin, P. G. Nixon, T. Tsukamoto, V. Kravtsov, and D. W. Johnson, *J. Am. Chem. Soc.*, 2005, **127**, 3242–3243.
21. L. Que Jr. and W. B. Tolman, *Angew. Chem. Int. Ed. Engl.*, 2002, **41**, 1114–1137.
26. R.L. Frost, P.A. Williams, W. Martens, P. Leverett, J.T. Kloprogge, *AM Mineral*, 2004, **89**, 1130-1137.
27. W. Marten, R.L. Frost, J.T. Kloprogge, P.A. Williams, *J Raman Spectrosc*, 2003, **34**, 145-151.